CRANFIELD UNIVERSITY

MAN SAN LI

2D LOW BYPASS-RATIO TURBOFAN MODELLING

School of Engineering

A thesis submitted in fulfilment of the requirements for the degree of

PhD

2004

CRANFIELD UNIVERSITY

SCHOOL OF ENGINEERING

DEPARTMENT OF POWER, PROPULSION AND AEROSPACE ENGINEERING

PhD

2004

2D LOW BYPASS-RATIO TURBOFAN MODELLING

Man San Li

Supervisors: Professor Pericles Pilidis

Dr. Junfei Yin

October 2004

ABSTRACT

Turbofan engines are normally bench-tested with a standard flared bellmouth intake. This is different from the aircraft situation. As a result, an engine installation may experience a degree of inlet flow distortion not normally present during tests. It is, therefore, very desirable to understand the effect of any radial inlet total pressure loss on turbofan engine performance.

Steady-state radial inlet distortion may occur, for example, as a result of boundary layers. An early awareness on distortion tolerance is very important to enable the prediction of surge margin. However, synthesis of turbofan performance with distortion is currently not available.

This work therefore, investigates in detail the modelling of the fan component of low bypass-ratio turbofan engines within an engine performance simulation program. For example, the air flow in turbofan engines is split after the fan between the core gas generator and the bypass flow. A fan model must be able to simulate the required flow and thermodynamic parameters to the core and bypass flows at fan exit. Conventional fan models, however, are restricted to a fixed bypass ratio versus non-dimensional speed schedule at which the fan has been rig-tested. The fan component also experiences a varying degree of inlet total pressure distortion. Existing engine simulation fan models are unable to quantify this effect on fan performance and on engine performance.

The turbofan modelling work conducted here is preceded by an analysis of rig data of Low Bypass Ratio (LBPR) turbo-fan engines to give a firm background basis. The engine modelling uses the component-based iterative solution method for gas turbine performance calculations.

Two key outcomes of the work are the following. Firstly, LBPR fans have large circumferential fan exit flow variations as well as radial variations. This includes total temperature profiles which are an order of magnitude higher than those for High Bypass Ratio Fans (HBPR) fans. Secondly, it is inconclusive, at a given non-dimensional speed and flow function, as to whether fan exit profiles are independent of BPR.

The fan radial profile modelling starts from an existing modification of a conventional compressor characteristic but also models in 2-D with dependency on the fan exit radial position. The inlet distortion fan model uses a throughflow streamline curvature for radial performance prediction coupled to the 2-D-LBPR fan model.

Against this background, a new fan characteristic model has been devised for LBPR fans. In addition, a new inlet distortion performance model has been developed which is able to predict engine performance changes with radial inlet total pressure distortion.

NOTATION

A	Area
a	sonic velocity
AIP	Aerodynamic interface plane
APNASA	NASA average passage code
BPR	Bypass ratio
chic	characteristic
C	Velocity
CMFF	Cumulative mass flow fraction
cp	Specific heat capacity at constant pressure
cv	Specific heat capacity at constant volume
cv	Control volume
cs	Control surface
DC(θ)	Distortion coefficient
FPR	Fan pressure ratio
h	Static enthalpy
H	Total enthalpy
HBPR	High bypass ratio
HPC	High pressure compressor
IGV	Inlet guide vane
LBPR	Low bypass ratio
LPC	Low pressure compressor
P	Stagnation pressure
p	Static pressure
PAV	Ring average pressure
PFAV	Face-average total pressure
M	Mach number
$\dot{m}$	Mass flow
MSPC	Multiple segment parallel compressor
N	Rotational speed
NPSS	Numerical propulsion system simulator
OGV	Outlet guide vane
PRI	Pressure recovery of inlet
RRAP	Rolls-Royce Aeroengine Performance
r	Radial direction
sfc	Specific fuel consumption
SLC	Streamline curvature
SOT	Stator outlet temperature
SRE	Simple radial equilibrium
t	Static temperature
T	Stagnation temperature
TET	Turbine entry temperature
U	Mean wheel speed
UTC	University technology centre
V	Velocity
VGV	Variable guide vane
w	mass flow rate
ZNLRT	Non-dimensional speed 'handle'

β	Arbitrary fan mapping parameter
γ	Specific heat ratio
δ	Referred pressure
$\bar{\nabla}$	Vector 'del' operator
$\bar{\varepsilon}$	Unit vector in cylindrical coordinate system
θ	Tangential direction
θ	Referred temperature
μ	Bypass ratio
π	Pressure ratio
ρ	Density
ψ	Pressure rise coefficient
ϕ	Flow coefficient

0D	0-dimensional
1D	1-dimensional
2D	2-dimensional
3D	3-dimensional

Subscripts

0	Stagnation conditions
1	Inlet to blade row or stage
2	Exit to blade row or stage
ax	Axial
casing	Casing station
crit	Critical
f	Face
hub	Hub station

i	Ring number
in	Compressor inlet
in	Inlet station
is	Isentropic
L	Low pressure spool
m	Meridional direction
nom	nominal
r	Radial direction
rad	radial
j	Streamline reference no.
s	Isentropic
SS	Static to static
t	Total (stagnation) condition
TS	Total to static
x	Axial direction
z	Axial direction
θ	Circumferential direction
θ	Angle in distortion parameter

TABLE OF CONTENTS

LIST OF FIGURES

LIST OF TABLES

ACKNOWLEDGEMENTS

The author wishes to thank:

The EPSRC and RR for their funding of this work, and the Royal Academy of Science for the conference grant.

The Cranfield/Rolls-Royce UTC team with whom I spent much time: Richard, Geoff, Matthew, Sandro, Suresh, Phil, Luca. John Martin, Tony Jackson for coming to the reviews.

Laura Vaughan and Dickon Skinner for their help with data in earlier days.

Barbara, Sue, Rachel and Caroline, Mike for all their help in SoE.

Friends during my time in Cranfield; Aseem, Mohsen, Judith, Clive, Friederike.

Joao Barbosa and Ken Ramsden for the essential compressor model.

Barry Curnock, for giving me the opportunity to work.

Dr. Junfei Yin, for all the technical help and other advice.

Special regards for Professors Pilidis and Singh for their understanding during difficult times and without whom I would be in a completely different place today.

Finally to my family and Erna.

Chapter 1

INTRODUCTION

1 INTRODUCTION

The overall aim of the project is to achieve an improvement in the performance modelling of low bypass ratio (LBPR) turbofans by improving the modelling of the fan or low-pressure compressor component.

1.1 ROLLS-ROYCE CRANFIELD UNIVERSITY AND UTC IN PERFORMANCE ENGINEERING

The work is done in conjunction with Rolls-Royce plc within the Rolls-Royce – Cranfield University UTC in performance engineering. It was partly funded by a UK Research Council EPSRC CASE studentship and by Rolls-Royce plc. The work was under 2D-fan modelling under work package 2.

1.2 LBPR TURBOFAN PERFORMANCE MODELLING

1.2.1 Gas turbine aeroengine performance modelling

Gas turbine modelling is a necessity in the aeroengine industry throughout the life cycle of an engine project. This can be to determine new engine capability or to assess an existing engine's performance against a standard, as examples.

The main method used throughout the industry to calculate gas turbine performance is the component-based iterative model. It divides the engine into discrete component bricks, usually with 1D input and output of flow and thermodynamic parameters. The bricks are maps of the performance of the components. The method iterates until all bricks are matched at unique operating points for the engine power setting for example.

1.2.2 Compressor modelling in engine performance simulation

Rolls-Royce for example has long established the need to rig test compressors to determine their performance (Hooker, 1990). The resulting compressor characteristics are the basis of the compresssor performance brick in component-based simulation programs. Typically, these are non-dimensional, with pressure ratio and isentropic efficiency as functions of non-dimensional speed, non-dimensional flow and compressor beta (an arbitrary mapping parameter).

1.2.3 Turbofan aeroengines

The Rolls-Royce Conway engine was the first bypass engine (turbofan) in civil service in the VC-10 aircraft in the 1960s. Bypassing some of the air through the fan around the core gas generator of the engine was adopted to improve propulsive efficiency of the aeroengine and thus improve sfc. The act of splitting the fan exit flow by a bypass splitter to core and bypass passages creates a modelling situation different to that of core compressors.

1.2.4 Fans

The fan component is situated at the front of the engine after the intake in turbofan engines. It fundamentally works with the same principles as an axial compressor. There are subtleties associated with its positioning, which provide the drivers for the research for this thesis.

1.3 RESEARCH FOR THIS THESIS

Two of the important phenomena associated with low bypass engines as are typically installed in military aircraft are looked at. One is the main cause of radial fan exit profiles. Due to the difference in rotational speed between the root and the tip of the fan blades, there is a significant difference in pressure delivery in the exit plane between these two positions. The second phenomenon is the major cause of a radial fan inlet profile in a steady state condition. The installation of the engine in the airframe of many military aircraft with LBPR engines can lead to considerable growth of boundary layer at the inlet at the tip of the fan. everal other factors will modify these profiles in a complex manner.

Traditional performance simulation deals with the fan exit radial profiles by averaging the thermodynamic and flow parameters radially across the annulus and applying the resulting one-dimensional values to form the compressor characteristic map. This map is used in the engine performance simulation program in which all the other engine components are also modelled one-dimensionally. Attempts to improve this have involved treating the fan as two compressor characteristics; one representing the outer region of the fan and the other representing the core or inner portion. There is no established method to model compressor performance with radial inlet profiles.

Recent collaboration between Rolls-Royce and the Performance UTC has led to a new 2-D fan radial profile model for high bypass ratio (HBPR) turbofans. This forms the starting point for this research work.

1.4 LAYOUT OF THE THESIS

After the introduction, the thesis is divided into 4 further sections.

1.4.1 Literature review

This is a more general view of the main topics related to this thesis. They can be divided into 4 main themes: turbofan engine performance simulation, compressor and fan modelling in engine performance simulation, radial inlet distortion modelling and circumferential inlet distortion modelling. Some of the greater detail is not shown here but within the later subject chapters as they are important inputs to the work there.

1.4.2 Fan radial profile and bypass modelling

This chapter explores the background of the fan characteristic representation in LBPR turbofan simulation and proposes a new model based on data analysis and review of the literature. The new model is described and then tested to compare with the previous fan models, and conclusions made.

1.4.3 Fan inlet distortion performance modelling

This chapter discusses the inlet distortion prediction method identified in section **1.4.1** , and then proposes a method of merging it with the turbofan engine simulation. The resulting model is described and a series of performance simulations are made and analysed.

1.4.4 Conclusions and further work

The overall conclusions to the work in this thesis are made. A list of suggested further work is then detailed.

1.5 AUTHOR'S CONTRIBUTION

The task of the author has been to assess the current state of fan performance modelling in LBPR turbofan engine performance and to see where improvements can be made in the accuracy and the information provided by existing methods.

The main contributions to knowledge have been to devise 2 new fan models in turbofan performance simulation.

In fan radial profile bypass modelling, the inputs are an existing engine performance simulation code, and LBPR fan rig test data. The main output is a new fan code integrated into the engine simulation code. The author has also modified 2 existing fan models with the LBPR fan rig data for the comparison analysis.

In the radial inlet distortion modelling, the inputs are the existing engine performance simulation code and an existing compressor performance prediction code. The main output is a new fan code integrated with the engine simulation.

1.6 SCOPE OF THE WORK

The main field of this work is in gas turbine aeroengine performance simulation and NOT in turbomachinery flow field prediction. At times, the work will delve into the turbomachinery field. However, the work has to be a practical application of fan/compressor modelling in the engine performance simulation field. It must lean towards the description of the fan in the engine simulation rather than the fidelity of the modelling of the physical processes.

Therefore, the use of the streamline curvature tool in Chapter 4 for example makes no attempt to improve the program or the accuracy of its prediction. The importance is to learn how it can interact with the performance simulation code. On the same theme, although a data analysis of fan rig tests has been carried out, the importance is stressed on how to model the findings rather than to gain the best physical understanding of the profiles found.

In the field of aeroengine modelling, validation of models with physical data is necessarily limited outside of the large engine manufacturers because of the extreme cost of testing. The form of validation in Chapter 3 is to compare with how the new fan model synthesizes performance compared to the previous methods. In Chapter 4, no prior method of modelling exists. The model is examined to see whether it gives realistic trends in results. It must be stressed that in the field of gas turbine performance in industry, simulation models are always adjusted to best match a measured engine test at one condition for example.

Chapter 2

LITERATURE REVIEW

2 LITERATURE REVIEW

This chapter examines some of the work carried out in the field of engine performance modelling and effect of inlet distortion modelling on aeroengines. The main subject of this thesis is turbofan performance modelling. Next, the fan component is considered as a compressor; the modelling of compressors in engine simulation codes is looked at followed by modelling methods for compressors. After this, some information is presented on distortion modelling. This thesis covers work on radial inlet distortion modelling, but information is also given on circumferential distortion modelling as background to future work planned.

2.1 TURBOFAN PERFORMANCE SIMULATION

The underlying theme of this thesis is computer simulation of a turbofan aero gas turbine engine.

2.1.1 Component level iterative models

The industry standard simulation model for calculating steady-state gas turbine off-design performance is an iterative guess-check method based on the following constraints: compatibility of flow; compatibility of work for compressors and turbines on the same shaft, conservation of momentum (bleed mixing and mixed flow nozzles), and satisfying the component maps throughout the gas turbine. Components are discretised as bricks; the passage of flow and thermodynamic parameters through the simulation are as 1-D parameters. An engine model will have a set of iterative guessed parameters and corresponding checks (constraints). The constraints are reduced to as small as practical to zero by an iterative solver, e.g. Newton-Raphson.

The fine details of these simulation codes will not be reviewed here but good accounts are available ([2]Saravanamuttoo, 1992, Cohen et al, 1996, Walsh, 1998) and a fairly current summary of the state of gas turbine simulation in the industry is given in RTO-TR-044 (2002). An example is the component based program used in this work (**Appendix 5**).

During the conceptual design of an engine, the performance of each component is estimated from an empirically derived database or from rig test results. For a new component, the performance would be derived from a database and would be a first approximation. The performance maps are updated later in the design process by an analysis of the components with CFD codes and eventually with test data.

The iterative scheme can be classed as serial iteration or a matrix method (Mattingly et al, 1987). Both depend on minimizing the error in the checks, the latter being able to reach convergence in fewer iterations.

Recent developments have attempted to model the components with greater detail in one dimension, (either radially or circumferentially), but with averaging after the component to obtain the 1D parameter values for the engine model e.g. Yin et al (1999), Riegler et al (2001).

2.1.1.1 Industry aeroengine simulation codes

Simulation programs of component level type are the most common e.g. Ismail and Bhinder (1991), Kurzke (1995), Sanghi et al, (1998). Some software is available to the general public either commercially, e.g. GasTurb (Kurzke, 1995), or freely available from a research establishment, e.g. GSP (Visser and Broomhead, 2000).

Some industry simulation codes in Fortran language are identified by Follen et al (1998) in **Table 1**

SOAPP – State of the Art Performance Program – Pratt & Whitney, originating from 1971	**GSA** – Boeing research propulsion program – 1960s
ROCETS – modular rocket design and analysis system	**FAST** – Allied Signal simulator – 1980s
CWS – General Electric Aircraft Engines performance system – 1980s	**ATEC** – Aerodynamic Turbine Engine Code in AEDC
RRAP – Rolls-Royce's modular simulation system	**TERMAP** – Allison Engine Company
NNEP – NASA Lewis Research Center simulation program	**BIEPP** – Boeing installed Engine Performance Program

Table 1 Industry simulation codes. (Follen et al, 1998).

2.1.2 Component zooming in NPSS

A large project has been undertaken in the USA to ultimately solve the whole flowfield through the engine with CFD, but to retain the former component level system in the interim. The effort has been driven by the fact that although component performances are defined by test or by prediction, they may not behave as predicted when inside the whole engine. This may be in large part due to the lack of knowledge of the dimensional (i.e. radial or circumferential or 3D) inputs to the components as they interact with each other inside the engine. There are current efforts in the field that attempt to model a gas turbine with the

components in greater detail. In its various modes, it ranges from "zooming" in greater detail on one component, to modelling a whole LP system

The project is overseen by NASA and is called the Numerical Propulsion System Simulation (NPSS) involving several US companies (**Table 2**). It is one of the few attempts to address the flowfield in a simulation program at 2-D and higher detail. Details of NPSS are given in Drummond et al (1994), Reed and Afjeh (1995, 1996), Lytle (1997), Evans et al (1998), Follen et al (1998), Follen and auBuchon (1999). NPSS is an environment within NASA's High Performance Computing and Communication Program (HPCC). The objective is to enable simulation of a complete aeropropulsion system in sufficient detail, with NPSS as a "numerical test cell" to resolve critical design issues early on in the design process before the engine is built. Complicating the issue is the decision to also integrate the different disciplines involved with the design of aircraft gas turbines, such as aerodynamics, structures, and heat transfer.

NASA Lewis Research Center	General Electric Aircraft engines
Pratt & Whitney	The Boeing Company
AlliedSignal Engines	Allison Engine Company
Williams International	Teledyne Ryan Aeronautical
WPAFB	AEDC

Table 2 NASA industry partners for NPSS. (Follen et al, 1998).

Initially, the underlying engine performance routine in NPSS is the National Cycle Program (NCP), which is being developed by NASA Lewis and industry partners (**Table 2**). NCP is based on object-oriented programming, which is a recent trend, as also in GSP (Visser and Broomhead, 2000). It is designed to have all conventional cycle simulation features as well as the specialised NPSS concepts of component code zooming and distributed/parallel processing.

New features of NCP compared to conventional simulation programs have had to be implemented to achieve the objectives of NPSS:

- Integration of higher order computational fluid dynamics.
- Integration of multidisciplines.
- Integration of parallel / distributed processing of each engine element whilst preserving an overall engine system view.

2.1.2.1 Engineering models of NPSS

The engineering models of NPSS have been divided into 3 areas:

- Component integration for large subsystem and system simulations
- Multidisciplinary coupling to capture critical interactions amongst the disciplines
- Variable complexity analysis – to apply the required level of complexity to the problem being studied

Regarding component integration, as stated earlier, zero-dimensional (parametric level) engine simulations cannot resolve the complex multi-dimensional flows within the engine. It should be noted that what NASA terms 0D is what others may classify as 1D. The NASA definition of 1D is for example, to "zoom" to the interstage flow parameters of a compressor. Traditional component design methods assume steady uniform boundary conditions. The NASA solution is to perform larger scale simulations, with the code run in parallel to reduce the overall analysis time. For turbomachinery, the analysis of each blade row can be also performed in parallel. The strategy for updating boundary conditions to account for the propagation of disturbances both upstream and downstream is critical. The APNASA code (Lytle, 1997) illustrates the kind of subsystem simulation being carried out: coupled fan – booster – core inlet, mixer – nozzle, inlet – fan, using a cluster of workstations with a simulation time about 10 hours.

In multidisciplinary coupling, the attempt is to simulate for example, in the compressor, aerodynamic, structural and thermal loadings contributing to changes in the geometry (casing, blade shape, tip clearances). This will affect the efficiency and stability of the compressor. Traditionally, the interactions are considered sequentially through different, unrelated codes. Several levels of coupling are being investigated.

Variable complexity analysis; it had probably been recognised that the ultimate goal of a full CFD computation of the engine would be difficult to achieve, and for simulations in a practical timescale, "zooming" has been adopted. An example is to determine the effect of a change in the shape of a fan blade on engine performance may only require a 3D simulation of the fan stage, with the rest of the engine modelled at lower levels of detail. In zooming a component, the 0D engine cycle will iterate much faster than the 3D simulation, so the 3D simulation must be performed in parallel over a cluster of workstations to minimise time.

No literature has been found so far that accounts for the different levels of zooming of the fan or compressor in NPSS, except for 3D Navier-Stokes computation of compressors.

2.1.3 Suitability for university research

As quoted by Lytle (1997), 3-D simulation of the primary flowpath in a full engine would require greater than 10^{12} floating point operations per second, which is only available in a very few expensive machines. NPSS would require 10^{15} FLOPS. No serial or moderately parallel machine can do this. Therefore, the NPSS approach is to use large numbers of parallel processors by using the large number of workstations and PCs normally existing within an organisation. The development of such software as a research project is probably too complex for one research student although a university should have the required equipment to make it work. If subsystem modelling and multidisciplinary modelling is embarked upon, it must be the focus of a team of researchers.

2.2 COMPRESSOR AND FAN MODELLING IN PERFORMANCE SIMULATION

This section reviews the modelling of the compressor or fan component within a component-level iterative engine simulation. The complexity of the flow field is looked at first, although this could equally well apply to section **2.3**.

2.2.1 The compressor flow field

Lakshminarayana (1996) has reviewed the compressor flow field in detail. Gallimore, (1999) introduces the flow field in a simpler form. The incorporation of three-dimensional effects into turbomachinery analysis is essential for accurate prediction of the performance. The three-dimensional effects examined here are inviscid and quasi-viscous effects. Both viscous and inviscid effects cause three-dimensionality in the flow. (Quasi-viscous analysis methods, take into account real fluids effects in an approximate or global manner. For example, secondary flow arises due to viscous boundary layer, but the analysis of its effect is treated inviscidly).

Some of the three-dimensional inviscid effects are due to:

- Compressibility, and radial density and pressure gradients.
- Radial variation in blade thickness and geometry.
- Presence of finite hub and annulus walls, annulus area changes, flaring, curvature and rotation.
- Radially varying work input or output.
- Radial component of blade force and the effects of blade skew, sweep, lean and twist.
- Leakage flow due to tip clearance and axial gaps.
- Non-uniform inlet flow and presence of upstream and downstream blade rows.
- Mixed-flow (subsonic, supersonic, and transonic flow) regions along the blade height with shock/boundary layer interaction.
- Secondary flow caused by inlet velocity/stagnation pressure gradient and flow turning.

Most of these are caused by inviscid effects, which can be treated by the use of inviscid equations of motion. The secondary flow is caused primarily by the presence of viscous layers on the walls. The dominant influence here is the velocity gradient normal to the wall or the presence of normal (to the streamline) vorticity upstream of the blade row. Three-dimensional inviscid (or secondary flow) theories have been developed to predict the nature of three-dimensional flow away from the walls. These theories account for effects of the velocity gradients upstream of the blade row.

In many cases, the inviscid and viscous effects augment each other. For example, even though the leakage flow arises due to blade unloading, its subsequent roll-up and diffusion is controlled by viscous effects. Likewise, two- and three-dimensional shocks are often associated with separation and hence the viscous interaction effects cannot be ignored.

6.2.1 → For losses

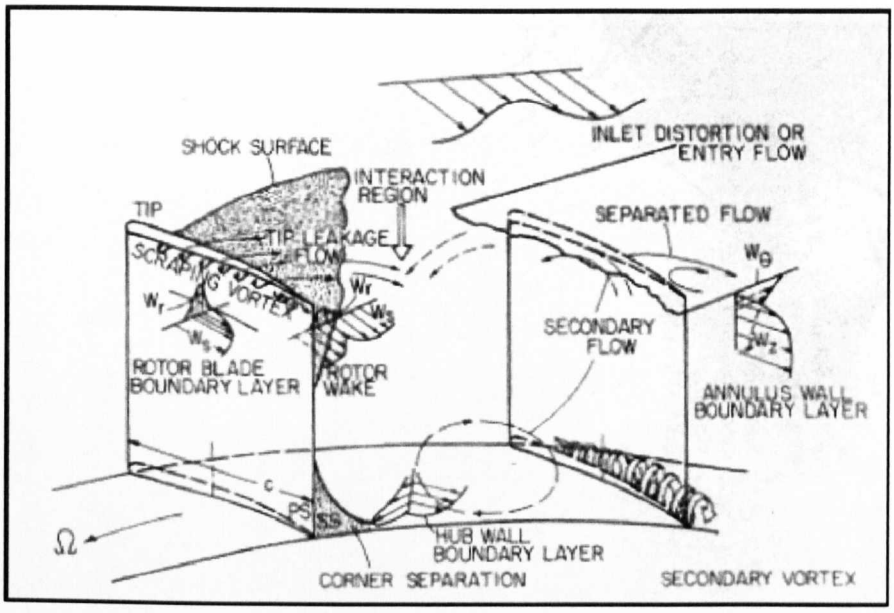

Fig. 2.1 Nature of flow in an axial flow compressor rotor passage, (Lakshminarayana, 1996).

The three-dimensional effects are illustrated in Figure 6.1 and Figure 6.2. Most of the inviscid effects are schematically shown in Figure 6.2. The radius change of the annulus and the hub walls, as well as change in stream tube height due to area changes, results in spanwise flows. The radial variation of blockage (and area changes in the radial direction) gives rise to radial or spanwise flows. Because the rotor blade is usually thicker at the root than at the tip (from structural considerations), radial shifts in the streamlines occur, thus resulting in radial flows. Likewise, radially varying work input or output also causes spanwise flow generation. The compressibility effect results in density discontinuity and deviation from the radial equilibrium equation, and induces radial flows inside the blade passage, even in situations where the flow is in simple radial equilibrium upstream and downstream of the blade row.

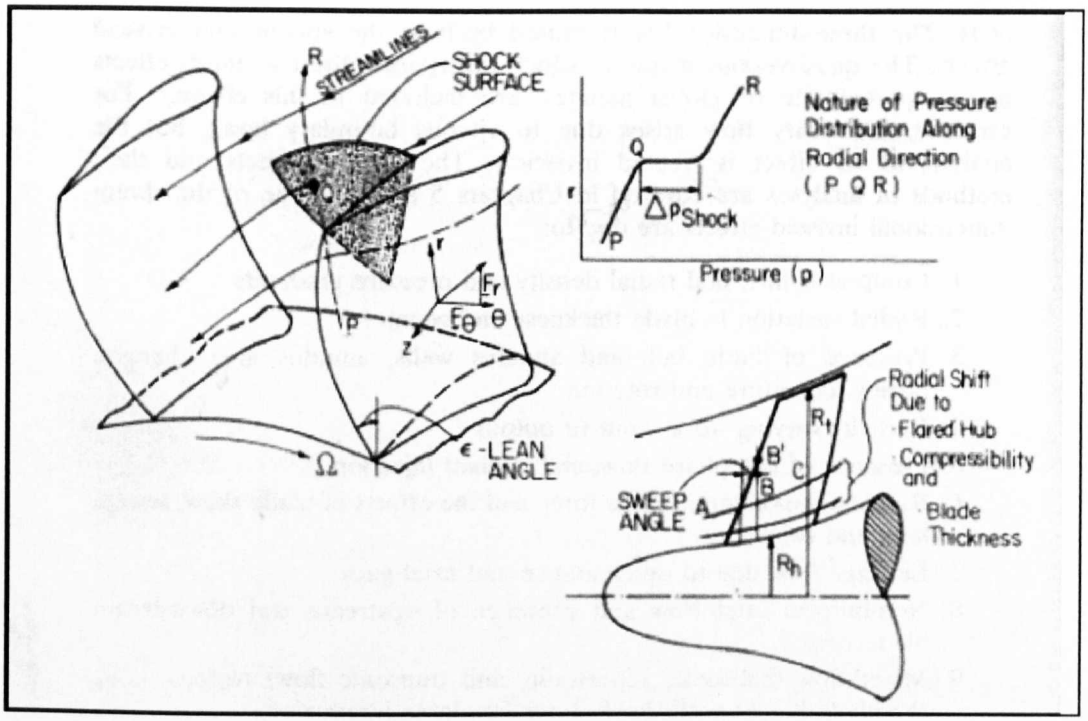

Fig. 2.2 Three-dimensional inviscid effects in turbomachinery, (Lakshminarayana, 1996).

This simple radial equilibrium equation indicates that the centripetal force is directly proportional to density, which changes along the streamline inside the passage, resulting in an imbalance between the radial pressure gradient and the centripetal force. This introduces additional acceleration terms. Thus additional radial flows arise due to the compressibility effect.

A similar argument can be put forward to explain the presence of spanwise flows in a passage with a three-dimensional (skewed) shock structure as shown in Figure 6.2. In this case, the pressure jump and streamline divergence across a shock (say Q in Figure 6.2) disturbs the simple radial equilibrium, giving rise to imbalance between the centrifugal forces and the radial pressure gradient. To achieve a new equilibrium condition (say from Q to R), radial acceleration and radial flows have to develop.

Additional three-dimensional effects arise due to sudden change in flow turning and the associated streamline divergence as well as jump in density across the shock. This disturbs the radial equilibrium and introduces three-dimensionality including radial flows. Measurements taken in transonic and supersonic turbomachinery reveal the presence of large radial flows due to three-dimensional shock structure. Even though these flows can be treated by inviscid theories away from blade and walls, the viscous effects and flow separation due to three-

dimensional shock/boundary layer interaction and the resulting radial flows in these separated regions make it necessary to include the three dimensional viscous effects.

Blade sweep and radial blade force introduces three-dimensionality. For example, the blade sweep shown in Figure 6.2 introduces large pressure gradients along BB'. Because of the absence of blade beyond B', the radial line spans the blade passage up to B' and the free stream beyond B'. This introduces appreciable radial pressure gradient and associated radial flows. Likewise, the radial blade force, Fr introduces radial acceleration.

The tip leakage flow results from the unloading of the blade, causing a very complex three-dimensional and vortex flow field at the tip. The upstream non-uniform flow (radial or circumferential) results in radially varying output/input or circumferentially non-periodic flow, both of which provide an additional mechanism for the generation of spanwise flows.

2.2.2 2 and 3-D viscous effects and losses

Both the geometric description of the fluid flow domain and the physical processes present are extremely complicated. The following features exist:

3-dimensional, viscous and unsteady flow.

Flow may be incompressible or compressible, with subsonic, transonic and supersonic regimes which may be present simultaneously in different regions.

The viscous flow usually has high freestream turbulence, which may include multiple length and time scales.

Regions of laminar, transitional and turbulent flows, separated flows and fully developed viscous profiles may all be present simultaneously due to the multiplicity of length scales introduced buy the complicated geometry of the flow field.

Viscous and turbulent regions encounter complex stress and strain due to the presence of 3-dimensionality, large pressure gradients in all directions, rotation, curvature, shock waves, shock wave-boundary layer interaction, interacting boundary layers and wakes, heat transfer and cavitation.

The flow field may be dominated by vortical flows: (secondary flow, tip leakage vortices, shed vortices, leading edge horseshoe vortices and scraping vortices).

The following flowpath parameters affect the flow: radial distribution of stagger angle, radial distribution of camber, radial distribution of thickness, lean, twist, dihedral, sweep, skew, flare, aspect ratio, hub-to-tip ratio, tip clearance, endwall curvature (hub and tip), axial

spacing between blade and vane rows, flow path area change, part-span dampers – this changes the domain from periodic simply connected to periodic multiply connected, recirculating passages at hub or tip, surface roughness, offtake bleeds.

The viscous effects of the flow which affect turbomachinery flow:
Laminar, transitional, turbulent and separated boundary layers and wakes due to blade profile (both 2D and 3D effects).
Annulus and hub-wall boundary layers.
Mixing of tip clearance leakage flow, secondary flow and horseshoe vortex, and annulus-wall boundary layers in the endwall.
Spanwise mixing downstream of the blade row.
Shock-boundary layer interaction.
Shock losses.

2.2.3 Real fluid effects

The following are the viscous and turbulent effects:

- Losses associated with viscous effects decrease the efficiency through stagnation pressure loss and increase in entropy. It also decreases pressure rise in compressors.
- Viscous effects affect the local and global flow properties inside the passage and downstream of the blade row.
- Viscous effects introduce 3-dimensionality in the flow and affects the flow properties (which vary in the spanwise and blade-to-blade directions), thus introducing off-design conditions in subsequent blade rows.
- Viscous layers introduce blockage to the flow, limiting the performance through decreased effective area, and decreased pressure rise. As the mass flow is reduced at constant rotational speed, pressure rise tends to increase due to increased angle of incidence to the blade. However, the viscous effects also increase, increasing the loss and blockage as the mass flow is reduced. This limits the increase in pressure rise, creating a characteristic pressure rise/flow curve which peaks as the mass flow is reduced. (Normally, on reducing W, increases, but here we reduce W by blockage, and area reduces so the flow angles don't increase as much as without blockage, therefore, there is less pressure rise. So reducing the mass flow, i.e. at off-design increases viscous effects

because of the higher angles).Beyond, the peak is system instability called rotating stall. If the mass flow is reduced beyond the peak pressure rise, rotating stall quickly degenerates into a more severe system instability called surge.

- In single-stage or multistage turbomachinery, with alternating stationary and rotating blade rows, the viscous layers (and wakes) introduce unsteadiness in the subsequent blade row. The viscous-induced unsteadiness causes vibration of the blade row and noise generation.

2.2.4 Compressor characteristic in simulation

The standard representation of the compressor in a simulation program is the plot of pressure ratio as a function of non-dimensional flow and beta and isentropic efficiency as a function of non-dimensional flow and beta (**Fig. 2.3**). Beta lines are also added as a mapping aid, to avoid ambiguity when speed lines are vertical (as near choke) and when speed lines are near horizontal (near stall/surge).

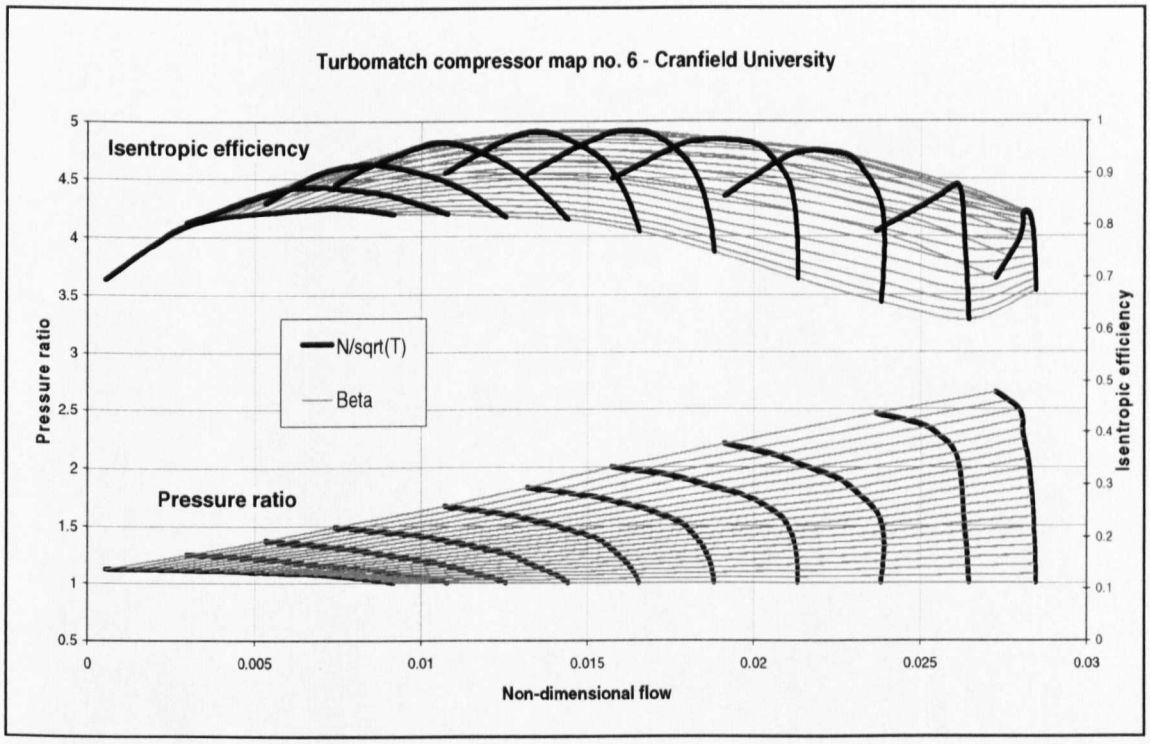

Fig. 2.3 Compressor characteristic map for turbofan engine performance simulation program.

Variations of this map can include using $\Delta H/T$ or and $\Delta H_{ID}/T$ instead of pressure ratio, which removes the need for isentropic efficiency. It also allows a direct match for spool

power for compressors and turbines rotating on the same shaft. The description of compressor characteristics for fans in turbofan engines is left until section **3.3**, as it is them main theme of Chapter **3**.

The standard rig measured compressor representation has been identified to have the following deficiencies (Serovy, 1976), part of which this thesis tackles in the context of engine performance simulation:

- Changes in gas properties such as molecular weight and specific heat ratio.
- Effects of Reynolds number and inlet turbulence on performance.
- Modified entrance flow distributions such as distorted or transient inlet pressure, temperature or velocity patterns.
- Influence of differences in discharge boundary conditions, which normally exist between a test compressor rig and the engine system.
- Location of blade flutter regions.

2.3 COMPRESSOR AND FAN MODELLING METHODS

Gas turbine development time and cost could be significantly reduced if the performance characteristics of the fan and compressor components could be predicted with precision and confidence. It is one of the most difficult problems in applied fluid dynamics as flow patterns at design point are complex, but at off-design flows and rotational speeds, or with non-design entrance flow distributions or exit boundary conditions, introduces additional regions of separated or choked flow, often accompanied by excessive aerodynamic or aeromechanical instability. See Section 6 outlining the complexity of the compressor flow field.

Several good reviews of compressor performance prediction methods supply the information for this section; (Serovy, 1976, Dunham, 1986, Cumpsty, 1989, Wennerstrom, 1991, Denton, 1999). Flow field definition or design analysis computation methods use as the input the compressor geometry. The output includes distributions of fluid properties and velocities throughout the compressor for specified off-design values of flow rate and rotational speed.

2.3.1 Methods for generation of component performance maps

All of the flow field prediction methods will be classified as computational fluid dynamics (CFD) methods. The definition (Dunham, 1986) is that a CFD method is a solution of the inviscid or viscous equations of fluid motion in two or three dimensions.

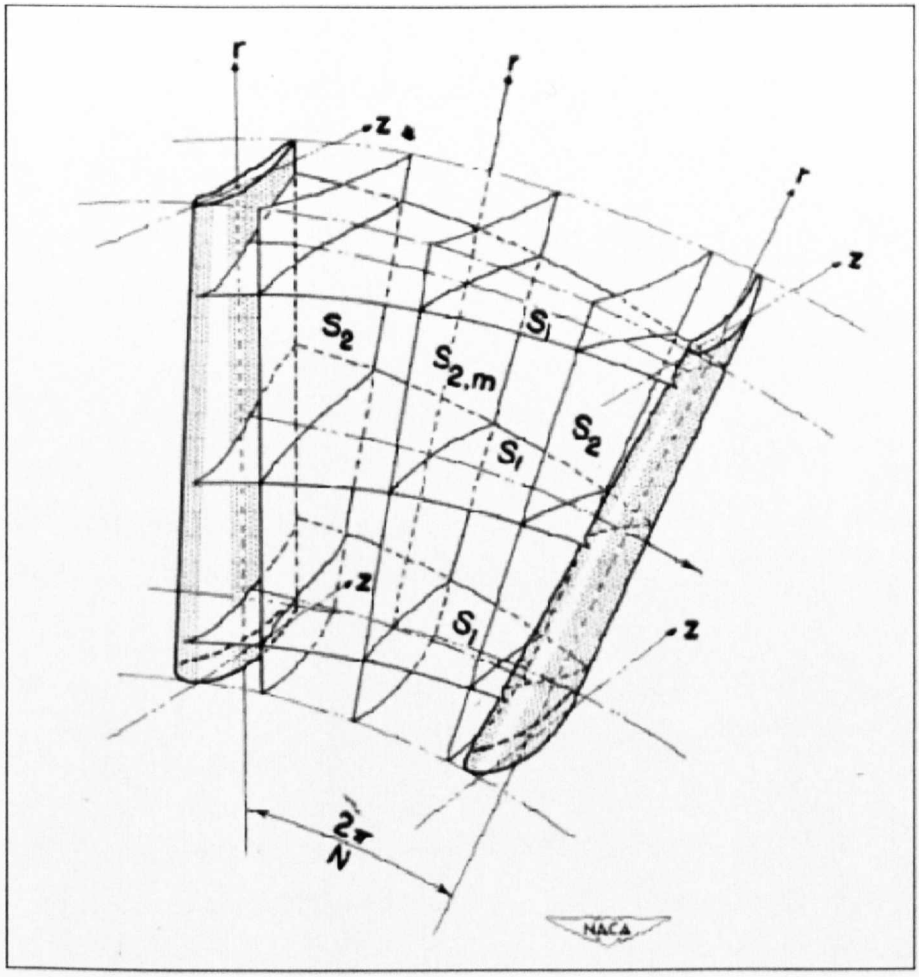

Fig. 2.4 Intersecting S1 and S2 stream surfaces in a blade row. (Wu, 1952).

2.3.1.1 Wu's S1/S2 method

For the purposes of definitions, it is convenient to begin with the first attempt at a three-dimensional solution (Wu, 1952), who analysed the flow as two intersecting and interrelated stream surfaces. These are the blade-to-blade (S1) and the hub-to-tip (S2) stream surfaces, (**Fig. 2.4**). The S1 surfaces start upstream as surfaces of revolution, but twist and warp as they pass through the blade row. The S2 surfaces form meridional (r-z) planes upstream of the blades, extending from hub to casing, and also warp in passing through the blades (Cumpsty, 1989). The equation of continuity is combined with the equation of motion in either the tangential or the radial direction through the use of a stream function defined on

the surface, and the resulting equation depends on the relative magnitude of the local velocity of sound and a certain combination of velocity components of the fluid. This approach is rarely attempted because of the stream surface shape changing with each iteration. Affordable computing power was not available until the 1980s.

2.3.1.2 Simplified S1/S2 methods – quasi-three-dimensional methods.

The most common approach for designing turbomachinery since the 1950s has been to predict the flow field using an idealised axisymmetric computation, which confines the flow to concentric streamtubes. This is defined as a quasi-three-dimensional solution, (Dunham, 1986). Traditionally, the assumptions are that no mass, momentum or energy is transported across the concentric stream surfaces. By adopting an axisymmetric flow, any variations circumferentially, (in the blade-to-blade direction), have been ignored by considering the flow in the meridional plane as an average, i.e. 2-dimensional flow. The blade-to-blade surface then becomes a surface of revolution (untwisted). The surfaces are untwisted when comparing **Fig. 2.5** (the quasi-3-D approach) with **Fig. 2.4**.

The hub–to-tip flow is also known as the "throughflow" (Cumpsty, 1989). The classical axisymmetric solution has a computation of the meridional plane flow field or of the flow in a hub-to-tip (S2) surface between blades of a given row, and has been an element of all quasi-three-dimensional methods. The second element is the computation or estimation of the flow through individual blade rows on blade-to-blade surfaces, (S1).

The first meridional plane computations were made after about 1955. They used a radial equilibrium condition with no allowance for streamline curvature or slope. These were included in later methods. Experimental data (cascades and blade rows) were used to estimate the blade-to-blade plane flow deflections and circumferentially averaged total pressure losses.

The quasi-three-dimensional methods have assumed steady flow relative to the individual blade rows. The rotor and stage performance curves computed by these methods were acceptable. The radial variations of velocity and properties computed at calculation planes between blade rows were not satisfactory. Additional assumptions have been necessary to make the radial calculation reasonable.

This type of idealisation also ignores the general class known as "secondary flows." This has in the past been described as flows associated with all components of streamwise vorticity and more recently, is described as having all the real flow features that tend to violate the assumption of steady flow confined to axisymmetric concentric stream tubes,

(Wennerstrom, 1999). This includes stream surface warp due to inviscid secondary flow and also other features such as tip leakage flows, boundary layer and wake centrifugation, and turbulent diffusion.

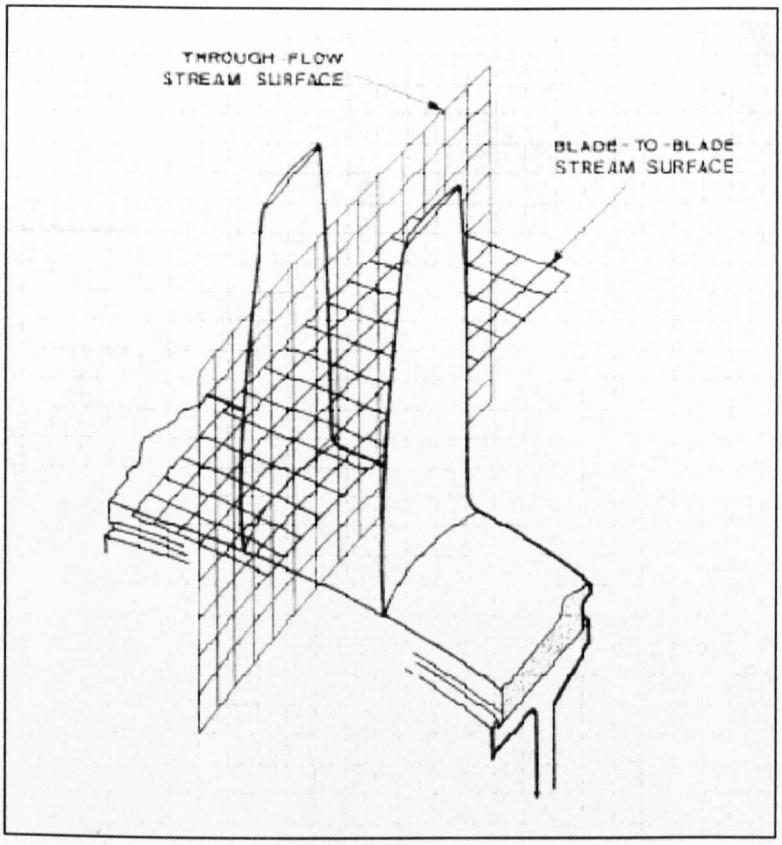

Fig. 2.5 The quasi-three-dimensional approach. (Dunham, 1986).

The quasi-three-dimensional approaches to secondary flow analysis for compressor design have also been classified as hybrid solutions, (Wennerstrom, 1999). The approach was to superimpose semi-empirical models of secondary flow features as corrections to a classical axisymmetric solution of which the most commonly used is the streamline curvature method.

2.3.1.3 Streamline curvature method

The streamline curvature method is the most common throughflow procedure for compressors, e.g. Glenny (1974), Novak (1976), Barbosa (1987), Cumpsty (1989), Klepper, (1998). It is a common flow field prediction tool in the gas turbine industry, capable of rapidly computing the flowfield and obtaining the compressor characteristic. It is the chosen method for Chapter **4** and is described in detail there.

2.4 INLET DISTORTION MODELLING: RADIAL TOTAL PRESSURE DISTORTION

There are various types of inlet flow distortion, and it is generally of the combined radial-circumferential type. Conceptualising the flow as either a pure radial or a pure circumferential distortion is a convenient method for simplifying the modelling procedure. Several researchers have previously suggested that pure radial distortion can be assessed using streamline curvature (SLC) methods for steady-state axisymmetric flows, e.g. (Stenning, 1980), (Williams,1987), and (NATO RTO-TR-044, 2002). The only cases reported using this method e.g. Tamaki and Nagano (1979), Hu (2000) only looked at a multistage compressor in isolation.

The approximation of axisymmetry is justified because this particular approximation is smaller than other approximations such as modelling of the annulus blockage (Cumpsty, 1989). It is recognised that no compressor performance prediction tool is capable of predicting the performance of any compressor perfectly. It is the intention of this method to begin with a known performance at a certain operating condition, which may come from a rig test, and then to use the tool to calculate trends in performance change as the operating point is altered.

Essentially, the method solves the inviscid equations of continuity, momentum and energy on a mesh through the compressor in the meridional plane. This mesh is formed from streamlines of the fluid flow. The method approximates the flow as axisymmetric (circumferentially uniform) and the viscosity of the flow is applied at the blades to arrive at the streamline nodes at blade exit stations. The method is iterative and the streamlines are adjusted until convergence.

Since the full radial equilibrium equations were described in the 1960s (Smith, 1966), (Novak, 1967), the major aeroengine companies have adopted the technique of throughflow streamline curvature as part of the compressor preliminary design process e.g. Q263 at Rolls-Royce, (Marshall, 1998), at SNECMA, (Escuret et al, 1998). The method is also used to analyse the result of design changes and to obtain a more detailed picture of flow parameters throughout a compressor from the result of a rig test. Most of the methods are proprietary (Cumpsty, 1989) so this made it difficult to find a tool for use in this thesis. The tool selected for use for this thesis is by Barbosa, (1987).

2.4.1 Compressor test results with inlet radial distortion

Williams and Yost (1973) reported on tests on a 7-stage, high specific flow axial compressor rig test, with 0.315 inlet hub-to-casing ratio. **Fig. 2.6** shows the result on the characteristic map of inlet total pressure distortions. Low hub pressures resulted in reduction of flow at a given compressor speed, and low tip pressures resulted in a flow increase when the compressor is unchoked. In neither case was there a significant change in surge margin.

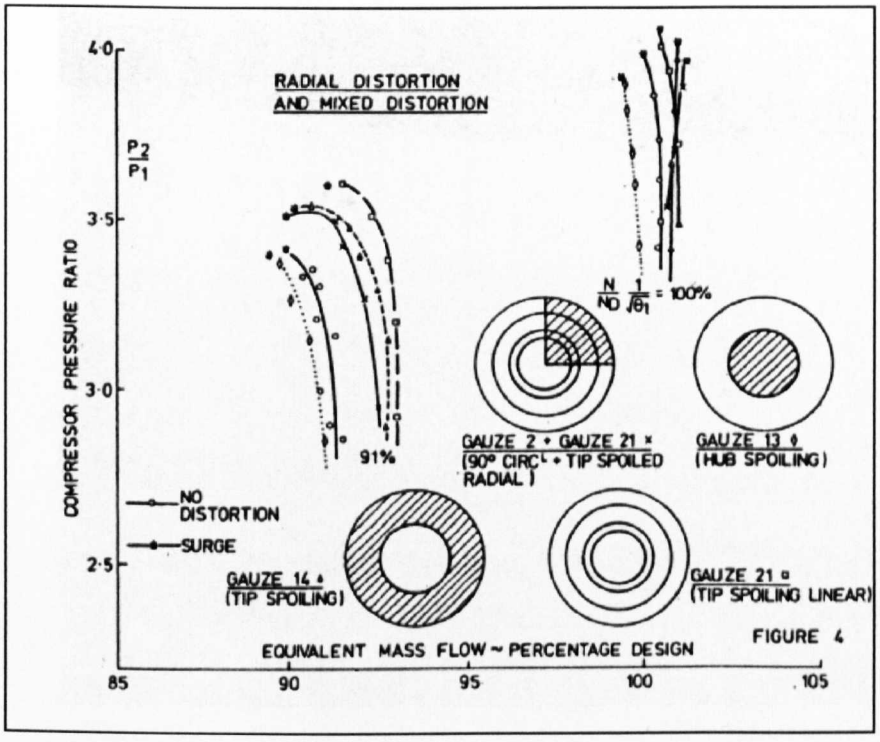

Fig. 2.6 7-stage compressor rig test with radial inlet total pressure distortion, (Williams and Yost, 1973).

However, the results can vary from one compressor to another. An example is a NASA test of a J85-GE-13 turbojet engine, which has an 8-stage compressor (Calogeras et al, 1971). In **Fig. 2.7**, this showed a large reduction in corrected mass flow for hub distortions at any speed with little change in surge margin, and much less effect on the corrected mass flow for tip distortions but with large reduction in surge margin. The authors also tested for an inlet mid-span radial total pressure distortion, finding very little differences in the speed lines compared with the undistorted flow.

Clearly, the results reflect the radial re-matching of the flow due to the inlet distortion, particularly in the front stages of the compressors. The re-matching depends on the satisfying of the radial equilibrium equation at each axial location in the compressor. The largest contribution to this is due to the whirl velocity, which depends on the blade design of the

radial distribution of work input. Another factor due to geometrical differences between compressors is due to the streamline curvature especially at the inlet hub, caused by the curvature of the endwalls at the inlet, (Cumpsty, 1989).

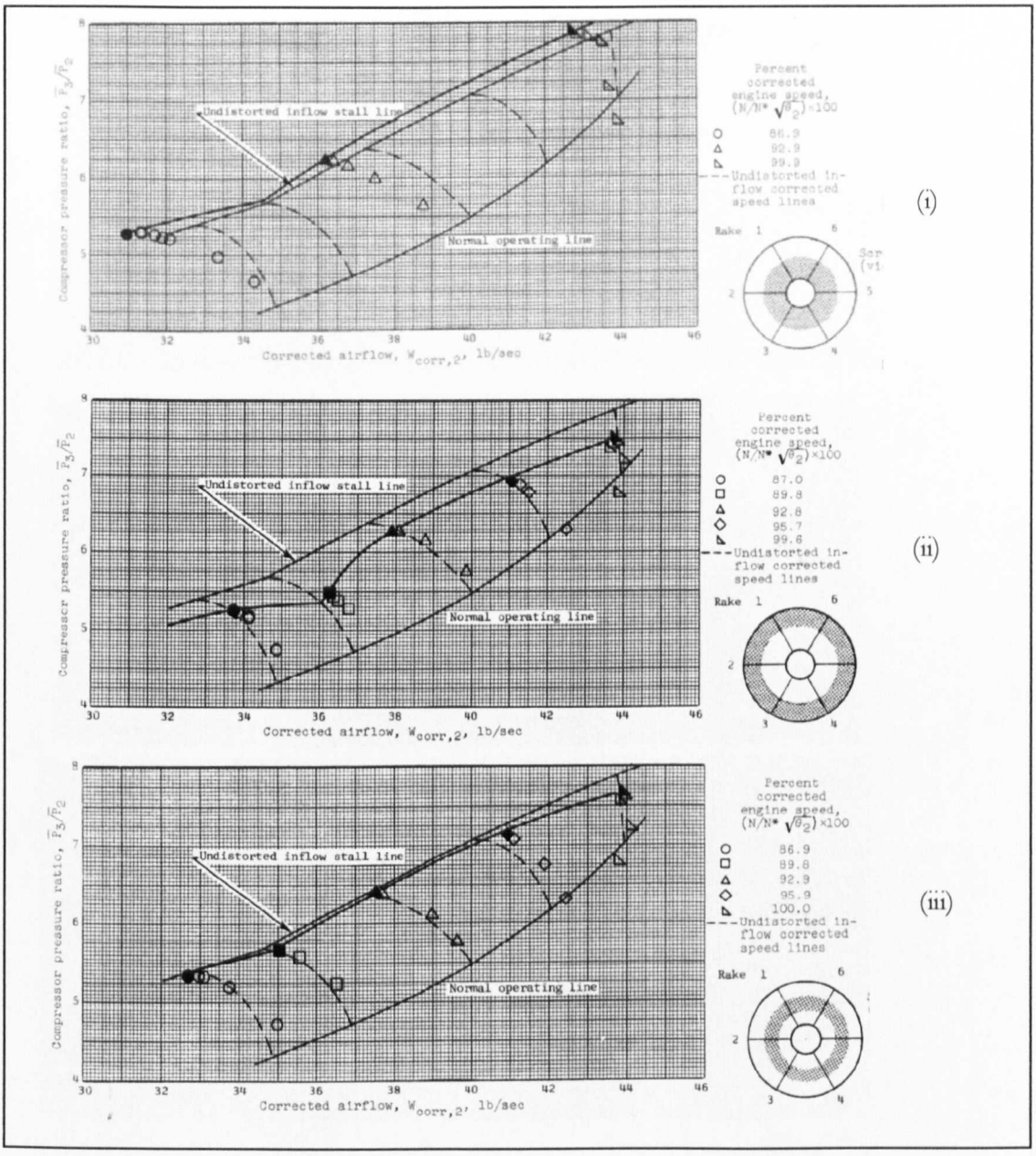

Fig. 2.7. Experimental measurement of effect of (i) tip-distorted, (ii) hub-distorted, (iii) mid-distorted, radial inlet total pressure distortion in the 8-stage compressor of the J85-GE-13 turbojet engine, (Calogeras et al, 1971).

2.4.2 Modelling of a compressor with radial inlet distortion

Tamaki and Nagano (1979) compared experimental and streamline curvature predictions of a 5-stage transonic compressor of design pressure ratio 4.5 and mass flow 8.08 kg/s. The

compressor has constant tip diameter and inlet hub to casing ratio of 0.75. The authors justified the use of the streamline curvature method on the basis that flow in the compressor with an axisymmetric radially distorted inflow is also essentially axisymmetric and steady. A tip-radial and a hub-radial distortion were created at design speed upstream of the compressor using distortion screens. The experimental results in **Fig. 2.8** show reduction both in mass flow and pressure ratio with the tip distortion, and similarly with the hub distortion except at the higher flow rate towards choke where the distorted speed line aligned with the clean uniform speed line. The streamline curvature model used by these authors predicted the low flow rate of the speed line well in the tip distortion case but failed to capture the distorted speed line at the higher flow rate towards the choking condition. They concluded that this particular code could not simulate the choking phenomena of transonic cascade flow. The hub distorted speed line was simulated by SLC with better fidelity.

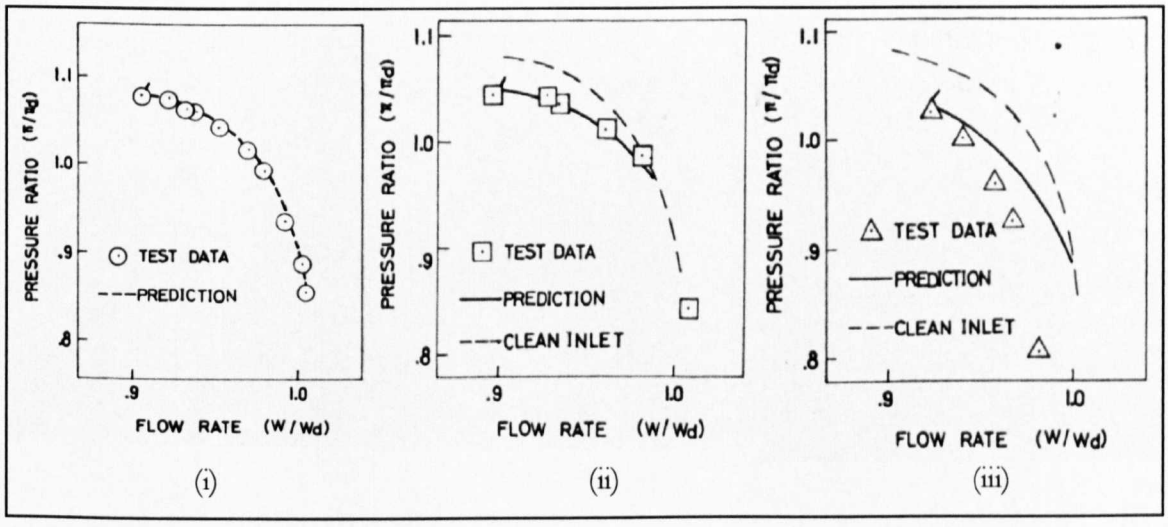

Fig. 2.8 Experimental measurement and streamline curvature predictions of effect of (i) clean, (ii) tip-distorted, (iii) hub-distorted radial inlet total pressure distortion in a 5-stage transonic compressor, (Tamaki and Nagano, 1979).

Of interest for this project is the radial total pressure profile and its development through the compressor. Total pressure readings were obtained in various positions within the compressor to investigate the attenuation of the distortion, and compared with the SLC prediction. In **Fig. 2.9**, the experimental profile in the tip-distortion case became nearly uniform by the end of the first blade row (rotor), whilst this occurred more downstream for the hub-distortion case. From the end of the 3rd stage rotor, the distortion in both cases has

been attenuated and the flow is nearly uniform in the rear stages. The tip-radial distortion attenuates more rapidly because the pressure rise is larger in that region of the first rotor.

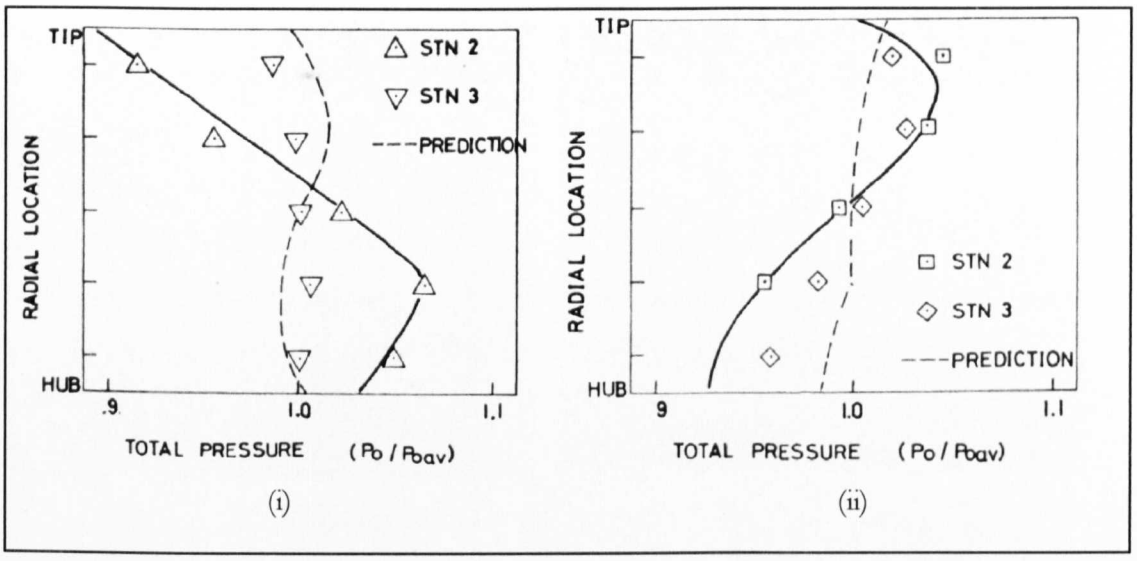

Fig. 2.9 Experimental measurement and streamline curvature predictions of radial total pressure profiles due to (i) tip-distorted, (ii) hub-distorted radial inlet total pressure distortion in a 5-stage transonic compressor, (Tamaki and Nagano, 1979). Stn 2 = inlet, Stn 3 = exit 1st rotor

The streamline curvature code captured well the radial profile of attenuated flow at the end of the first blade row, in fact, much better for the tip-distorted case. It can be seen from this study that the SLC was effective in predicting the effect of radial distortions in terms of both the overall performance and the 2-D profiles, particularly at the lower mass flow end of the compressor speed line.

2.5 INLET DISTORTION MODELLING: CIRCUMFERENTIAL TOTAL PRESSURE DISTORTION

There was insufficient time to implement a performance model for this thesis, but a review of the field is given here to give a complete view of inlet distortion. It is widely accepted that circumferential distortions are more detrimental on the engine performance in terms of eroding the surge margin, (Cumpsty, 1989, NATO RTO-TR-044, 2002). Circumferential-flow distortion has a significant impact on compressor performance. As a result, empirical and correlative approaches (ARP 1420, (1978), AIR 1419, (1999)) have been devised based on compressor testing to estimate the aerodynamic response. These approaches are really aimed at estimating whether an engine under development or being

tested can fulfil stability requirements or achieve a "pass-off" test. Correlative approaches are not aimed at predicting engine performance.

Circumferential methods have additional fluid dynamic effects associated with flow unsteadiness. A different class of methods is therefore needed to assess the response of compressors to circumferential distortions. Usually, distortion degrades the stall margin and performance of the compressor. It is to be stressed now that the literature contains a vast quantity of information concerning compressor stability response to circumferential inlet distortions. For this thesis, only the performance changes are to be investigated. Therefore, the vast quantity of methods for inlet distortion that have been aimed at obtaining stability estimations will be omitted from this investigation.

2.5.1 General trends in compressor response to inlet distortion

The distribution of the inlet total pressure is usually measured at an aerodynamic interface plane (AIP) approximately a radius upstream of the compressor face. Propulsion system internal performance is normally assessed by evaluating installed engine performance at the corresponding value of AIP face-average total pressure (PFAV). The AIP airflow is treated as an equivalent one-dimensional flow. Assessment considers changes in engine and matched engine-component performance resulting from losses of inlet total pressure, (AIR 1419, 1999).

2.5.1.1 Face average total pressure

There is a fundamental fluid mechanical difficulty in constructing a unique one-dimensional or equivalent face-average flow that can simultaneously account for mass flow-, momentum- and energy-flux variations across the AIP. Definitions that are employed include flow-continuity, area-weighted (area-averaged), mass-flow-weighted, momentum-weighted, and entropy-derived face averaging, (Pianko, 1983). Differences with these face-average definitions can be of the order of 1% of the face-average total pressure level, depending on the shape of the pattern (AIR 1420, 1999).

Area-averaged total pressure is widely used throughout the aerospace industry, is simple and easy to apply, and eases inlet and engine data acquisition and processing requirements. Area-averaging facilitates the definition and quantification of distortion at the AIP, and is the

recommended basis of ARP 1420. Alternative definitions that are appropriate to a particular propulsion system development such as mass-flow weighting for compressor efficiency accounting can be related to the area-averaged value for defined AIP patterns. The distortion descriptors given in ARP 1420 show, when instrumentation rings are located at centres of equal area:

$$PFAV = \frac{1}{N}\sum_{i=1}^{N}(PAV)_i = \frac{1}{N}\sum_{i=1}^{N}\left[\frac{1}{360}\int_0^{360} P(\theta)_i\, d\theta\right]$$

N is the number of instrumentation rings and (PAV)i are the ring-averaged total pressures.

The numerical distortion descriptor elements are defined relative to the area-averaged, AIP, mean total pressure PFAV. The above definition implies that:

$$\sum_{i=1}^{N}\left(\frac{\Delta PR}{P}\right)_i = 0$$

where $\left(\frac{\Delta PR}{P}\right)_i$ are the radial intensity elements.

ARP 1420 guidelines for assessing installed engine performance in distorted flow conditions therefore involve accounting for baseline uniform-flow performance using the area-averaged AIP total pressure and performance changes due to distortion relative to this area-averaged datum. It is noted that because of area-weighting, PFAV is related to the conservation of momentum flux at the AIP.

2.5.1.2 Compressor and engine performance data

Fig. 2.10 is the result of three time-averaged circumferential distortion patterns on a five-stage axial compressor at levels typical of those in mixed radial and circumferential patterns of inlets at cruise conditions. Flow and efficiency losses were less than 1% and of the order of the measurement accuracy. Area-averaged compressor performance was not greatly affected. **Fig. 2.11** is the result of circumferential screen patterns on a seven-stage axial compressor test. The more severe patterns (3 and 4) result in the loss of corrected flow close to surge and in efficiency changes. Differences are difficult to see at the less severe distortions (screens 1, 3 and 2 of no. 1), due to measurement scatter.

Fig. 2.12 shows the results of testing on a three-stage turbofan with the inlet pattern of **Fig. 2.13**. The overall fan performance is significantly affected, with corrected flow and efficiency changes being approximately 2%. In this case, additional data relevant to changes in split-flow outer diameter and inner diameter performance characteristics and bypass ratio may be required for analysis.

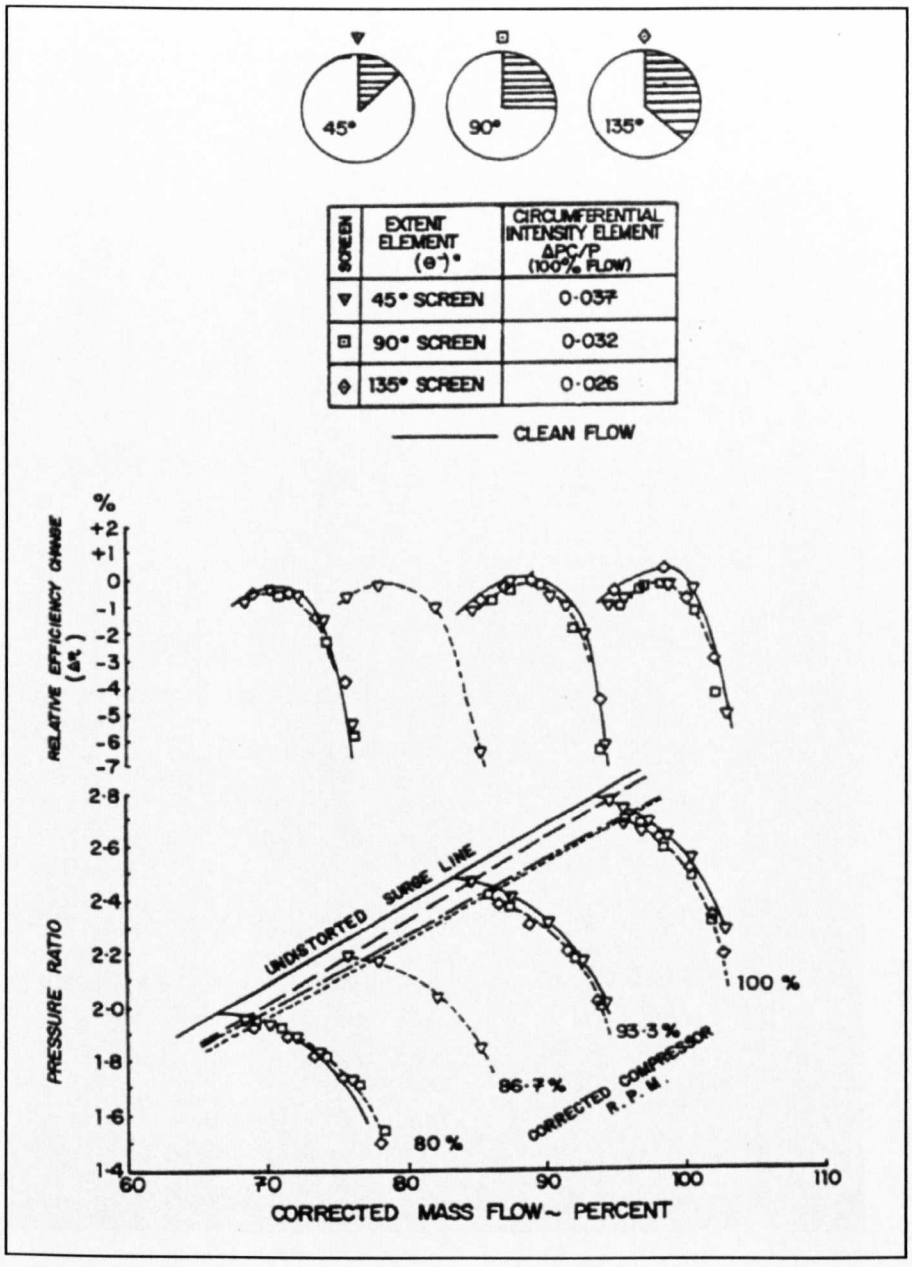

Fig. 2.10 Effect of classical circumferential inlet distortion patterns (AIR 1419, 1999).

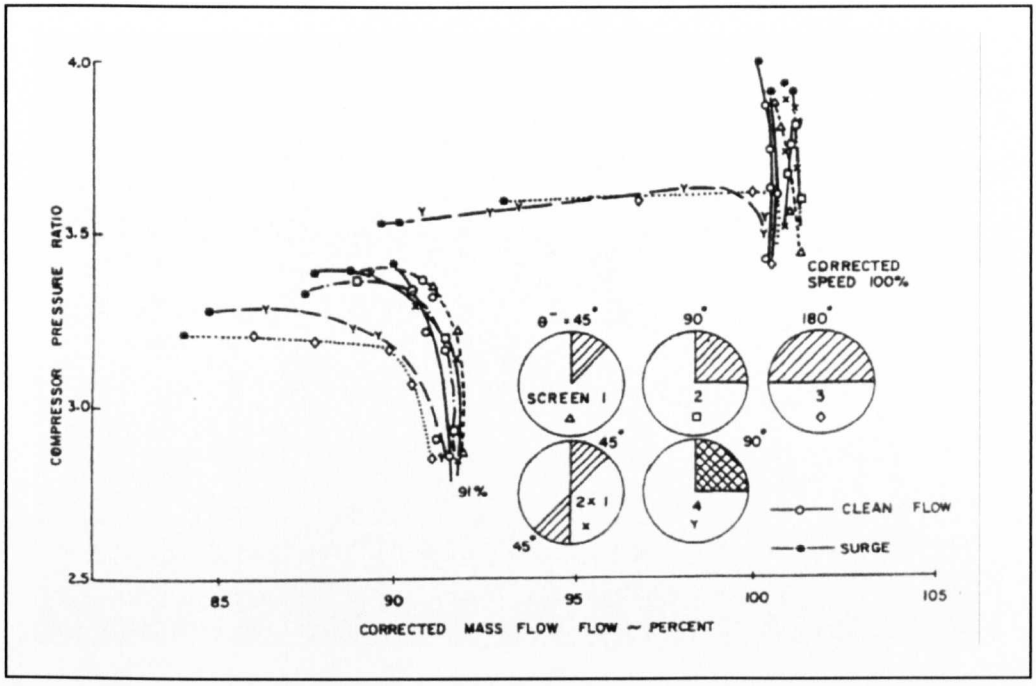

Fig. 2.11 Rig compressor tests – classical distortion (AIR 1419, 1999).

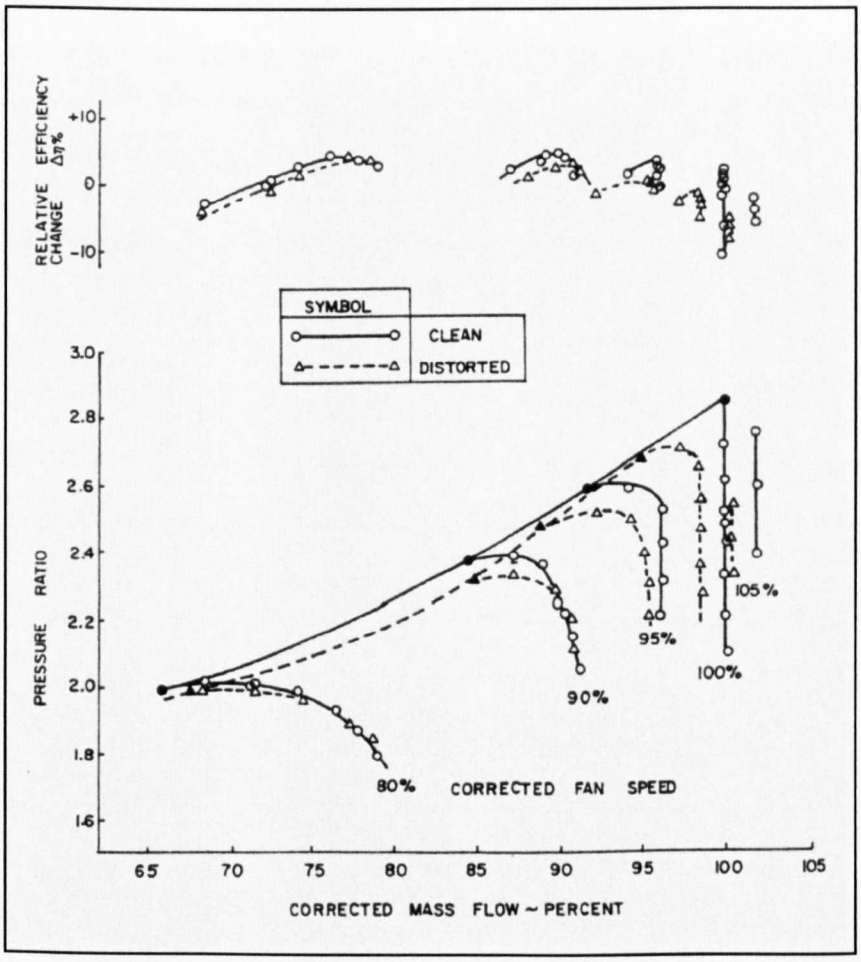

Fig. 2.12 Rig compressor tests – screen simulated distortion (AIR 1419, 1999).

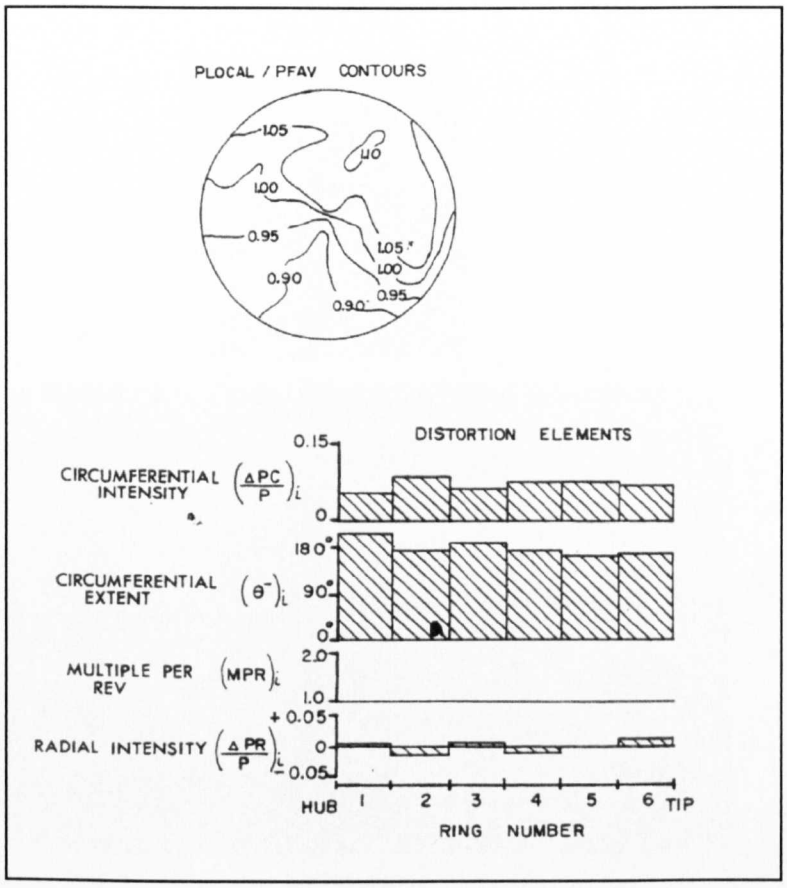

Fig. 2.13 Simulated inlet distortion screen (AIR 1419, 1999).

2.5.2 Two compressors in parallel method

This method does is normally used for surge line analysis and does not compute performance well. The main points have been well described, Reid (1969), Longley (1992). Reference is made to a compressor in a steady, circumferentially non-uniform flow field with 2 streams of different total pressure entering the inlet. A square wave ("top-hat") circumferential distortion with equal extents of high and low pressure (**Fig. 2.14**). At the compressor exit, the flow angle from the last row of stator vanes can be approximated as uniform around the circumference. With a straight exit duct of constant area, uniform exit angle implies uniform static pressure at exit. This is an idealised condition. In the engine, there may be a circumferential distribution of static pressure at fan exit due to the downstream HPC and bypass duct components.

With uniform exit static pressure and two streams of different inlet total pressure, the compressor can be idealised as two compressors in parallel, compressing air from two streams of different inlet total pressures to a common exit static pressure. One assumption is

of negligible circumferential flow between the two streams. This is a good approximation since circumferential length scales are large compared to the axial gaps in an aeroengine compressor, (Cumpsty, 1989, Longley, 1992). Even in a multistage compressor, the axial length for redistribution is small. Therefore, with close-spaced compressor blading, any mass flow non-uniformity at the compressor inlet will also be present at the compressor exit, because there is little opportunity for further redistribution within the compressor. Additionally, since the circumferential static pressure gradients are greatest at the front of the compressor, any significant internal flow redistribution is likely to occur within the first few stages.

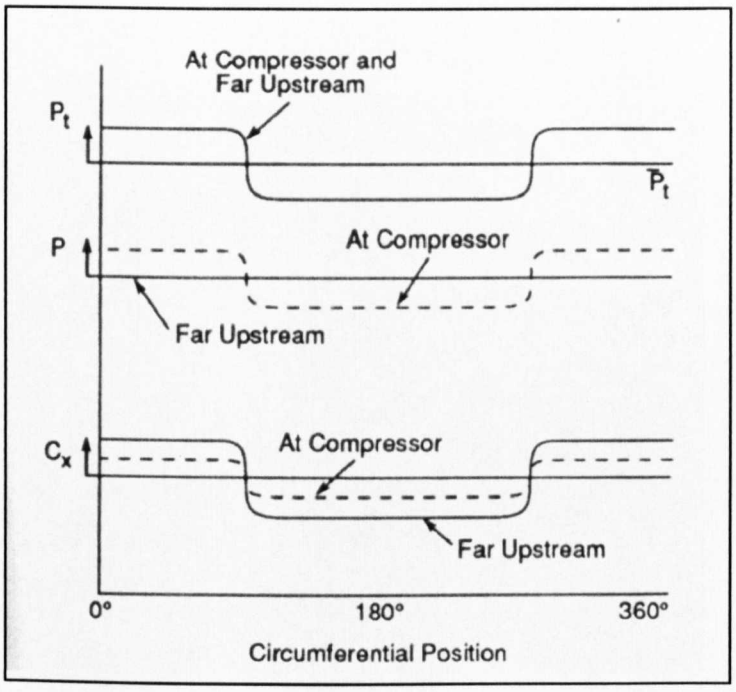

Fig. 2.14 Total pressure, static pressure and axial velocity distributions at a far upstream station and at the compressor inlet (Longley, 1992).

It is then assumed that each compressor operates at a point on the uniform flow compressor characteristic appropriate to the local mass flow. **Fig. 2.15(a)** shows compressor pressure rise ψ_{TS} as the exit static pressure minus the inlet total pressure, non-dimensionalised by ρU^2, against the flow coefficient $\phi = Cx/U$. It can be seen that the mean pressure rise is below what would be achieved in undistorted flow at the mean mass flow, given by $\Delta\psi$.

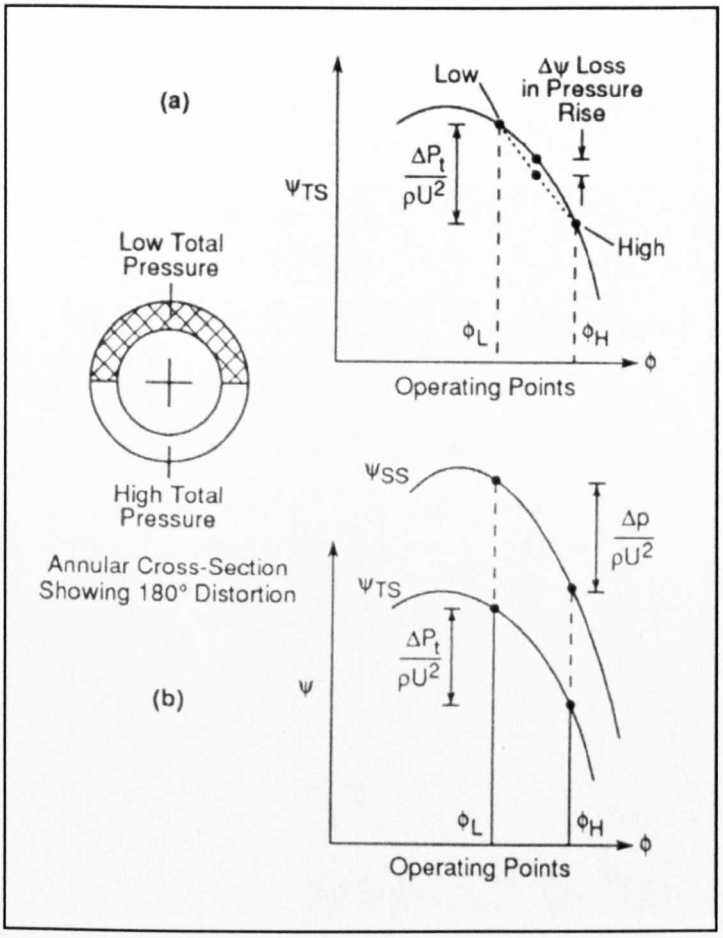

Fig. 2.15 Basic parallel compressor for compressor response to circumferential total pressure distortion (Longley, 1992).

Also, the two parts of the compressor annulus operate at different points on the characteristic. With a common exit static pressure for both streams, the difference in level between the pressure rise in each stream must be the difference in the inlet stagnation pressures. The lower inlet total pressure stream has a higher pressure rise, operating nearer to the stall limit for uniform flow. The mean operating point may not be close to the stability boundary but a large portion of the compressor circumference may be operating at a flow equal to or below the boundary value. It might therefore be expected that instability could be initiated at a higher annulus average mass flow than with undistorted axisymmetric flow. One of the assumptions of this basic parallel compressor model is that the flow stability limit in distorted flow is reached when the operating point for the low total pressure stream reaches the undistorted compressor stability limit. This parallel compressor model using pressure rise coefficient and flow coefficient is suited for low Mach number flows.

In high speed compressors where compressibility effects are especially important, performance is expressed as pressure ratio versus corrected flow (mass flow function $\dot{m}\sqrt{c_p T}/P$) for different values of corrected speed $N/\sqrt{T}$.

Parallel compressor theory is generally valid if the segment arc is greater than the 60 degrees critical angle (RTO-TR-044, 2002). Secondary flow mechanisms become more significant with arcs less than the critical angle and parallel compressor theory cannot predict segments less than the critical angle well.

2.5.3 Features required by a circumferential distortion compressor flow prediction model

2.5.3.1 Upstream flow redistribution

When operating in non-uniform flow, the compressor generates an upstream static pressure field causing a redistribution of the flow upstream of the compressor (Plourde, 1967). This is shown in **Fig. 2.14**, where it can be seen that the axial velocity distortion at the compressor is smaller than far upstream. This is explained by **Fig. 2.15(b)**, looking at the parallel compressor model in terms of the static to static pressure rise characteristic with the pressure rise coefficient given by ψ_{ss}. The compressor exit static pressures are equal so there is a difference in the compressor inlet static pressures. Far upstream of the compressor, the static pressure is uniform, so the change in static pressure from far upstream to inlet implies a change in axial velocity between the two stations. The effect of the upstream reaction is to decrease the axial velocity non-uniformity compared with the far upstream value.

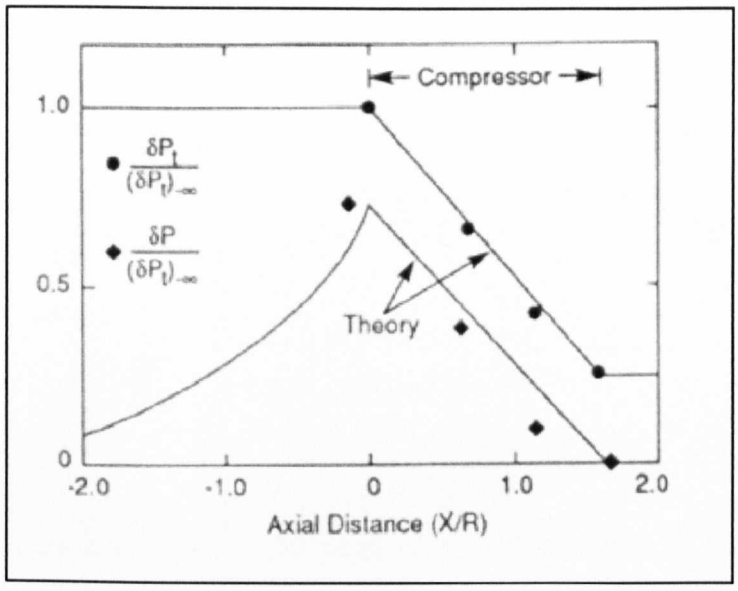

Fig. 2.16 Overall variation of static and total pressure upstream and through three stage compressor (Stenning, 1980).

The overall behaviour of the total and static pressures upstream and through a compressor are shown in **Fig. 2.16**, for a 3-stage low speed compressor. For low speed flows, small amplitude departures from a uniform static pressure obey Laplace's equation (Stenning, 1980) as an indicator of the axial scale of upstream flow redistribution.

2.5.3.2 Distortion attenuation

The static pressure at the exit of the compressor can often be regarded as uniform, but exit total pressure cannot be since the two streams have different velocities. The exit non-uniformity is experienced by any downstream aeroengine components. The distortion attenuation, (the ratio of the exit total pressure distortion amplitude to that of the inlet) is of interest. The size of the exit total pressure non-uniformity is determined by the difference between the exit velocity in the high and low flow streams. The flow velocities in the two streams are set by the shape of the total-to-static pressure rise characteristic as shown in **Fig. 2.17**. The steeper the compressor characteristic, the greater is the distortion attenuation, (Plourde, 1967). For the same total pressure distortion, the velocity non-uniformity at the compressor is less for the steeper compressor characteristic C1 than for the flatter one C2.

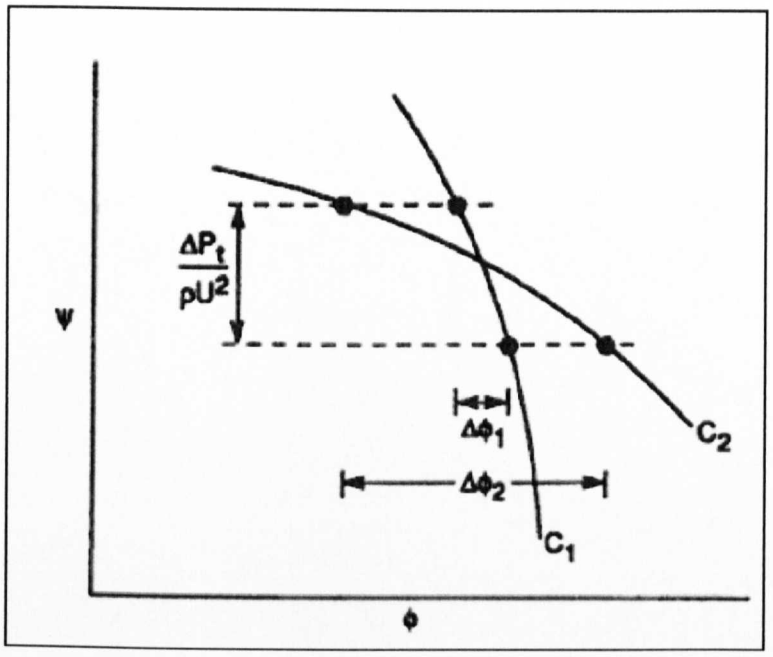

Fig. 2.17 Increased compressor characteristic slope implies increased distortion attenuation (Longley, 1992).

Compressors with steep characteristics will create nearly uniform inlet flow and therefore, nearly 100% distortion attenuation of the total pressure field. However, the greater pressure rise in the low flow region requires a greater work input and therefore, a higher total temperature at exit. Downstream of the compressor, there will therefore be a total temperature distortion, which is then imposed on the downstream components.

2.5.4 Performance prediction

2.5.4.1 DYNTECC

One software for modelling circumferential inlet distortion effects is DYNTECC (NATO-RTO-TR-044, 2002). It is a one-dimensional (US definition, stage stacking), stage-by-stage, compression system mathematical model able to analyse any generic compression system (**Fig. 2.18**).

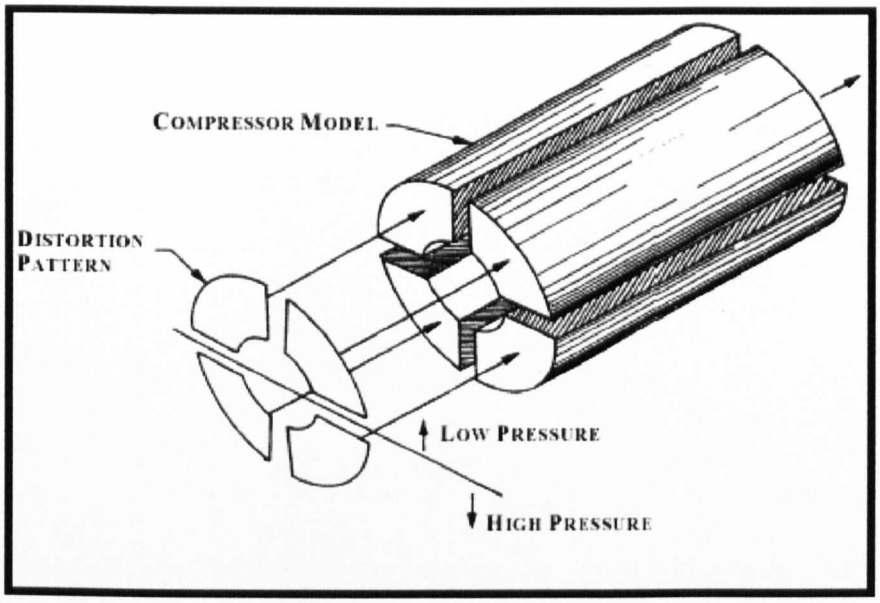

Fig. 2.18 DYNTECC parallel compressor model (NATO RTO-TR-044, 2002).

It uses a finite difference numerical technique to simultaneously solve the mass, momentum and energy equations with turbomachinery source terms (mass bleed, blade forces, heat transfer, and shaft work). The source terms are determined from a complete set of stage pressure and temperature characteristics. DYNTECC can be operated as a parallel compressor model with or without circumferential and radial crossflow approximations.. Modified parallel compressor theory is used to simulate dynamic inlet distortion. The compression system control volume is sub-divided into parallel circumferential segments. Each segment is a parallel compressor exiting to the same exit boundary condition, but different magnitudes of inlet total pressure and temperature can be imposed upon each segment. In the simplest case, each segment is independent of the others except through the exit boundary condition.

For complex distortion patterns, the circumferential and radial crossflow terms are approximated. System instability occurs when any segment becomes unstable as a result of the inlet and exit conditions. Both pressure and temperature characteristics are required. During pre-stall operation, the steady-state compressor characteristics are used. During post-stall, the change in compressor operating conditions is lagged using a first order equation.

2.5.4.2 TEACC

This is the Three-Dimensional Turbine Engine Analysis Compressor Code (TEACC), (Hale, 1997). The authors used a 3D Euler code for the compressor except at the blades where it was recognised that the computational effort was too great. At these positions, within the blading, the compressor was divided into circumferential segments, each running a streamline curvature code to provide the turbomachinery source terms (bleed, blade forces and shaft work), for the Euler solver.

2.5.4.3 Multiple segment parallel compressor model

For performance prediction, the multiple segment parallel compressor (MSPC) model, developed at Pratt and Whitney, (Mazzawy, 1977), gives useful results for a certain class of problems and has physical basis in the associated fluid dynamics. It gives the result of a loss of stability margin and stalling pressure ratio, and also for effective attenuation of distortion, a given compressor should have a steeper slope in the unstalled pressure rise characteristics. The disadvantage is an inadequate stall point prediction, (Longley, 1992), (Williams, 2002).

More than the two idealised operating points of the basic parallel compressor model can be used. In the multiple segment parallel compressor model, the annulus is split into segments of equal circumferential width. Within these multiple parallel segments, individual blade row performance characteristics are used, or the whole compressor characteristic if these are not available, to account for the two-dimensionality of the distorted flow field. It is applicable to distortions with large extent relative to blade pitch. The calculated flow properties in each segment can be considered to be the average over several blade passages, (most adverse distortions are this large). Use of multiple segments allows full description of downstream non-uniformities regardless of their circumferential orientation relative to the inlet distortion.

The operating point of each segment is determined by the local inlet total pressure and the local exit static pressure, and the overall performance is the average of the individual segments. The model accounts for fluid dynamic effects not considered in the basic parallel compressor theory. This includes upstream flow redistribution, giving an asymmetric inlet angle and relative dynamic pressure. This gives better agreement with data. It also models some non-steady flow phenomena associated with rotor blades passing through non-uniform flow, which is important for the inlet distortion tolerance of a compressor.

The stall point stability criterion for basic parallel compressor theory was to take the uniform stall condition. The new model is not constrained by this uniform undistorted inlet performance. A new criterion is required, taking instability to be when there is some portion of the circumference where sufficient pressure rise cannot be attained to match the local exit boundary condition. Each segment has a different peak pressure rise capability, which must be obtained from the distorted flow field solution.

The model deals with the two main assumptions that are experimentally in dispute:

(i) The distorted compressor does not behave like the undistorted one. Distorted overall compressor performance in any circumferential sector can be different from the undistorted compressor performance with the same boundary conditions because of unsteady flow effects and distortion-induced compressor stage matching differences. The individual blade row performances may extend beyond the stability boundary in undistorted flow.

(ii) Uniform compressor exit static pressure. A non-uniform exit static pressure can be generated by a downstream diffuser or by another compressor in a multispool configuration.

Chapter 3

FAN RADIAL PROFILE AND BYPASS MODELLING

3 FAN RADIAL PROFILE AND BYPASS MODELLING

3.1 INTRODUCTION

This chapter discusses the issues of modelling the fan component of LBPR turbofans in an engine simulation program including comparisons with HBPR fans, looks at the current existing methods, and explores test data of LBPR fans. As a result, a new method is devised to model differences in LBPR fans and this is implemented and the results discussed.

3.2 BACKGROUND TO FAN MODELLING IN TURBOFAN ENGINES

The following subsections explore the particular differences of fans from compressors and their unique modelling requirements.

3.2.1 Fan modelling requirement for turbofans

Figure 3.1 shows the layout of the Rolls-Royce/Turboméca Adour turbofan engine. Firstly, the normal requirements for the fan characteristic model are as for any compressor, as discussed by Cumpsty (1997). Given the dependent variables of rotational speed and the position of the exit throttle, as characterised by the mass flow, the performance of a compressor can be obtained.

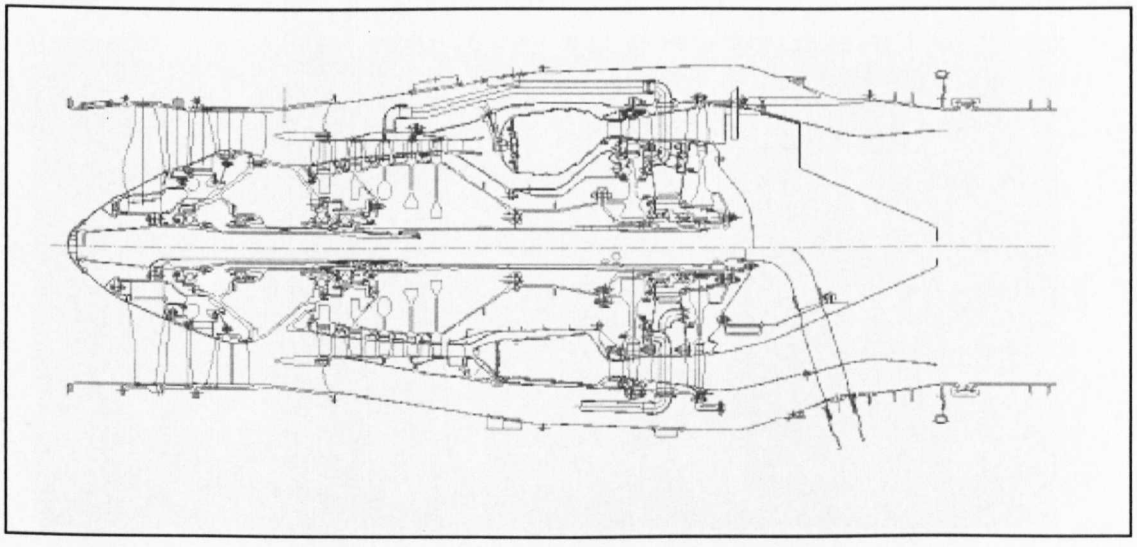

Fig. 3.1 Air flowpath in a Rolls-Royce Turbomeca Adour turbofan engine. (Rolls-Royce plc)

However, modelling of the fan of a turbofan differs from that of say a core compressor in two ways. Firstly, the fan is directly adjacent to the intake system and is

susceptible to inlet flow distortions (dealt with in Chapter 4). Secondly, an annular splitter divides the airflow aft of the fan component into the inner or core engine flow, and the outer or bypass flow. The fan model must therefore be able to provide the correct delivery temperatures, pressures and mass flows to the two downstream passages. It will later become apparent that the bypass ratio (bypass mass flow ÷ core mass flow) is also a dependent variable in setting the fan performance.

For a core compressor, although the flow at the exit of the compressor may not be radially uniform, it is common practice to average the radial non-uniformities to single 1-dimensional values and to use these as inputs to the downstream component. This is not possible in the fan of the turbofan because applying the same averaged 1-dimensional value at the entry of the core and the bypass channels is not the actual real situation. Firstly, the fan may produce radially a highly non-uniform profile of flow variables at the exit, so that pressures and temperatures are passing to the core and bypass are always different, and secondly, the BPR varies widely across the power range of the engine with the fan speed.

3.2.2 Source of fan exit radial non-uniformity

The average pressures and temperatures that arrive at the inlets to the engine core compressor and the bypass duct can be very different in turbofan engines even in the case of a uniform inlet flow to the engine. The flow field is extremely complicated to describe but it can be viewed as the result of the compression process being modified by several other factors. In the basic compression process, pressure rise is caused by the rotors imparting work to the airflow and the flow of the air through an overall diffusing passage. At the same time, the airflow is subjected to several other effects, due to real flow phenomena or due to geometrical effects. All of these may contribute to overall 3-dimensional non-uniformity. The following specifically result in radial non-uniformity.

3.2.2.1 Difference in blade speed from hub to tip

The hub-to-casing ratio determines the difference in rotational speed along the blade. It is known that the pressure ratio is approximately proportional to the square of the rotational speed (Mazzawy, 1977).

3.2.2.2 Designed work input variation across the blade span

This is manifested in the turning imparted to the flow by the blading as a result of both the blade rotational speed and the blade angles.

The Euler work equation in the simple case with equal inlet and exit radius of a mean streamtube is: $W = H_2 - H_1 = U(V_{\theta 2} - V_{\theta 1})$. The blade speed is proportional to the radius $U = r\omega$. Therefore, if it is desired to have a uniform work input radially, the designed radial change in whirl velocity V_θ has to be inversely proportional to radius, which is a free vortex distribution. It has been noted e.g. Cumpsty (1989), Cohen et al (1996) that one such solution used in the past is:

$$V_{\theta 1} = ar - \frac{b}{r} \text{ and } V_{\theta 2} = ar + \frac{b}{r}.$$

Cumpsty (1989) notes that the more usual requirement is uniform stagnation pressure rise. It is usual to vary the work input to allow for the predicted radial variation of loss in order to achieve a uniform total pressure.

3.2.2.3 Geometry effects

Particularly in the fan component, the path of a streamline along the meridional plane can be highly curved. The inlet annulus area of the compressor has to pass as much airflow as possible and with the air there being at its lowest density, the area is desired to be maximised. In the context of military fans, the fan diameter is desired to be minimised to create an engine of high specific thrust, and with the minimum frontal area for minimum drag. Sometimes, the engine may be buried within the airframe, and is accessed via swan-neck ducts. Curvature will set up a static pressure distortion and may also give a swirl distortion.

3.2.2.4 Real flow effects

These occur particularly at the hub and tip regions. Real flow effects include viscous boundary layer effects, secondary flow effects, shocks, and boundary layer interaction. This is well documented by Lakshminarayana (1996).

The sum of all these effects is that use of a single 1-dimensional compressor characteristic providing single averaged values of the overall fan exit flow properties may give unrealistic values of total pressure and total temperature at the core and bypass entry axial stations. This

is because the effect of averaging the two portions of the fan exit flow profiles divided by the flow split streamline to their respective downstream passages is not addressed.

3.3 EXISTING FAN CHARACTERISTIC METHODS

This section explores some of the methods in use for fan representation in simulation programs as reported in the public domain literature. It is quite possible that other methods exist, which are proprietary and undisclosed.

3.3.1 Inner and outer fan method

This appears to be the traditional method by aeroengine design companies, e.g. Rolls-Royce (Marshall,1997), MTU (Kurzke, 1996), Pratt and Whitney, (Shaw, 1982), is by using split inner and outer fan maps.

3.3.1.1 MTU (Kurzke, 1976)

For low bypass ratio engines, either the inner or the outer fan is assigned as the primary compressor. If the nominal bypass ratio is less than one, the inner fan is the primary map, and if the nominal bypass ratio is greater than one, the outer fan is the primary map. For each measured point, there are five data: total compressor mass flow $W\sqrt{T_1}/P_1$, bypass and core stream pressure ratios: P_{13}/P_1 and P_{21}/P_1 respectively, and the bypass and core stream efficiencies: η_{13} and η_{21} respectively.

If the bypass ratio is less than one for example, the primary map will have the variables:

$P_{21}/P_1 = f\left(N/\sqrt{T_1}, W\sqrt{T_1}/P_1\right)$ and $\eta_{21} = f\left(N/\sqrt{T_1}, W\sqrt{T_1}/P_1\right)$.

β is defined on the pressure ratio, flow graph as parabolic lines intersecting the constant speed lines.

The outer bypass fan characteristic is then obtained by profile factors $f_{P/P} = \dfrac{P_{13}/P_1}{P_{21}/P_1}$ and

$\eta_{P/P} = \dfrac{\eta_{13}}{\eta_{21}}$.

The primary map will give smooth lines of β against the speed lines. However, if the map for the outer fan was to be drawn with this beta, it would not be possible to have smooth

lines because the pressure profile factor is not constant, i.e. the β defined on the primary graph plotted onto the secondary characteristic would not form smooth parabolic lines.

3.3.1.2 Rolls-Royce (Marshall, 1997)

Rolls-Royce models low bypass and high bypass ratio turbofans differently using the method of split characteristics.

RRAP low bypass ratio fan model – β is defined for the overall fan against speed and overall mass flow. (Dependent variable $W_1\sqrt{T_1}/P_1$, and independent variables $N/\sqrt{T_1}, \beta_{overall}$). The other dependent variables are then within separate inner and outer characteristics against the same dependent variables. They are: $\frac{\Delta H_{21}}{T_1} = f\left(N/\sqrt{T_1}, \beta_{overall}\right)$, $\eta_{21} = f\left(N/\sqrt{T_1}, \beta_{overall}\right)$ for the inner fan, and $\frac{\Delta H_{13}}{T_1} = f\left(N/\sqrt{T_1}, \beta_{overall}\right)$ and $\eta_{13} = f\left(N/\sqrt{T_1}, \beta_{overall}\right)$ for the outer fan.

The scheme for a low bypass ratio fan in a turbofan with separate exhaust nozzles:

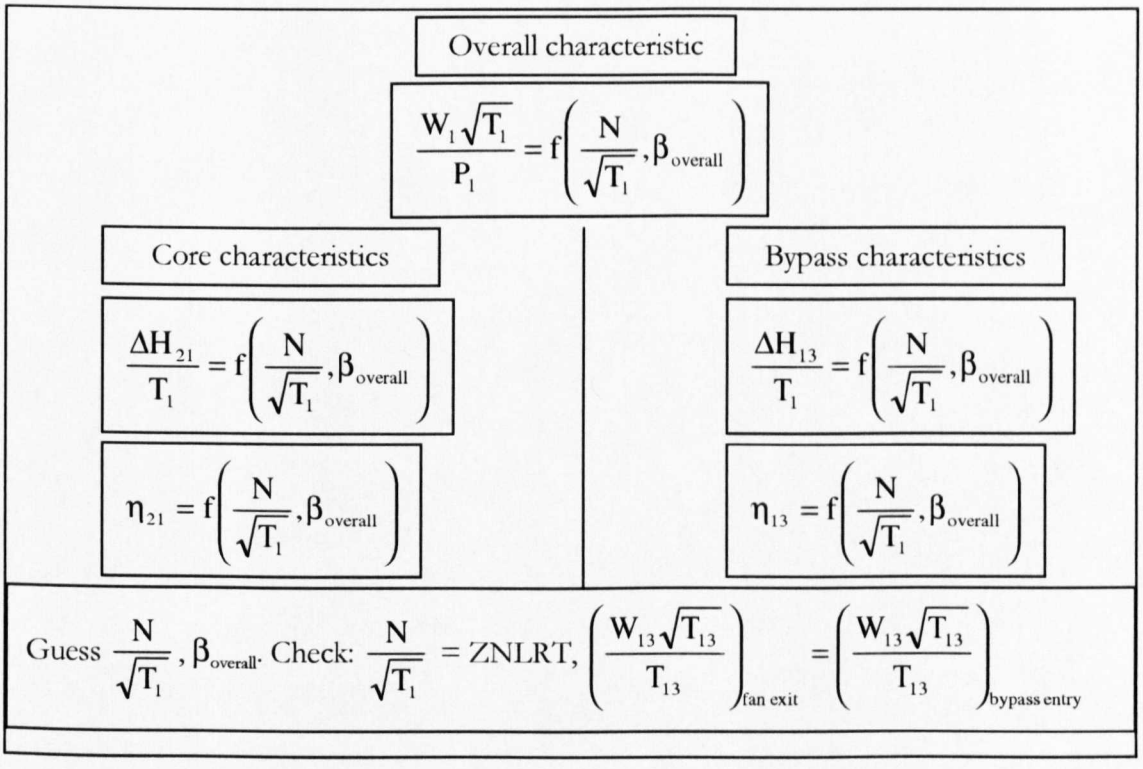

RRAP high bypass ratio fan model - β is defined separately for the inner and outer fans against separate flow characteristics, i.e., inner fan: (dependent variable $W_{21}\sqrt{T_1}/P_1$, and

independent variables $N/\sqrt{T_1}, \beta_{core}$), outer fan: (dependent variable $W_{13}\sqrt{T_1}/P_1$, and independent variables $N/\sqrt{T_1}, \beta_{bypass}$). The other dependent variables are graphed against the respective β for each compressor. They are: $\frac{\Delta H_{21}}{T_1} = f\left(N/\sqrt{T_1}, \beta_{core}\right)$, $\eta_{21} = f\left(N/\sqrt{T_1}, \beta_{core}\right)$ for the inner fan, and $\frac{\Delta H_{13}}{T_1} = f\left(N/\sqrt{T_1}, \beta_{bypass}\right)$ and $\eta_{13} = f\left(N/\sqrt{T_1}, \beta_{bypass}\right)$ for the outer fan.

The scheme for a high bypass ratio fan in a turbofan with separate nozzles:

Core characteristics	Bypass characteristics
$\frac{W_{21}\sqrt{T_1}}{P_1} = f\left(\frac{N}{\sqrt{T_1}}, \beta_{core}\right)$	$\frac{W_{13}\sqrt{T_1}}{P_1} = f\left(\frac{N}{\sqrt{T_1}}, \beta_{bypass}\right)$
$\frac{\Delta H_{21}}{T_1} = f\left(\frac{N}{\sqrt{T_1}}, \beta_{core}\right)$	$\frac{\Delta H_{13}}{T_1} = f\left(\frac{N}{\sqrt{T_1}}, \beta_{bypass}\right)$
$\eta_{21} = f\left(\frac{N}{\sqrt{T_1}}, \beta_{core}\right)$	$\eta_{13} = f\left(\frac{N}{\sqrt{T_1}}, \beta_{bypass}\right)$

Guess $\frac{N}{\sqrt{T_1}}, \beta_{core}, \beta_{bypass}$.

Check: $\frac{N}{\sqrt{T_1}}$ = ZNLRT, $\left(\frac{W_{21}\sqrt{T_{21}}}{T_{21}}\right)_{fan\ exit} = \left(\frac{W_{21}\sqrt{T_{21}}}{T_{21}}\right)_{core\ entry}$,

$\left(\frac{W_{13}\sqrt{T_{13}}}{T_{13}}\right)_{fan\ exit} = \left(\frac{W_{13}\sqrt{T_{13}}}{T_{13}}\right)_{bypass\ entry}$

3.3.1.3 Pratt and Whitney multiple segment parallel compressor model (Mazzawy, 1977)

The scheme is also an inner and outer fan model denoted as the inner diameter (ID) and outer diameter (OD). The difference is in the use of the dependent parameters. The model uses blade row performance characteristics.

1. Each rotor and stator is represented by a static pressure rise characteristic ψ.
2. The rotor is also represented by a total temperature rise characteristic λ.
3. These are a function of mass flow parameter/area, ϕ/A.

$$\psi = \frac{p_{out} - p_{in}}{p_{in}} \cdot \frac{\left(N/\sqrt{\theta}\right)^2_{DES}}{\left(N/\sqrt{\theta}\right)^2}$$

$$\lambda = \frac{T_{out} - T_{in}}{T_{in}} \cdot \frac{\left(N/\sqrt{\theta}\right)^2_{DES}}{\left(N/\sqrt{\theta}\right)^2}$$

$$\frac{\phi}{A} = \frac{W\sqrt{\theta}}{A\delta} \cdot \frac{\left(N/\sqrt{\theta}\right)_{DES}}{\left(N/\sqrt{\theta}\right)}$$

The multiple segment aspect is for calculation of circumferential inlet distortion.

3.3.1.4 Obtaining inner and outer characteristics by rig test

When a turbofan is throttled back, the flow capacity of the first core compressor reduces more quickly than the bypass nozzle flow capacity due to the lower total pressure there. This results in an increase of bypass ratio when reducing speed along the working line of the fan.

First, a nominal bypass ratio schedule dependent on non-dimensional speed is calculated with a performance simulation model: $BPR_{nom} = f\left(\frac{N}{\sqrt{T_1}}\right)$ and the rig test is then performed following this schedule. The fan rig delivers airflow to two streams in which throttle valves are situated and can be varied separately.

1. At each speed, adjust bypass & core throttles to run on the nominal working line at the nominal bypass ratio according to the above schedule that had been pre-calculated.
2. Fix core mass flow at the working line value and then adjust the bypass throttle to change bypass mass flow incrementally from choke to stall whilst maintaining the core flow at the working line, to obtain the bypass characteristic (measured at bypass duct entry). This gives

the observed values of bypass ratio along a speed line in the overall fan characteristic from a rig test.

3. Fix the bypass mass flow at the nominal working line value and then adjust the core throttle to change the core mass flow incrementally from choke to stall whilst maintaining the bypass flow at the working line, to obtain the core characteristic (measured at core entry).

4. The following diagrams are typical core and bypass characteristics.

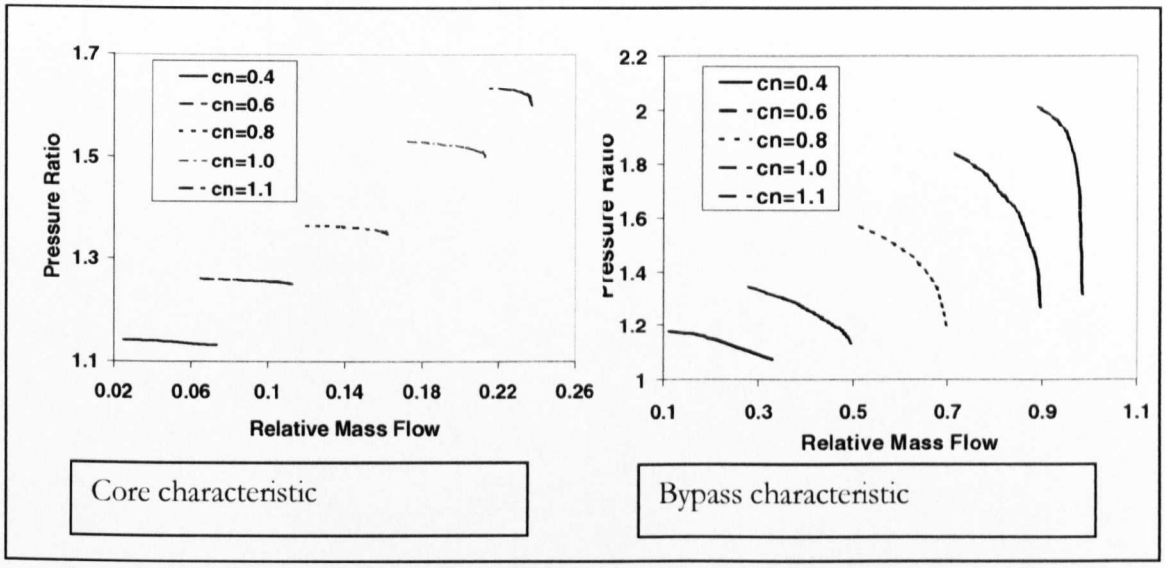

Fig. 3.2 Inner and outer fan characteristics for high BPR fan (Yin, 1999).

3.3.1.5 Applicability of these models?

The use of inner and outer fan maps in this manner limits the applicability of the resulting characteristics to the bypass ratio schedule at which they were tested.

Take the RRAP low bypass fan model. Guessing the overall flow characteristic, $\beta_{overall}$ and $N/\sqrt{T_1}$ gives the overall flow function $W_1\sqrt{T_1}/P_1$ from which W_1 can be obtained. The same $\beta_{overall}$ is used for the bypass and core characteristics and this relationship was fixed due to the geometry of exit throttles run during the rig test according to the bypass ratio vs. $N/\sqrt{T_1}$ schedule. For the separate nozzle turbofan calculation, the bypass nozzle capacity check must match that of the fan bypass exit.

Thus, a bypass ratio vs. $N/\sqrt{T_1}$ relationship or "schedule" refers to one fixed geometry. The model is accurate unless the gas turbine is run at a deviation from the schedule. This can be a change in geometry (altered exit throttle areas), a power offtake, bleed, engine

deterioration or transient manoeuvres (Riegler, 2001). For example, the effect of decreasing the bypass nozzle exit area is to move the working line on the overall fan pressure ratio flow characteristic towards the surge line. A new combination of inner and outer fan maps based on a new bypass ratio schedule would be required for this new model. This is because the nominal flow split streamline has changed and now defines two compressors that are different from before.

Therefore, for rigorous, accurate turbofan modelling, the simulation scheme should include bypass ratio as an iteration variable (**Fig. 3.10**). The fan should be tested at different schedules of bypass ratio vs. $N/\sqrt{T_1}$. However, this would be extremely costly and time consuming and is never performed.

In the RRAP high bypass ratio fan model, the core and bypass characteristics are defined using a nominal schedule of bypass ratio vs. $N/\sqrt{T_1}$. In this case, the flow function is defined for both the core and bypass fans, and β is defined separately for both sets of characteristics.

3.3.2 More general turbofan models.

There have been two similar solutions to extend the capability of modelling the turbofan that runs at a deviation from the nominal bypass ratio schedule.

3.3.2.1 Rolls-Royce model (Yin et al, 1998)

A study of high bypass ratio fan rig test data (Marshall, 1998) resulted in 2 major conclusions:

(i) Radial profiles of flow parameters remain constant at the fan rotor trailing edge at a fixed non-dimensional speed and at a fixed exit non-dimensional mass flow, when BPR is varied.

(ii) These profiles display very little variation in the circumferential direction, compared to the radial variations.

Therefore, there is no need for testing other than for the nominal BPR vs. non-dimensional speed schedule, since the profile stays the same at other bypass ratios for the fixed speed and mass flow. This saves on a lot of rig testing.

This then led to a new representation of the fan characteristic, one that retains the raw 2D radial profile information along with the conventional one-dimensional compressor characteristic (**Fig. 3.4**).

There would be a new independent variable based on the position of the split point at the fan rotor exit that divides the flow into the core and bypass streams of the downstream components. This could be radius or more conveniently, the bypass ratio itself. (The radial profiles of mass flow against radius will give the radial position of split).

Once the radial split point is found on the basis of bypass ratio, the flow profiles can be integrated from the split streamline point up to the casing for the bypass average values of parameters, and to the hub for the core average values (**Fig. 3.3**). The integration process for averaging at each β point is:

$$BPR = W_{13}/W_{21} \tag{1}$$

$$W_{13} = W_{R,tip} - W_{R,split} \tag{2}$$

$$W_{21} = W_{R,split} \tag{3}$$

$$\frac{P_{13}}{P_1} = \frac{1}{W_{13}} \int_{R,split}^{R,tip} PR_{fan,2D}\,dW \tag{4}$$

$$\eta_{1\text{-}13} = \frac{1}{W_{13}} \int_{R,split}^{R,tip} \eta_{fan,2D}\,dW \tag{5}$$

$$\frac{P_{21}}{P_1} = \frac{1}{W_{21}} \int_{R,hub}^{R,split} PR_{fan,2D}\,dW \tag{6}$$

$$\eta_{1\text{-}21} = \frac{1}{W_{21}} \int_{R,hub}^{R,split} \eta_{fan,2D}\,dW \tag{7}$$

To divide the profiles according to the position of the split streamline, a profile of mass flow is required. The one used is defined as the 2D-cumulative mass flow fraction where:

$$CMFF = \frac{W_{2D}\sqrt{T_1}/P_1}{W_{tot}\sqrt{T_1}/P_1} \tag{8}$$

W_{2D} is the mass flow from the hub to a given radius R. At any radius, CMFF varies at the most by only approximately 4% for a constant speed line (Yin, 1999).

Validation exercises have been run with the 2D fan to demonstrate its applicability to replace the inner and outer fan model. Using the same overall 1D fan characteristic constructed from the same 2D flow profile data, a hypothetical high bypass ratio fan has

been modelled within a 2 shaft turbofan with separate exhausts (Yin, 2000), with both the inner and outer fan model and the 2D fan model. In addition, the use of only a 1D model was also compared. The inner and outer fan characteristics were constructed using a nominal curve of bypass ratio against $N/\sqrt{T_1}$.

For calculations of off design thrust and specific fuel consumption, as expected, the results were the same for the inner and outer model and the 2D fan model. This ceased to be the case on altering the relationship of bypass ratio against $N/\sqrt{T_1}$, for example, by a small reduction in the bypass nozzle area.

Both the inner and outer and 2D fan maps differed from the 1D map modelling of the fan. The 1D model overpredicts the core delivery pressure and therefore the capability of the engine.

Transient modelling of the same fan with the two models also highlighted differences due to the relationship between bypass ratio and power setting being altered during the transient, rendering the inner and outer fan model characteristics inappropriate. The 2D fan is a more general model that can accommodate this phenomenon.

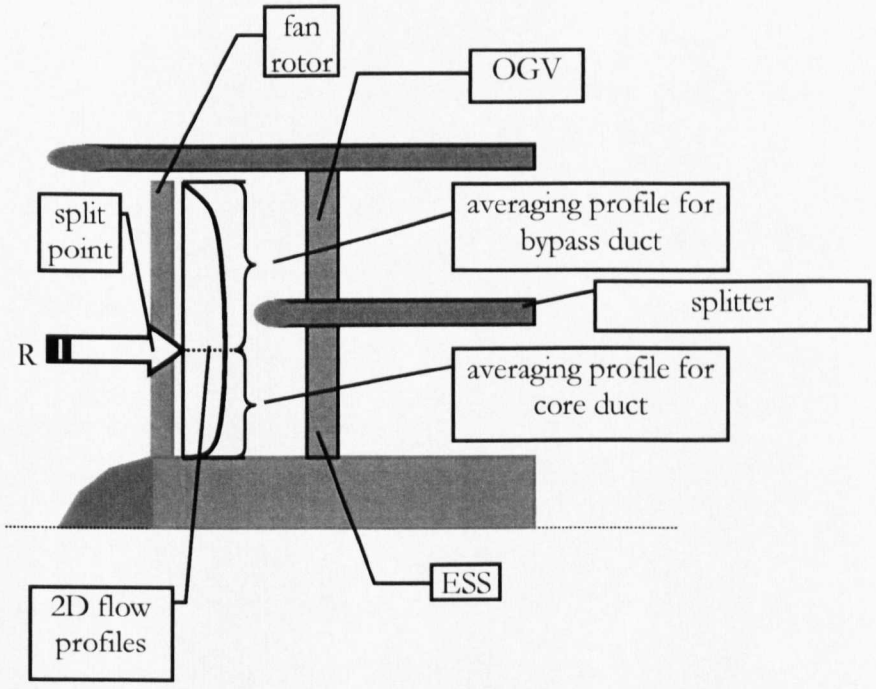

Fig. 3.3 2D-HBPR fan concept of flow split and averaging.

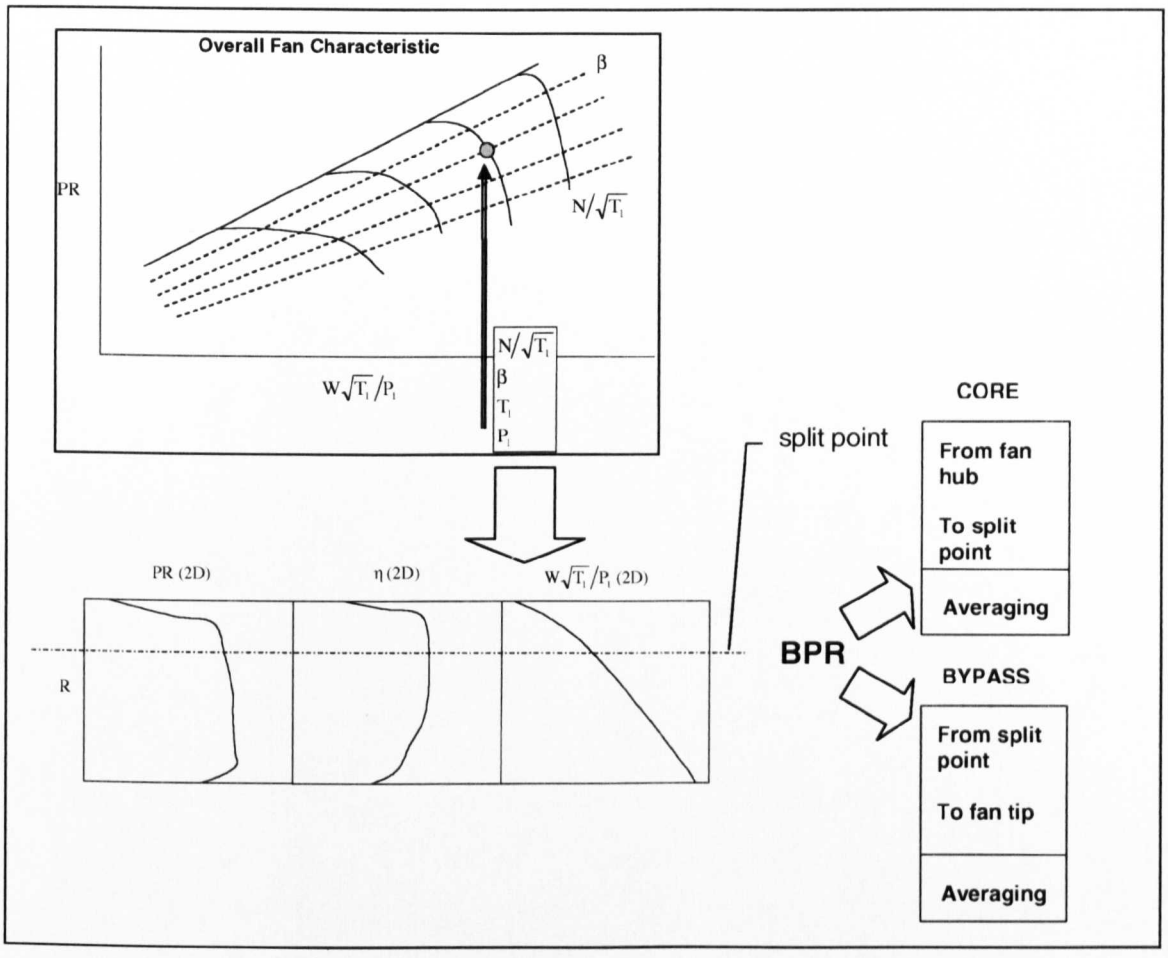

Fig. 3.4 2D fan concept of obtaining 2D profile information at each 1D operating point.

3.3.2.2 MTU model (Riegler et al, 2001)

The inner and outer fan map system can be extended to include maps at deviations from the nominal bypass ratio.

There is now the common flow characteristic also dependent on bypass ratio:

$$W\sqrt{T_1}/P_1 = f\left(\mu - \mu_{nom}, N/\sqrt{T_1}, \beta\right)$$

The core characteristics:

$$P_{21}/P_1 = f\left(\mu - \mu_{nom}, N/\sqrt{T_1}, \beta\right) \text{ and } \eta_{21} = f\left(\mu - \mu_{nom}, N/\sqrt{T_1}, \beta\right).$$

The bypass characteristics:

$$P_{13}/P_1 = f\left(\mu - \mu_{nom}, N/\sqrt{T_1}, \beta\right) \text{ and } \eta_{13} = f\left(\mu - \mu_{nom}, N/\sqrt{T_1}, \beta\right).$$

μ is the bypass ratio, μ_{nom} is the nominal bypass ratio. Recognising that the cost of the extra testing would be prohibitive, MTU set out to compute approximate values at the

deviated bypass ratios. Their model applied to fans where the bypass splitter is set back far enough from the fan not to exert any influence on the work done on the airflow.

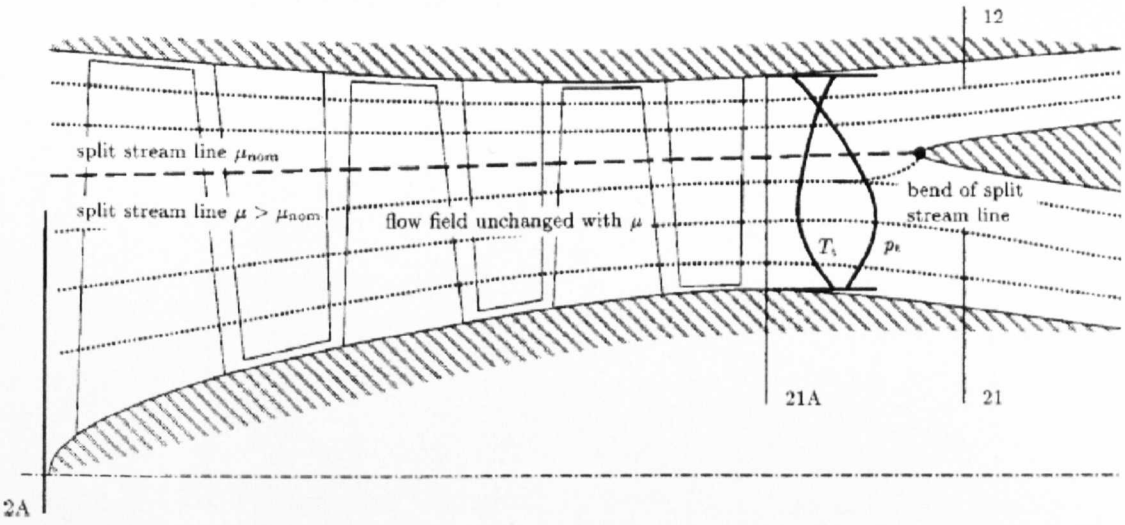

Fig. 3.5 Fans with splitter downstream and typical split stream lines (Riegler et al, 2001).

Fig. 3.5 demonstrates this by showing that if the inlet corrected flow is kept constant, then varying the bypass and core throttles to alter the bypass ratio has no effect on the position of the streamlines passing through the fan. Any change to alter the flow through the two throttles takes place downstream of the last stator row by a bend of the split streamline towards the leading edge of the splitter. The overall fan characteristic remains the same.

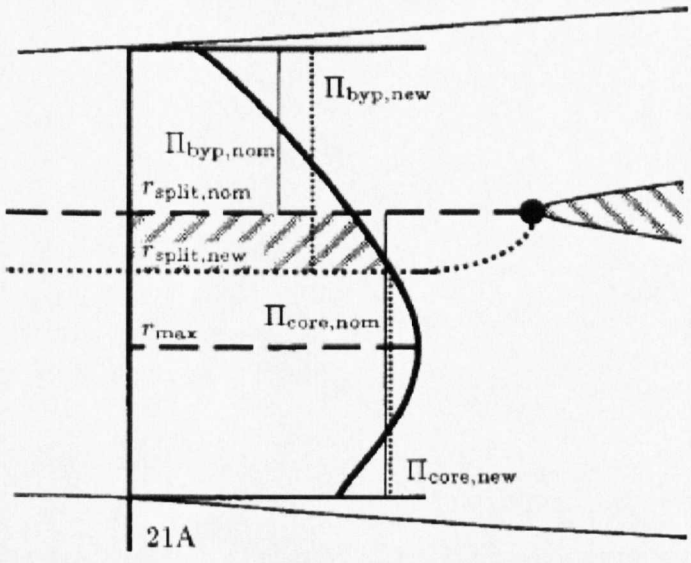

Fig. 3.6 Correcting algorithm for pressure ratio (Riegler et al, 2001).

This means that pressure and temperature profiles at the fan exit position 21A in **Fig. 3.5** will be constant as the fan overall performance stays constant. The profiles can be used to calculate the characteristics for different bypass ratios by calculating the mean values in the core and bypass and integrating the radial profiles beginning with the radius on the split streamline which is dependent on the actual bypass ratio.

The correcting algorithm is described thus. Only temperature and pressure profiles for $\mu = \mu_{nom}$ are available from the rig test. See **Fig. 3.6**.

1. The temperature and pressure profiles are approximated to parabolic curves versus radius. The pressure profiles have a maximum value estimated to be located at a constant radius r_{max}, and the temperature profiles are estimated to have a minimum value at the same radius. The bypass and core stream measurement gives the average values of pressure and temperature in the bypass and core stream ducts. Therefore, for each profile of pressure and temperature, there exists three boundary conditions which make up the coefficients that can form a parabola to approximate the pressure and temperature profiles. This reduces the information that is stored from a rig test. Only the average downstream values and the value of r_{max} are retained for the simulation procedure.
2. The radius of the split stream line $r_{split,nom}$ for μ_{nom} can then be calculated using basic gas dynamics assuming constant static pressure in station 21A for simplicity.
3. The radius for the new split streamline $r_{split,new}$, for μ_{new} can then be calculated using μ_{new}, based on the pressure and temperature profiles calculated. The mean characteristic stays constant so the static pressure at 21A and the total mass flow stays the same as for μ_{nom}.
4. Next, the pressure and temperature profiles can be integrated from the new split streamline radius to the inner wall radius for the core parameters, and to the outer wall radius for the bypass parameters. This is equivalent to a shift of the hatched part of the pressure profile in **Fig. 3.6** from the core to the bypass flow. The new averaged parameters form the new characteristics at the deviated bypass ratios.

It is the shape of the pressure and temperature profiles at station 21A that determines how much influence bypass ratio has on the deviated performance. For example, if the nominal profile shows a higher pressure ratio in the core than in the bypass stream (which is the profile shown by the fan modelled in this study), then a deviation of bypass ratio which is

an increase would result in the bypass pressure ratio increasing. Typical results from the study of Riegler et al (2001) for a 3 stage fan of design bypass ratio of 0.4, can show for a BPR deviation of $\mu - \mu_{nom} = 0.4$ at 100% speed, a 2% increase in bypass pressure ratio over the nominal value and a 5% increase in bypass efficiency over the nominal value.

It was also noted in this study that the nominal bypass ratio is also an important figure. For example, when bypass ratio is increased, the change in bypass and core characteristic performance is caused by the part of the mass flow moved from the core to the bypass flow. A low bypass ratio fan is affected much more than a high bypass ratio fan in this respect. A 10% increase in bypass ratio causes a 5% increase in bypass mass flow when $\mu_{nom} = 1$, but only a 0.8% increase in bypass mass flow when $\mu_{nom} = 10$ (Riegler et al, 2001).

In summary, the Rolls-Royce and MTU methods are similar in philosophy. Rolls-Royce however uses the raw fan data from the result of rig testing and throughflow streamline curvature analysis directly in the iteration scheme. MTU has removed this data and approximated the profiles as paraboli. Some accuracy may be lost with this operation.

3.4 SELECTION OF FAN REPRESENTATION FOR FANS OF LBPR TURBOFAN ENGINES

Strategy: (i) HBPR model discussed above. Can any of this be applied to LBPR? (ii) Examine test data. (iii) Examine past results in papers, e.g performance models and CFD.

3.4.1 Background on differences between LBPR and HBPR fans

Low bypass turbofan (typically found in military jet aircraft) characteristics have already been investigated (Li, 1999) and the following are the main differences compared to high bypass civil turbofans, (see **Fig. 3.7**).

a) The low bypass fan has less variation in blade speed between the tip and the root of the blade due to higher hub-to-tip ratios. The outcome is a relatively smaller radial variation of fan outlet pressure and temperature.

b) The low bypass fan usually has more than one stage and correspondingly higher pressure ratios.

c) The fan architecture is typically different. In the high bypass fan, which invariably has just one stage, the fan rotor exit leads to a splitter dividing the bypass and core ducts with the respective stators for the ducts, namely the outlet guide vanes and the engine section stators, situated downstream of the splitter leading edge. For typical low bypass fans, there are full-

span stators crossing the annulus after the last rotor and this is then followed by a splitter, which divides the flow to the bypass duct and the high pressure compressor.

d) With low bypass fans, due to the higher hub-to-tip ratio, boundary layers occupy a relatively larger part of the flow than in high bypass fans. It is also significant that these boundary layers are usually larger in magnitude than for high bypass fans as well due to the typical installation having a very long intake compared to the typical short pitot intakes of podded civil gas turbines. Boundary layers exacerbate the secondary flows in multistage fans or compressors, especially with lower aspect ratio blades.

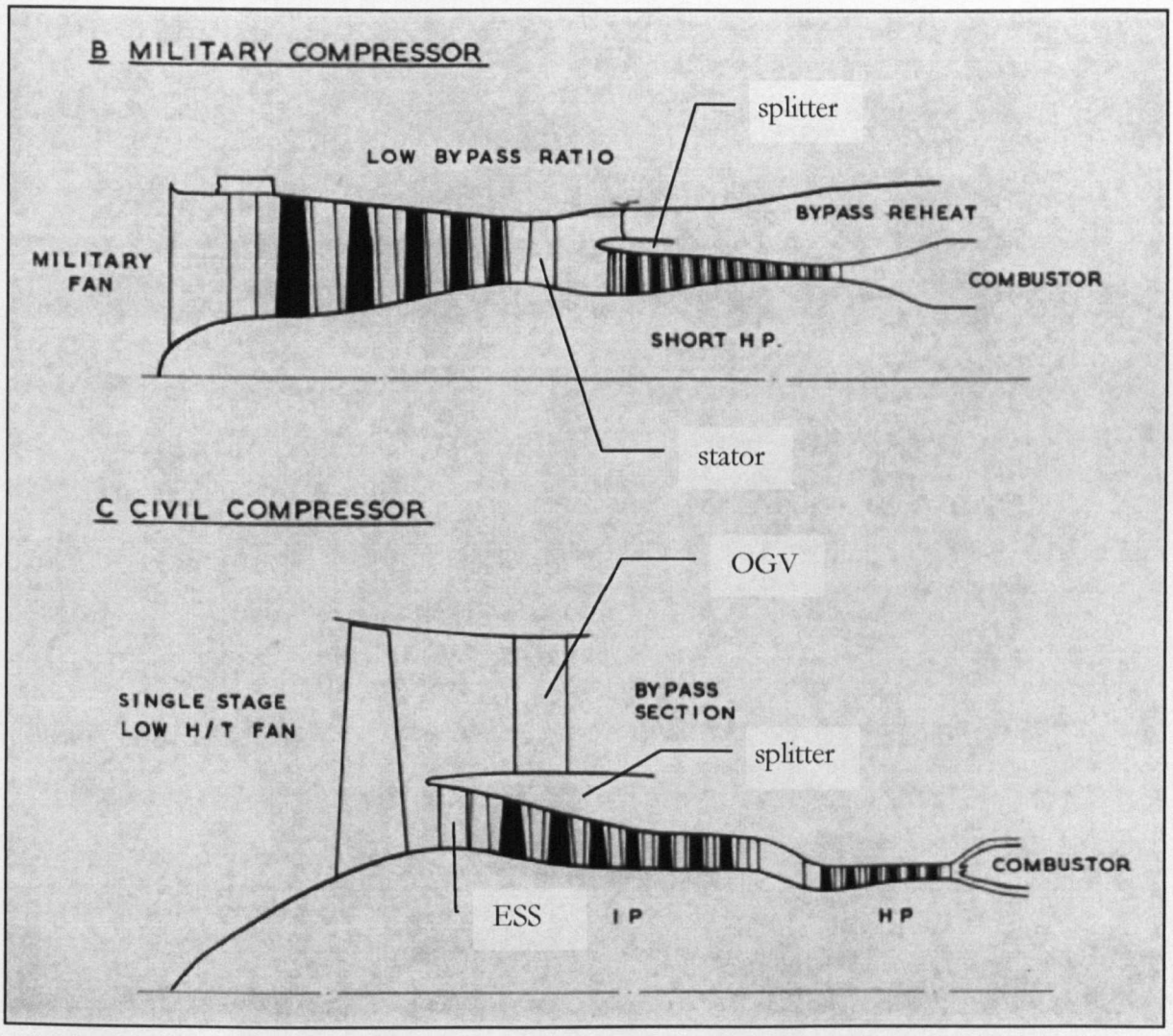

Fig. 3.7 Comparison of fans in military and civil turbofans, (Wall, 1976).

3.4.2 Rig test and engine data – high bypass ratio fan rig test data

A study was made of HBPR fan rig test data (Marshall, 1998). The two main conclusions were:

- Fan exit profiles of independent parameters were independent of BPR at a fan speed and inlet flow function.
- Circumferential variations of total pressure and total temperature at fan exit were negligible.

3.4.3 Rig test and engine data – low bypass-ratio fan rig test data

As part of this thesis, an extensive analysis of LBPR fan rig test data was carried out with access to various LBPR fans of varying nominal BPR ('Li, 1999). This work includes proprietary company information so the data is not published here. The main conclusions will be given.

3.4.3.1 Analysis of the Data

The data was for LBPR fans with a maximum BPR of approximately 1, ranging from 2 to 3 stages. For each test point, the ambient conditions were supplied, with BPR and fan exit total temperature and total pressure radially and around the circumference of the annulus. In almost all cases, the fan exit total temperature and total pressure measurements were on combination rakes in the HPC duct and bypass duct aft of the bypass flow splitter. In one case, the measurement rakes were directly at the splitter. No measurements were taken directly at the fan trailing edge stator. Engine tests were also available for some of the fans, with the BPR being controlled by partially blocking the exhaust nozzle with a bung.

3.4.3.2 Limitations of the Data

As indicated above, the data was mostly for after the fan splitter whereas better information would be gained of fan exit conditions at the fan stator trailing edge. The profile of flow after the fan splitter compared to at the fan trailing edge may be modified by the division of the flow into 2 different area ducts with 2 different mass flows (e.g. streamtube contraction), and any losses at the casing and splitter walls. No data existed with the measurements at the required position in LBPR fans in contrast to HBPR rig tests, due to the constraint of space required for instrumentation.

The range of fans was limited. Data was unavailable for a higher BPR range, bridging the gap to the large civil fans. This could have given an indication of a range of behaviour from very high BPR to very low BPR fans in conjunction with the earlier study (Marshall, 1998).

3.4.3.3 Summary of Data analysis

The following main findings were made:

- Both HBPR and LBPR fans exhibited large radial variations of total pressure and total temperature (**Fig. 3.8** and **Table 3**). Radial variations were slightly higher in the HBPR fan.
- Circumferential variations in LBPR fans are an order of magnitude higher than in HBPR.
- Circumferential variations in LBPR fans also exist in total temperature.

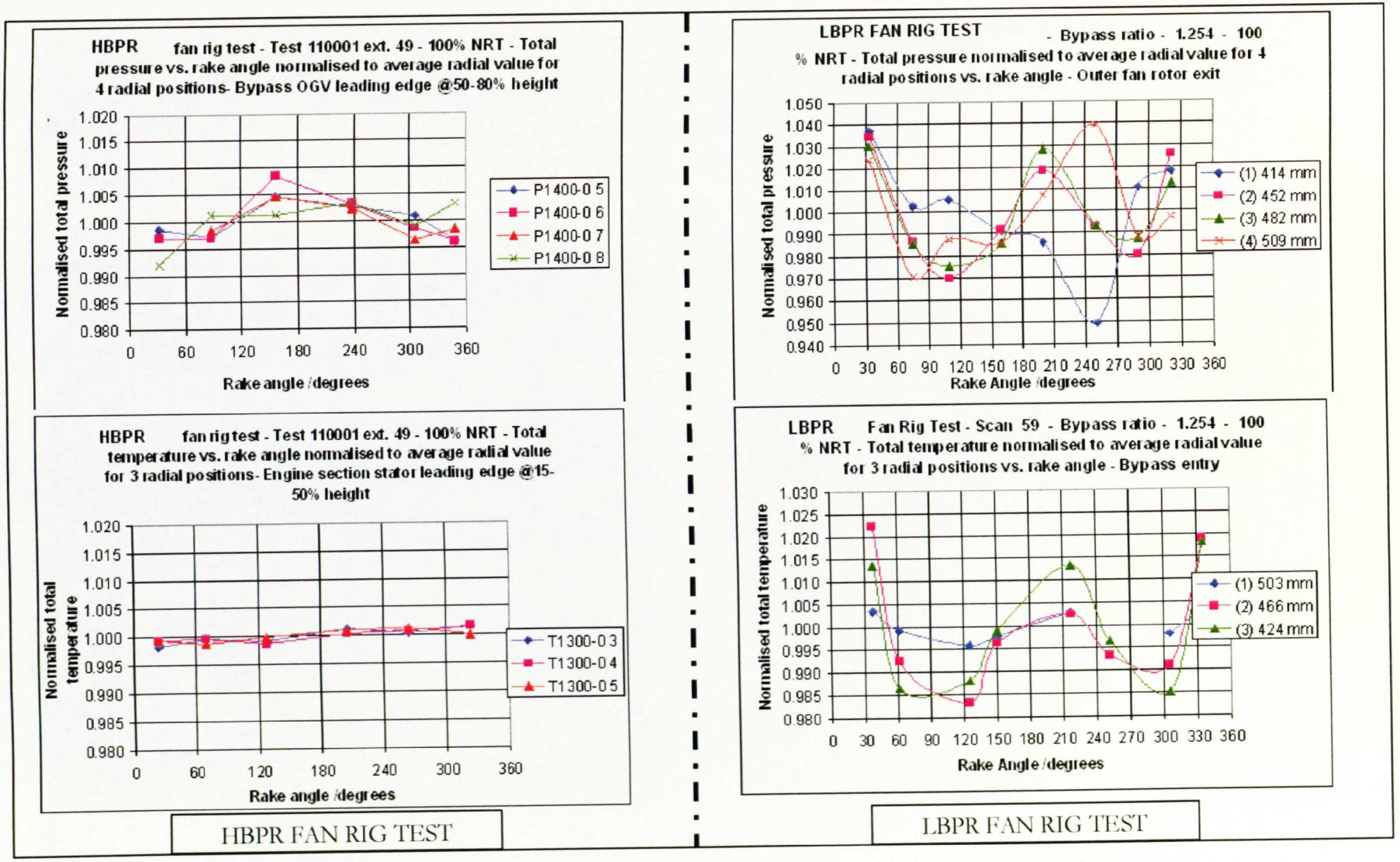

Fig. 3.8 Comparison of rig test measured normalised radial fan exit profiles between a HBPR fan and a LBPR fan.

		HBPR fan rig test at 100% $\frac{N}{\sqrt{T}}$	LBPR fan rig test at 100% $\frac{N}{\sqrt{T}}$
Maximum circumferential variation as percentage of average	Total pressure	0.84%	5.10%
	Total temperature	0.32%	2.24%
Maximum radial variation as percentage of average	Total pressure	16.1%	12.0%
	Total temperature	4.6%	4.6%
Approximate circumferential to radial variation	Total pressure	5.6%	42.0%
	Total temperature	7.5%	48.6%

Table 3 Comparison of radial and circumferential variations of fan exit values between a high and a low bypass ratio fan.

- The circumferential variations are multiple per revolution.
- The BPR range in the LBPR test was very small. No data could be discerned for a case at a speed and flow function that was appreciably different in BPR.

3.4.3.4 Conclusions of data analysis

It was therefore inconclusive as to whether the fan exit profiles are independent of BPR at a fixed non-dimensional speed and inlet flow function in LBPR fans.

The 2D-HBPR fan model (section **3.3.2.1**) was applied on the basis of negligible circumferential distortion at fan exit, so that the radial profiles could be treated as an axisymmetric average profile. To do the same in LBPR fans would require the assumption that the circumferential variations could be averaged and the resulting average radial profile would be representative of the flow. This may not be the case if the variations are large compared with the average levels of total pressure or total temperature at the fan exit.

Further investigation is required before modifying the 2D-HBPR fan or devising a new fan model.

3.4.4 The bypass ratio effect

The basis of the 2D fan model is that the splitter is far enough downstream of the fan so as not to affect the flow streamlines passing through the fan at a fixed non-dimensional

operating point on the overall fan map. This has been found to be the case in large civil turbofans (Marshall, 1998) and in some low bypass ratio fans (Riegler et al, 2001). The key factor appears to be the axial spacing between the splitter and the exit of the fan. The spacing is larger in high bypass fans, although the stators tend to be situated aft of the splitter nose, thus placing the splitter nearer the rotor. However, the spacing is still larger than in some low bypass ratio turbofans. A well analysed case is the Pratt and Whitney F100 fan (Shaw, 1982).

Two versions of this three-stage fan were used; a remote splitter configuration for the F-15 aircraft and a proximate splitter configuration for the F-16 aircraft. The turbomachinery was equivalent and the difference was with the splitter spacing from the final rotor of the fan. Fig. 3.9 shows the effect of situating the splitter too close to the rotor.

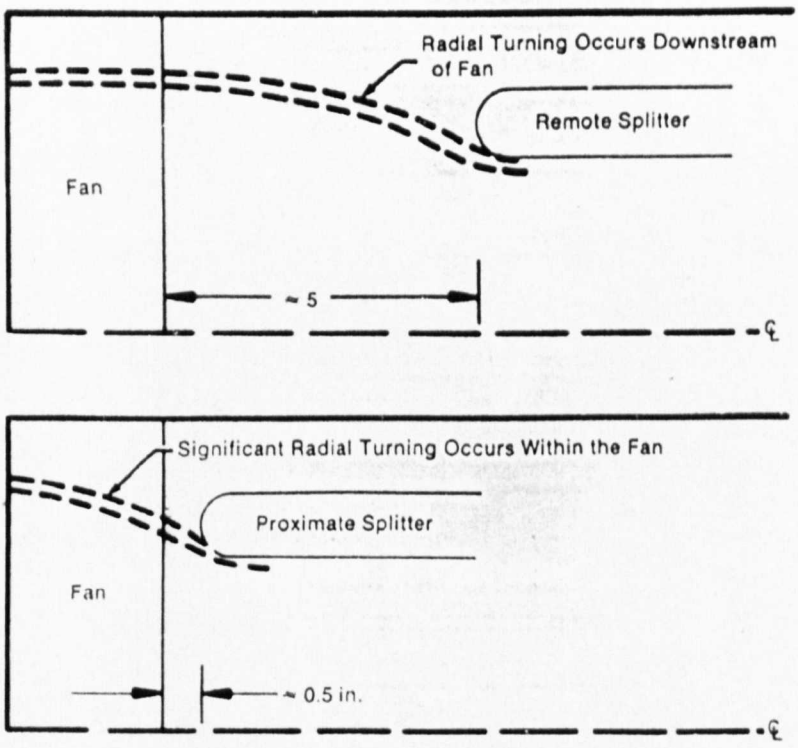

Fig. 3.9 F100(3) splitter configuration affects location of radial turning of streamlines, (Shaw, 1982).

Instead of the bend of the flow split streamline occurring well downstream of the rotor, it can occur within the rotor stage and stator if present. At a fixed non-dimensional speed and overall mass flow, changing the bypass ratio changes the radius of the split streamline. The

new split streamline has to bend towards the bypass splitter nose and the presence of this varying radial flow in the stator with bypass ratio means that different work is done on the airflow according to the bypass ratio. This means that different averaged values of pressure and temperature are delivered to the bypass and core duct entries according to the bypass ratio. An inner and outer fan system therefore needs to account for the change in bypass and core characteristics with changes in bypass ratio.

A scheme has been put forward for the effect of changing streamline curvature through the fan (Walsh, 1998).

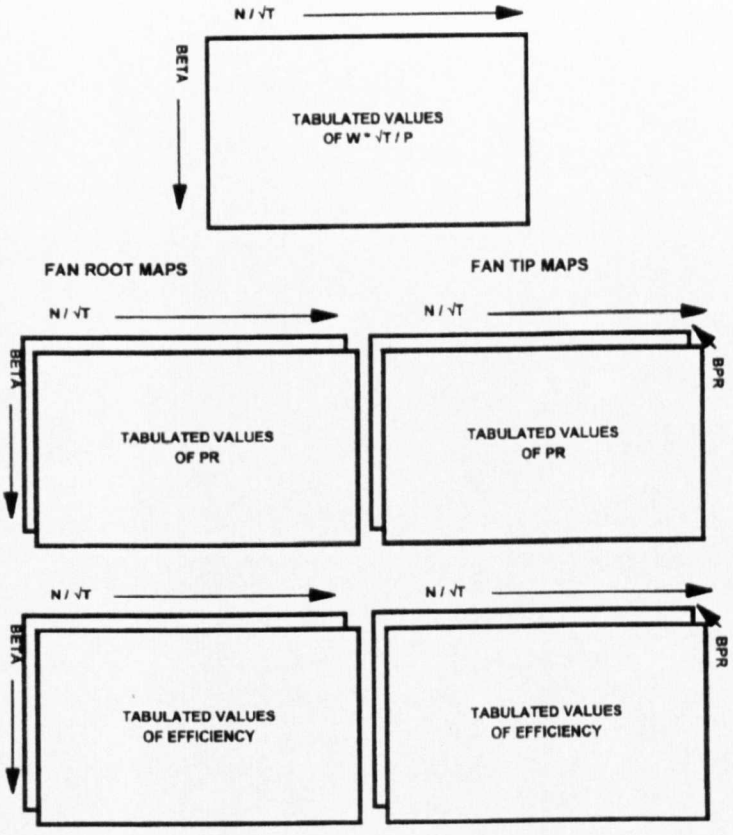

Note:
Fan root and fan tip maps are repeated at intervals of 0.5 bypass ratio.

Fig. 3.10 Fan maps required for rigorous off design modelling (Walsh, 1998).

Pratt and Whitney collected rig test data of stage characteristics and investigations showed that the first 2 stages of the fan were unaffected by the bend of the streamline. The third

rotor and intermediate casing strut characteristics were altered on the basis of changing bypass ratio. Because static pressure characteristics were used, there was also a modification for the change in flow area towards the bypass or core ducts of the split streams. With this particular fan, it was concluded that with the rotor approximately 1inch beyond the splitter, the effect was relatively small.

Fig. 3.12 shows the new bypass ratio representation of the overall fan characteristic of the F100 remote splitter configuration that shows the least effect of bypass ratio. A similar proximate splitter configuration to the F100 is that of the TFP-30 turbofan (**Fig. 3.11**) and it shows a significant bypass ratio effect on the overall fan characteristic at the higher corrected speeds.

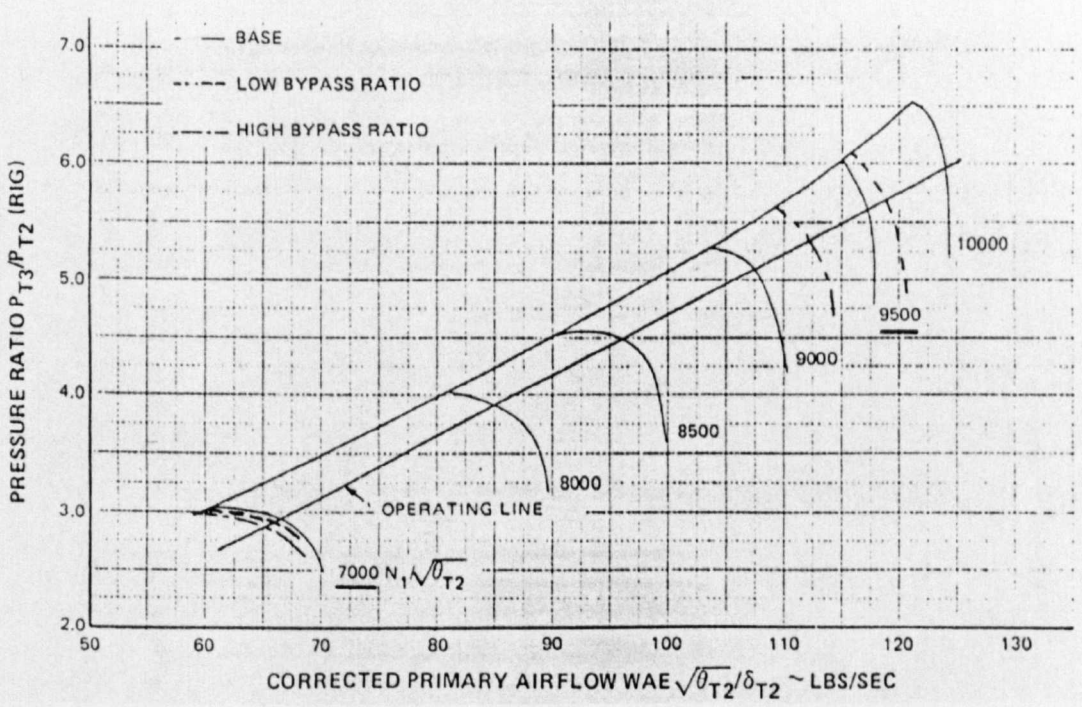

Fig. 3.11 Bypass ratio effect on TF30-P3 low pressure compressor rig performance (Mazzawy, 1977).

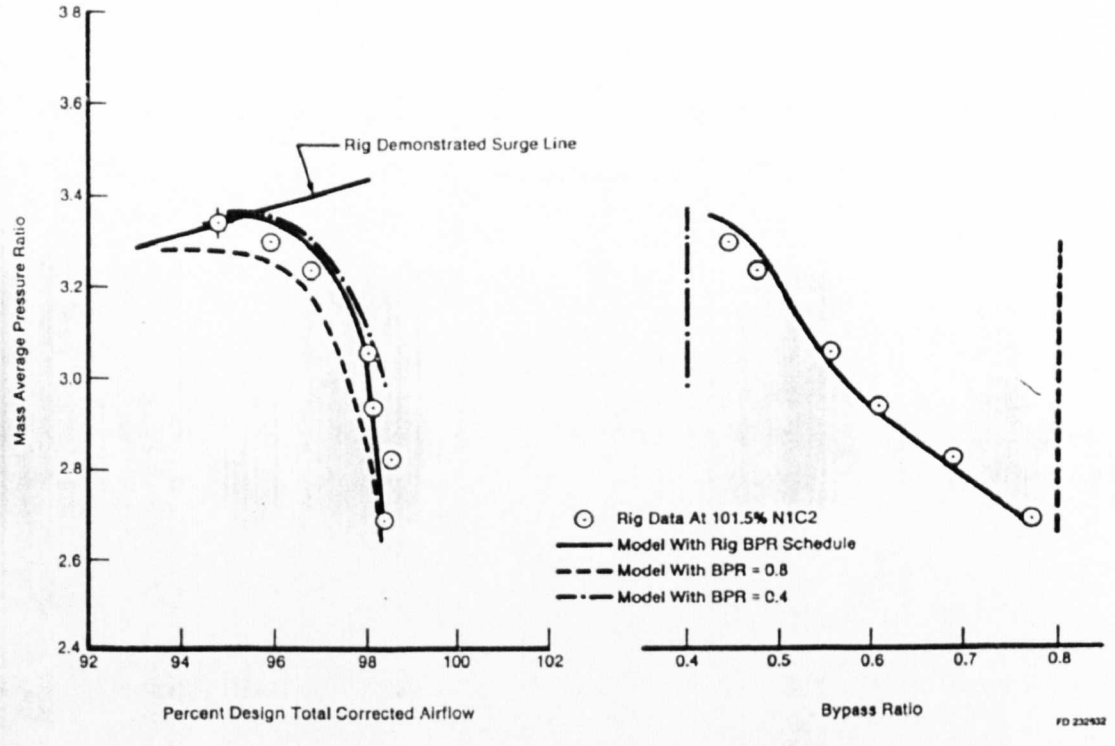

Fig. 3.12 Effect of input bypass ratio on revised remote splitter model predicted fan performance (Shaw, 1982).

The issues of having the streamlines changing shape in passing through the rotor is this. By changing radius through the rotor, a particular streamline will experience a different blade speed and a different flow turning effect with altered efficiency. The resulting flow will have a different static pressure 2D profile distribution to that before the bypass ratio was changed and different axial velocity profile. The flow streamlines change radius because of this to regain radial equilibrium. This may even adjust the flow before the fan rotor and not just after it.

3.4.5 Summary of factors for selection.

It would be ideal to be able to run compressor rig tests over a wide operating range to obtain the compressor characteristics necessary for gas turbine performance simulation. However, this is not possible because of the cost of testing, estimated in the order of £millions. Therefore, rig tests are only run to obtain the dominant effects in a small operating

range (Riegler et al, 2001). This reports highlights one aspect of fan performance in turbofan engines that is necessary for improved fidelity performance calculations but is not routinely obtained during rig testing, namely, the effect of splitter proximity on fan performance.

3.4.6 Cost-effective solution – 2D-LBPR fan model

It is excessively costly in terms of money and time to extend the rig test to a range of bypass ratios away from the nominal schedule. The aim is to be able to compute the characteristics for the altered bypass ratios.

At this stage, two different issues are identified.

(i) A need for a fan model to enable different schedules of bypass ratio vs. $N/\sqrt{T_1}$ to be modelled for the case of changing the geometry or for transients. The 2D-HBPR fan was devised as a general model that could accomplish this, but it relied on the profiles being unaffected by the changing bypass ratio at a fixed overall fan operating point.

(ii) With the profiles being affected by change of bypass ratio at a fixed β and non-dimensional speed, it means that the 1D overall characteristic changes with a change in bypass ratio. The 2D-HBPR fan model has to be revised to include the capability of being able to calculate new profiles at fixed speed, β, and altered bypass ratio. The new model must also retain the bypass ratio information that was recorded during the rig test at the nominal bypass ratio vs. $N/\sqrt{T_1}$ schedule. The current method of obtaining an inner and outer fan characteristic by rig testing according to a pre-calculated bypass ratio schedule is not expected to be changed. For a new model to take into account bypass ratio would more ideally have speed lines at a fixed bypass ratio.

Fig. 3.14 shows the new 2D fan concept based on a change of profile with bypass ratio. The nominal 1D overall characteristic is that taken from the rig test. This will contain a series of speed lines which across the working line should contain the 1D fan performance at the nominal bypass ratio vs. $N/\sqrt{T_1}$ schedule. The other points on the speed line have bypass ratios that reflect the nature of the rig test.

1. For the bypass characteristic, the core is kept at the working line flow:
    a. Increase the bypass mass flow until choke → ↑ BPR
    b. Reduce the bypass mass flow until stall → ↓ BPR
2. For the core characteristic, the bypass is kept at the working line flow:
    a. Increase the core mass flow until choke → ↓ BPR
    b. Reduce the core mass flow until stall → ↑ BPR

The result is a fairly random set of bypass ratios along a speed line with in increasing and decreasing corrected mass flow from the nominal working line point. (**Fig. 3.13**).

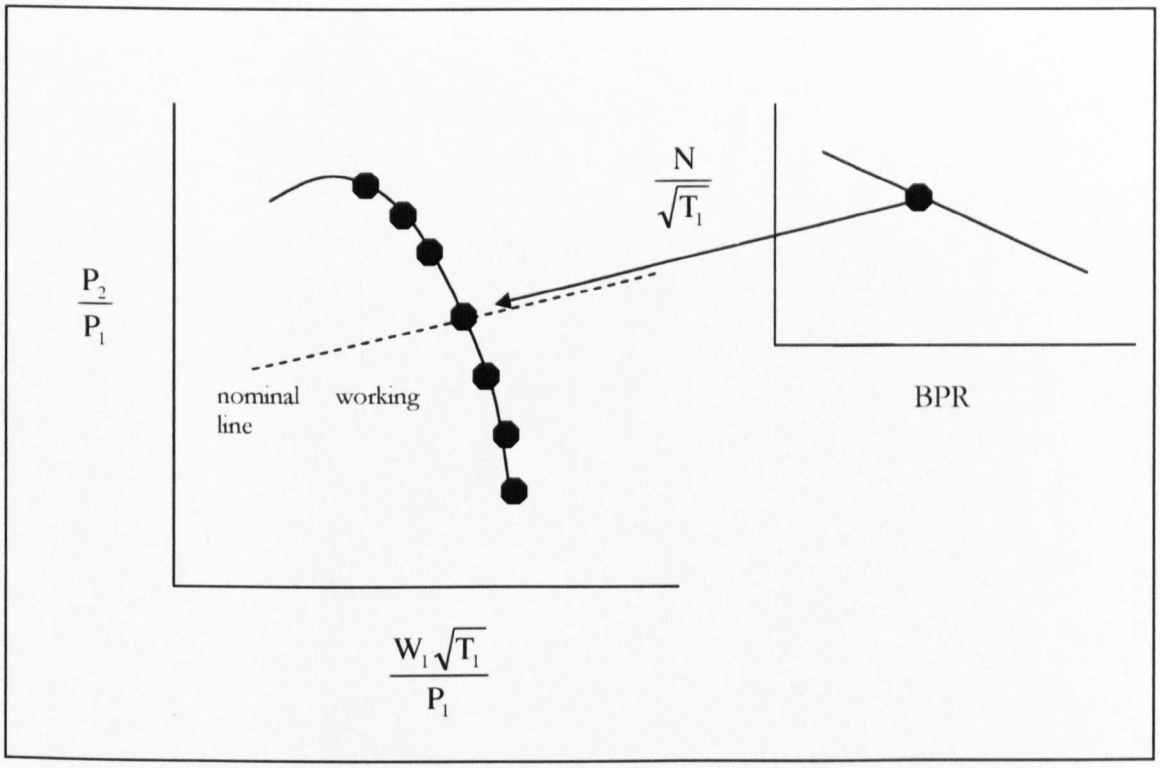

Fig. 3.13 Nominal bypass ratio at working line.

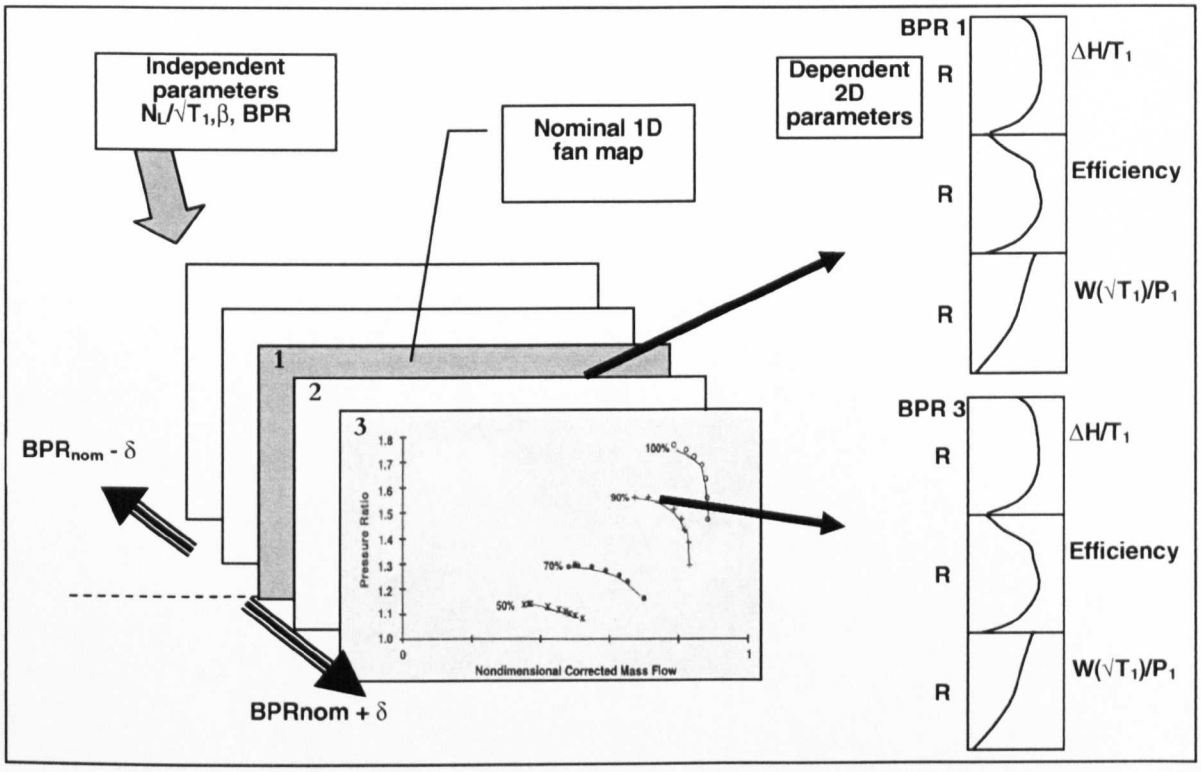

Fig. 3.14 2D-LBPR fan concept of obtaining 2D profile information at each 1D operating point, dependent on the bypass ratio.

3.4.7 Conclusions of model selection.

Effectively, there are currently 2 types of fan model. The inner and outer fan model family has fan data from a rig test at a fixed BPR vs. $N/\sqrt{T}$ schedule. This data requires modification for when the any change is made that alters this schedule, such as for nozzle area changes.

To counteract this, a class of 2D fans modelling the fan exit radial flow profiles has appeared. The Rolls-Royce model (section **3.3.2.1**) uses rig-derived fan exit profiles. The MTU model (section **3.3.2.2**) replaces test data with parabolic curves set by 1D data. In the author's opinion, it is unnecessary to discard the data obtained from testing and to increase the potential for inaccuracies from using a simplified curve fit. The MTU model may be acceptable for LBPR fans with smaller fan exit profile variations, but may not model the HBPR fans with large variations in profiles. It is felt that it is better to use one method to model all fans (i.e. use of rig profiles). There is today no computing power limit on doing so. The disadvantage is the need for more operator input to generate the fan maps (whereas the

MTU method uses existing 1D data), but rake checking and other automated processes may relieve this load.

The 2D-LBPR fan has the potential to deal with BPR vs. $N/\sqrt{T}$ schedule changes. No other method of conventional component based iterative performance simulation methods is known to exist. The method depends on the availability of test data for multiple bypass ratios at a speed and flow function. Other methods that may be able to deal with BPR variations are CFD-predictive based, such as NPSS component zooming but these are extremely intensive in computing power and it may be a long time before such methods are routine.

3.5 STRATEGY FOR COMPARISON OF THE MODELS

So far, the work has identified 3 models for comparison. These are (i) the conventional inner and outer fan map model (section **3.3.1**), (ii) the 2D-HBPR fan model (section **3.3.2.1**) and (iii) the new 2D-LBPR fan model devised in this study (section **3.4.6**). In the first two cases, the fan models already exist in work done previously in the Cranfield University School of Engineering (Yin, 1999). Several codes need to be written to enable the new fan model to be used in the comparison.

The strategy used is to base all model comparisons on 1 set of actual rig test data from an LBPR fan. The 3 models, i.e. inner and outer fan, 2D-HBPR fan and 2D-LBPR fan will be set to be equal, all modelling the same geometry engine with the same BPR vs. $N/\sqrt{T}$ schedule. All 3 models should then give the same results, being the same geometry engine. The flow of data in the strategy scheme is shown in **Fig. 3.15**.

The rig test data is used to create the 2D-HBPR fan data set. This is applied to the turbofan simulation program and the design point is scaled, giving a set of component scaling factors. In all performance simulations, this same set of component scale factors will be used, to ensure the same engine is being compared each time and the only difference will be the fan component. The converged performance run of the 2D-HBPR fan provides the BPR vs. $N/\sqrt{T}$ schedule to generate inner and outer fan maps. This is done with an inner and outer fan generator program (flowchart in **Appendix 9**). The inner and outer fan map data contains the bypass and core maps as 1D maps of pressure ratio, flow function, $\Delta H/T$ and $\Delta H_{IDEAL}/T$ as functions of $N/\sqrt{T}$ (11 speed lines) and fan beta (21 beta lines). The inner and outer map is applied to the above turbofan engine and should give the same performance.

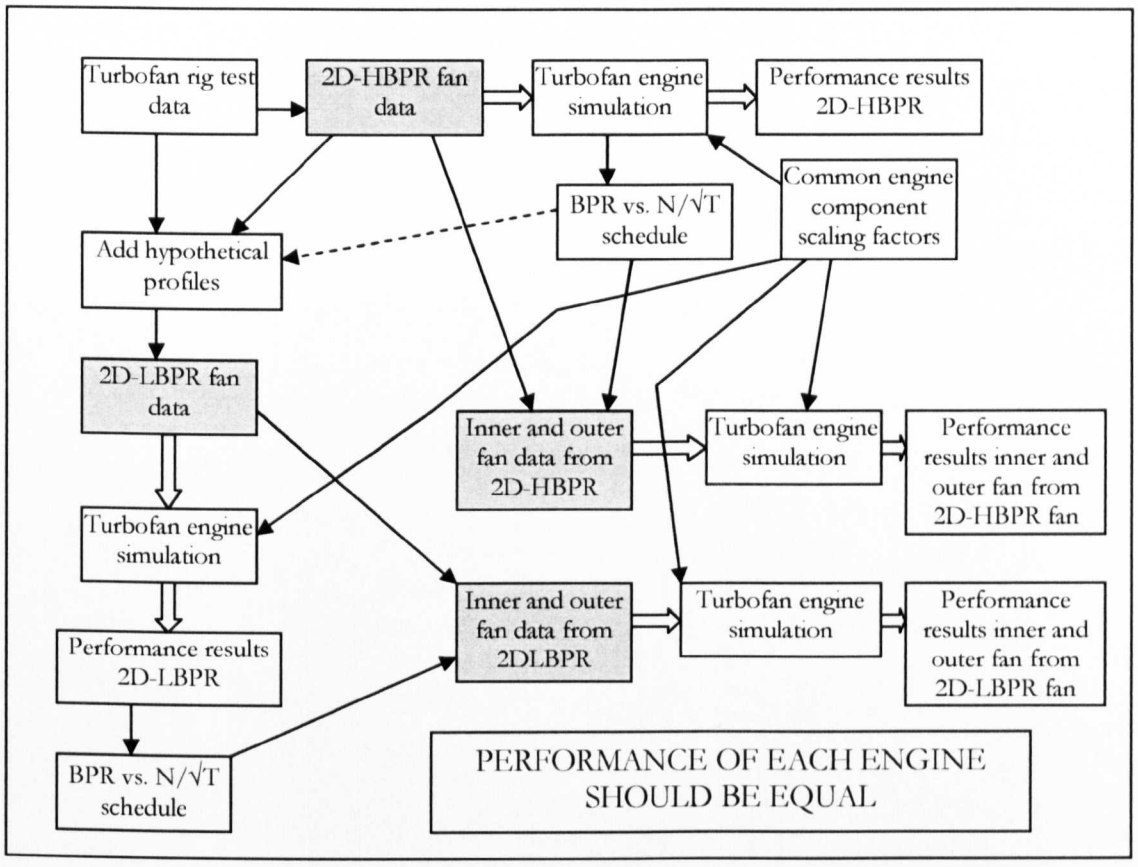

Fig. 3.15 Flow of data in fan model comparison strategy.

The 2D-HBPR fan data set is then used as the basis for 2D-LBPR data. The data is exactly the same as for 2D-HBPR fan for the given BPR vs. $N/\sqrt{T}$ schedule. Hypothetical data is generated for 2 extra BPR values; in this instance at ±0.3 BPR increments from the original BPR vs. $N/\sqrt{T}$ schedule so that the data contains 2D profiles of pressure ratio, flow function, $\Delta H/T$ and $\Delta H_{IDEAL}/T$ as functions of $N/\sqrt{T}$ (11 speed lines), fan beta (21 beta lines) and BPR (3 values). The performance run of the same engine with the 2D-LBPR fan data should give the same results.

As a final comparison, the 2D-LBPR fan data is used to create the inner and outer fan maps. The BPR vs. $N/\sqrt{T}$ schedule taken from the 2D-LBPR turbofan results is applied to a modified version of the inner and outer fan map generator that can accept multiple bypass ratios at a speed. As the BPR schedule should be equivalent to the result from the 2D-HBPR performance run, it should give the same inner and outer fan map set as before.

The fan model data for the 3 models are then each incorporated into the separate exhaust turbofan engine simulation code. Each is scaled to give design point at 1500K. The other engine components are exactly the same. The fan models are effectively the same and the

first test is to demonstrate this. Following this, an effect to alter BPR vs. $N/\sqrt{T}$ schedule (core nozzle area change) is introduced to show the capability of the 2D-HBPR fan over the inner and outer fan. The same is done for the 2D-LBPR fan. Next, more BPR schedule changes are made to show that the 2D-LBPR fan differs from the 2D-HBPR fan. Finally, a series of different component changes are made to the engine to demonstrate the operation of the 2D-LBPR fan to calculate the new fan working line.

3.6 TURBOFAN PERFORMANCE SIMULATION PROGRAM

The performance procedure used to test the 2D fan subroutines is shown in the flowchart of **Appendix 5**. This routine has an error in the sequence of guesses and checks which was worked around as described in section **3.6.2**.

3.6.1 Description of performance model changes

The model is derived from work by Yin, (1999). The following additions have been made for this work.

- The 2D-LBPR model has been added to the same code as an option to the 2D-HBPR code. This avoids having 2 concurrent programs and the need to maintain equivalent changes to both.
- An autoscale procedure has been added. The previous method was laborious and needed the operator to scale the components for design point sequentially until spool powers and mass flow continuity was obtained. This process took over 1 hour to achieve so the automatic procedure allows good time saving.

3.6.2 Iteration fault correction

During trials of the 2D-LBPR program turbofan simulation code as adapted from the 2D-HBPR fan with no changes apart from the fan, it was found that the guess of HPC beta would diverge to infinity. Investigations of the Newton-Raphson solver output showed that a match of HPC characteristic flow function and fan core exit flow function could not be made so that the guess of HPC beta (linked to this guess), would go to infinity. It was apparent that the wrong guesses and checks were linked. A different guess would need to be linked to HPC flow capacity in order to enable the full range of HPC speed to be iterated. The revised iteration scheme is shown in **Appendix 5** and was done for the work in Chapter

4. For this chapter, a temporary workaround was devised by selecting a HPC characteristic with flatter speed lines that covered a larger range of flow function (the original map used had very vertical speed lines). This work has as yet not been repeated on the revised model.

3.7 2D-HBPR FAN MODEL

The HBPR fan performance model as described in section **3.3.2.1** replaces the original fan routine in the turbofan performance code described in section **3.6**. A flow chart of the fan module is shown in **0**.

3.7.1 The 2D-HBPR fan data

The 2D-HBPR fan generator program (Yin, 1999) converts rig test measurements or streamline curvature predictions of radial temperatures and pressures for a HBPR fan into 2D fan data for the 2D-HBPR fan model. The fan data for this work is obtained from rig test data of a LBPR turbofan engine as raw data (ambient conditions, fan exit total pressures and total temperatures) and fan rotational speed. This is incorporated into the 2D-HBPR fan data file set, containing the 2D profiles of pressure ratio, flow function, $\Delta H/T$ and $\Delta H_{IDEAL}/T$ as functions of $N/\sqrt{T}$ (11 speed lines), fan beta (21 beta lines) and fan exit area ratio (12 values). The area ratio values are based on the test recorded fan exit radial positions of the measurement probes. In fact, the probes are situated at entry to the core entry and fan bypass duct entry after the flow splitter. It was decided to assume that profiles were independent of BPR at a speed and flow function for this fan and to assume these profiles were equivalent at the fan final stator exit.

A second assumption was made to increase the number of radial stations. There were 5 measurement stations in the core and 4 in the bypass in the rig test. The number of radial stations was increased by using spline interpolation to add another 3 stations to make 12, to match that of the HBPR fans. These were added at the raw data stage. The necessary amendments were made to the 2D-HBPR fan data generator to accept the LBPR fan rig data.

3.8 2D-LBPR FAN MODEL

The 2D-LBPR fan model is described in section **3.4.6**. The current engine simulation code contains a switch to choose between the 2D-LBPR or 2D-HBPR codes. The changes

of the 2D-LBPR model from the HBPR model can be seen in the flowchart in **Appendix 7**. The model is a modification of the 2D-HBPR fan, making fan inlet pressure recovery factor, pressure ratio, $\Delta H/T$, $\Delta H/T_{ideal}$, and $(W_{2D}\sqrt{T}/P)/(W\sqrt{T}/P)$ dependent on BPR as well as $N/\sqrt{T}$, fan beta and fan outlet area ratio.

The following points are noted. The fan data file contains both 2D profiles of independent parameters and 1D independent parameters. The only 1D parameter used is total fan inlet flow function. 2D pressure ratio profiles are not used. They are calculated from the $\Delta H/T$ and $\Delta H_{ID}/T$ profiles.

The method takes many more fan model iterations to converge than 2D-HBPR. It depends on the closeness of the initial guess to the final solution, but the maximum number of iterations in the 2D-LBPR model is about 70000 iterations max. compared to 25000 for 2D-HBPR.

3.8.1 The 2D-LBPR fan data

A separate Fortran code has been written to take the 2D-HBPR fan dataset as the input and the BPR vs. $N/\sqrt{T}$ schedule (result of 2D-HBPR fan engine simulation). Since the 2D-HBPR fan is independent of BPR, so that BPR does not appear as a independent variable in the 2D-HBPR fan dataset, the schedule is then set as the nominal schedule for the new 2D-LBPR fan dataset.

In generating hypothetical 2D-profiles for the 2D-LBPR fan for different BPRs, some indicators have been taken from the pressure ratio characteristic of an existing fan (**Fig. 3.11**). The procedure for generating the hypothetical data is shown in **Fig. 3.16**. Only the 1D pressure ratio at a speed and mass flow has been changed for the new BPRs in this work as shown in **Fig. 3.17**. A larger increment of pressure ratio has been set for higher speeds compared to lower speeds as indicated by **Fig. 3.11**. The 2D profiles of pressure ratio have been made to be consistent with the new 1D pressure ratio. An attempt has been made to give the new pressure ratio profiles more physical basis by adjusting the shape according to the bypass ratio. The fan exit split radius has been computed for a bypass ratio given the flow function profiles, and weighting is applied to the new 2D pressure ratio profile on either side of the split. Efficiency profiles and fan inlet flow function are as for the nominal BPR schedule.

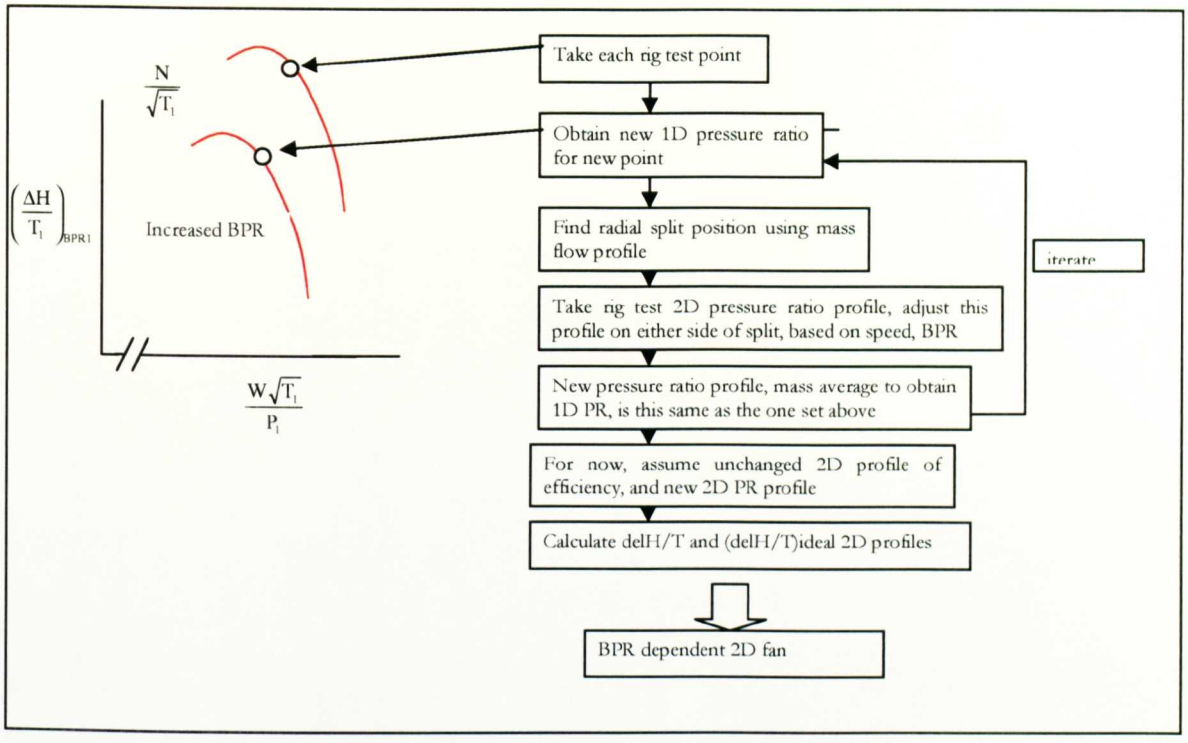

Fig. 3.16 Diagram showing how new hypothetical profiles are generated from known profiles.

3.9 INNER AND OUTER FAN MODEL

The inner and outer fan model data is generated from the 2D profile data of the 2D-HBPR fan model given an input BPR vs. $N/\sqrt{T}$ schedule. The program used was derived from work done by Yin(1999). The program was modified to enable it to convert the 2D data from the 2D-LBPR fan into an inner and outer fan map. This was added to the same program with a switch.

To enable the 2 inner and outer models (based on 2D-HBPR and 2D-LBPR respectively) to be compared, the same BPR schedule is used for each. The schedule is an output of running the 2D-HBPR fan model. A flowchart is shown in **Fig. 3.15** to show the data generation path.

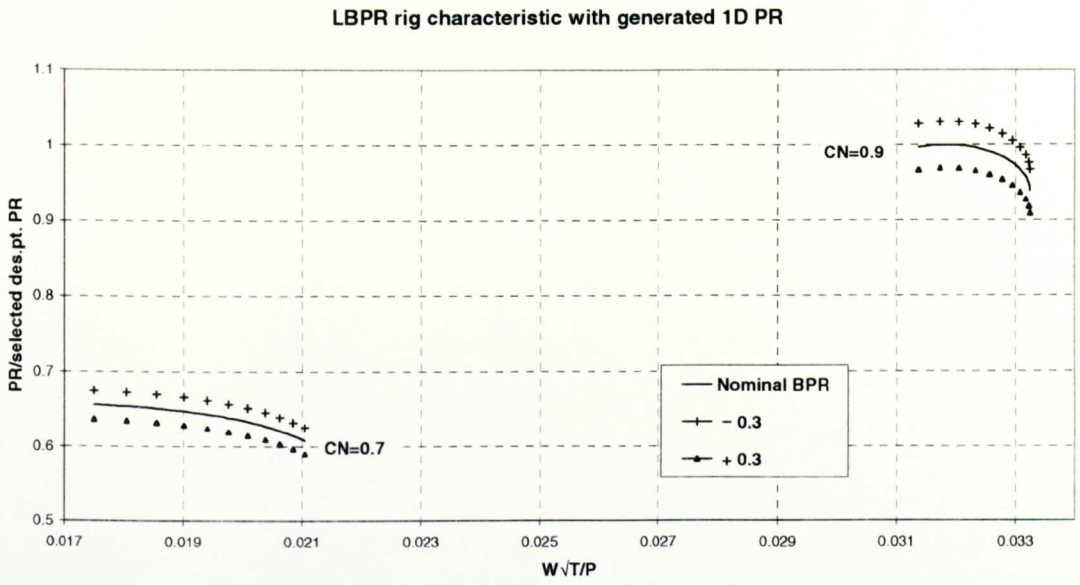

Fig. 3.17 Creating new 1D speed lines for bypass ratio dependent 2D-LBPR fan model from the original characteristic.

3.10 ENGINE PERFORMANCE MODELLING COMPARISONS WITH 3 FAN MODELS

3.10.1 Comparisons of engine performance with 2D-LBPR fan, 2D-HBPR fan and inner and outer fan models (derived from 2D-HBPR data and 2D-LBPR data

Fig. 3.18 to **Fig. 3.23** show the comparison between off-design performance of a LBPR turbofan engine with the inner and outer, 2D-HBPR, and 2D-LBPR fan models using TET as the handle. It is emphasised that the 2D-HBPR fan model is running with LBPR fan data. The inner and outer fan is run in 2 versions; one is derived from the 2D-HBPR fan dataset and the other from the 2D-LBPR fan dataset. All models are in the turbofan engine simulation model with no changes except for the fan model. Clearly, all four models give the same result.

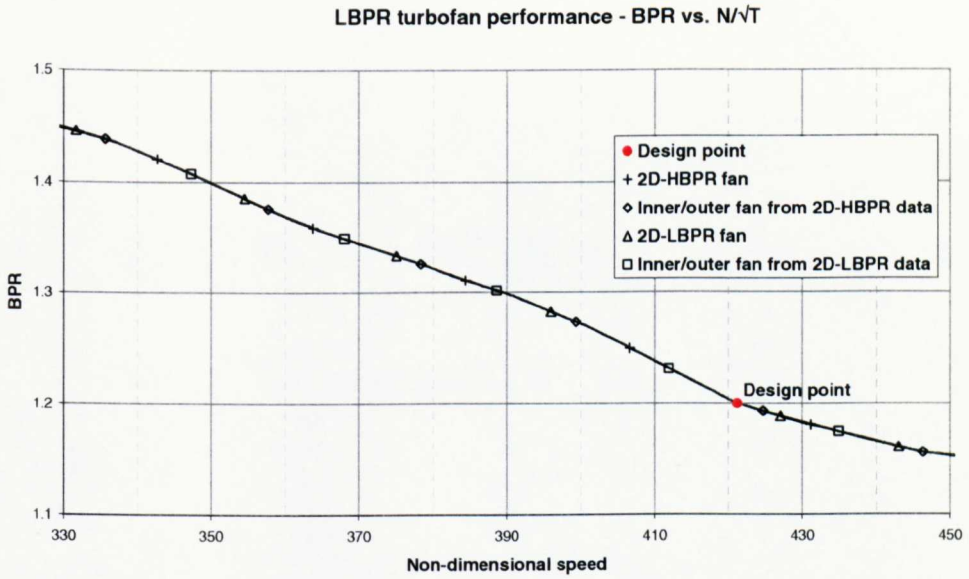

Fig. 3.18 BPR vs. $N/\sqrt{T}$ comparison for engine with different fan models, ISASLS.

3.10.1.1 2D-LBPR fan compared to 2D-HBPR fan model

The 2D-HBPR fan had been run to give a nominal curve of BPR vs. $N_L/\sqrt{T_1}$ as shown in **Fig. 3.18**. The 2D-LBPR fan was generated using this nominal BPR vs. $N_L/\sqrt{T_1}$ and the 2D-HBPR fan data. Therefore, running it in an engine with the same nozzle areas and all other components unchanged from which the 2D-HBPR fan was run will give the same result. This gives confidence that the iteration procedure in the 2D-LBPR model works correctly to calculate the correct performance, eventually selecting the correct BPR after using the other

BPR dependent map data during the iterative calculation. Furthermore, since the 2D-HBPR data is derived from an engine rig test data, it also gives a degree of confidence that it is possible to use LBPR fan rig data within 2D fan-type methods, directly taking the raw data and smoothing the profiles before adding β lines.

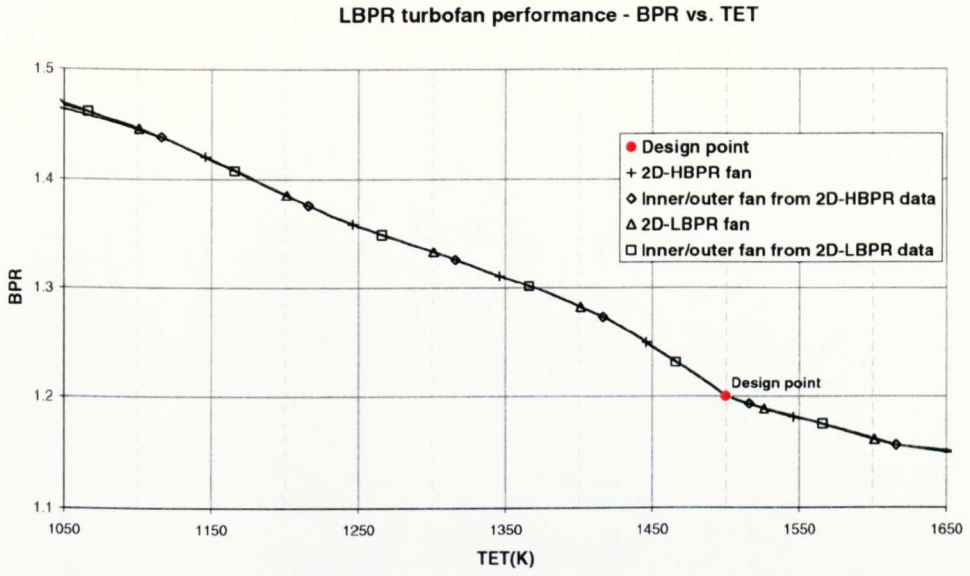

Fig. 3.19 BPR vs. TET comparison for engine with different fan models, steady-state, ISASLS.

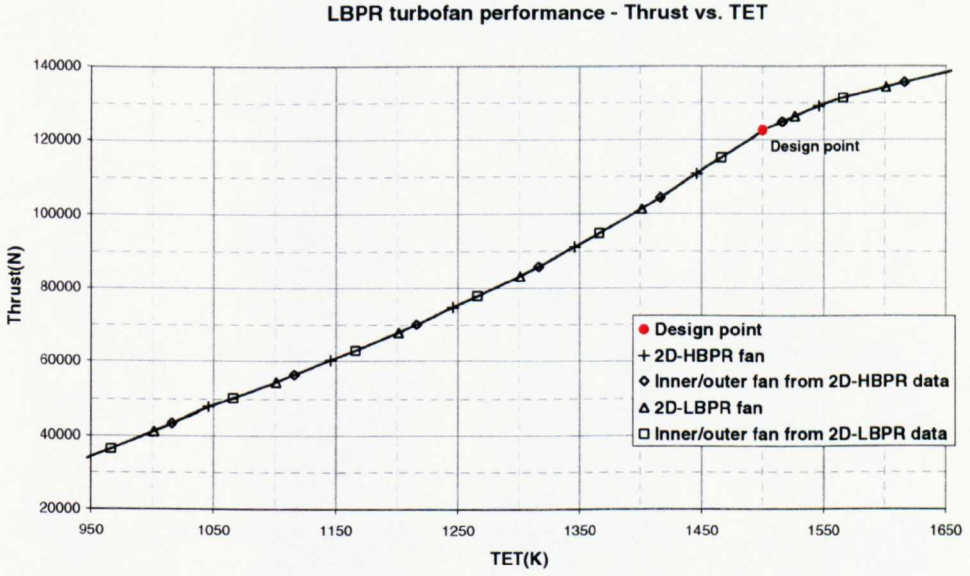

Fig. 3.20 Thrust vs. TET comparison for engine with different fan models, steady-state, ISASLS.

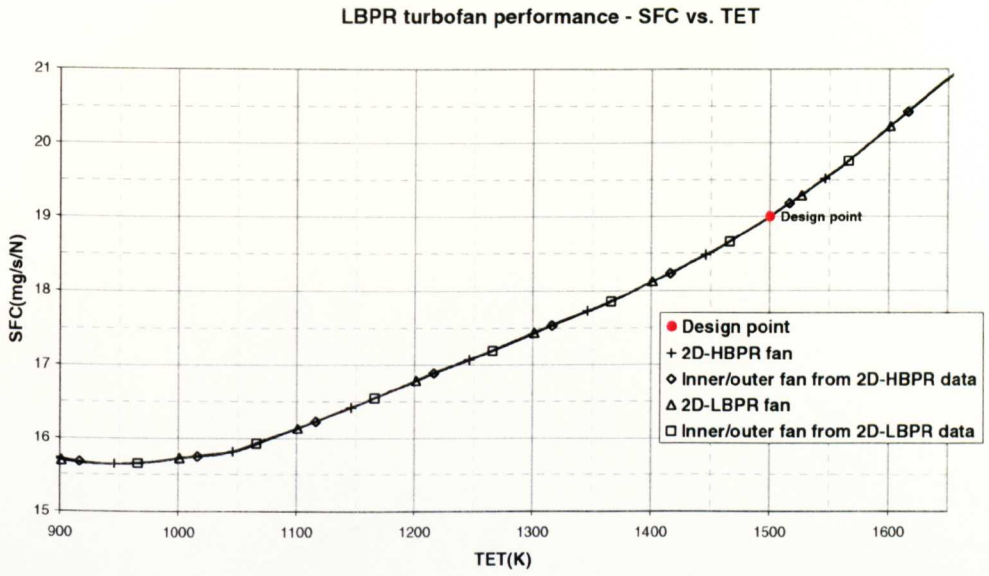

Fig. 3.21 SFC vs. TET comparison for engine with different fan models, steady-state, ISASLS.

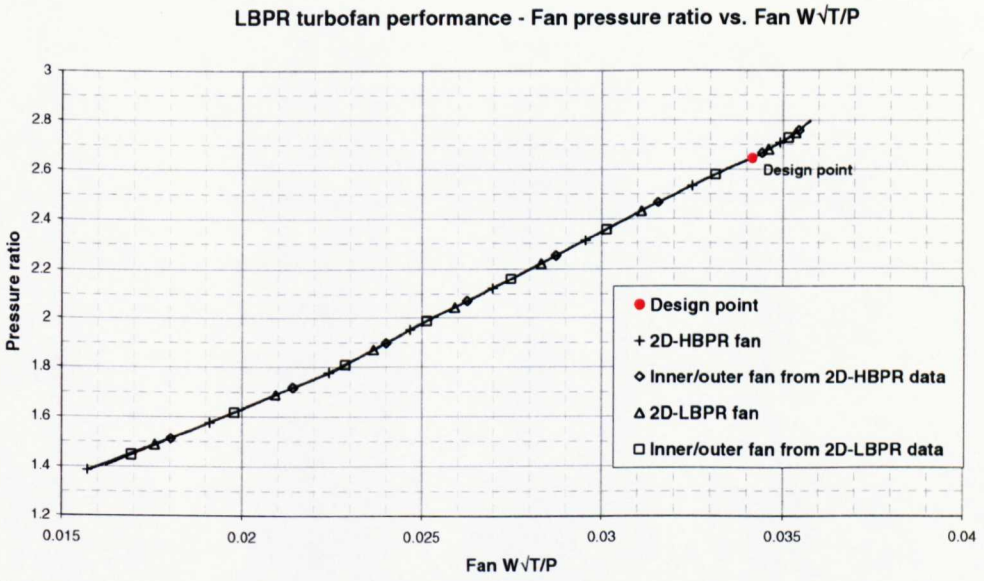

Fig. 3.22 PR vs. W√T/P working line comparison for engine with different fan models, ISASLS.

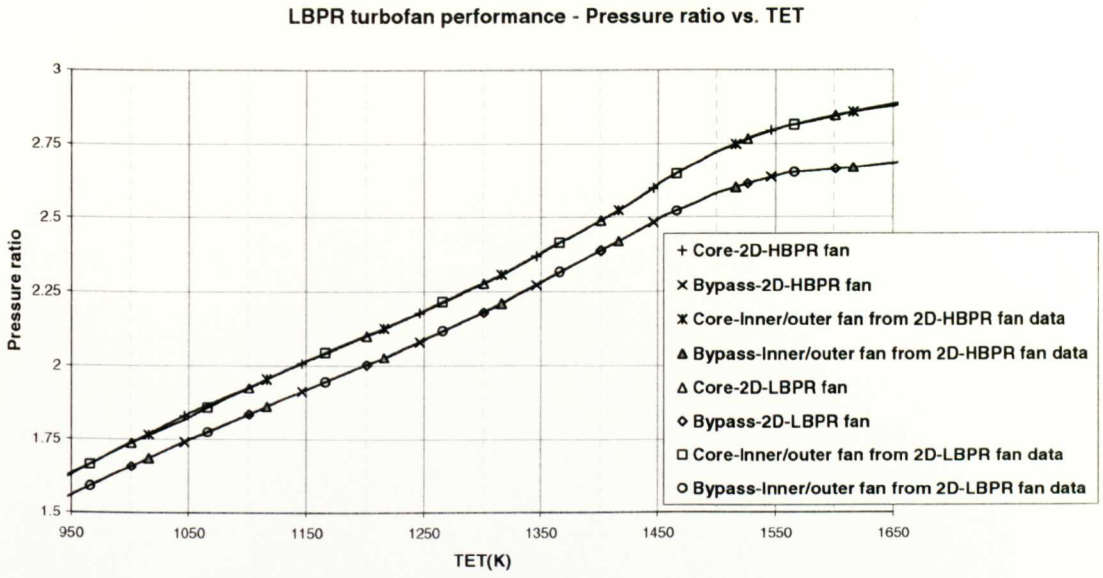

Fig. 3.23 PR vs. TET comparison for engine with different fan models, ISASLS.

3.10.1.2 Inner and outer fan models compared to 2D fan models

The BPR vs. $N_L/\sqrt{T_1}$ schedule of the resulting fan working line from the 2D-LBPR off-design results (obtained from **Fig. 3.18**) is used to extract inner and outer maps from the 2D-LBPR fan data set. This resulting inner and outer fan map data run in the same geometry engine as the 2D-LBPR fan gives the same result. This then gives confidence that it is possible to replace the inner and outer fan with the 2D-LBPR method. **Fig. 3.23** confirms that the inner and outer fans converge with the same thermodynamic and flow parameters passed to the core and bypass streams as the 2D-LBPR fan model.

3.10.2 Bypass ratio vs. speed schedule changes by hot nozzle area change

Having confirmed the ability of the 2D-LBPR fan to give the same result as the inner and outer fan when using the same geometry of the engine, a change was made to force the fan to work at a different BPR vs. $N_L/\sqrt{T_1}$ relationship by making a change in hot nozzle area. The inner and outer fan model using 2D-LBPR fan data and the 2D-LBPR fan model are then compared. The off-design calculations are again with decreasing TET as the handle, shown in Fig. 3.24 to **Fig. 3.28**. The hot nozzle area is altered from the setting for the previous results at 1450K downwards in the calculation sequence. **Fig. 3.24** shows that the bypass ratio vs. speed schedule is the same for both models until the area increase. The fan models rematch at new operating points at a higher speed and different BPR.

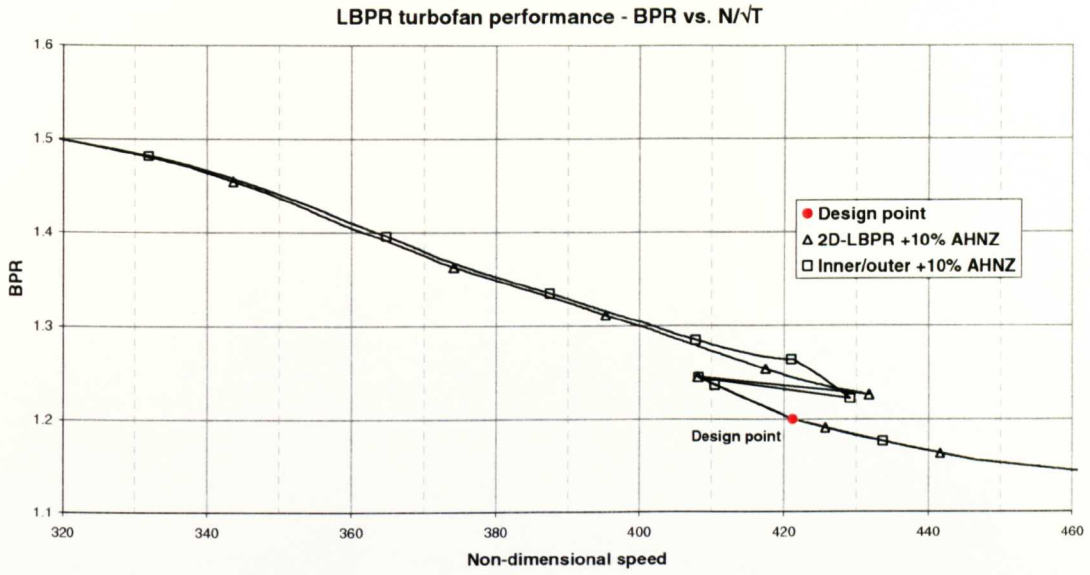

Fig. 3.24 BPR vs. N/√T comparison for engine with 2D-LBPR and inner and outer fan models with 10% hot nozzle area increase at 1450K downwards, ISASLS.

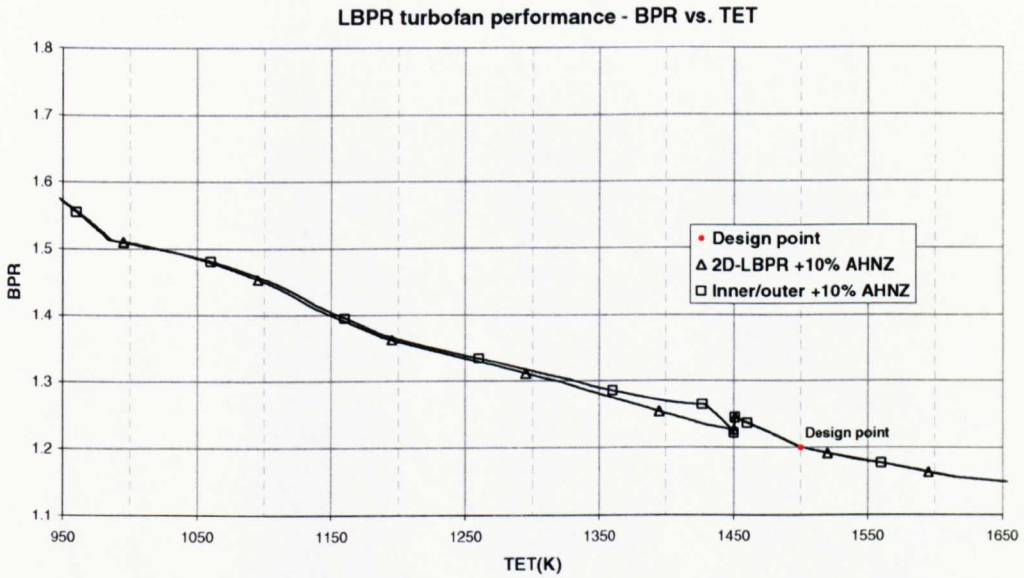

Fig. 3.25 BPR vs. TET comparison for engine with 2D-LBPR and inner and outer fan models with 10% hot nozzle area increase at 1450K downwards, ISASLS.

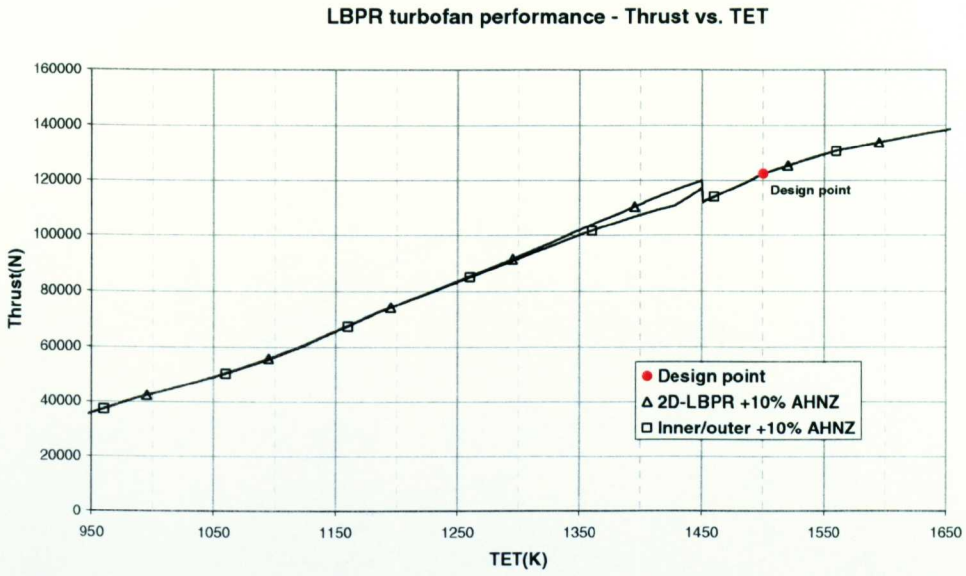

Fig. 3.26 Thrust vs. TET comparison for engine with 2D-LBPR and inner and outer fan models with 10% hot nozzle area increase at 1450K downwards, ISASLS.

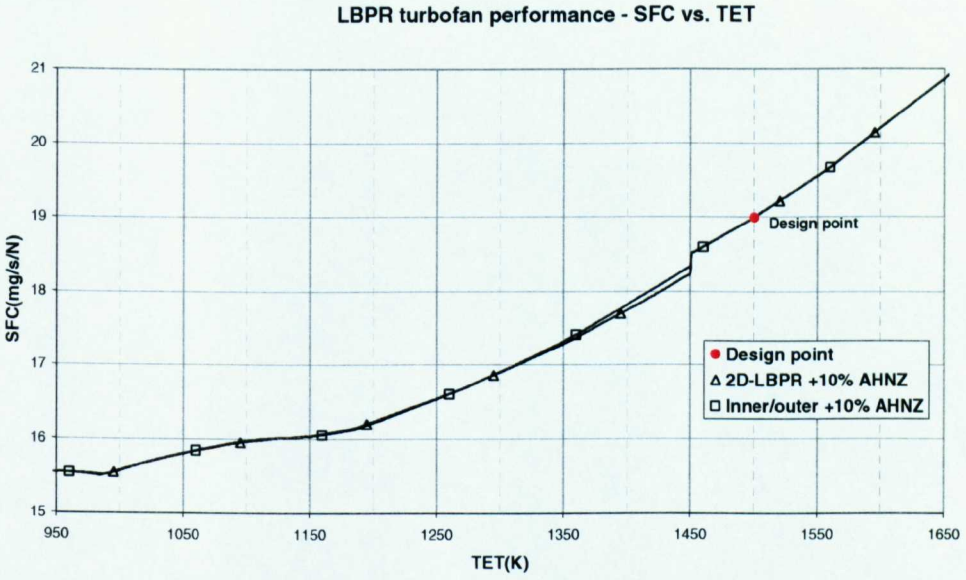

Fig. 3.27 SFC vs. TET comparison for engine with 2D-LBPR and inner and outer fan models with 10% hot nozzle area increase at 1450K downwards, ISASLS.

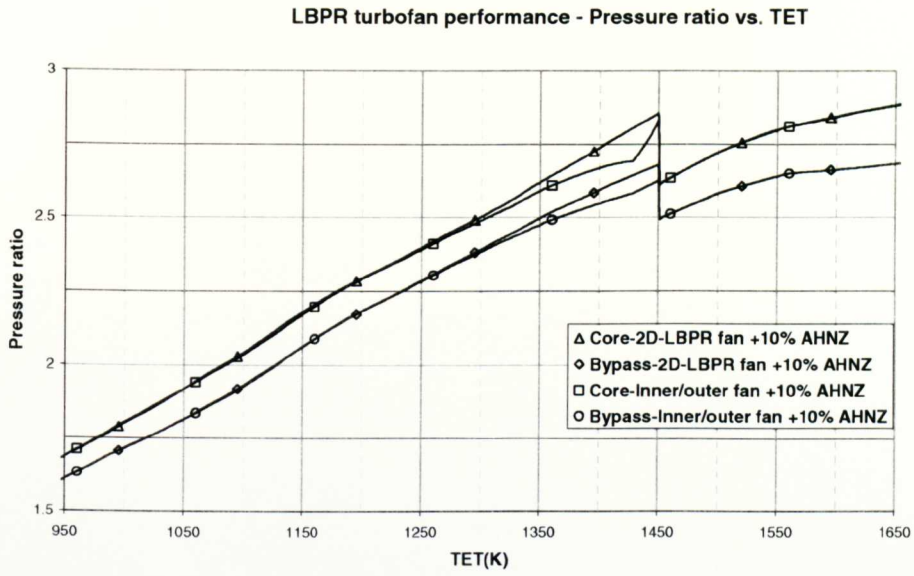

Fig. 3.28 PR vs. TET comparison for engine with 2D-LBPR and inner and outer fan models with 10% hot nozzle area increase at 1450K downwards, ISASLS.

As expected, the performance of the two models is the same until the area change, when the BPR vs. $N_1/\sqrt{T_1}$ relationship is altered. The inner and outer fan maps apply only to the engine geometry prior to the change and so will give an incorrect performance prediction, as shown by the different core and bypass pressure ratio computations (**Fig. 3.28**). The 2D-LBPR model should be able to account for the changes in BPR with power setting and give a different result. It should be noted that the actual results that are calculated are dependent on the author's arbitrarily generated profiles at different BPRs, which may not reflect that of an actual fan. However, the model will give the capability of a better performance prediction if the real profiles are available from rig test or able to be computed with sufficient accuracy by flow prediction methods.

3.10.3 Other working line change comparisons

Apart from changing the area of the hot nozzle, other component changes can be made to demonstrate the effect of changes in the fan working line and hence in the BPR vs $N/\sqrt{T}$ relationship.

3.10.3.1 Effect of HPC efficiency change

A change in HPC efficiency can be caused by degradation for foreign object damage, and leads to a change in working line of the HPC. The turbines and nozzles are choked and the effect is to alter the LPT work at a fixed TET and therefore change the fan working line. To demonstrate this, the LBPR-2D fan code is run at decreasing TET from 1500K until at 1450K, a 2% delta change in HPC efficiency is introduced to the whole HPC characteristic. The fan working line is shown in **Fig. 3.30** compared to the engine with the original characteristic.

3.10.3.2 Effect of HPT efficiency change

A change in HPT efficiency can occur due to degradation. With turbines and nozzles choked, the pressure and temperature ratios across these components are constant. A change in HPT efficiency leads to different entry total temperature into the LPT and hence changes the fan work and therefore, the fan working line. To demonstrate this effect, the LBPR-2D fan code is run at decreasing TET from 1500K with a 2% delta change in HPT efficiency of the original HPT characteristic. The fan working line is shown in **Fig. 3.30** compared to the engine with the original characteristic.

3.10.3.3 Effect of LPT efficiency change

A change in LPT efficiency directly alters the work available for the fan and therefore will change the fan working line. To demonstrate this effect, the LBPR-2D fan code is run at decreasing TET from 1500K with a 2% delta change in LPT efficiency of the original LPT characteristic. The fan working line is shown lowered in **Fig. 3.30** compared to the engine with the original characteristic. The new working line and BPR vs. $N/\sqrt{T}$ schedule is different from that computed by the inner and outer fan model with the same LPT efficiency change.

3.10.3.4 Effect of bypass nozzle area change

A change in bypass nozzle area directly changes the fan working line; e.g. a reduction in bypass nozzle area drives the operating point up the non-dimensional speed line towards the surge line. To demonstrate this effect, the LBPR-2D fan code is run at decreasing TET from 1500K until at 1450K, a 5% decrease in bypass nozzle area is introduced. The fan working

line is shown raised in **Fig. 3.30** compared to the engine with the original characteristic. The new working line and BPR vs. $N/\sqrt{T}$ schedule is different from that computed by the inner and outer fan model with the same nozzle area change.

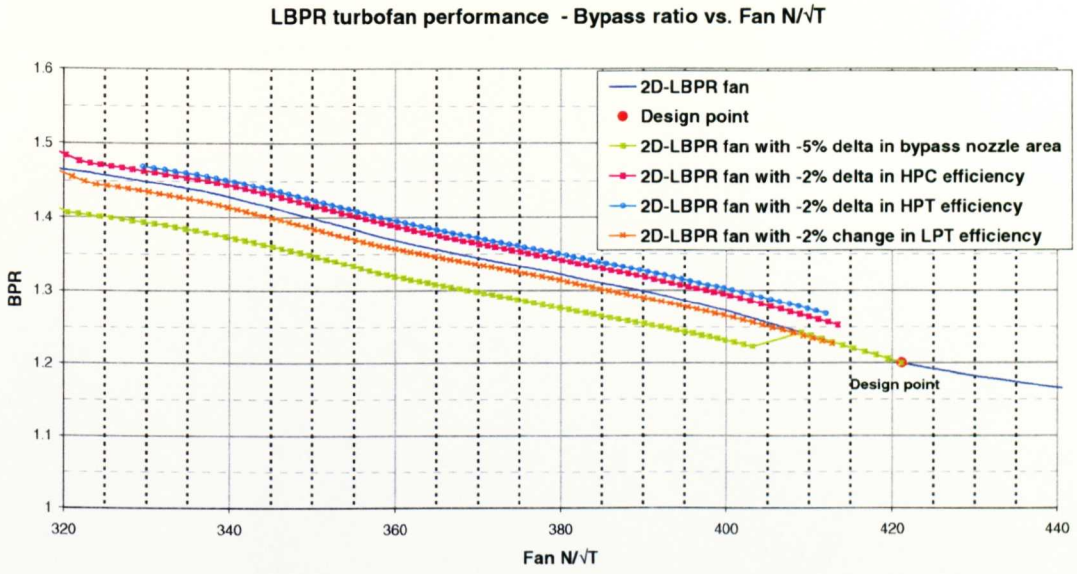

Fig. 3.29 Effect of component changes on bypass ratio-speed schedule for engine simulation with 2D-LBPR fan model.

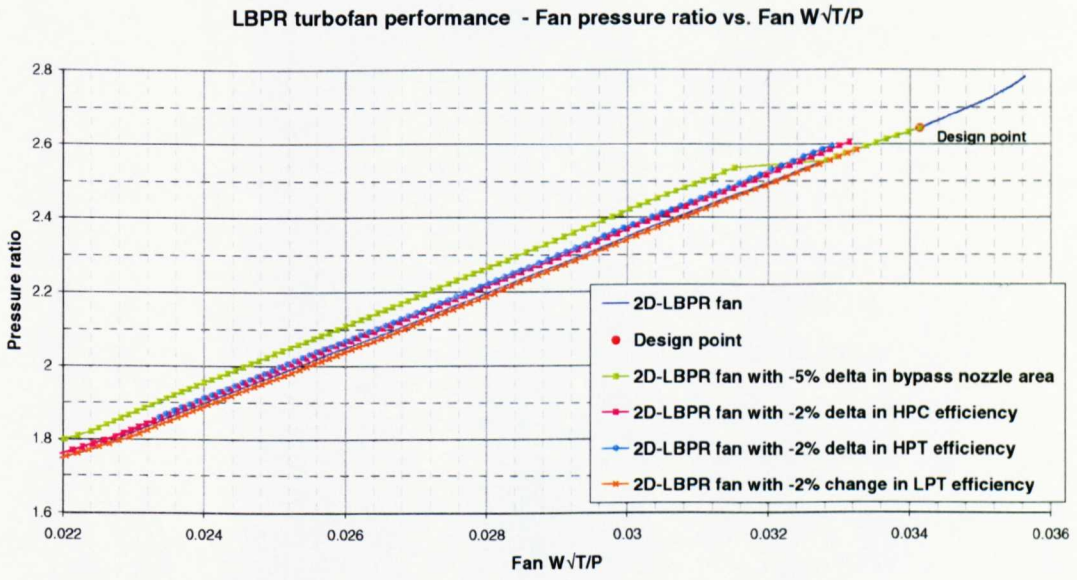

Fig. 3.30 Effect of component changes on working line for engine simulation with 2D-LBPR fan model.

3.11 SUMMARY OF MODELLING 2D-LBPR FAN MODEL

The current work has demonstrated the following points:

- The 2D-LBPR fan model gives the same performance output as the 2D-HBPR fan and inner and outer fan model provided that all 3 models have the equivalent BPR vs. $N/\sqrt{T}$ schedules.
- The 2D-HBPR fan model is based on the fan performance being fixed at a fixed non-dimensional speed and flow function with changes in BPR. The 2D-LBPR fan model is for a fan where the fan performance at fixed non-dimensional speed and flow function is affected by changes in bypass ratio.
- The 2D-HBPR fan model is able to adjust without modification to calculate the effect of component efficiency changes and nozzle area changes that affect the fan working line and the fan BPR vs. $N/\sqrt{T}$ relationship. The inner and outer fan will need new fan data to accomplish this. The 2D-LBPR fan model has an advantage over both 2D-HBPR and inner and outer fan models in that it can adjust without modification to calculate the same effects where bypass ratio changes at fixed $N/\sqrt{T}$ and $W\sqrt{T}/P$ also change the fan performance.

3.12 CONCLUSIONS OF MODELLING FOR BPR EFFECTS

The contribution to knowledge in this chapter is to understand an existing scenario of LBPR fan performance from literature review evidence and examination of fan test data to provide a fan model within an engine simulation model that can model the scenario in a higher detail than presently possible, and also to provide a more versatile fan model that is able to automatically adjust to the effect of changes in other components' performances for example. The following are the key points.

- HBPR fans show constant fan performance at fixed non-dimensional speed and flow function when the bypass ratio is varied. They have small fan pressure ratios and low hub-to-casing ratios. The design bypass ratio is very high to maximise propulsive efficiency of the engine. Bypass ratio changes in the normal operating region of the fan are higher than for LBPR fans, which have smaller BPR and higher fan pressure ratios. Fan exit profile changes in HBPR fans should have a proportionally larger effect than on LBPR fans.
- The data available to study LBPR fans was inconclusive as to whether fan performance is independent of bypass ratio at fixed non-dimensional speed and flow function for 2 reasons. One was the situation of the measurement probes for these rig tests were not

exactly at the fan exit station before the bypass splitter. Secondly, LBPR data that was examined showed the presence of fan exit circumferential total pressure and total temperature profiles, possibly an effect of the presence of stators and other struts in the flow field on fan work input. Information has been obtained in the literature review to conclude that cases of LBPR turbofans occur where the bypass ratio affects the fan performance at fixed speed and flow function with the effects being a significant change in the fan characteristic compared to an unaffected case. The expense of testing has meant that these cases may occur but are not normally tested for.

- The fan exit circumferential profiles were arithmetically averaged to give axisymmetric radial profiles for modelling. These profiles have not greatly affected the use of the resulting fan characteristic in performance simulation possibly because the profiles are a small proportion of the absolute average thermodynamic parameters at the fan exit due to relatively high fan pressure ratios.
- The conventional industry method is the inner and outer fan model. This is restricted to the BPR vs. $N/\sqrt{T}$ schedule used to obtain the inner and outer fan data. Deviation from the schedule can occur for example with component efficiency changes, bleeds, transients and nozzle area changes. Factors and deltas will need to be applied to the inner and outer fan to model these changes.
- The 2D-HBPR method is able to accept variable BPR vs. $N/\sqrt{T}$ schedules as it changes the split fan exit streamline position with BPR changes to effectively obtain different inner and outer fan maps. This depends on performance being independent of BPR at a speed and flow function.
- The 2D-LBPR has the same capability as the 2D-HBPR method but in addition, can use the extra fan data if available for when the fan performance is dependent on BPR at a speed and flow function.
- The method will produce savings of time for studies using scaled fans from past engines for example when designing a new engine. The BPR vs. $N/\sqrt{T}$ schedules are automatically computed.
- The method of averaging exit radial profiles divided by the split flow streamline dependent on BPR has been used in this work for radial inlet distortion modelling, where the working line and BPR vs. $N/\sqrt{T}$ will also be altered.

- Rig to engine effects may in part be accounted for when more of the engine can be modelled in 2D detail. The 2D profiles can then be transmitted from one component to the next with subtle changes in component performance. It is likely that the components least affected are where deviations from the average of the radial profile are a small proportion of the average. This is seen in higher pressure ratio LBPR fans compared to lower pressure ration large civil fans.

3.13 FURTHER WORK

The following further work would enhance knowledge:

3.13.1 General

- A wider range of low-bypass ratio fan data should be examined where possible, to understand better the relationship between the fan geometry and architecture, fan pressure ratio with the fan exit profiles. In particular, a range of multistage fans should be examined that range with hub-to-casing ratios down to the large civil fans. This includes some of the older LBPR civil fans.
- Similar work can be done to model a turbofan engine with smaller fan pressure ratios and lower hub-to-casing ratios. The work in **Chapter 4** has shown that bypass ratio changes over the higher power region of the engine are very small in a higher pressure ratio fan. This suggests that bypass ratio changes will be greater in turbofans with lower hub-to-casing ratios (larger pressure ratio differences between hub and casing) and in fans with lower fan pressure ratios (fan exit profile changes are larger proportionally to the absolute exit profiles).

3.13.2 Current modelling

- The user can arbitrarily alter the profiles for varying BPR to achieve the 1D map requirement. For example, the map in **Fig. 3.11** can be reproduced in 1D terms at least to give an idea of the degree of performance changes due to working line excursions in BPR affected fans. The present work has not yet considered a flow function change or efficiency change for the new BPR values.
- More cases of engine BPR vs. $N.\sqrt{T}$ changes may be investigated. This includes the effect of bleeds and transient performance calculations where the working line excursions are very significant.

- The engine simulation would be enhanced with 2 additions. One is the mixed exhaust turbofan, which already exists in the Cranfield School of Engineering (Yin, 1999), and the other is to implement the matrix method of iteration with Newton-Raphson solver. A range of solver strategies may be investigated. The current 2D-LBPR fan takes longer to converge than the 2D-HBPR and inner and outer fan models.

3.13.3 Future modelling

- The profiles created for varying bypass ratio are purely hypothetical. The fan flow field model used in Chapter **4** may be developed to investigate the effect of the bypass splitter proximity to the fan turbomachinery in order to compute profile changes that have a better physical basis. The use of a physical model will be a great advantage and will relieve the need to obtain test data for this research that is usually hard to obtain. It will allow the user to vary all of the important contributing fan parameters to carry out a systematic study to understand when profiles are BPR affected and when the effect on fan performance becomes significant.
- The model computes axisymmetric radial fan exit profiles. These are averaged for the entry conditions to the next components downstream. This work can be viewed as one part of a move to greater detail performance modelling. Eventually, all components may be examined in 2D (radial) and also circumferential. This fan model may also be experimented as part of a circumferential parallel compressor model (section **4.11**), as part of a scheme to model inlet distortions as discrete radial and circumferential parts.

Chapter 4

RADIAL INLET DISTORTION PERFORMANCE MODELLING

4 RADIAL INLET DISTORTION PERFORMANCE MODELLING

This chapter describes firstly, the scenario to be modelled and the tools that are used to model it. Next, a description is made of the 3 fan models that are formed from the tools. Model runs are then described, documenting the work done to converge to performance results. A series of inlet distortion cases are then analysed and conclusions and further work proposed.

4.1 SCENARIO TO BE MODELLED AND PROPOSED CAPABILITY

It is to investigate the effect of a steady-state radial profile of inlet total pressure on engine performance. This could be due to the installation. Normally, engines are bench-tested with a standard flared bellmouth intake, which will be different from the aircraft situation. As a result, an engine installation may experience a degree of inlet distortion not present during tests. It is necessary to understand the effect of any radial inlet total pressure loss on the turbofan engine performance.

4.1.1 Role within performance modelling.

Fig. 4.1 gives a view of when a fan characteristic model is required for performance modelling within the life cycle of an engine project. An accurate estimate of fan performance is especially required during the design phase, when no test information is available. Correcting errors after hardware is built is always expensive. At this stage, the engine model is run in synthesis, when the performance of an engine is computed from the available component data in the engine model.

Later in the life cycle, performance analysis is essentially equally in requirement of a high fidelity fan model as in synthesis, for example, to refer test results of different engines to a comparable ISASLS condition after bench testing. This may be done for example as "Analysis by Synthesis" or ANSYN (Biraud et al, 2001).

At present, there is no engine performance model that can receive arbitrary inlet distorted total pressure profiles and synthesise turbofan engine performance. Table 4 gives the author's opinion on how higher detail fan modelling may have a role in performance activities in industry.

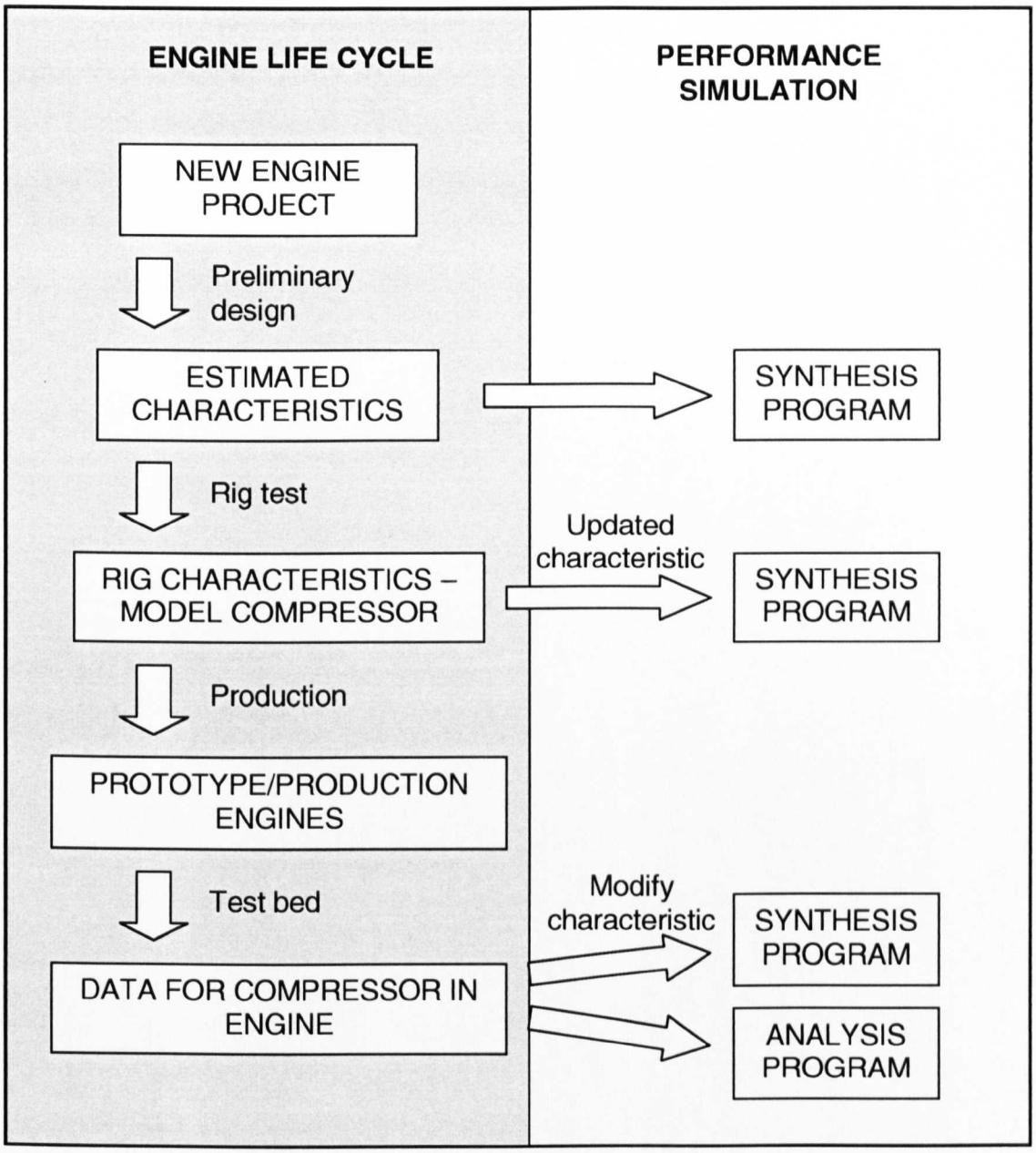

Fig. 4.1 Life cycle of engine and role of performance codes.

4.1.1.1 Performance prediction.

In new engine projects, there is likely to be no tested fan characteristic, also true of the engine with a uniform inlet. Normally, past experience is used, but blade shapes are becoming more complex, with lean and sweep and the blade profile, rather than being of a fixed type, is increasingly being prescribed to achieve the required performance. Steady-state radial inlet distortion may occur as a result of boundary layers for example. An early check on distortion tolerance is necessary to plan the amount of surge margin to allow. However, the synthesis of turbofan performance with distortion is currently not available.

Point in life cycle	Activity	Traditional characteristic representation	Long term proposed characteristic representation
Design phase Synthesis	(i) Steady-state performance	Uniform inlet only. Estimated chic or scale from previous chic.	Flow field calculation of a proposed fan. Loss models etc. from database.
	(ii) Intake effects on flow	No estimate of performance change due to radial or circumferential intake effects.	Estimate performance due to radial and circumferential inlet profiles due to installation.
	(iii) Stator vane scheduling	Modify 1D characteristic as fn $(N/\sqrt{T})$	Flow field recalculation due to fan geometry change.
	(iv) Bleed modelling	No change in characteristic, mass flow change only.	Flow field recalculation due to bleed.
	(v) Inlet distortion modelling	Approximations from past experience.	Discretize into radial and circumferential distortions. Flow field recalculation for new performance. Surge line estimate requires empirical information.
	(vi) Rig to engine effects	No information except past experience	Transfer of 2D profiles between components. Long term addition of coupling and backpressuring effects for recalculation of flowfield.
	(vii) Bypass ratio effects	No information	Include splitter in the domain to recalculate the flow field.
Synthesis with tested rig characteristic	(i) – (vii)	Changes from above: More accurate characteristic for uniform flow unless tested with representative intake.	Changes from above: Can adjust loss models etc. to align performance with rig test.
Synthesis with information from test engines	(i) – (vii)	Changes from above: From tests in sea-level and altitude test beds, can account for altitude and Reynolds number effects, rig-to-engine effects, all by factors and deltas of the rig characteristic to align with test data. Stator scheduling modelled by equation modifying the characteristic with speed. Still no modelling of bypass ratio effects if not tested for. No info on installation unless intake tested for. Distortion gauze engine testing normally only to check distortion tolerance.	Changes from above: Further adjustment of loss models etc., and of coupling model to align with test data.

Table 4 Highlights of the different synthesis capabilities of the fan codes in traditional method and with the long term proposed method.

Currently, compressor design will check for distortion tolerance (combined radial and circumferential). Synthesis models use characteristics from a uniform inlet rig test when available. Any current estimate of distorted performance is based on application of factors and deltas to the fan characteristic, for example, based on DC60 parameter for circumferential distortion.

2nd order effects on compressors are also applied as characteristic modifications. The effect of distortion on these is unknown. A prediction tool based on fluid dynamics may be able to predict these secondary effects, such as Reynolds number corrections. The presence of 2D modelling may also partly explain rig to engine effects, if consecutive components can interact with each other wth this higher accuracy.

4.1.1.2 Performance analysis.

From engines on the test-bed, measured performance must be used to align synthesis models with the test results. Factors and deltas are used on existing characteristics, which are from uniform rig tests. When ANSYN is performed, an undistorted intake flow is usually assumed with the synthesis code, but sometimes, the installed intake may be used on test. If the synthesis code could take into account distortion, it could then be aligned to test to give a synthesis code that should give better off-design prediction. Also currently required are altitude test bed measurements for P1, T1 and Reynolds effects. There would be cost savings to be gained with a predictive tool based on physics. Although an implemented predictive tool would still need to be aligned to test results, it may require a lesser amount of test data, for example, to adjust loss models.

4.1.2 Scope within performance modelling

A fully-capable tool will have the roles shown in **Table 4**. The current work is an initial exploration in this field. This section lists the capabilities of a working code as intended, and then scopes the current work.

4.1.2.1 Intended scope in performance modelling

This is with the assumption of a mature model or set of models in the long-term. It will predict radial distortion into and out of the fan. For new engine performance prediction, it will give a better estimate for "guarantee" of engine distortion capability. If more confidence in the tool is possible, it lessens the requirement for surge margin, and improves engine performance availability by having smaller SOT margin stack-up.

In the turbofan, the fan model will be modelling BPR effects to a short distance downstream of the bypass splitter up to the core compressor. It will be able to predict the effect BPR on fan performance (Chapter **3**). It has the potential to much reduce testing or to make better use of available tested data. More information may be used for the money invested in rig/engine tests.

It will be able to model bleeds. The effect of bleeds on flow through compressors in general may be for low speed handling, or aircraft services, and will give predictions of the performance losses.

It will be able to model VGV schedules. This predicts performance due to different stagger angles of VGVs. The developed code will be able to change blade geometry for any operating point calculation.

It will be able to model radial inlet distortion and coupled with a model for the intake system will allow performance to be obtained through the steady-state flight envelope. In the synthesis tool, this will be another guess and check, possibly to match the static pressure profile between intake and fan face. If there is no CFD map model of the intake, the fan inlet profile may be input by some empirical knowledge of boundary layer of intake.

4.1.2.2 Scope of current work

This work will produce a research tool to test the viability of the method. For this initial work, inlet total pressure distortion is the theme, with the emphasis is on exploring the iterative scheme within the performance program, and the time required to obtain a performance point. It will give information on the integration of different codes of different fidelity. It is desired to capture the effects on performance in a broad sense to see if the trends are correct, by looking at the deltas between performance with and without distortion. The effects of different profiles of distortions will be investigated as will the effect of levels of distortion. The possibility of improvement in this method will be discussed. At this stage, there will be no work on bleeds, VGVs, BPR modelling, circumferential distortion modelling, circumferential and radial combined or 2nd order effects.

4.1.2.3 Advantages and disadvantages

In the workplace, there will be a more complex tool, which initially may require a lot of different inputs. The tool may normally be operated by an aerodynamicist or compressor specialist. Training will need to be supplied for the performance engineer, but the advantage will be to gain a greater understanding of fan/compressor theory.

In many cases, BPR has little effect, so introducing a complex tool is not required in such cases. There may therefore be a need to have concurrent tools, with the associated overheads in maintaining all of these by a small number of specialists. In mature engine projects, current tools have been capable of synthesis and analysis with factors and deltas.

4.2 STREAMLINE CURVATURE TOOL

4.2.1 Fundamentals of streamline curvature methods.

The design and analysis of compressors required a model that could give the conditions at the exit of one blade row from hub to casing in order to present the inflow for the next blade row. Wu (1952) gave a method for the 3-D solution of the flow in a compressor that was only restricted by the computational resources at the time. It is often acknowledged as the source that led to the concept of the blade-to-blade surface (S1), and the hub-to-casing surface (S2). These surfaces represent streamsurfaces in the flow, which twist and warp on passing through the blade row, due to static pressure differences between the surfaces of neighbouring blades and due to differences in static pressure distribution from hub to tip. In order to achieve sufficient accuracy within reasonable computational power, streamline curvature methods were developed by the turbomachinery industry in the 1960s. Typically, the meridional surface or throughflow surface (Cumpsty, 1989) is calculated at points between blade rows. The meridional surface represents Wu's S2 surface and represents an axisymmetric profile of the flow in the annular space between blade rows. Cumpsty (1989) has noted that any inaccuracies that arise from the assumption of axisymmetric flow are more than outweighed by other assumptions such as blockage distributions. These throughflow methods have been so successful that they remain an integral part of the design and analysis procedure in gas turbine companies to this day (e.g. Marshall, 1998, Escuret, 1998). Cumpsty (1989), Novak (1967), Jansen and Moffatt (1967) give good accounts of how the procedure works.

Now the following discussion can be confined to that of an axisymmetric 2-D flow through the compressor or fan. The flow can be considered to be divided by streamtubes, or as streamlines viewed in the meridional plane. The streamlines will undergo a radial shift on passing through a blade row because of the temporary imbalance between the centrifugal forces exerted on the fluid and the radial pressures that restore radial equilibrium. Radial equilibrium is observed at some point upstream and downstream of the blade row in the flow between blade rows. This is achieved when sufficient radial redistribution of mass flow

occurs to change the static pressure distribution to achieve radial equilibrium. Radial equilibrium flow is commonly used to describe flow in an annular passage, with streamlines lying in circular, cylindrical surfaces, with no radial component of velocity (Dixon, 1998).

The main contributor to the pressure gradient acting on the flow is the swirl distribution. In the past, the simplified radial equilibrium (SRE) method would be used for design, and it will still give a good indication of the basic trends. It is applied to an idealised compressor with a parallel annulus. In actual compressors, the streamlines change radius along the axial length through the stages, creating an additional pressure gradient acting on the flow. The simple radial equilibrium (SRE) equation can be used for preliminary calculations on an individual stage but does not take into account the additional pressure gradient from the streamwise change of streamline curvature (Wilson and Koriakanitis, 1999). Also, the SRE method assumes that the shift in radial position of the streamlines occur completely within the blade rows with the flow outside being in radial equilibrium, and not some distance up and downstream. Therefore, the SLC method is chosen as it solves the full radial equilibrium equation, which is described in Smith (1966). For this work, the SLC code used has been written by Barbosa (1987) at Cranfield University, UK and was validated against a transonic test compressor.

4.2.1.1 Review of streamline curvature equations for compressor off-design analysis

Novak (1967), Jansen and Moffatt (1967), for example, have given the basic method of solution of SLC methods, from which other methods can be compared. The derivation steps and further notes are shown in **Appendix 4**. Basic notes are shown below.

4.2.1.2 Program requirements and basic calculation procedure

Table 5 shows some of the requirements of a typical streamline curvature model. It is not proposed to go to any great detail of the procedure here. This can be found in accounts such as Glenny (1974), Cumpsty (1989). The basic difficulties of the method are noted in Macchio (1985). Streamlines are first fitted by a curve fitting procedure in the meridional plane to points at the leading and trailing edges of blade rows as shown in **Fig. 4.4**. The initial guess of streamline position may be equal mass flow inside equal annulus areas.

The main equations to be solved are, for example, in Novak's (1967) method:

Radial meridional velocity distribution:

$\frac{\partial V_m}{\partial r} = \frac{1}{2} D(r) \frac{1}{V_m} - \frac{1}{2} E(r) V_m$ with D(r) and E(r) being known functions of r.

Continuity equation:

$\dot{W} = \int_{rhub}^{rcasing} 2\pi r \rho V_m \cos\phi dr$ where ϕ is the angle between the streamline and axial.

V_m is the meridional velocity. These can only be solved by an iterative method as shown in **Fig. 4.3**. One meridional velocity is first guessed at a reference location, and the radial velocity equation used to calculate the neighbouring streamline velocities. When all streamline velocities are computed, the density profile can be calculated and the velocity profile integrated to obtain overall mass flow, which is checked against the input mass flow. A new reference velocity is guessed until the mass flows match. This loop is performed for all the blade rows.

Geometry	**Correlations or physics models**	**Program input**
Annulus wall coordinates	Losses	Mass flow
Coordinates of leading edge and trailing edge of all blade rows	Deviation	Compressor rotational speed
Axial location of blade rows	Blockage	Inlet total pressure profile
Blade pitch to chord ratio	Spanwise mixing	Inlet total temperature profile
Blade camber angle	Cascade	Inlet flow angle profile
Blade stagger angle		
Blade thickness to chord ratio		
Blade blade profile shape		
Number of blades per row		

Table 5 Requirements of streamline curvature models.

When the overall continuity is satisfied, the new radial positions are calculated for the streamlines as in **Fig. 4.2**, given that the mass flow between streamlines is kept as before. This provides a new guess for the streamline position, but it has to be achieved in gradual

steps in order to maintain stability in the program. Final convergence occurs when the new streamlines position guess stays constant.

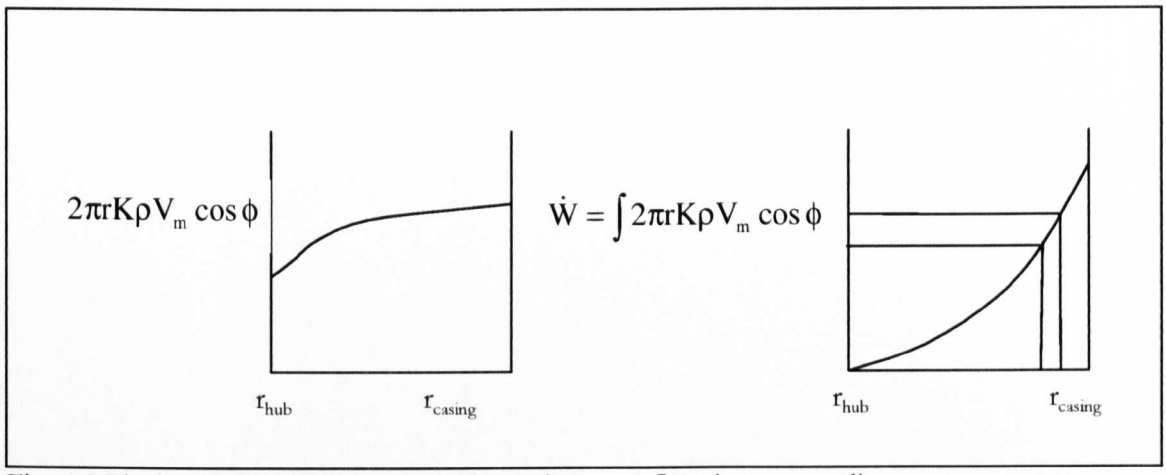

Fig. 4.2 Finding new radial positions from the mass flow in a streamline curvature program, (Daneshyar and Shaalan, 1972).

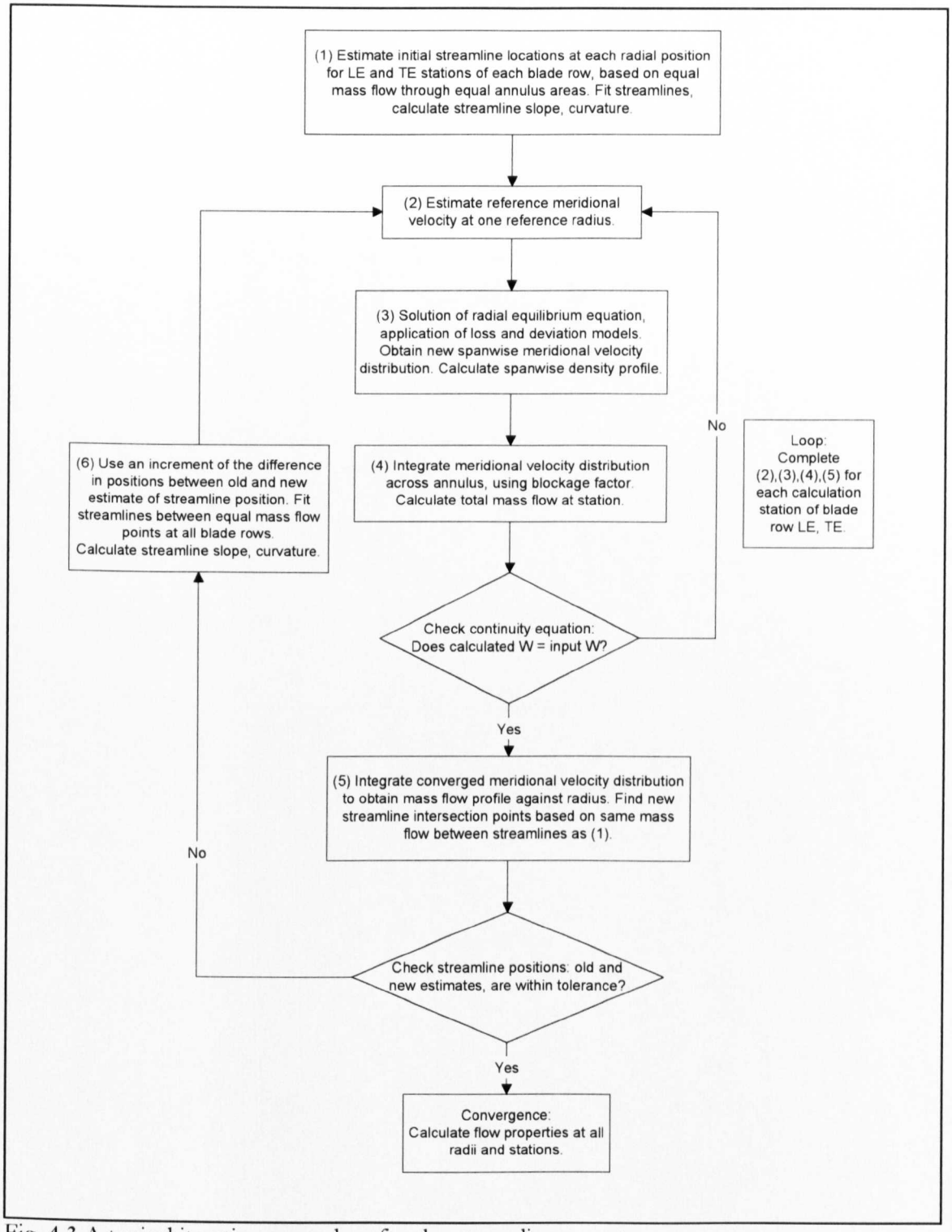

Fig. 4.3 A typical iteration procedure for the streamline curvature.

4.2.2 Summary of streamline curvature code.

4.2.2.1 Advantages

The following are the advantages of using this SLC code for the research work. It can analyse multiple stages, allowing research of fans of different pressure ratio. It is capable of modelling swept and blades with lean, and different blade profiles, allowing a range of compressor types. The user can add to this a specific blade profile. The user can also apply different loss models. The source code is available, which gives the potential to properly integrate the SLC code into the performance code.

4.2.2.2 Disadvantages

The code was written at a time when computational power was expensive. It uses single precision variables and communicates within itself via text files, and may partly have also been written this way in order to have a restart capability for its original role as a teaching tool. This slows down the current implementation of the performance model severely. It is not easy to understand and adjust numerous parameters required to enable convergence of the various iterative loops in the code. It is currently especially prone to failures in calculation of outlet velocity distributing the blade exit streamline positions. This has necessitated an interface error handling code.

It currently has no blade lean, which is a feature of some modern fans. The loss/deviation/blockage parameter settings are related to a fixed geometry so that reanalysing is required for example, for changes in angle of VGVs.

4.3 SLC TOOL WITH TEST COMPRESSOR

The SLC code has been validated (Barbosa, 1987) for a 3-stage transonic test compressor. **Fig. 4.4** shows a meridional view of the design point converged streamlines which are formed by the intersections of the nodes with the blade rows. There are 12 blade rows. The first 3 are "dummy" blade rows, which are computation aids. These are followed by a set of IGVs, followed by 3 stages of rotors and stators. At the rear of the compressor are 2 more dummy blade rows. The user needs to set up 3 input files: compressor geometry, general parameters and reference parameters.

The computation begins at the front and ends at the back of the compressor. Inlet profiles are actually set at the leading edge of the first dummy blade row. The beginning guess is for 11 streamlines dividing equal radial increments. The calculation divides the

meridional plane into 10 streamtubes carrying equal mass flow at convergence, with the necessary change in radial position of all nodes. The inlet profile is maintained at the same position after convergence by interpolating for the new streamline positions.

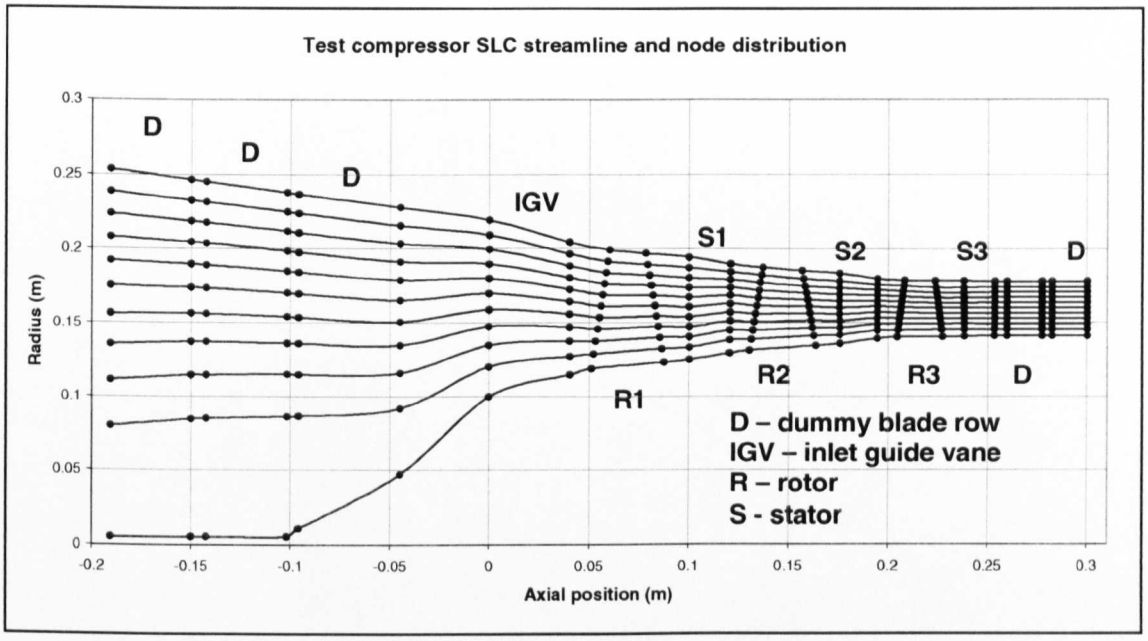

Fig. 4.4 SLC converged design point with undistorted inlet flow showing streamline positions and node intersections with blading.

4.4 MODEL OF LBPR TURBOFAN WITH INTEGRATED SLC TOOL

The SLC code will replace the rig-test measured characteristic of the fan in the performance code in different ways. The prediction of performance will be done by an integration of the turbofan performance simulation code, 2D-HBPR fan model code (BPR independent of speed and inlet flow function), and the SLC code.

4.4.1 Performance code

This is as used in Chapter **3**. but with the amended iteration (**Appendix 5**) scheme to enable convergence on the HPC. A change was also made to the checks of rotational speed guesses of the 2 spools. The original program used a power surplus to check for convergence of the fan speed by checking whether the shaft still accelerates using the surplus power difference between the turbine and the compressor. However, when switching to the small test compressor, it was found that several increments of TET setting did not change the fan speed and changing the spool inertia or ΔT did not achieve equal fan and LPT speeds. It was

decided to change the check of guess of LP and HP rotational speeds to a compressor and turbine power balance by the Newton-Raphson solver.

The same turbofan code handles all of the fan SLC implementations and a switch is set to choose which fan model to use. A switch can also set to enable design point scaling with a particular fan model.

4.4.2 2D-HBPR fan code

In this chapter, only the 2D-HBPR fan model (section 3.7, Yin (1999)) has been used (considering a fan where performance is independent of bypass ratio at a fixed non-dimensional speed and flow function). The 2D-HBPR fan model reads the multiple speed lines of a full compressor map. Modifications have been made to convert from multiple speed line method to a 2-speed and 1-speed method as will become apparent. All 3 methods are available, each associated with one fan model. The original 2D-HBPR fan code read the fan map data via a text file. This step has been retained in the SLC fan model – 2D-HBPR fan interaction, with the obvious disadvantage of having to read the fan map from text file every time the map needs changing to converge for one operating point.

In addition, the 2D-fan data generator program is also required to be integrated. This program converts the radial pressure and temperature information from the SLC code into 2D fan data.

4.4.3 SLC code

The program (Barbosa, 1987) originally required the user to manually input via the keyboard a single mass flow and rotational speed to calculate one compressor operating point.

For this work, the SLC code has been modified to work automatically through receiving text file inputs of speed and mass flow, to enable integration with the engine performance code. It has been modified to output all radial performance parameters for inlet and exit of each blade row to one output text file, and to output all points calculated in one run consecutively to this file, e.g. for one speed line.

A change had been made to allow the SLC code to continuously calculate points on a speed line in a loop, but this feature was not used. Instead, single points will be requested by

the performance/2D fan code, exiting the SLC program after each convergence. This is another factor that will slow down the performance calculation.

Error capture has been added to the SLC code to allow exiting the program without stopping the code. This will enable the performance code to continue running. A separate set of error handling subroutines has been written into the performance code to handle these errors. The SLC code will return a "fail" flag in the output file for any failed attempt at computing an operating point, to be read by the performance code error handler.

4.5 IDEALISED IMPLEMENTATIONS OF LBPR TURBOFAN MODEL WITH SLC FAN MODEL

Three models of SLC-integrated fan model have been implemented. This section discusses the desired implementation that was not achieved for practical reasons in this work.

4.5.1 WholeMap

This describes a complete compressor map calculated by the SLC code but is able to be changed each time a new inlet distortion condition is requested (**Fig. 4.5**). The 2D-HBPR fan model originally read the undistorted fan input data at the beginning of the performance simulation. Here, it will have to be constantly updated. The fan map is the complete 2D-HBPR fan data with 2D exit profiles of inlet pressure recovery, cumulative inlet flow function $(W_{2D}\sqrt{T}/P)/(W\sqrt{T}/P)$, $\Delta H/T$, $\Delta H_{ID}/T$ as functions of $N/\sqrt{T}$, fan beta and fan exit area ratio.

In fact, it is unnecessary to compute the whole compressor map when only part of it is required for convergence in any particular part of the map. This model has been included as it is conventional to read in a complete fixed map at present, in order to see if any lessons can be learned when compared to using a zonal map that concentrates on a small part of the whole.

The ideal implementation for steady-state performance synthesis will have the environmental and flight conditions (atmosphere calculation) feeding into an intake model. This will either produce profiles for the fan model, or another way must be devised to guess the fan input and match this with the output of the intake. The intake model requires careful thought and has not been attempted in this work. This work has looked only at an ISASLS condition, imposing an inlet total pressure profile on the fan.

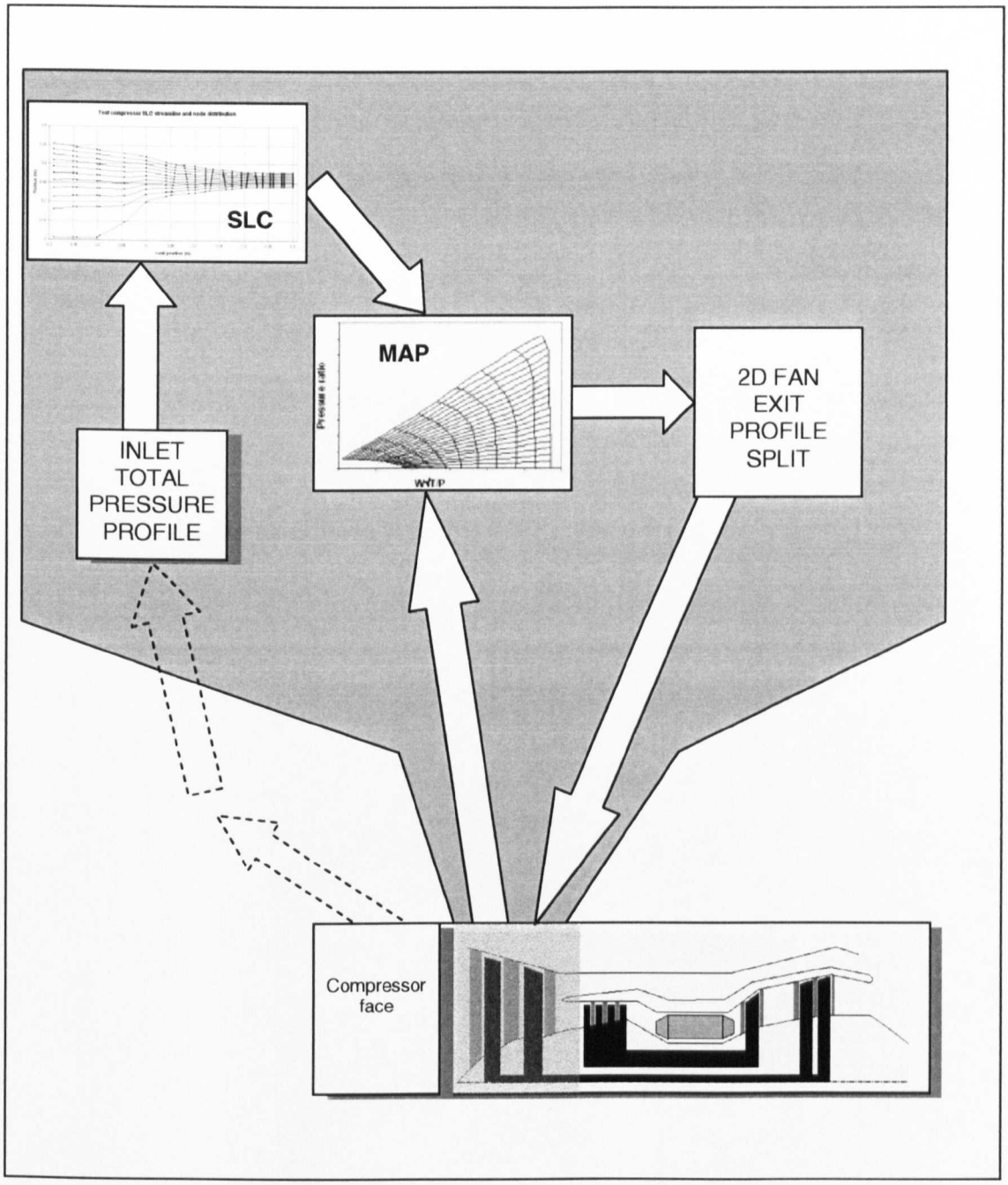

Fig. 4.5 Overview of WholeMap fan model, showing integration of streamline curvature/2D-fan method/engine performance simulation.

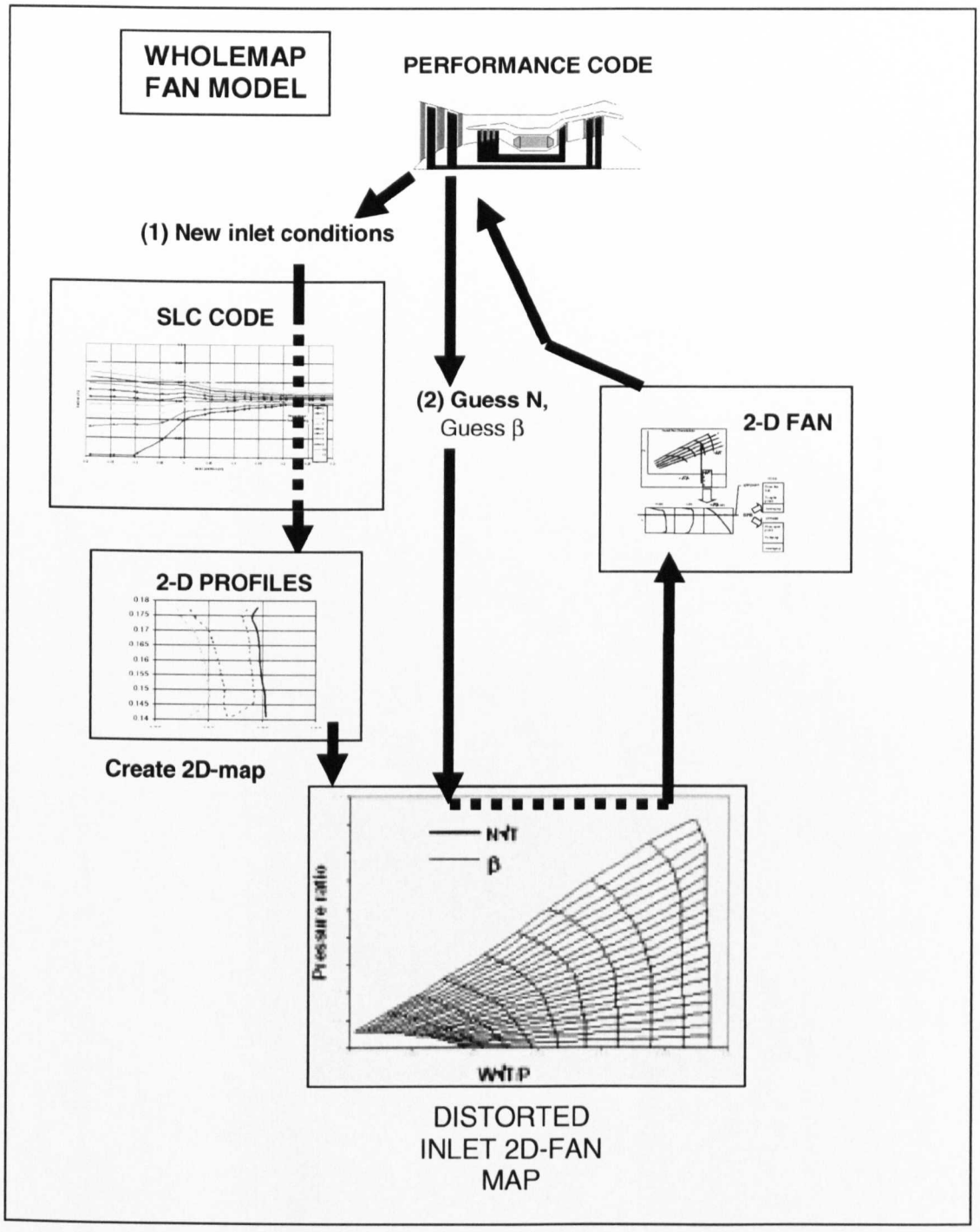

Fig. 4.6 WholeMap fan model. SLC program called to create whole fan 2D characteristic with distorted inlet conditions.

4.5.2 ZonalMap

This implementation attempts to reduce convergence time by using a small zone of 2 speed lines around the guess of fan speed and computing a distorted fan map with 2D-HBPR fan data based only on these 2 speeds.

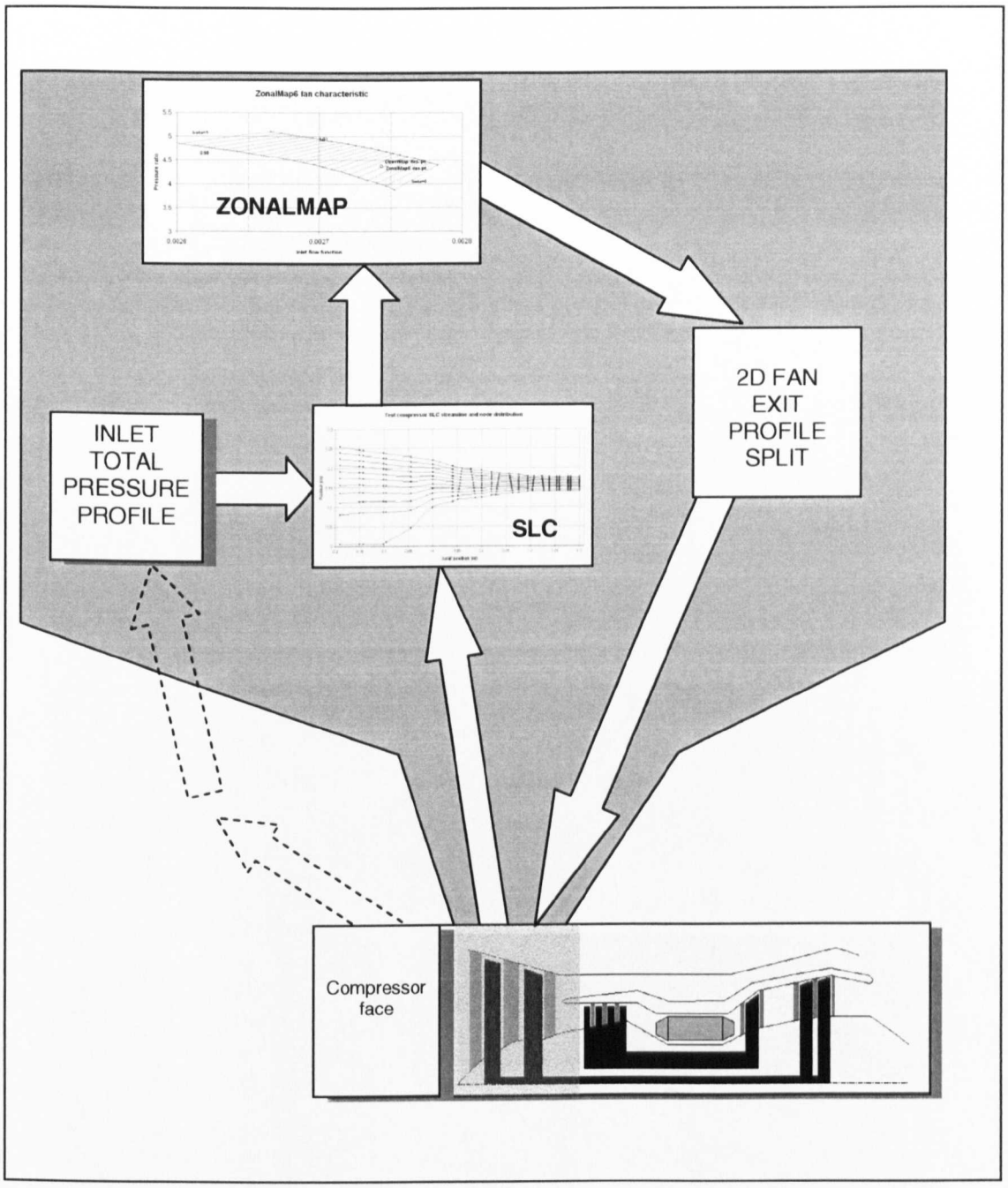

Fig. 4.7 Overview of ZonalMap fan model, showing integration of streamline curvature/2D-fan method/engine performance simulation.

As with WholeMap, the idealised model would have an intake model coupled to it and for this work, only the ISASLS condition with inlet profiles imposed on the fan is considered. The SLC code will compute the flow field for the 2 speeds, and this is converted into 2D-HBPR fan map data for the performance code.

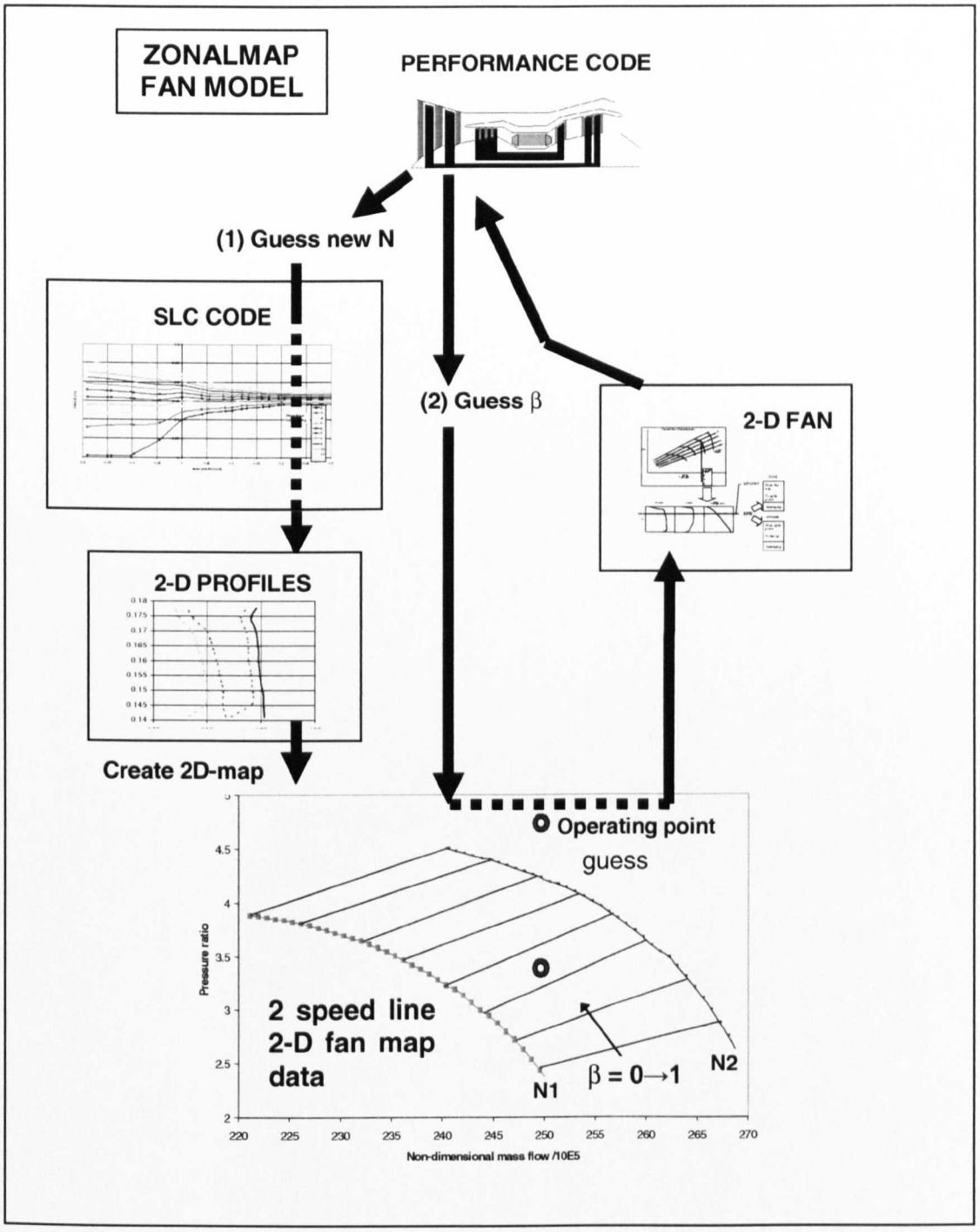

Fig. 4.8 ZonalMap fan model. SLC code called for each new guess of rotational speed falling outside previous 2-speed line fan map.

When a guess of speed results in falling well outside the 2-speed zone, the program checks whether the new speed is within a certain tolerance of one of the previous 2 speed lines. If so, it computes one new speed line to form a new zone. If it is outside this tolerance, a new 2-speed zone is computed around the new guess of speed.

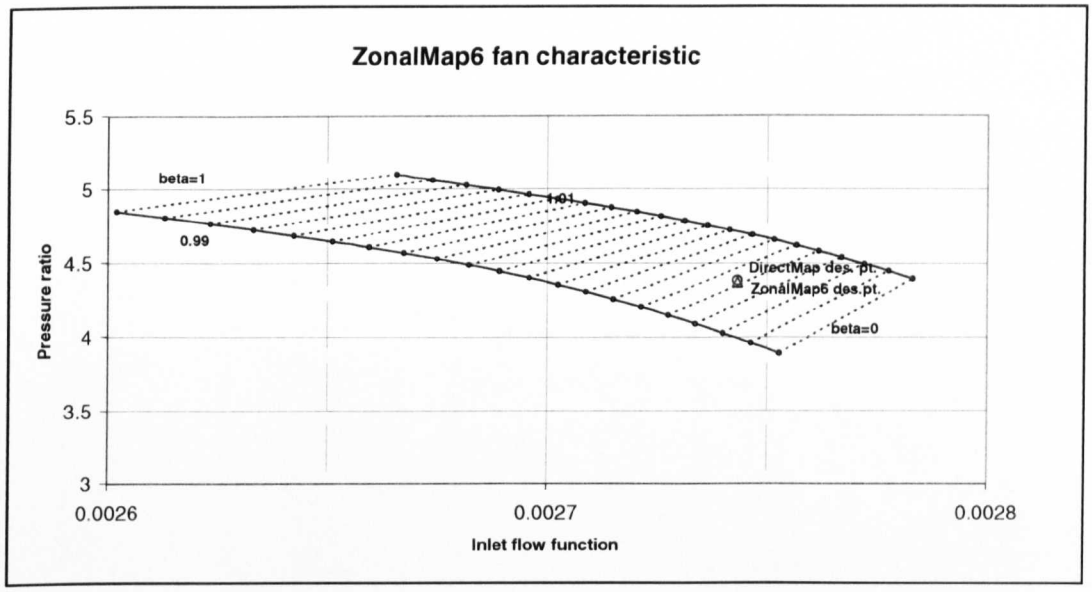

Fig. 4.9 Selection of variable width of speed line zone in ZonalMap fan model, set as percentage of design speed.

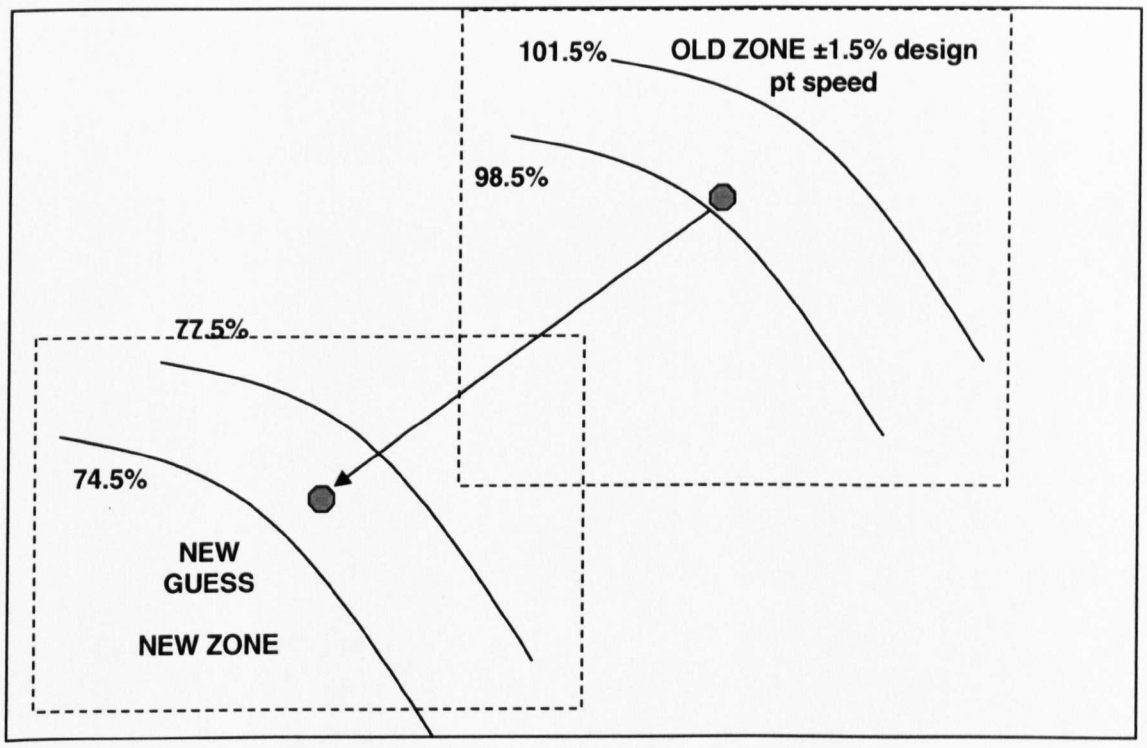

Fig. 4.10 ZonalMap computation of new fan map zone once guess of N falls outside the existing zone.

4.5.3 DirectMap

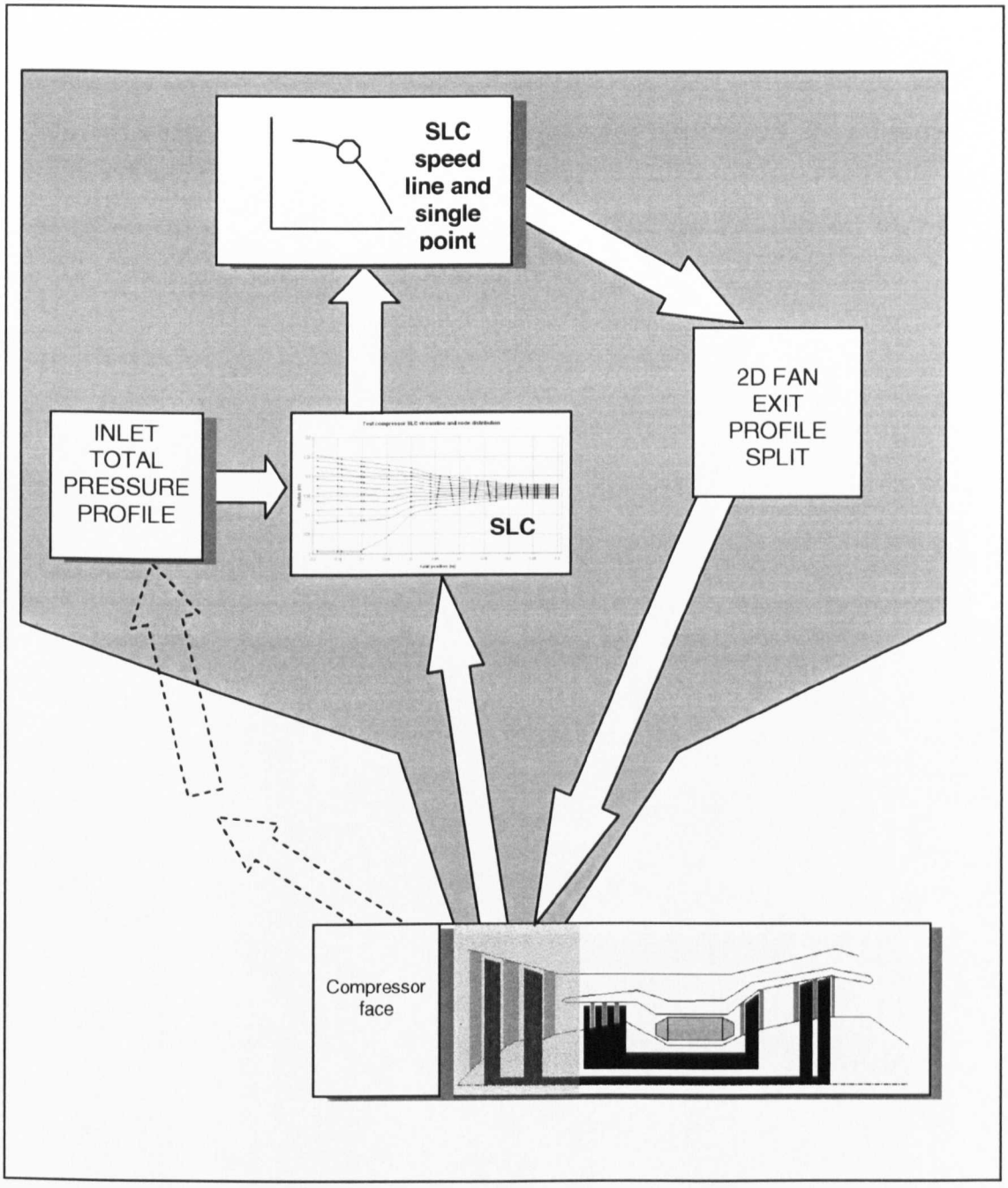

Fig. 4.11 Overview of DirectMap fan model, showing integration of streamline curvature/2D-fan method/engine performance simulation.

This implementation has the SLC code computing the fan performance for every guessed fan operating point within the performance iteration scheme. The 2D-HBPR fan generator is not required as the profiles are taken directly from the SLC profile data, with any data analysis where necessary. These are fed to the 2D-HBPR method for splitting and averaging.

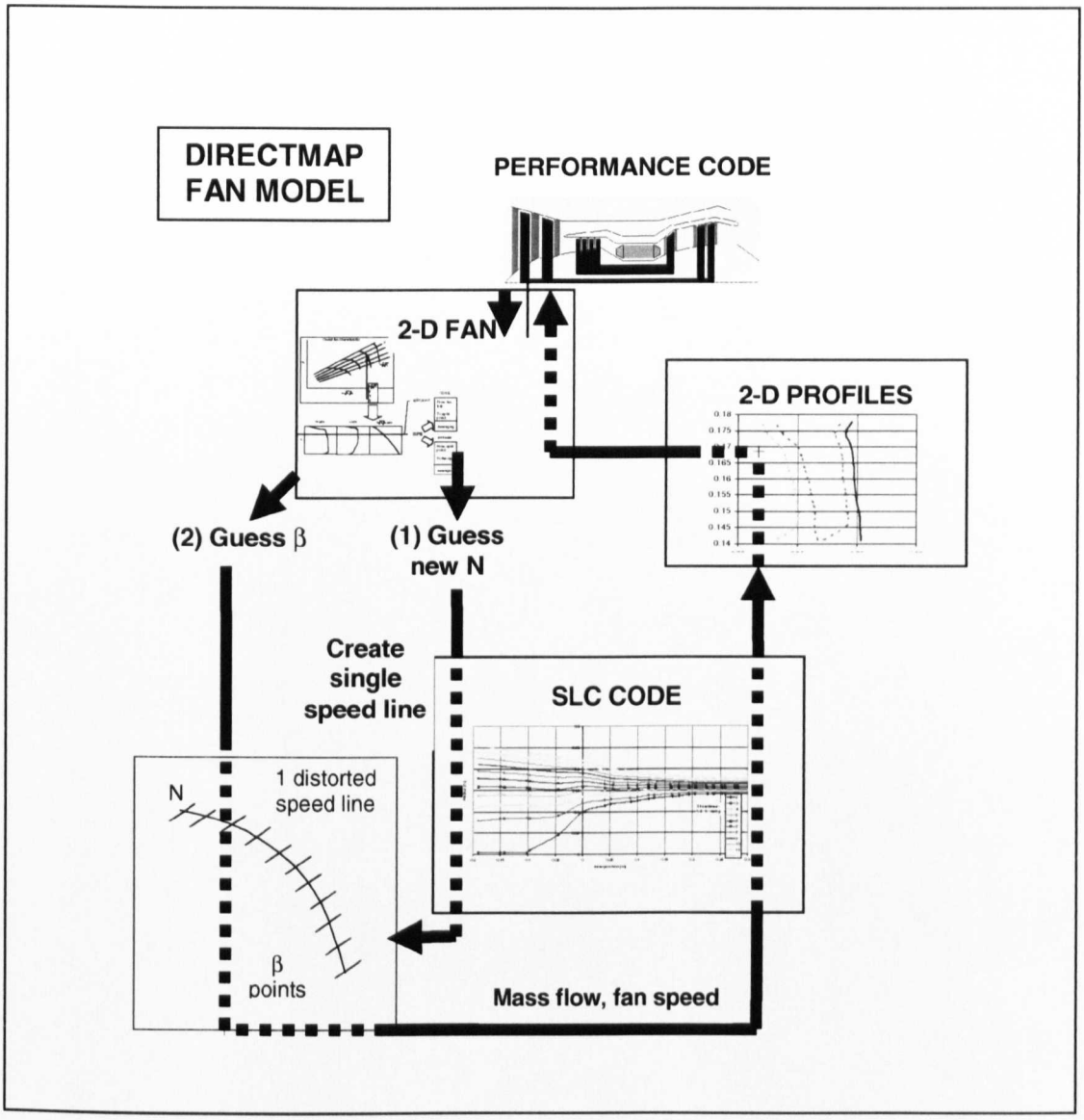

Fig. 4.12 DirectMap fan model. SLC called to compute single speed line for each new guess of rotational speed to utilise beta as independent parameter. SLC called for each guess of beta.

However, to avoid any potential problems with the steep speed lines near choke, the procedure will compute a full speed line for the first guess of rotational speed, and then apply beta values along it. The iteration in the fan will therefore remain the guess of fan beta. This beta is used with the single speed line to interpolate for the mass flow input to the SLC code. For the single speed line computation, only the beta mass flow relationship is required and calculation time can be minimised.

4.6 ACTUAL IMPLEMENTATION OF SLC WITH PERFORMANCE CODE

This section discusses the actual implementations of the 3 fan models due to practicality.

4.6.1 Issues of merging 2D fan code with SLC code and performance code

Effectively, there are several different codes that have to be merged. It was a decision that to rewrite all the codes to form a fully implemented program would take too long for this project and would give insufficient value although it should speed up convergence.

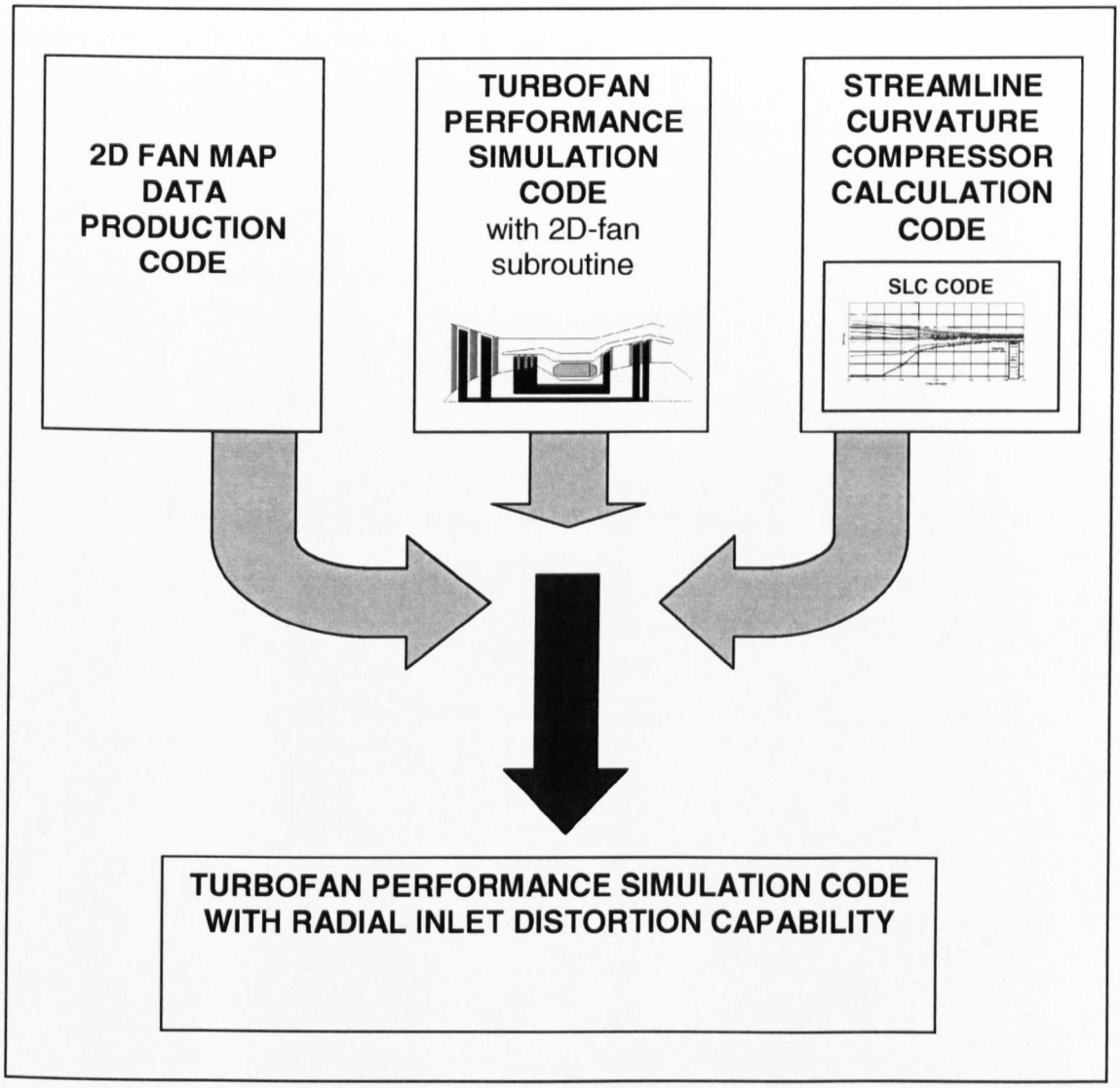

Fig. 4.13 Merging 3 separate programs to create a turbofan performance code with radial inlet distortion capability.

4.6.1.1 Issues of the specific SLC code

As discussed earlier and will be clear later, it has insufficient precision and uses cumbersome text files to transfer data. The user has to manage stall and choke by defining

limits for speed line calculations to avoid instability. An error checker should be capable of finding "limits" by automatic trial and error. This has been written but not tested yet.

4.6.1.2 Interface "shell" program

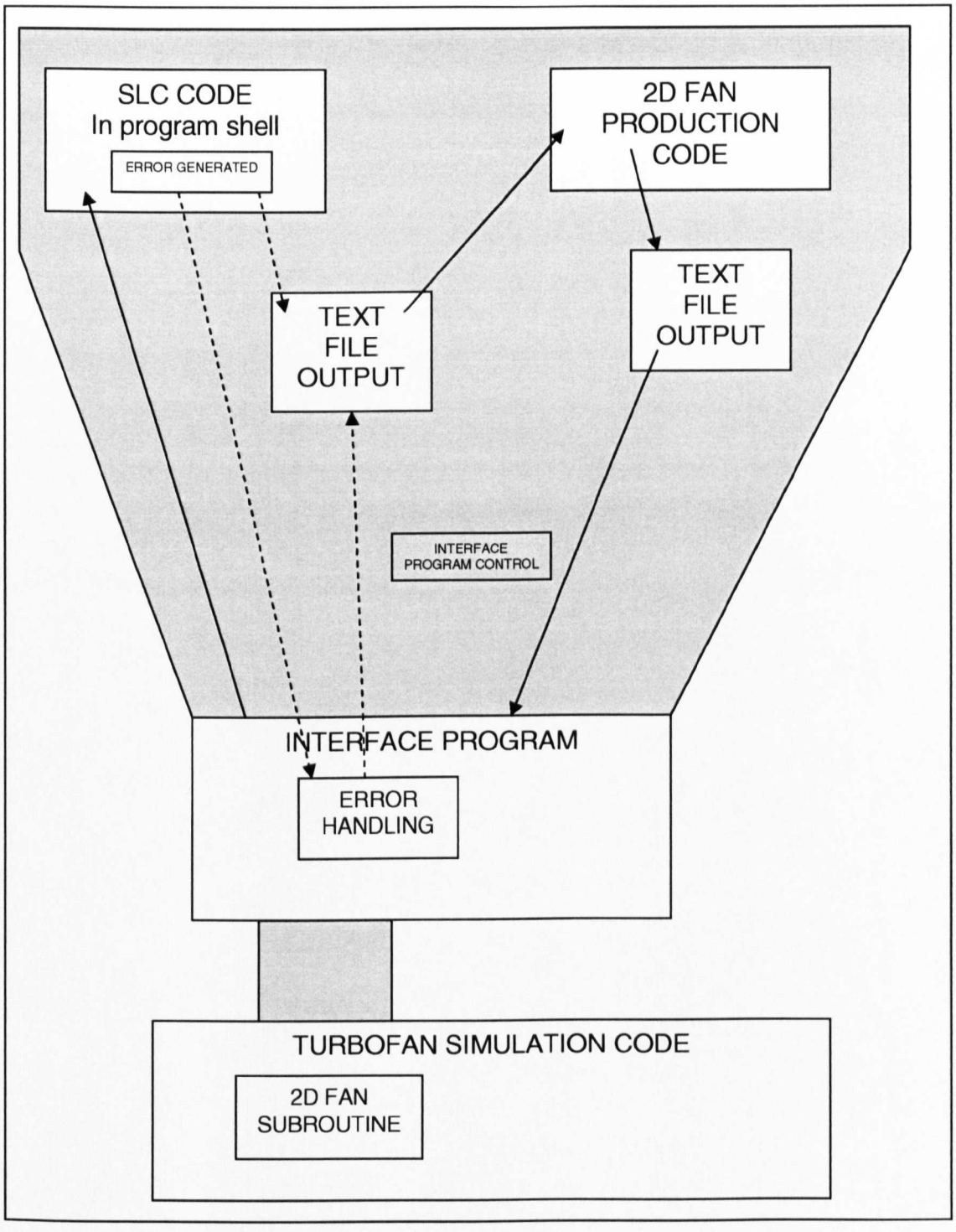

Fig. 4.14 Role of interface program controlling flow of data between the 3 codes

4.6.2 Actual model implementations

This section discusses the main points of the actual implementations.

4.6.2.1 WholeMap

See **Fig. 4.15**. This method was produced before the error handler, hence currently unautomated. Further work will be necessary to fully implement it but may not have value.

4.6.2.2 ZonalMap

The undistorted fan map with the flow-speed relationship has been manually mapped and stored. ZonalMap uses the middle of a speed line interpolated from this as an initial guess for the undistorted flow. It then computes the remainder of the distorted speed line on either side of the initial guess. The current program only allows the distorted flow to calculate to a mass flow greater than the undistorted surge/stall mass flow, and a mass flow less than the undistorted choke mass flow as the computation in these regions is very unstable.

Information for two speed lines are stored in the SLC output file. A subroutine reads this into another text file for the 2D-HBPR fan generator (another source slowing down the overall convergence times). Once 2D fan data is generated, the simulation can proceed.

In the error handler, as the performance simulation calculates speed lines but does not iterate with the SLC code, an SLC error just results in a search for a new point on the speed line to compute.

4.6.2.3 DirectMap

For the calculation of the single speed line, the same procedure as ZonalMap occurs regarding the start point using the undistorted map, and the truncation of the speed line.

4.6.3 Issues with autoscaling

The autoscaling procedure was rewritten to take into account the 3 different fan models. In the original turbofan simulation, the engine is scaled to design pressure ratio or beta. Here, the test fan is scaled to design mass flow. Design beta cannot be used because it can change in the ZonalMap and DirectMap methods. Design pressure ratio has been implemented but not used in this work.

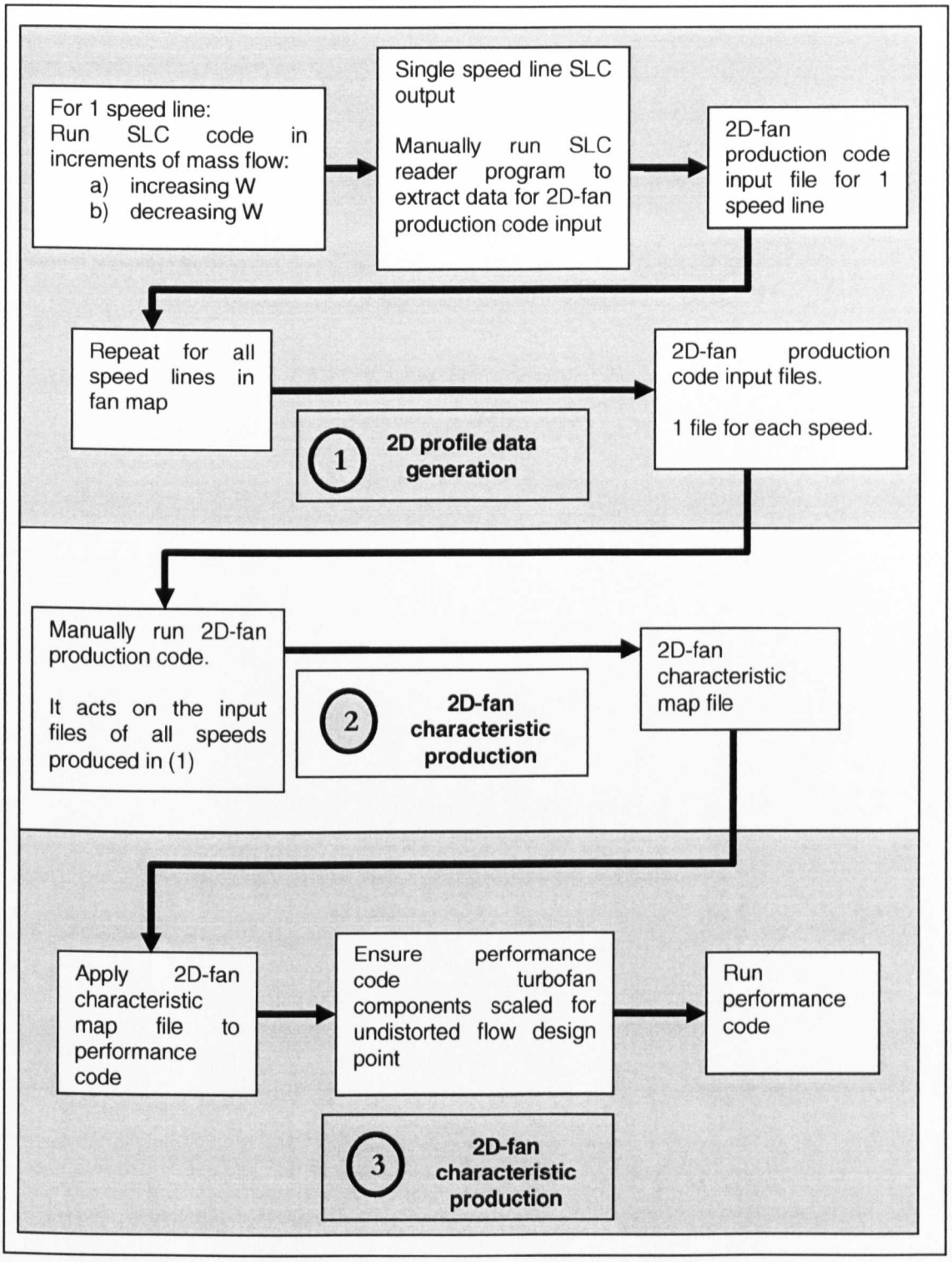

Fig. 4.15 Current implementation of WholeMap fan model showing manual running of the separate modules needed to create 2D-fan characteristic map in the correct format for the engine performance model.

4.6.4 Error handling procedure

The SLC program was originally written as a research and teaching tool. It was meant for the user to manually input speed and mass flow to slowly map out a compressor characteristic if desired. It was not intended to be a robust compressor flow field calculation tool which would be capable of continuous calculations of operating point without failure. The code is prone to certain errors; particularly in the calculation of the outlet velocity from each blade row when attempting to match the outlet flow profile to the overall mass flow.

It is well known for streamline curvature codes in general to be unstable. It was decided that to attempt to make the SLC procedure more robust was a difficult deviation from the objectives of this thesis. It was decided to produce subroutines that would detect when the SLC code resulted in failure and to manage this in such a way that estimated compressor characteristic points could be calculated from known successfully converged points. The only modification to the SLC code for error detection would be a subroutine to enable SLC execution to continue without resulting in cessation of the performance routine.

Different methods were implemented according to the method of implementation of the compressor map in the performance program. For each method, several options were written according to the status of the performance iteration code.

4.6.4.1 Error handling in SLC code

The current SLC implementations all run the SLC code in an MSDOS shell and communicate with the performance code via text files (section **4.6.1.2**). The strategy is to detect a fault in the SLC code within it's shell operation and to label the output file with a "FAIL" statement. The performance code will then run a check after every call of the SLC code to see if the operation was a failure or success with a check of the output file.

SLC code errors fall in two main groups:

(i) Illegal run-time errors. These include domain errors such as square root of negative numbers.

(ii) Loop errors. These are when the SLC code runs into endless loops that effectively freeze the performance code operation.

Illegal run-time errors are detected by using the Compaq Visual Fortran v6.6 provided subroutine Matherrqq.f90. This allows the SLC program to continue normally in the event of illegal run-time errors and for the user to code for the desired response when one is detected. The presence of these kinds of errors is one reason why it was decided to call the SLC code

from the performance code one point at a time to calculate a compressor speed line, instead of allowing the SLC code to more quickly compute a speed line in one call. Any domain errors would lead the program to be unstable for further operation. Therefore, it is better to exit the SLC code in order that all memory registers can be reset for the next compressor point calculation.

Loop errors were detected over a period of testing of the SLC code using the Visual Fortran debugger. Instead of attempting to rectify the code, counters were put in such that when any loop was iterated considerably more times than the average required for normal convergence, the code would exit with failure. This was done by deliberately planting an illegal run-time operation on exceeding a preset figure for a loop count, so that the Matherrqq.f90 subroutine would be called to exit the SLC program without catastrophic failure.

4.6.4.2 Error handling subroutine

In the performance code, this is handled by the subroutine SLCI_SLCErrorCheck.f90. It is designed to be called with the integer variable NErrorMode, which can have a value of 1-4, corresponding to 4 different general regimes within the performance code for when the SLC program is operated:

1. Speed line calculation with increasing mass flow.
2. Speed line calculation with decreasing mass flow.
3. Single operating point calculation – first beta point guess after guess of N.
4. Single operating point calculation – subsequent beta point guesses.

The strategy when encountering SLC failure is to compute that failed point by linear interpolation between two successful SLC-converged points. Thus for each of the above regimes, all possible envisaged scenarios are coded for. For example, for NErrorMode = 1, if the first point for the speed line calculation is a failure, then two successful points must be calculated with increments of higher and lower mass flow in order to be able to carry out interpolation. Three attempts are allowed for the SLC to be called to compute a point to enable interpolation before abandoning this and using extrapolation from a previous point.

The SLC code can operate with a fractional mass flow change on either side of a failed point. It is possible for three increments of mass flow to still produce failed points if for example, the point is close to stall or choke. Currently, the stall and choke points have been

truncated to avoid instability. This had been done before the error detection code was written. For future work (section **5.3**), the error detector should be used to detect surge and choke, for example, if after certain number of increments of reduction of mass flow failed to result in convergence, along with a check of the diffusion factor from the nearest known converged point, then it could be reasonably assumed that the computation is being performed beyond or near the stall region.

4.6.4.3 ZonalMap SLC error handling

In ZonalMap mode, the SLC program is used to compute compressor speed lines. Therefore, it is not necessary to compute a particular speed and mass flow. An error during speed line computation is detected, and results in the next successful point being retained.

4.6.4.4 DirectMap SLC error handling

In contrast to ZonalMap where a specific operating point is not required but merely a point on a speed line, it is very important in DirectMap to be able to generate interpolated profiles for a beta guess as true as possible to what the SLC program would have successfully produced. If the point in question is actually a converged performance point, the inability to compute it would mean that the performance code would never cease iterating to try to achieve that compressor performance.

4.6.4.5 DirectMap implanted SLC error case study

A study was made to check whether the error handler could produce acceptable fan exit profiles by interpolation when the SLC failed. This was done by implanting a failure for a point at which the SLC code is known to be able to succeed after a successful convergence for a prior guess of beta during iteration along a speed line.

As intended, the performance code recognised the "failed" point and incremented the beta value to compute a new compressor point. This point was used for interpolation for the failed point profiles (**Fig. 4.16** and **Fig. 4.17**).

The mass flow and rotational speed were recorded for the failed point and were input to the standalone SLC code producing the profiles separately for comparison with the interpolated profiles. **Fig. 4.18** and **Fig. 4.19** compare the total pressure and total temperature profiles respectively, calculated by the error handler in a simulated SLC failure to those calculated by successful convergence of SLC.

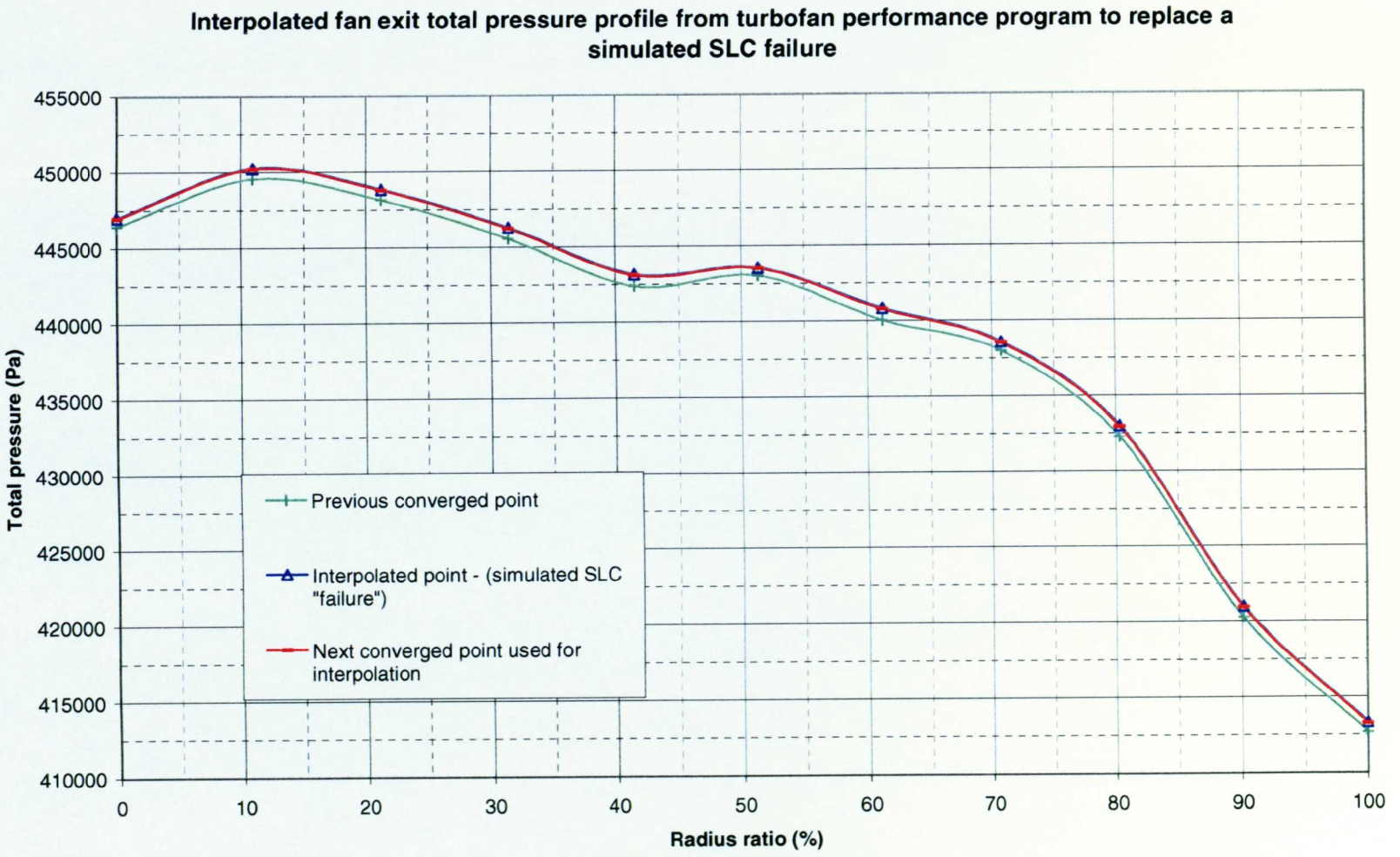

Fig. 4.16 DirectMap interpolation to replace failed SLC calculation: comparison of interpolated fan exit total pressure profile with profiles from two adjacent converged points.

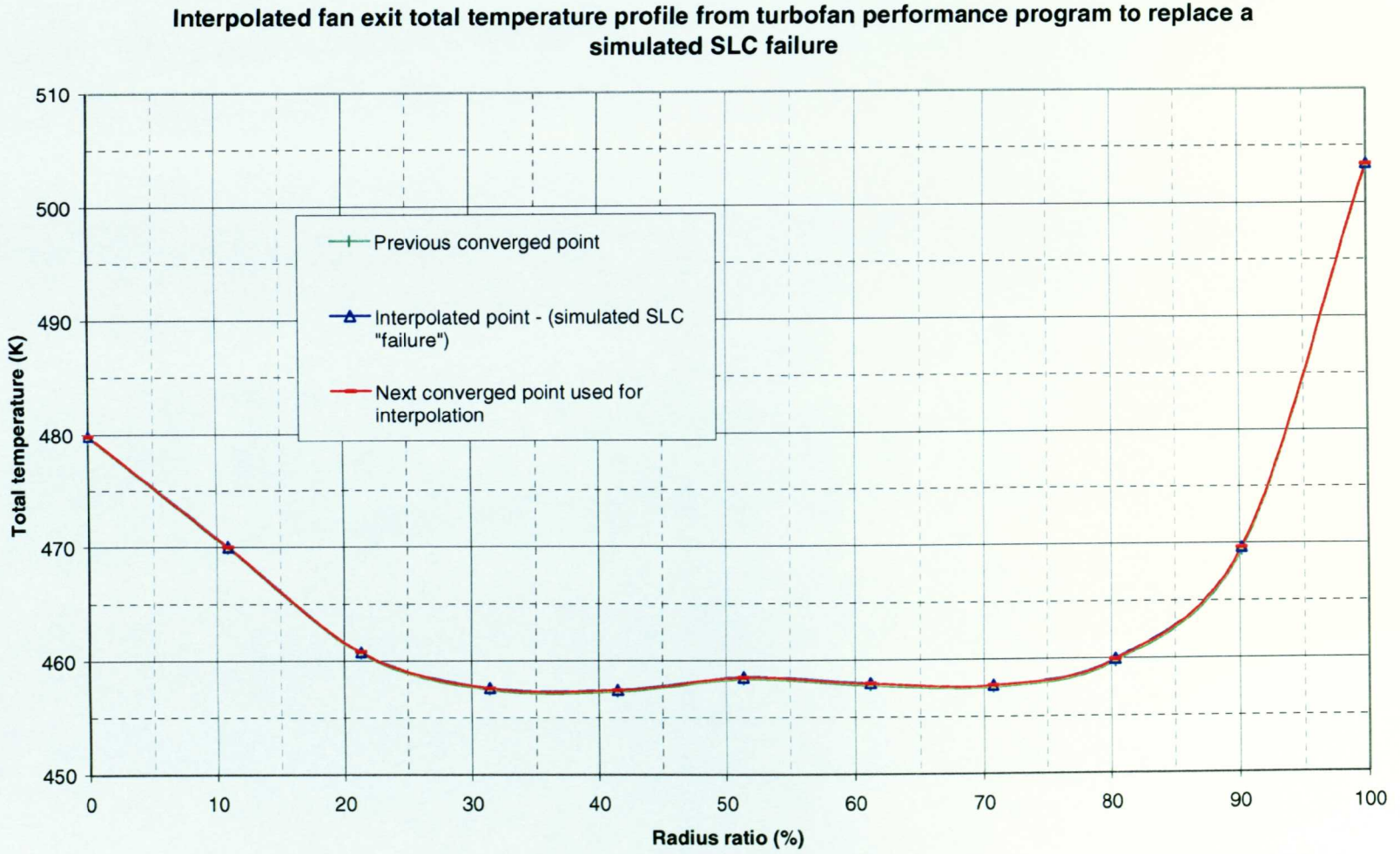

Fig. 4.17 DirectMap interpolation to replace failed SLC calculation: comparison of interpolated fan exit total temperature profile with profiles from two adjacent converged points.

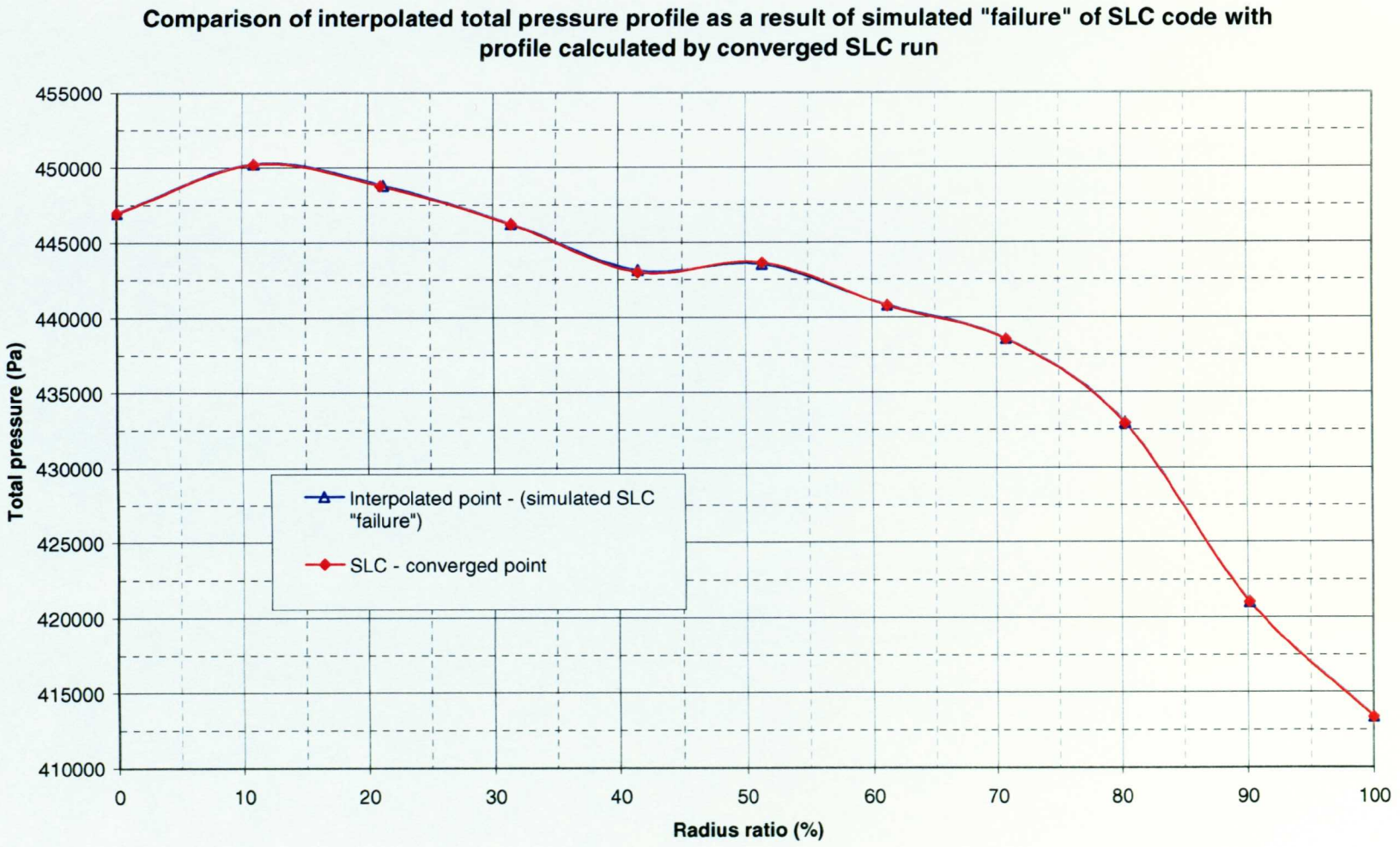

Fig. 4.18 Comparison of total pressure profile calculated by interpolation for implanted SLC failure with profile calculated by SLC program.

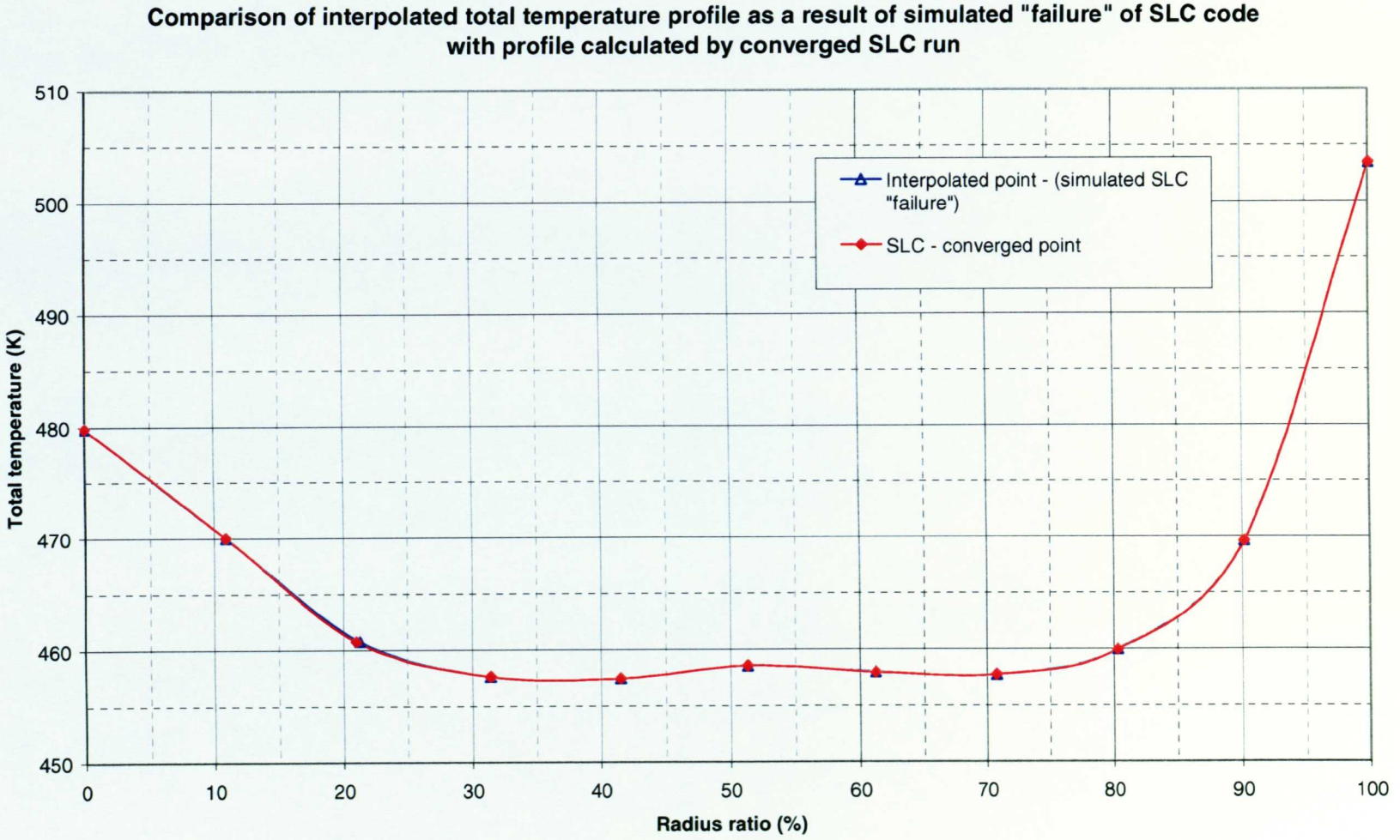

Fig. 4.19 Comparison of total temperature profile calculated by interpolation for implanted SLC failure with profile calculated by SLC program.

4.7 UNDISTORTED INLET CASE STUDIES OVERVIEW

4.7.1 Scaling the engine model components

Scaling of components is necessary to size the engine model components to achieve the desired engine design point. To carry out a proper comparison of the modelling of the test engine using the three fan methods, the same scaling factors should be used in the respective models for all components so that the same geometry engine is being modelled. The nature of each fan model leads to slightly different pressure ratio profiles being calculated when run at the same speed and mass flow. This leads to varying design point conditions when each model is scaled to achieve the same TET for example.

The parameters in **Table 6** were common for all models in the autoscaling procedure (section **4.6.3**). In this work, it was desired to use an unscaled fan model, i.e. the fan would directly be the output from the SLC program.

4.7.1.1 Choice of fan design point

The nominal design point of the SLC model of the test compressor which is used for the fan in the engine models of this work is set at 16.375kg/s (Barbosa, 1987), which gave a pressure ratio of 4.60 and isentropic efficiency of 0.858.

The calculation of the SLC program is determined by input of rotational speed and mass flow. In its original form, the performance code gave the user the choice of setting a design point pressure ratio or $\Delta H/T$. In conjunction with the SLC code, this would have meant inputting flow and speed and iterating until the required pressure ratio was obtained. However, in the present work, it was only necessary to investigate a hypothetical engine using the test compressor as the fan without the added complexity of scaling the output from the SLC code. It was decided to maintain the input of design point mass flow. For any future work, it may be necessary to be able to scale the fan model. However, this brings up new issues as to whether it is realistic to scale a streamline curvature output and is discussed in section **5.3.4**.

The fan design point mass flow was ultimately set at 16.374967 kg/s. Although 16.375 kg/s was originally set, the DirectMode operation of SLC was unable to converge using this as design mass flow. This was due to the continuous failure of the SLC code at a point near to 16.375 kg/s. In the DirectMode procedure, the mass flow is obtained by interpolation on a single speed line using an input guess of beta (section **4.6.2.3**). The autoscale procedure

thus guesses beta, obtains a mass flow from the speed line and feeds this into the SLC code. The program runs through its normal iteration routine to converge onto the design flow, i.e. a loop is set up to calculate design point beta. Thus beta is adjusted and the fan flow checked after calculation by the SLC code. Although the error handler could cope with this failure, the iteration procedure continuously guessed this same failure point as the Newton-Raphson solver directed convergence towards the design mass flow. The program then continued in an endless loop without convergence.

Parameter	**Program variable name**	**Value**
Fan		
Rotational speed	RPMFan_DPNom	21892 rpm
Mass flow	FanDPMassNom	16.374967 kg/s
Bypass ratio	BPR	1.2
HPC		
Overall pressure ratio	EngOPRNom	20.0
Map number	NoMap_HPC	6
Unscaled map design pressure ratio	HPC_OrigMapDP	1.883
Rotational speed	RPMDP_HPC	25000 rpm
Isentropic efficiency scale factor	SF_HPCETA	1.125
Combustor		
Pressure loss	PDROP	0.95
Fuel calorific value	FCVL	$4.3x10^7$ J/kg
Combustion efficiency	SF_BNETA	0.99
Turbine Entry Temperature	TET_DP	1300 K
HPT		
Map number (Turbomatch)	NoMap_HPT	5
Isentropic efficiency scale factor	SF_HPTETA	1.0
LPT		
Map number	NoMap_LPT	5
Isentropic efficiency scale factor	SF_LPTETA	1.0

Table 6 Scaling parameters input set for scaling procedures (all models).

A miniscule change in the design mass flow was sufficient to rectify this problem. This problem was only experienced during the scaling procedure and never in the performance

iteration routine. It is likely that this scenario is not repeated in the main performance iteration routine as computations downstream of the fan alters the next guess for the fan operating point so that an endless loop does not result. A future improvement could be to directly set the fan design mass flow to the required value during the scaling procedure instead of allowing the fan subroutine to run by guessing beta.

4.7.1.2 Differences between fan implementations

The differences in the fan implementations lead to small differences in the converged design point component scaling factors. WholeMap and ZonalMap methods are described in sections **4.6.2.1** and **4.6.2.2** respectively. Essentially, WholeMap and ZonalMap operate in the same manner, using calculated fan characteristics from which points within are interpolated. The WholeMap fan characteristic is a pre-calculated entire characteristic, and in this work, the 100% design speed line of 21892 rpm is present in the fan characteristic map data (**Fig. 4.20**). In the ZonalMap method, the first guess of a rotational speed is calculated by setting this in the middle of a zone of two speed lines. Therefore, the two speed lines forming the zone used to compute the design point are set respectively above and below the 100% design speed. Given the fan design mass flow as input, the WholeMap method needs to locate the design point by interpolation between known points on the 100% speed line. This should give a better result than in ZonalMap, where the 100% speed line has to be calculated first within the map zone before interpolation for the required mass flow.

DirectMap, described in section **4.6.2.3** is fundamentally different by directly computing the fan performance from the design mass flow without interpolation. This theoretically gives the best answer, with no interpolation of the fan operating point, and is therefore set as the datum result in any comparisons of the design point calculations.

Table 7 shows the comparison of the calculated scaling factors for the engine for the three fan model implementations. The handle is TET and is set at 1300K. The ZonalMap setting is for the two speed lines in the zone to be ±0.5% of the 100% design speed. Note that the design point fan beta (betafan_dp) is an irrelevant comparison and is included only for information. **Table 8** shows the comparison of scaling factors with the datum DirectMap case. The scaling factors are within ±0.4% of the datum case. The largest difference is in the core nozzle area

TWO-SPOOL TURBOFAN MILITARY ENGINE			
	WHOLEMAP	ZONALMAP (ZM1)	DIRECTMAP
Flight conditions			
alt	0.00E+00	0.00E+00	0.00E+00
fmach	0.00E+00	0.00E+00	0.00E+00
Fan			
rpmfan_dp	21892	21892	21892
btafan_dp	0.311969411	0.242194059	0.280315082
bpr_dp	1.2	1.2	1.2
HPC			
rpmdp_hpc	25000	25000	25000
nomap_hpc	6	6	6
btadp_hpc	0.699618598	0.699618598	0.699618598
prhpc_dp	4.567690446	4.568286014	4.563764253
dhhpc_dp	-1	-1	-1
sf_hpcnt	1162.478663	1162.324661	1161.584747
sf_hpcmf	1.99067E-06	1.99146E-06	1.99087E-06
sf_hpcpr	4.040419531	4.041094013	4.035973107
sf_hpceta	1.125	1.125	1.125
Combustor			
pdrop	0.95	0.95	0.95
tet_dp	1300	1300	1300
fuel_dp	-1	-1	-1
fcvl	43000000	43000000	43000000
sf_bneta	0.99	0.99	0.99
handle_no	1	1	1
HPT			
nomap_hpt	5	5	5
dhhpt_dp	202.3625582	202.4372564	202.5314997
prhpt_dp	-1	-1	-1
sf_hptnt	315.170566	315.170566	315.170566
sf_hptmf	6.33896E-07	6.33978E-07	6.34003E-07
sf_hptpr_dh	35342.85034	35355.89646	35372.35616
sf_hpteta	1	1	1
LPT			
nomap_lpt	5	5	5
dhlpt_dp	353.0109894	353.4354627	354.7469089
prlpt_dp	-1	-1	-1
sf_lptnt	302.3767383	302.3884404	302.4038604
sf_lptmf	1.43662E-06	1.43728E-06	1.43795E-06
sf_lptpr_dh	61653.76975	61727.90449	61956.95004
sf_lpteta	1	1	1
Nozzles			
anhnz	4.2678151E-02	4.2910812E-02	4.3568581E-02
ancnz	1.0885115E-02	1.0888336E-02	1.0883123E-02

Table 7 Comparison of engine scaling factors for turbofan performance model with three fan implementations.

Parameter	Differences from datum (DirectMap)	
	WholeMap	ZonalMap (ZM1)
Fan		
FanPR	0.080%	-0.128%
HPC		
prhpc_dp	0.110%	0.127%
sf_hpcmf	-0.010%	0.030%
sf_hpcpr	0.110%	0.127%
HPT		
dhhpt_dp	-0.083%	-0.047%
sf_hptnt	0.000%	0.000%
sf_hptmf	-0.017%	-0.004%
sf_hptpr_dh	-0.083%	-0.047%
LPT		
dhlpt_dp	-0.489%	-0.370%
sf_lptnt	-0.009%	-0.005%
sf_lptmf	-0.093%	-0.046%
sf_lptpr_dh	-0.489%	-0.370%
Nozzles		
anhnz	-2.044%	-1.510%
ancnz	0.018%	0.048%

Table 8 Comparison of WholeMap and ZonalMap computation of design point scaling factors with datum (DirectMap).

In order to gain an idea of what effect these changes have on engine performance, some performance parameters for the three models are tabulated in **Table 9**. The effect of the different fan models is to calculate slightly different 2D profiles of pressure ratio (**Fig. 4.21**) and efficiency (**Fig. 4.22**) for the set design point mass flow. ZonalMap has lower pressure ratio but slightly higher efficiency. This is reflected by the differences in inner and outer fan pressure ratios (using the same design bypass ratio in all cases). The lower pressure ratio results in a lower profile of total temperature (**Fig. 4.23**). These are the differences due to interpolation in the WholeMap and ZonalMap methods compared to the DirectMap. There are two instances of interpolation; one being to obtain the required speed line, and secondly

to interpolate to the required operating point (beta line). The calculations used in this program produce a speed line used 0.15kg/s increments of mass flow to create the data from the SLC program. As many points as possible are obtained and then processed into a fan characteristic map of 21 beta lines (21 points per speed line). The models therefore match to different fan pressure ratio and efficiency design points, essentially being different characteristics and result in engines of slightly different geometry after the remaining components are scaled. The thrust difference is 0.453% increase for the ZonalMap case.

4.7.1.3 Effect of variations in ZonalMap setup on design point performance

It was decided to make a systematic study of how subtle variations in the setup of, particularly the ZonalMap method, would affect results compared with the datum DirectMap method. This was done in order to make recommendations for the optimum setup of the ZonalMap method and to assess its suitability as a replacement for DirectMap when calculation time and computing power is a constraint. The inputs that can be made are (i) to change the magnitude of the two speed line increments in the map from the design speed, and (ii) to change the increment of mass flow used to produce the data from the SLC program for the speed lines in the map.

Parameter	Performance parameter differences from datum (DirectMap)				
	DirectMap	WholeMap		ZonalMap (ZM1)	
	Value	Value	Difference	Value	Difference
Thrust (N)	7592.692	7639.854	0.621%	7627.113	0.453%
SFC (kg/s/MN)	16.529	16.451	-0.475%	16.473	-0.342%
Fuel flow (kg/s)	0.12550	0.12568	0.143%	0.12564	0.110%
RFAN	4.382	4.379	-0.111%	4.378	-0.128%
RFAN_inner	4.397	4.394	-0.086%	4.393	-0.121%
RFAN_outer	4.371	4.366	-0.152%	4.366	-0.154%
ETAfan	0.8586	0.8593	0.082%	0.8583	-0.041%

Table 9 Comparison of engine model design point performance parameters using WholeMap and ZonalMap fan models compared with datum (DirectMap).

The number of beta lines is kept the same. Another important variable in ZonalMap is the use of the cessation of calculation before reaching the ends of the speed lines (effectively producing truncated speed lines). This feature had been put in using a mass flow range interpolated from a pre-calculated complete map at ISASLS with undistorted flow (section **4.6.2.2**) to avoid instability of the SLC program in the stall and choke regions. The latest version of the program has an artificial stall and choke check (trial and error by decreasing and increasing mass flow respectively until the program no longer converges). This has not been run for the results in this thesis, because transient excursions from the working line have not been studied here and there is sufficient margin for the steady state iteration procedure. The mass flow limits for speed line calculations in both ZonalMap and DirectMap methods have been set at: interpolated undistorted choke mass flow limit -0.2 kg/s and stall mass flow limit + 0.4 kg/s. The current implementation of WholeMap is a manual one so that the surge and choke limits are manually searched for by the user to extract the maximum possible flow range for the speed lines.

A range of ZonalMap setups was tested as shown in **Table 10. Fig. 4.24** to **Fig. 4.27** show the range of setups of ZonalMap in terms of the fan characteristic. **Fig. 4.24** (set A) explores a range of speed line zones of magnitude 6% of design speed difference. It is expected that the nearest result to the datum DirectMap case should be for the upper speed line being on the design point (ZM8), this case only has to involve interpolation along a speed line and not in between 2 lines.

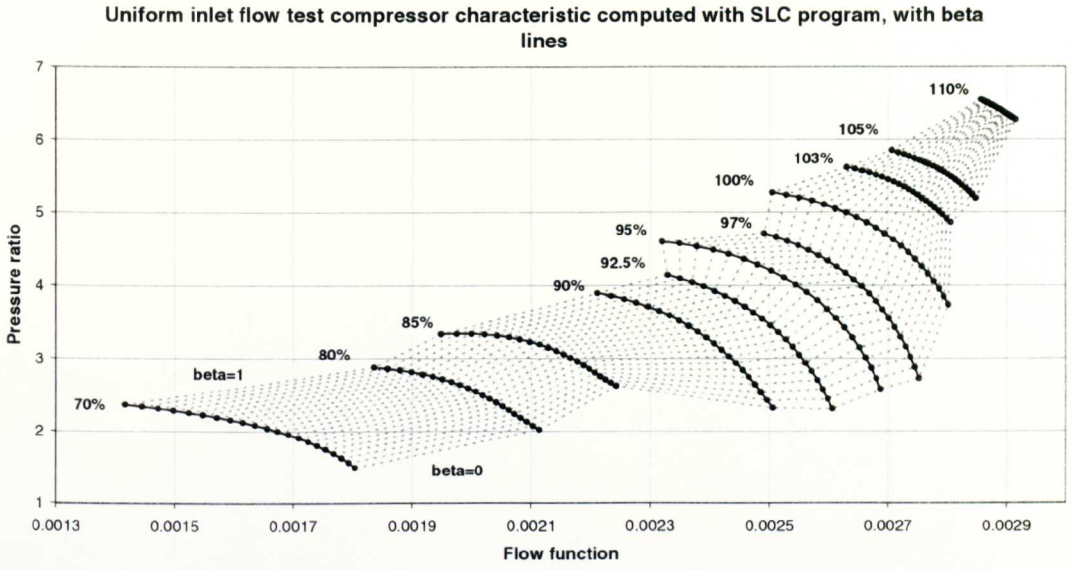

Fig. 4.20 WholeMap layout of undistorted fan characteristic with applied beta lines.

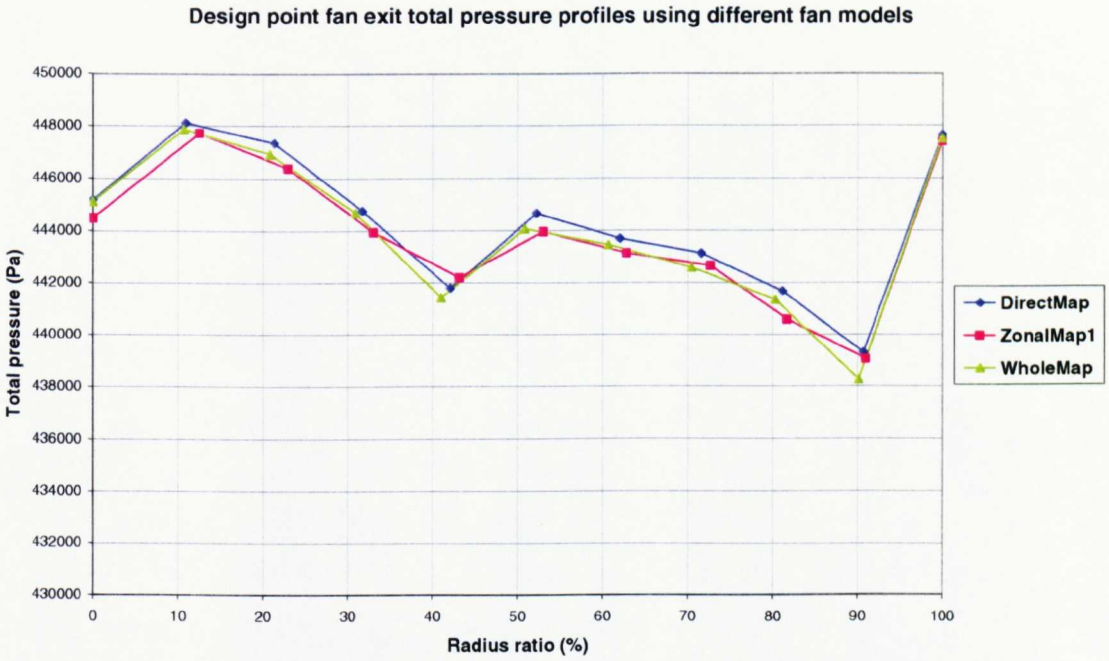

Fig. 4.21 Comparison of design point fan exit total pressure profiles from turbofan simulation program with 3 fan methods.

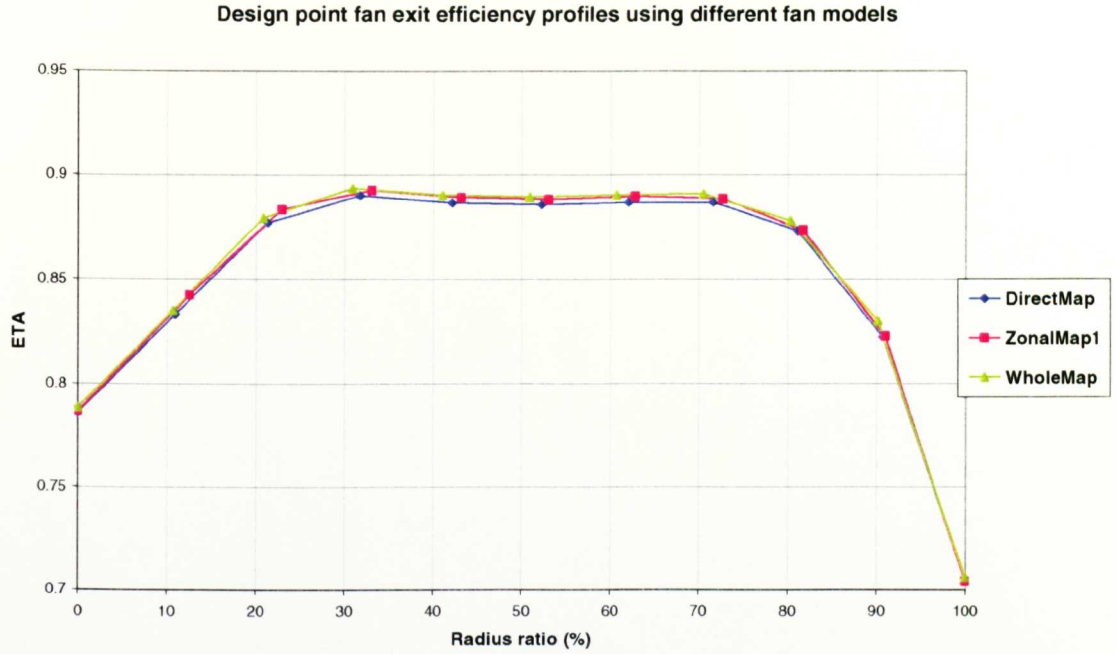

Fig. 4.22 Comparison of design point fan isentropic efficiency profiles from turbofan simulation program with 3 fan methods.

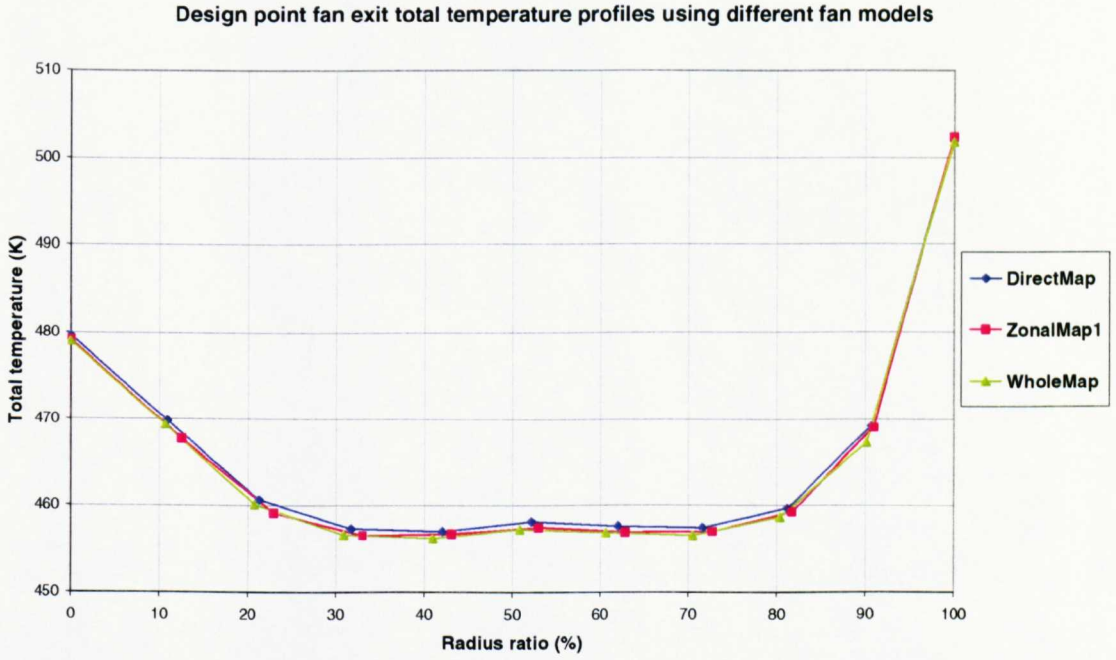

Fig. 4.23 Comparison of design point fan exit total temperature profiles from turbofan simulation program with 3 fan methods.

Code	Fan model	Difference of speed line from 100% design speed		Increment of speed line calculation (kg/s)
		Lower speed line	Upper speed line	
DM	DirectMap	N/A	N/A	0.15
ZM1	ZonalMap	-0.5%	0.5%	0.15
ZM2	ZonalMap	-1%	0%	0.15
ZM3	ZonalMap	-0.5%	0%	0.15
ZM4	ZonalMap	-0.3%	0.3%	0.15
ZM5	ZonalMap	-0.1%	0.1%	0.15
ZM6	ZonalMap	-1%	1%	0.15
ZM7	ZonalMap	-3%	3%	0.15
ZM8	ZonalMap	-6%	0%	0.15
ZM9	ZonalMap	-0.5%	0%	0.05
ZM10	ZonalMap	-1.5%	1.5%	0.15
ZM11	ZonalMap	-4%	2%	0.15
ZM12	ZonalMap	-5%	1%	0.15
ZM13	ZonalMap	-2%	4%	0.15
ZM14	ZonalMap	-1%	5%	0.15
ZM15	ZonalMap	-0.5%	0%	0.30

Table 10. Cases of input setup of ZonalMap for design point scaling comparisons. Lightly-shaded cases use design speed for the upper speed line. Dark-shaded cases compare increment in SLC program call.

Fig. 4.25 (set B) explores a series of zones which are all ± equal increments of speed relative to the design speed from ±0.1% to ±3%. This is the intended operation of ZonalMap, where the zone allows guesses above and below the first guess for a sufficiently long period before a new speed line calculation is required. The aim here is to find out the sensitivity of the calculation to the size of the size of the zone.

Fig. 4.26 (set C) is a check to ensure that with the upper speed line fixed on the design speed, the selection of the lower speed line should not affect the interpolated design speed. Finally, **Fig. 4.27** (set D) is a check on the effect of calling the SLC program to calculate the speed line with varying degrees of resolution of mass flow between points of 0.05,

0.15(datum) and 0.30 kg/s. The SLC data in each case is processed into 21 point speed lines as is done throughout this work.

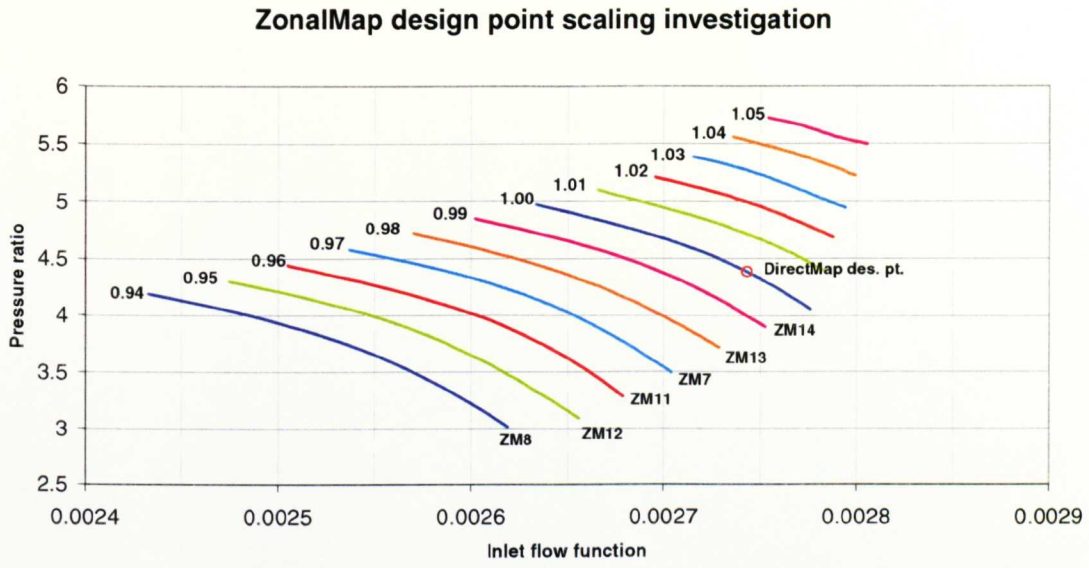

Fig. 4.24 ZonalMap design point scaling investigation (set A): 6% speed difference between speed line pairs, interpolation from above and below design speed. (21 point speed lines, straight line join between points).

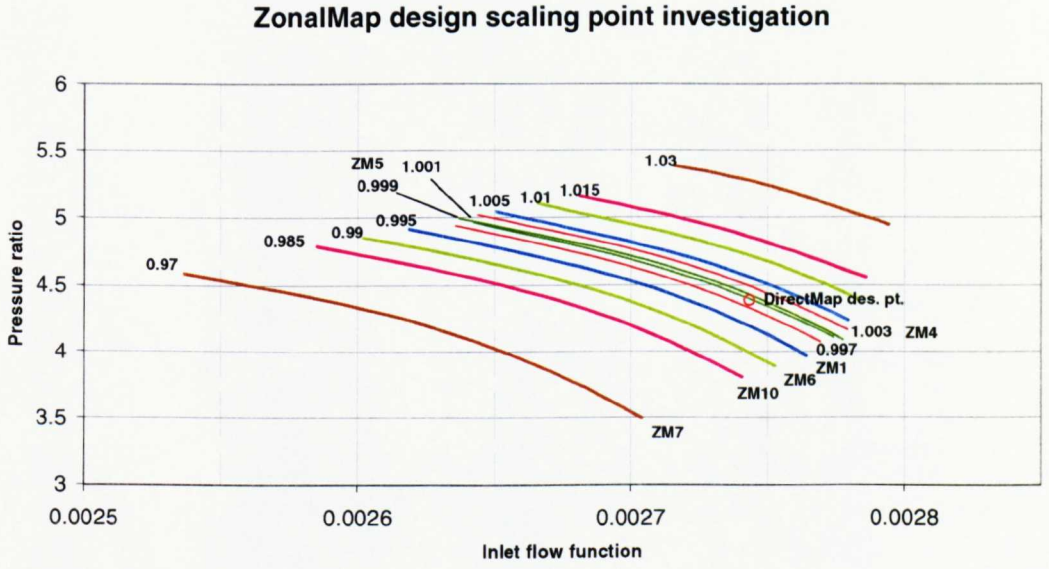

Fig. 4.25 ZonalMap design point scaling investigation (set B): interpolation of design speed in middle of speed line zones, speed line pairs from ±0.1% to ±3% design speed. (21 point speed lines, straight line join between points).

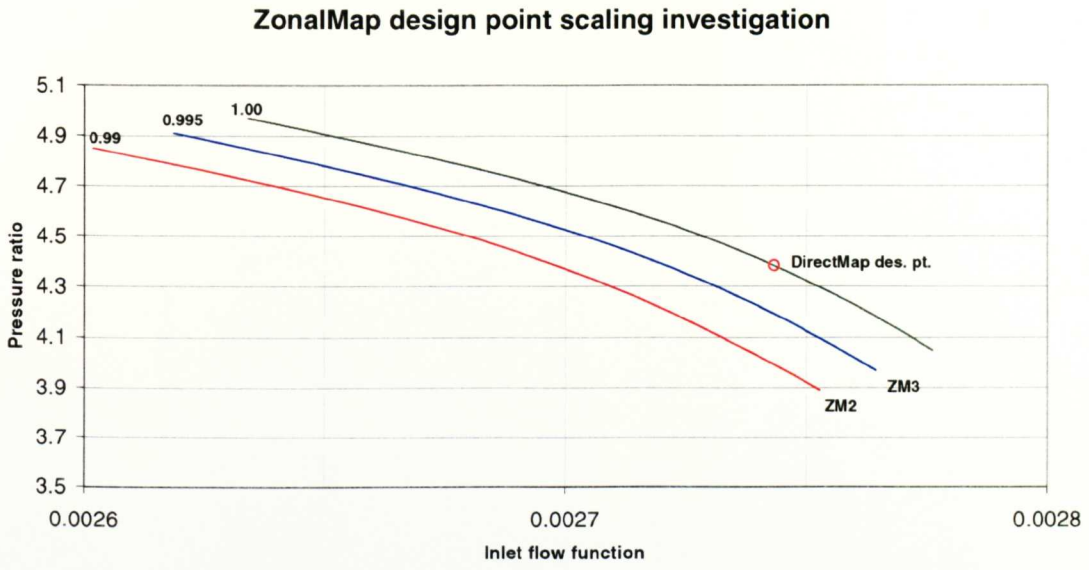

Fig. 4.26 ZonalMap design point scaling investigation (set C): interpolation of design speed with upper speed line of each zone on design speed. (21 point speed lines, straight line join between points).

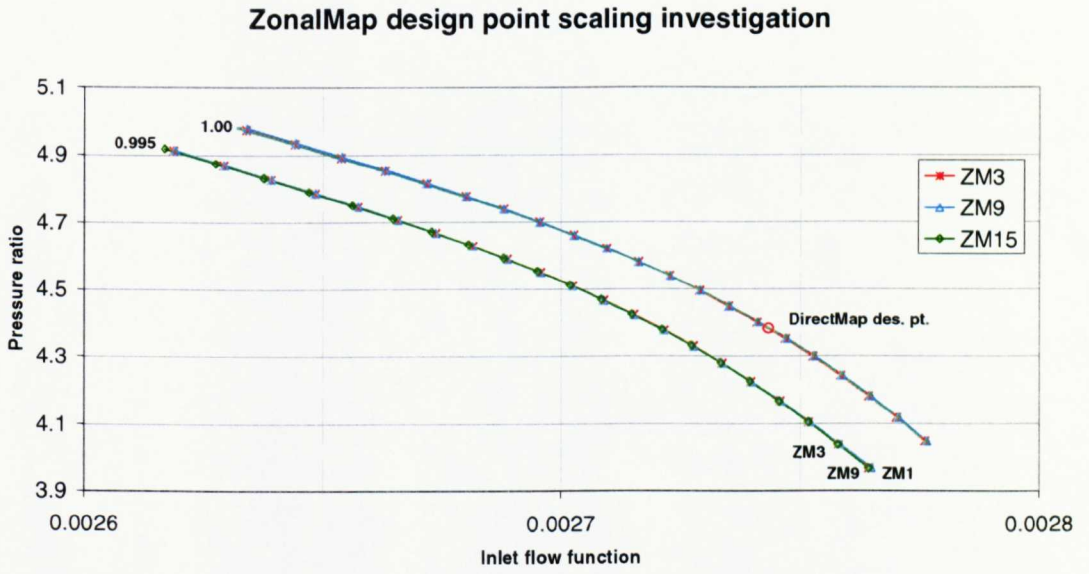

Fig. 4.27 ZonalMap design point scaling investigation (set D): interpolation of design speed with upper speed line of each zone on design speed, speed lines calculated with varying resolutions. (21 point speed lines, straight line join between points).

Table 11 and **Table 12** show the comparison with datum values of scaling factors and performance/fan parameters respectively for ZonalMap set A. **Fig. 4.28** to **Fig. 4.33** show the fan pressure ratio characteristics for ZonalMap set A with the calculated design points compared to datum. **Fig. 4.34** and **Fig. 4.35** show respectively the fan exit total pressure

profiles and the isentropic efficiency profiles for ZonalMap set A compared to datum. The following conclusions can be made:

- The nearest match to the datum DirectMap "correct" answer is with the speed line directly on the operating point to be matched as shown by ZonalMap8. The difference in pressure ratio and efficiency is within ±0.02%. This is most clearly seen from the exit total pressure profiles of **Fig. 4.34** where the best match is between ZM8 and DirectMap. This result gives good confidence that the two different methods have been written to process the SLC program data in the same way.
- Although the 1D isentropic efficiency value of ZM8 is calculated to be nearest to the DM case at -0.016% difference, the difference from DM from the profile (**Fig. 4.35**) is not so distinct from the other cases and indeed, the profile of ZM8 appears to have a higher value at all radii than DM although the 1D value appears lower. The difference between the two calculations that may cause this is the radii for the area averaging method. In the ZonalMap method, the radial positions have been set for all points on all speed lines to be the same as the first point on the first speed line (beta=0) in order to allow interpolation between points in the performance simulation iteration.
- When interpolating for the speed line to calculate the operating point, as shown by the other ZonalMap cases in set A, the magnitude of the difference of the interpolated speed (design speed) from the speed lines of the zone may distort the interpolated speed profiles and therefore cause slight deviations of the speed line. This can be up to ±4.5% of pressure ratio as shown by ZonalMap7. The total pressure profile (**Fig. 4.34**) is the furthest from the datum of set A. **Fig. 4.31** demonstrates the distortion caused by the result of interpolating the 100% speed line from the 97% and 103% speed lines. This diagram also shows the 100% speed line calculated by DirectMap for comparison. This line is clearly longer in the higher speed zone relative to the ZonalMap speed lines. All of these speed lines have been formed by the same subroutines in the code (see section **4.6.2.2**). Therefore, the situation is caused firstly, by the unpredictability of the SLC code in this region that allows a more stable calculation in the higher flow region for particular speed lines, and secondly, by the truncation of the calculation to deal with this instability.

Differences from datum (DirectMap)						
Parameter	**ZM8**	**ZM12**	**ZM11**	**ZM7**	**ZM13**	**ZM14**
Fan						
FanPR	0.016%	-1.488%	-3.473%	-4.351%	-3.497%	-2.078%
HPC						
prhpc_dp	-0.016%	1.488%	3.528%	4.450%	3.552%	2.087%
sf_hpcmf	-0.060%	0.994%	2.481%	3.180%	2.538%	1.501%
sf_hpcpr	-0.016%	1.488%	3.528%	4.450%	3.552%	2.087%
HPT						
dhhpt_dp	-0.121%	0.655%	1.616%	2.070%	1.660%	0.942%
sf_hptnt	0.000%	0.000%	0.000%	0.000%	0.000%	0.000%
sf_hptmf	0.010%	-0.026%	0.022%	0.057%	0.043%	0.055%
sf_hptpr_dh	-0.121%	0.655%	1.616%	2.070%	1.660%	0.942%
LPT						
dhlpt_dp	-0.318%	-0.593%	-1.132%	-1.273%	-1.086%	-0.804%
sf_lptnt	-0.013%	0.067%	0.166%	0.213%	0.171%	0.097%
sf_lptmf	-0.099%	0.567%	1.494%	1.948%	1.556%	0.910%
sf_lptpr_dh	-0.318%	-0.593%	-1.132%	-1.273%	-1.086%	-0.804%
Nozzles						
anhnz	-1.423%	-1.125%	-1.323%	-0.967%	-1.029%	-1.250%
ancnz	-0.058%	1.061%	2.476%	3.125%	2.477%	1.401%

Table 11 ZonalMap (set A) design point comparison of scaling factors with datum.

	Thrust		**Fuel flow**		**SFC**	
	(N)	Diff.	(kg/s)	Diff.	(kg/s/MN)	Diff.
DM	7592.692		0.125500		16.52911	
ZM8	7627.139	0.454%	0.125662	0.129%	16.47562	-0.324%
ZM12	7601.592	0.117%	0.125419	-0.065%	16.49910	-0.182%
ZM11	7583.357	-0.123%	0.125203	-0.237%	16.51028	-0.114%
ZM7	7564.808	-0.367%	0.125073	-0.341%	16.53350	0.027%
ZM13	7575.787	-0.223%	0.125156	-0.274%	16.52053	-0.052%
ZM14	7598.020	0.070%	0.125352	-0.118%	16.49804	-0.188%

	RFAN		**RFAN-inner**		**RFAN-outer**		**ETAFan**	
		Diff.		Diff.		Diff.		Diff.
DM	4.38235		4.39689		4.37093		0.85864	
ZM8	4.38289	0.016%	4.39707	0.005%	4.37110	0.005%	0.85850	-0.016%
ZM12	4.33203	-1.488%	4.34750	-1.454%	4.31916	-1.536%	0.85396	-0.545%
ZM11	4.26486	-3.473%	4.27792	-3.502%	4.25400	-3.469%	0.84915	-1.105%
ZM7	4.23519	-4.351%	4.24660	-4.424%	4.22570	-4.308%	0.84619	-1.450%
ZM13	4.26407	-3.497%	4.27618	-3.553%	4.25399	-3.469%	0.84870	-1.157%
ZM14	4.31206	-2.078%	4.32391	-2.148%	4.30220	-2.039%	0.85299	-0.658%

Table 12 ZonalMap (set A) design point comparison of performance and fan parameters with datum.

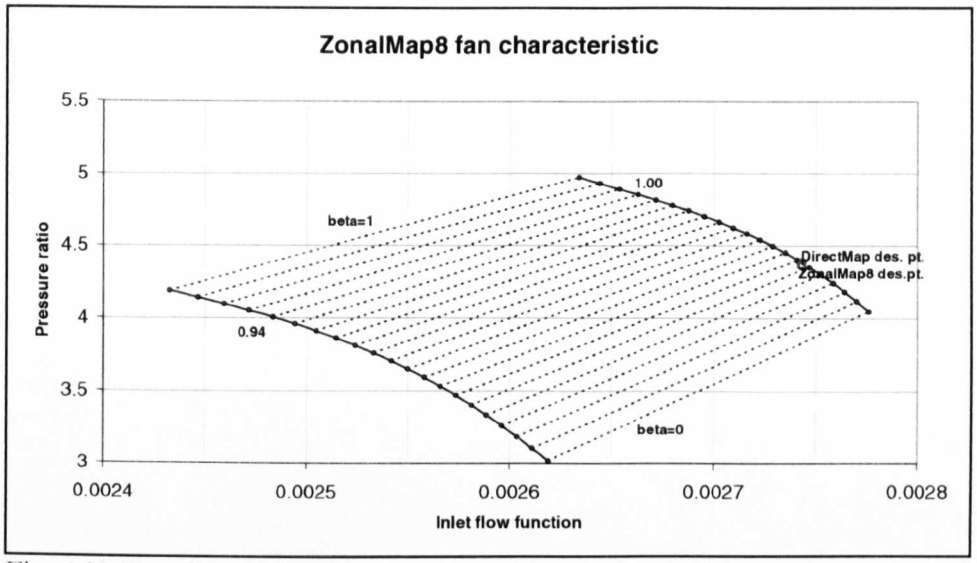

Fig. 4.28 ZonalMap8 fan characteristic with calculated design point compared to datum.

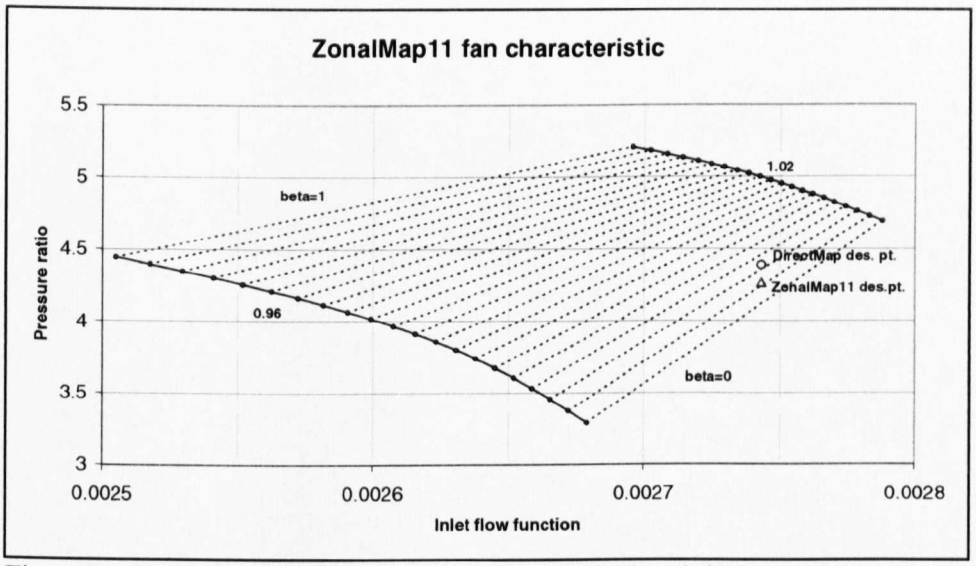

Fig. 4.29 ZonalMap11 fan characteristic with calculated design point compared to datum.

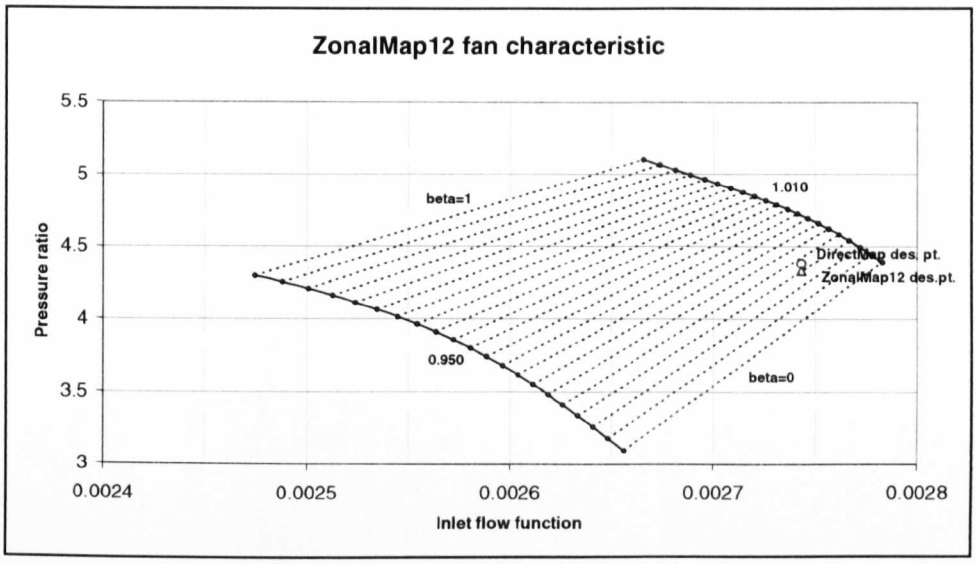

Fig. 4.30 ZonalMap12 fan characteristic with calculated design point compared to datum.

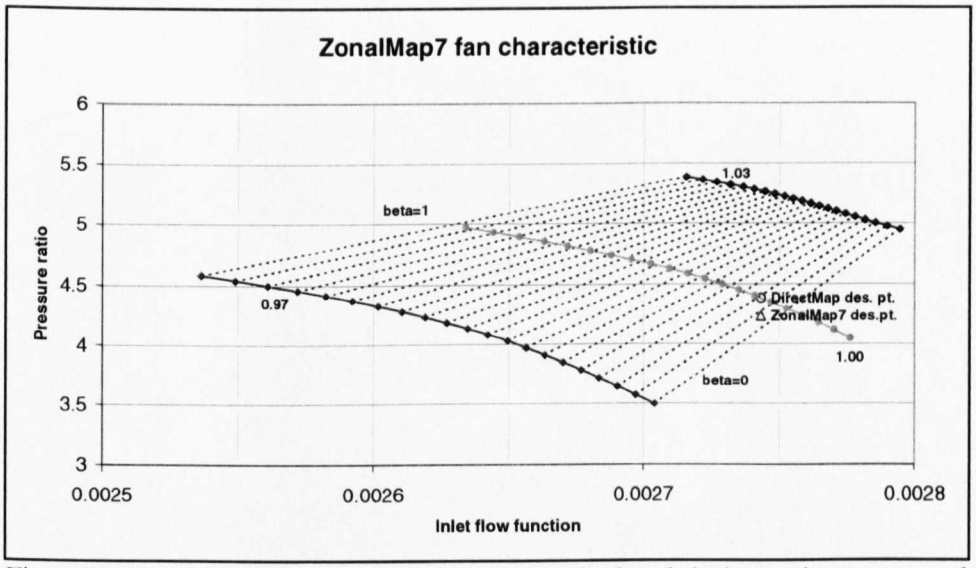

Fig. 4.31 ZonalMap7 fan characteristic with calculated design point compared to datum.

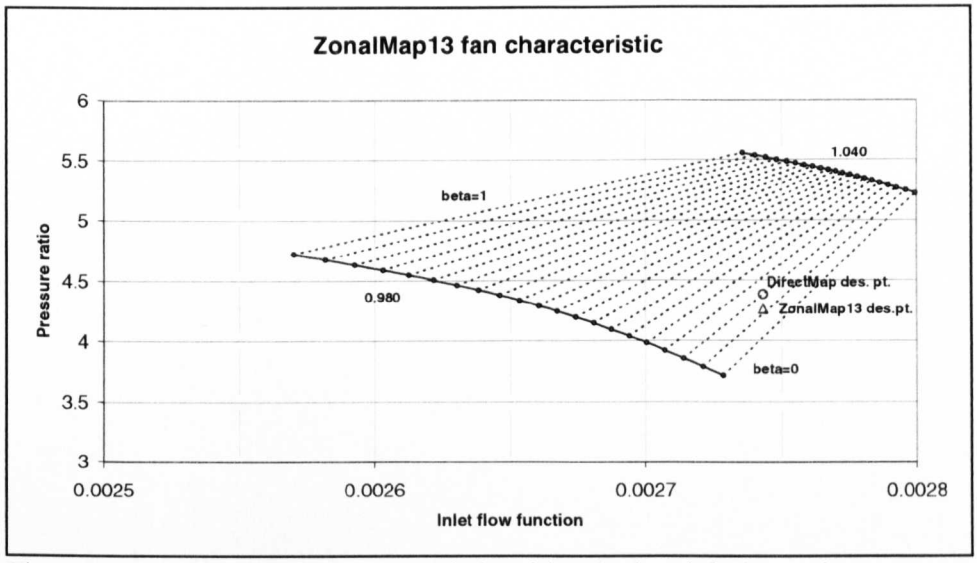

Fig. 4.32 ZonalMap13 fan characteristic with calculated design point compared to datum.

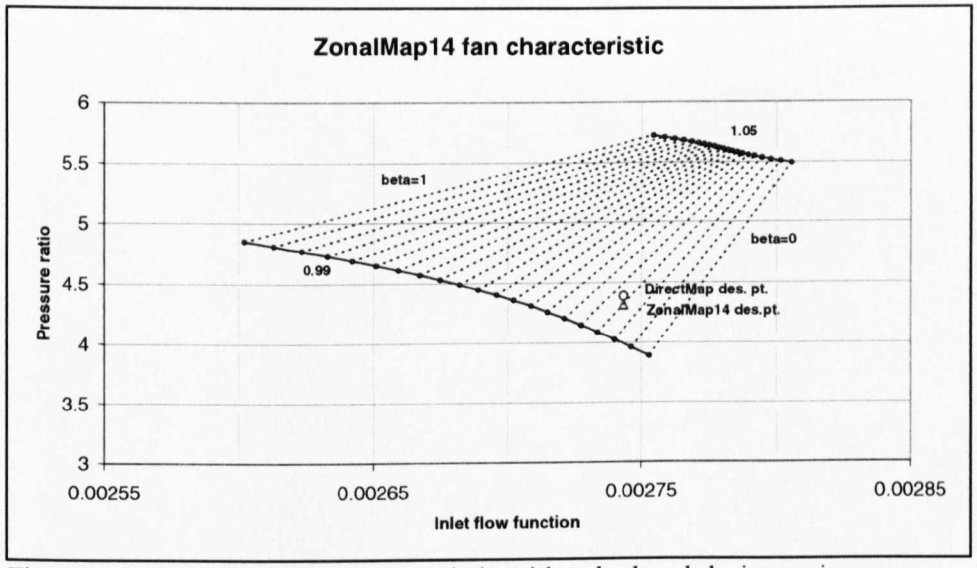

Fig. 4.33 ZonalMap14 fan characteristic with calculated design point compared to datum.

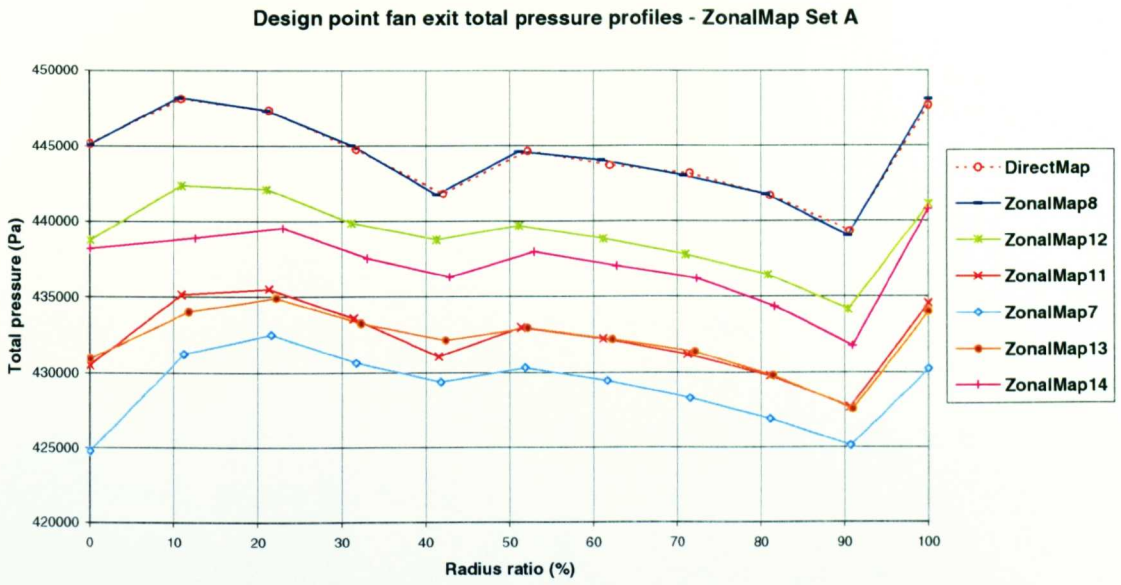

Fig. 4.34 ZonalMap (set A) design point fan exit total pressure profiles compared with datum (DirectMap).

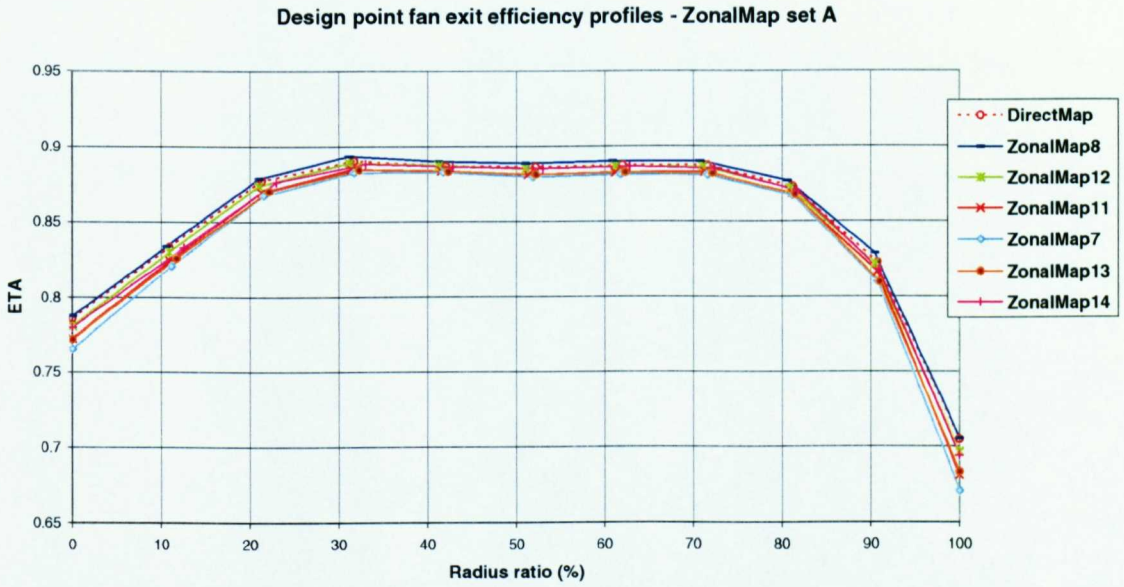

Fig. 4.35 ZonalMap (set A) design point fan isentropic efficiency profiles compared with datum (DirectMap).

- The application of a fixed delta for truncation in the undistorted flow map will remove a larger part of the speed line as the speed line becomes more vertical in the high flow regions, this tending to be the case at the higher speed lines. This gives more scope for distorting an interpolation and can be clearly seen in **Fig. 4.32** and **Fig. 4.33** for ZonalMap13 and ZonalMap14 respectively. In particular, these two cases converge at

design point with flatter total pressure profiles towards the hub as shown by **Fig. 4.34**. It is therefore recommended that future versions of the program should have the artificial stall and choke check feature activated, and efforts should be made to improve modelling of stall and choke in SLC programs.

- Fan parameters have been examined because it is effectively the modelling of this is the only difference in all the comparisons. It is noted that although ZM8 is the nearest to the datum, the other methods, although worse in terms of replicating the datum fan performance, are often nearer to the datum performance parameters (**Table 12**). This shows how certain changes can compensate for others when considering comparison of performance parameters with the small levels of differences of fan performance being considered.
- The design fan beta value decreases due to the distortion of the zone by the truncated higher speed lines as the difference between the speed lines become larger. This is clear from ZonalMap7 (**Fig. 4.31**), where the value of beta is 0.0513. It was found that increasing the size of the difference between the two speeds with the design speed in the middle eventually led to beta dropping below zero and the program was unable to converge. It is therefore recommended not to allow the difference in speeds in a zone to be set below a magnitude of 5% design speed.

Table 13 and **Table 14** show respectively the ZonalMap data set B scaling factor and performance/fan parameter comparisons with DirectMap datum. The following are the findings:

- As expected, the result of the ZonalMap fan design operating point improves towards the datum DirectMap value as the width of the zone decreases, with the design speed directly in the middle of the zone. This can be clearly seen from the fan exit total pressure profiles in **Fig. 4.41**. There is very little difference between ZM5, ZM4 and ZM1 (±0.1%, ±0.3%, and ±0.5% speed zones respectively). The ZM4 (±0.3%) fan pressure ratio being less than 0.01% of datum is probably fortunate as the ZM5 difference is larger.

Differences from datum (DirectMap)						
Parameter	**ZM5**	**ZM4**	**ZM1**	**ZM6**	**ZM10**	**ZM7**
Fan						
FanPR	0.094%	0.008%	-0.128%	-0.331%	-1.036%	-4.351%
HPC						
prhpc_dp	-0.093%	-0.008%	0.127%	0.328%	1.032%	4.450%
sf_hpcmf	-0.118%	-0.077%	0.030%	0.178%	0.678%	3.180%
sf_hpcpr	-0.093%	-0.008%	0.127%	0.328%	1.032%	4.450%
HPT						
dhhpt_dp	-0.148%	-0.104%	-0.047%	0.047%	0.402%	2.070%
sf_hptnt	0.000%	0.000%	0.000%	0.000%	0.000%	0.000%
sf_hptmf	0.001%	-0.019%	-0.004%	0.004%	-0.002%	0.057%
sf_hptpr_dh	-0.148%	-0.104%	-0.047%	0.047%	0.402%	2.070%
LPT						
dhlpt_dp	-0.295%	-0.328%	-0.370%	-0.422%	-0.595%	-1.273%
sf_lptnt	-0.015%	-0.011%	-0.005%	0.005%	0.041%	0.213%
sf_lptmf	-0.132%	-0.113%	-0.046%	0.046%	0.361%	1.948%
sf_lptpr_dh	-0.295%	-0.328%	-0.370%	-0.422%	-0.595%	-1.273%
Nozzles						
anhnz	-1.403%	-1.485%	-1.510%	-1.522%	-1.546%	-0.967%
ancnz	-0.111%	-0.037%	0.048%	0.187%	0.690%	3.125%

Table 13 ZonalMap (set B) design point comparison of scaling factors with datum.

	Thrust		**Fuel flow**		**SFC**	
	(N)	Diff.	(kg/s)	Diff.	(kg/s/MN)	Diff.
DM	7592.692		0.125500		16.52911	
ZM5	7627.158	0.454%	0.125655	0.123%	16.47469	-0.329%
ZM4	7627.746	0.462%	0.125643	0.113%	16.47178	-0.347%
ZM1	7627.113	0.453%	0.125638	0.110%	16.47253	-0.342%
ZM6	7625.272	0.429%	0.125620	0.095%	16.47417	-0.332%
ZM10	7617.206	0.323%	0.125519	0.015%	16.47833	-0.307%
ZM7	7564.808	-0.367%	0.125073	-0.341%	16.53350	0.027%

	RFAN		**RFAN-inner**		**RFAN-outer**		**ETAFan**	
		Diff.		Diff.		Diff.		Diff.
DM	4.38235		4.39689		4.37093		0.85864	
ZM5	4.38554	0.094%	4.40013	0.095%	4.37341	0.074%	0.85869	0.006%
ZM4	4.38261	0.008%	4.39807	0.035%	4.36976	-0.035%	0.85858	-0.007%
ZM1	4.37801	-0.128%	4.39279	-0.121%	4.36572	-0.154%	0.85829	-0.041%
ZM6	4.37115	-0.331%	4.38554	-0.334%	4.35919	-0.348%	0.85779	-0.099%
ZM10	4.34732	-1.036%	4.36184	-1.032%	4.33525	-1.058%	0.85603	-0.304%
ZM7	4.23519	-4.351%	4.24660	-4.424%	4.22570	-4.308%	0.84619	-1.450%

Table 14 ZonalMap (set B) design point comparison of performance and fan parameters with datum.

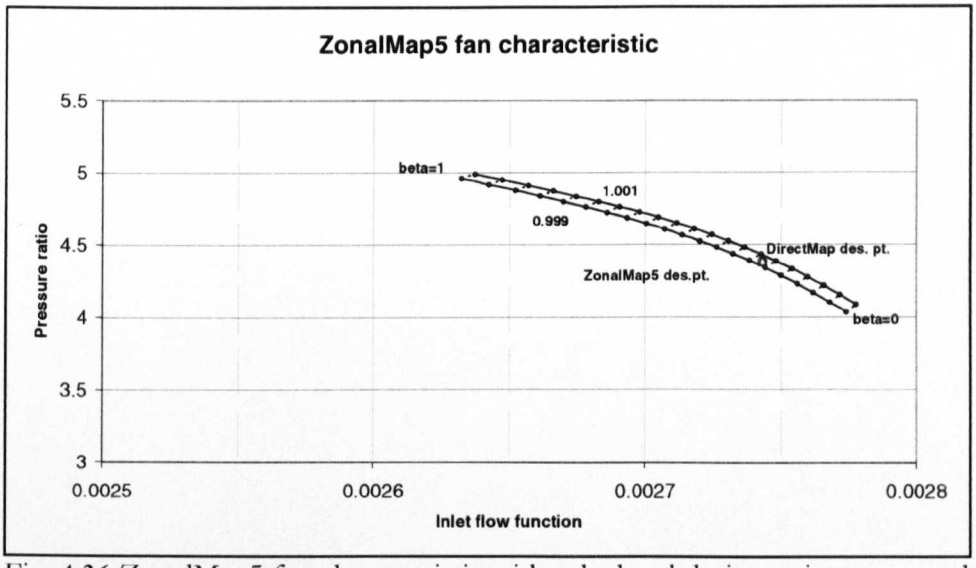

Fig. 4.36 ZonalMap5 fan characteristic with calculated design point compared to datum.

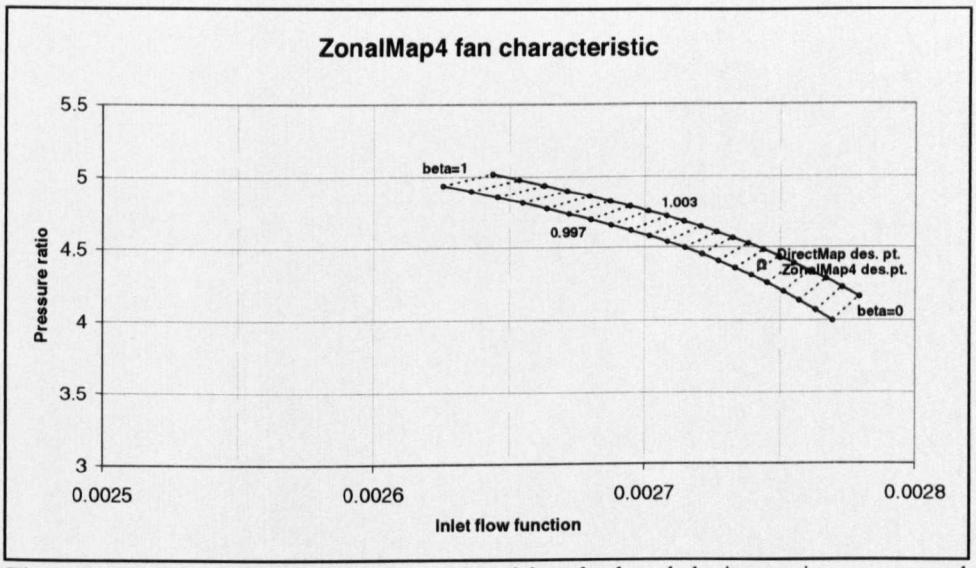

Fig. 4.37 ZonalMap4 fan characteristic with calculated design point compared to datum.

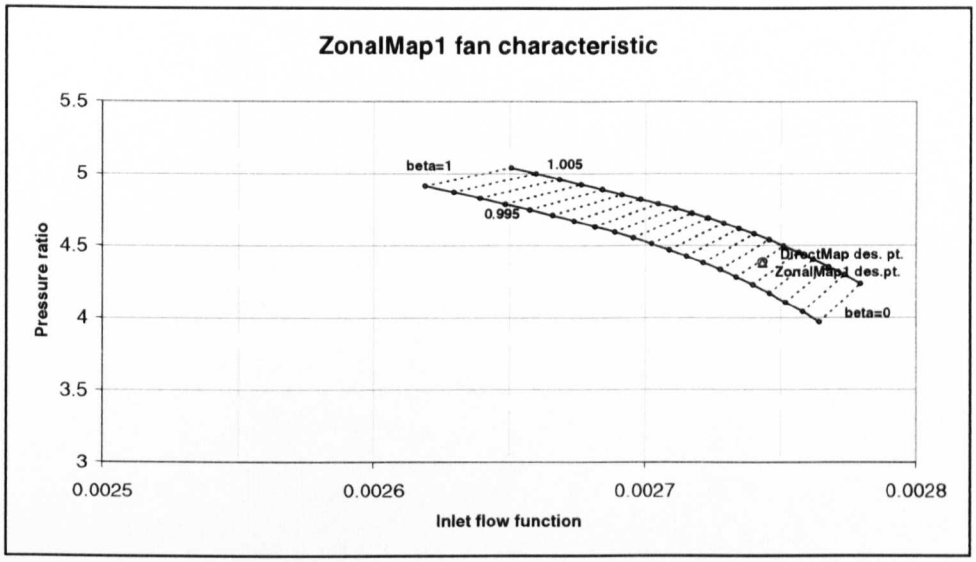

Fig. 4.38 ZonalMap1 fan characteristic with calculated design point compared to datum.

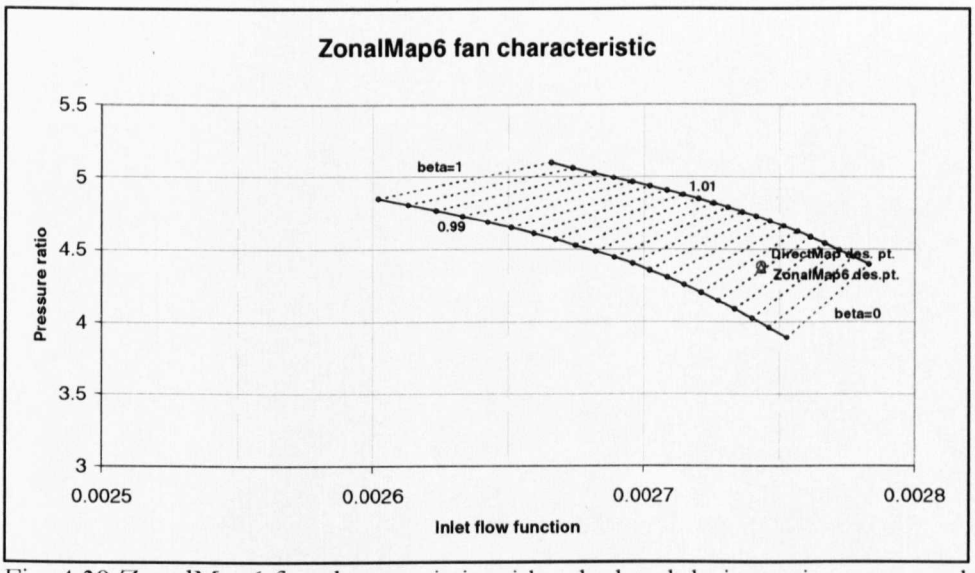

Fig. 4.39 ZonalMap6 fan characteristic with calculated design point compared to datum.

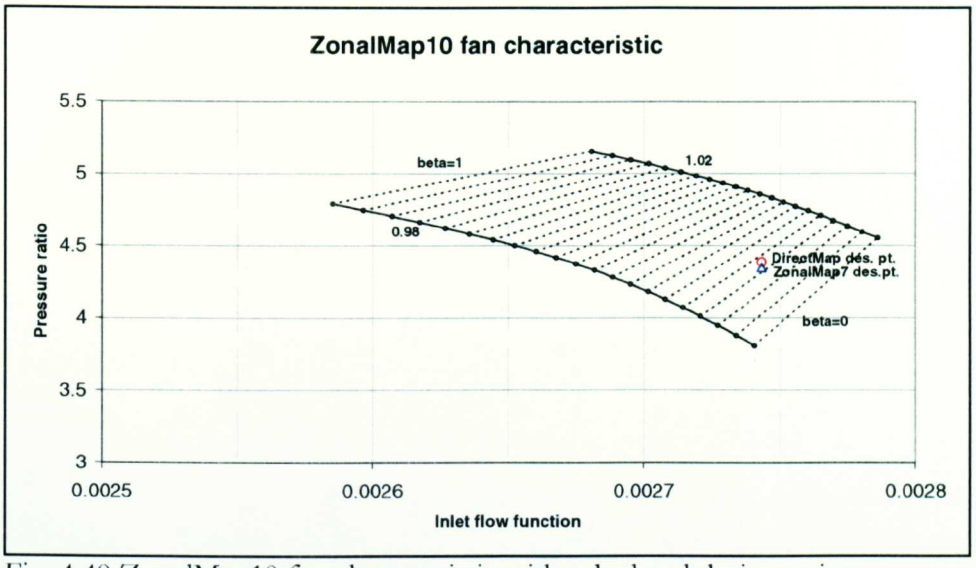

Fig. 4.40 ZonalMap10 fan characteristic with calculated design point compared to datum.

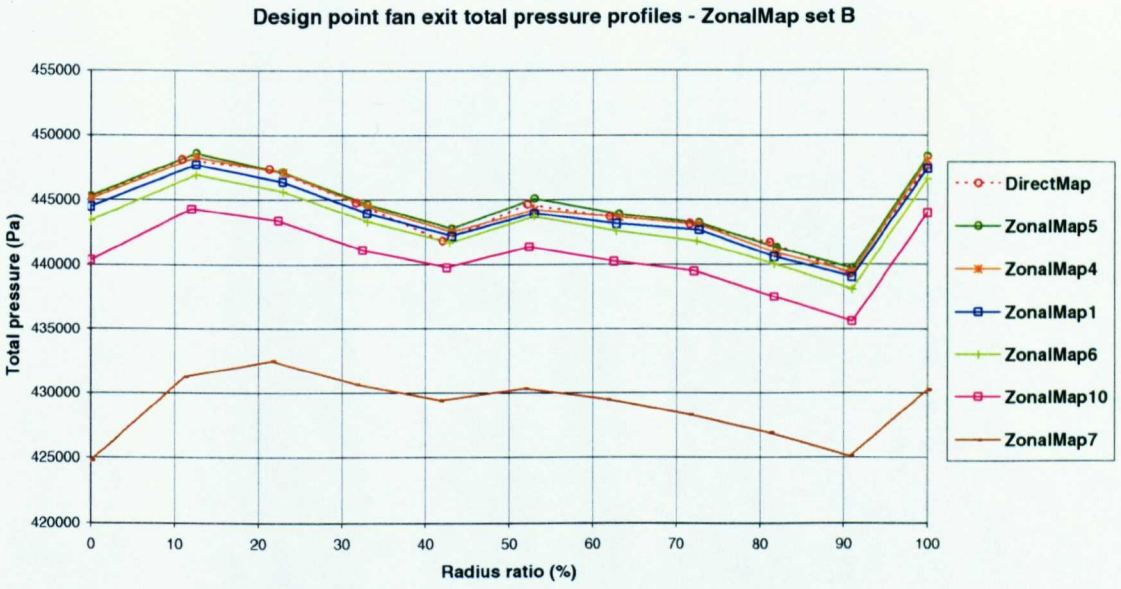

Fig. 4.41 ZonalMap (set B) design point fan exit total pressure profiles compared with datum (DirectMap).

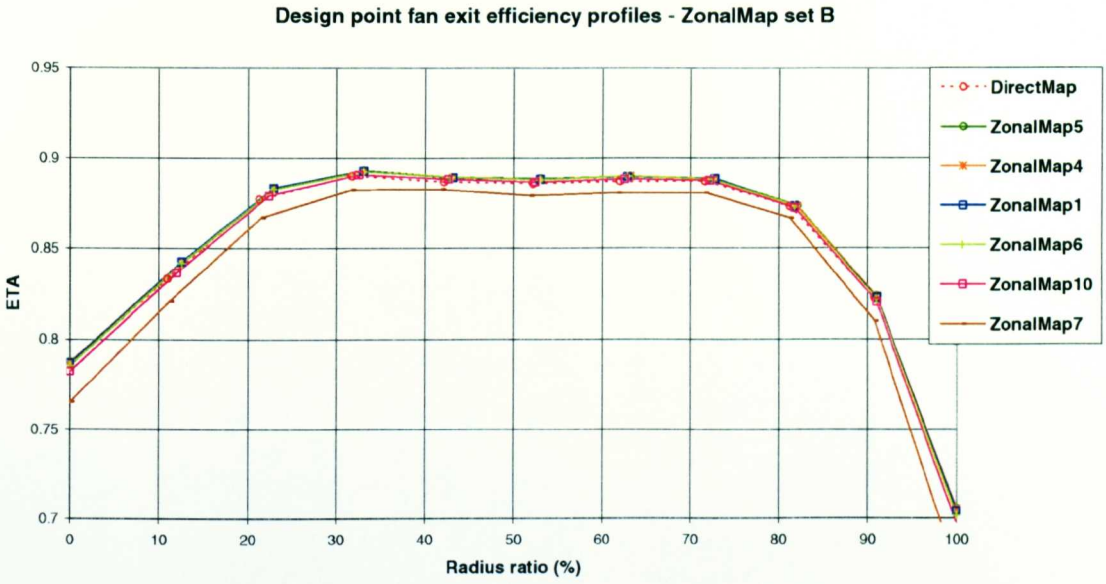

Fig. 4.42 ZonalMap (set B) design point fan isentropic efficiency profiles compared with datum (DirectMap).

- The zones up to ±1% give sufficiently accurate fan design point results. The zones larger than this (ZM10, ZM7) are distorted by the truncated upper speed line as described above.
- The recommendation is therefore to take the largest acceptable zone in order to best compromise the need for accuracy and for having fast computation. The smaller the zone, the more that new speed lines need to be guessed and computed by the SLC program, for example when drawing a working line. It is recommended to adopt the ±0.5% speed line zone (ZM1) as standard in this work bearing in mind that the artificial stall/choke detector is not activated.

Table 15 and **Table 16** contain respectively the scale factors and performance parameter comparisons with datum for both ZonalMap sets C and D.

- Set C confirms the correct operation of the interpolation procedure, where the speed line nearest to the operating point has the dominant contribution to the profiles computed (**Fig. 4.47** and **Fig. 4.48**). There is no significant difference between ZM2 and ZM3, with the profiles contributed completely by the 100% speed line (**Fig. 4.43** and **Fig. 4.44**).
- Set D examines the effect of a higher resolution calculation of the speed lines by the SLC code. **Fig. 4.27** shows the first finding that although the three setups using 0.05,

0.15 and 0.30 kg/s increments of mass flow were used (ZM9, ZM3, ZM15 respectively), there is no perceptible difference in the position of the speed lines (this graph shows points joined-up with straight lines).

Differences from datum (DirectMap)						
Parameter	**ZM2**	**ZM3**			**ZM9**	**ZM15**
Fan						
FanPR	0.007%	0.008%			0.101%	0.078%
HPC						
prhpc_dp	-0.007%	-0.008%			-0.100%	-0.077%
sf_hpcmf	-0.046%	-0.047%			-0.136%	-0.084%
sf_hpcpr	-0.007%	-0.008%			-0.100%	-0.077%
HPT						
dhhpt_dp	-0.116%	-0.116%			-0.174%	-0.095%
sf_hptmf	0.000%	0.000%			0.000%	0.000%
sf_hptmf	0.017%	0.017%			0.000%	0.000%
sf_hptpr_dh	-0.116%	-0.116%			-0.174%	-0.095%
LPT						
dhlpt_dp	-0.338%	-0.337%			-0.341%	-0.165%
sf_lptnt	-0.012%	-0.012%			-0.018%	-0.010%
sf_lptmf	-0.088%	-0.089%			-0.157%	-0.085%
sf_lptpr_dh	-0.338%	-0.337%			-0.341%	-0.165%
Nozzles						
anhnz	-1.476%	-1.475%			-1.623%	-0.814%
ancnz	-0.064%	-0.064%			-0.119%	-0.075%

Table 15 ZonalMap set C (ZM2, ZM3) and set D (ZM9, ZM3, ZM15) design point comparison of scaling factors with datum.

	Thrust		**Fuel flow**		**SFC**	
	(N)	Diff.	(kg/s)	Diff.	(kg/s/MN)	Diff.
DM	7592.692		0.125500		16.52911	
ZM2	7628.201	0.468%	0.125660	0.127%	16.47308	-0.339%
ZM3	7628.182	0.467%	0.125660	0.127%	16.47308	-0.339%
ZM9	7632.764	0.528%	0.125688	0.149%	16.46684	-0.377%
ZM15	7612.715	0.264%	0.125590	0.071%	16.49739	-0.192%

	RFAN		**RFAN-inner**		**RFAN-outer**		**ETAFan**	
		Diff.		Diff.		Diff.		Diff.
DM	4.38235		4.39689		4.37093		0.85864	
ZM2	4.38258	0.007%	4.39645	-0.013%	4.37104	0.003%	0.85863	-0.001%
ZM3	4.38262	0.008%	4.39651	-0.011%	4.37107	0.004%	0.85863	-0.001%
ZM9	4.38578	0.101%	4.40045	0.105%	4.37358	0.079%	0.85907	0.050%
ZM15	4.38498	0.078%	4.39957	0.079%	4.37285	0.057%	0.85758	-0.123%

Table 16 ZonalMap set C (ZM2, ZM3) and set D (ZM9, ZM3, ZM15) design point comparison of performance and fan parameters with datum.

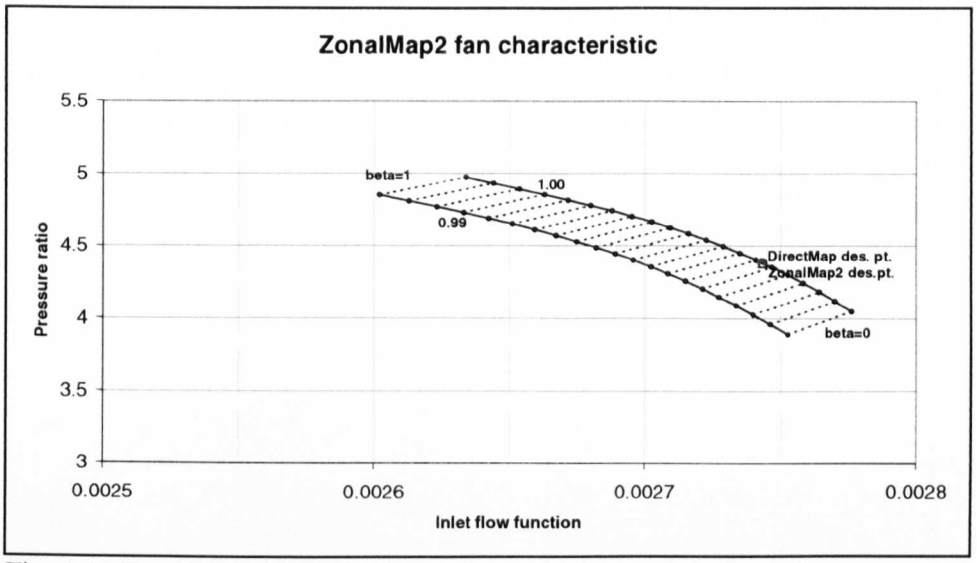

Fig. 4.43 ZonalMap2 fan characteristic with calculated design point compared to datum.

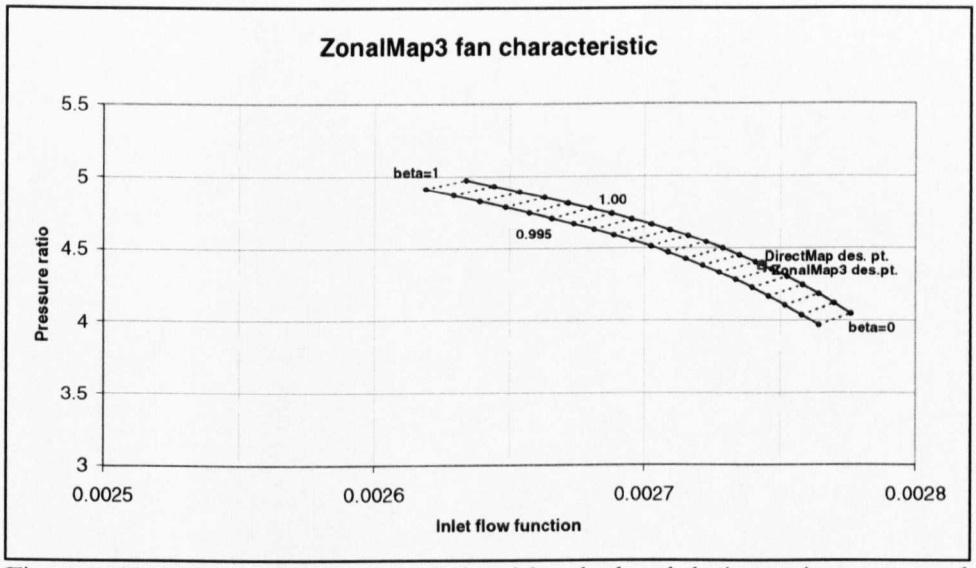

Fig. 4.44 ZonalMap3 fan characteristic with calculated design point compared to datum.

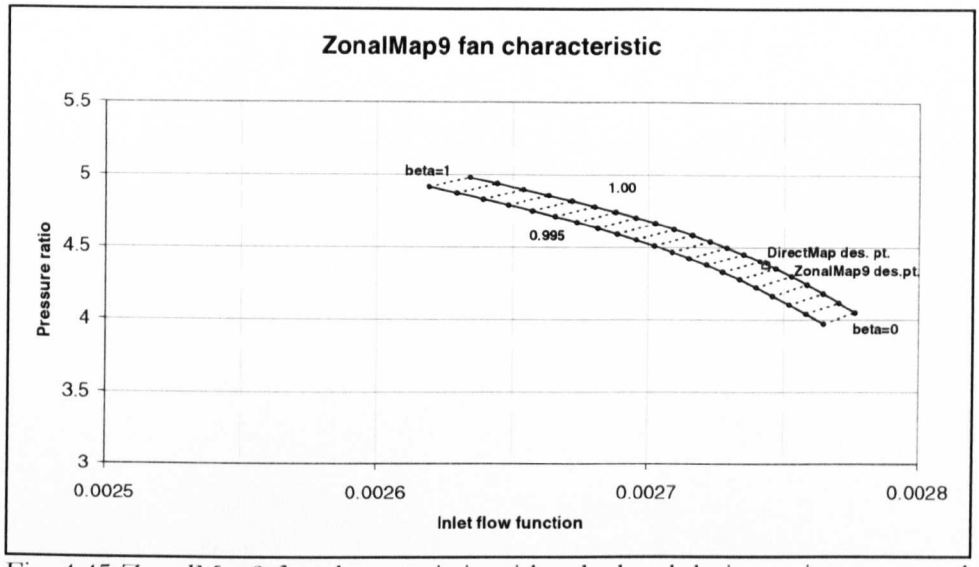

Fig. 4.45 ZonalMap9 fan characteristic with calculated design point compared to datum.

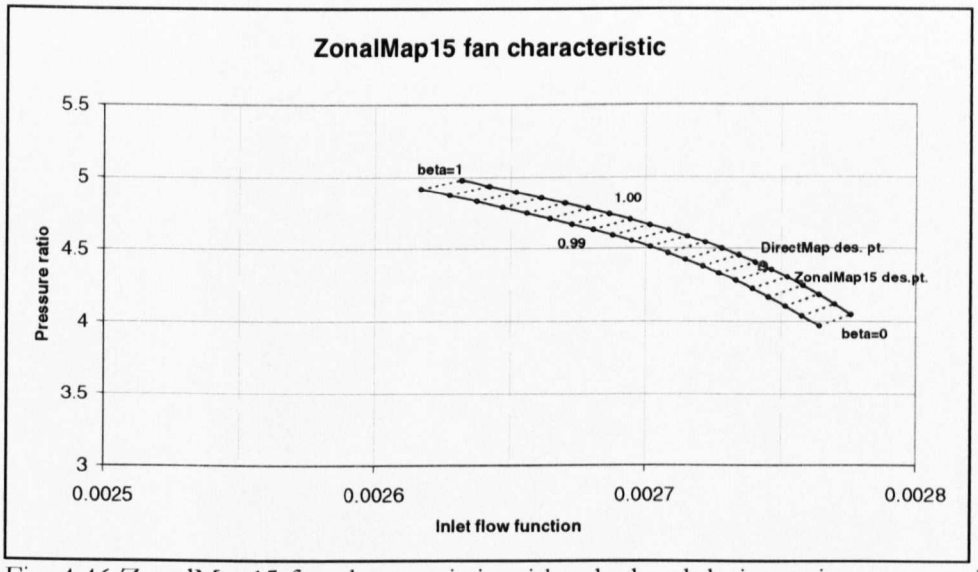

Fig. 4.46 ZonalMap15 fan characteristic with calculated design point compared to datum.

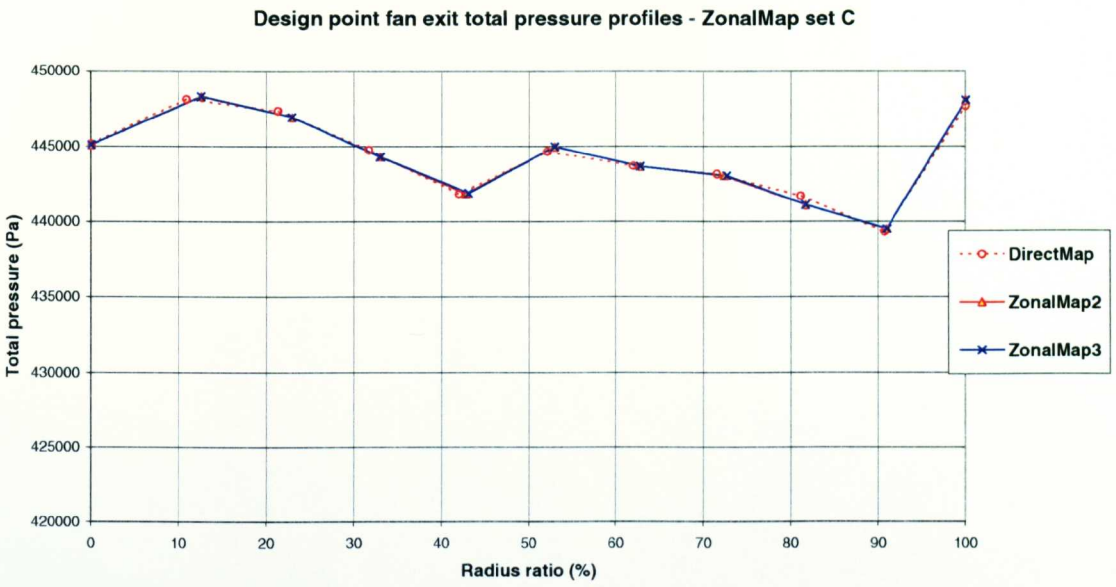

Fig. 4.47 ZonalMap (set C) design point fan exit total pressure profiles compared with datum (DirectMap).

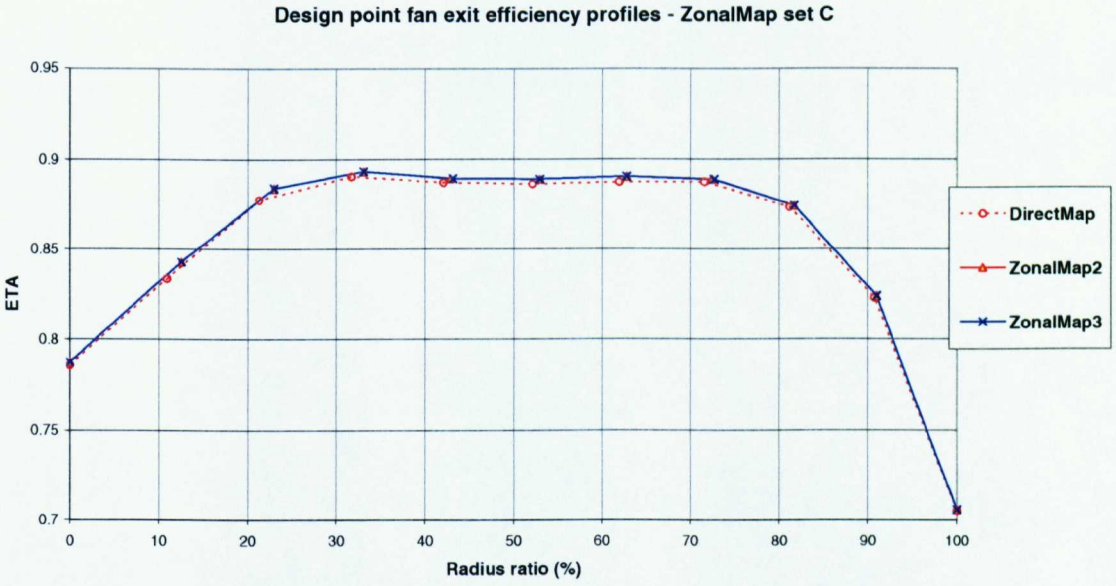

Fig. 4.48 ZonalMap (set C) design point fan isentropic efficiency profiles compared with datum (DirectMap).

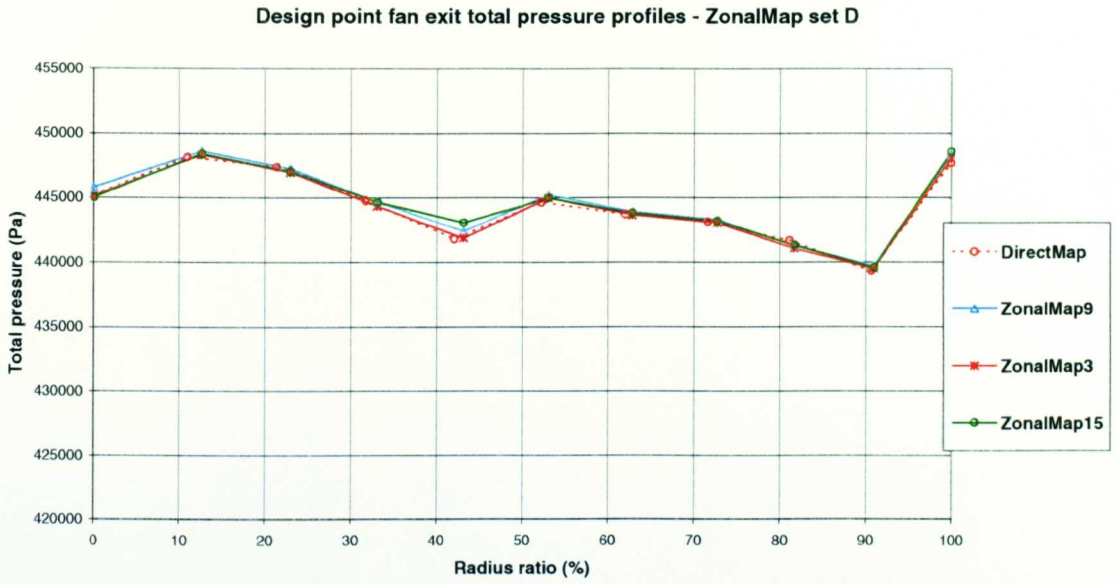

Fig. 4.49 ZonalMap (set D) design point fan exit total pressure profiles compared with datum (DirectMap).

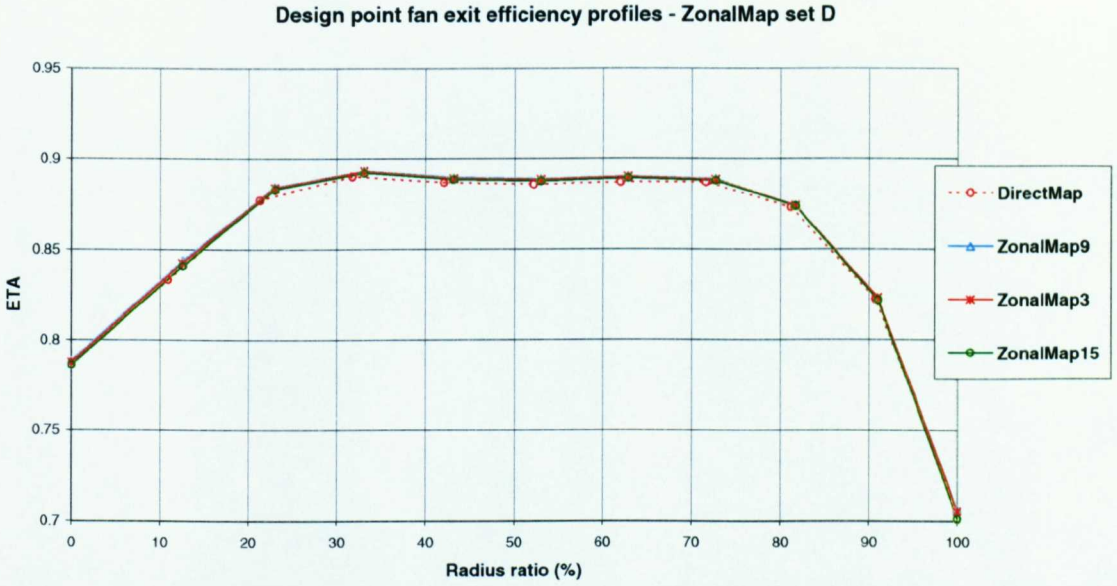

Fig. 4.50 ZonalMap (set D) design point fan isentropic efficiency profiles compared with datum (DirectMap).

4.7.2 Conclusions from uniform inlet design point studies

- Differences in calculating the fan operating point between the chosen ZonalMap method (ZM1), WholeMap and DirectMap method are sufficiently small to be able to say the differences are due to the ZonalMap and WholeMap methods being based on interpolation between speed lines and between beta lines compared to direct calculation.

- In order to compare the three engine models containing the different fan models, they must all be modelling exactly the same engine except for the differences in the fan module. Therefore, the engine models should run the same input scaling factor file as the method which will be taken to be the datum one for comparison, namely the DirectMap method.
- With almost the same fan operating point, the DirectMap difference in performance is generally about 0.5% difference in thrust from the ZonalMap cases. This is despite a similar isentropic efficiency and the same mass flow. The difference may be explained by differences in the 2D fan exit profiles, but may also be due to differences in the calculation methods between DirectMap and the other 2 fan models. This should be carefully checked again.
- The design point studies have given an idea of the small differences between the 3 fan models. For the off-design computations comparing the 3 models, the same scaling factors must be used so that the engine can be compared with the only differences being the fan models. The DirectMap set of scaling factors will be used.

4.7.3 Achieving performance program convergence with SLC fan models

The separate-exhaust turbofan performance simulation code was explained in section **3.6**. The model used with the SLC fan combinations is that of the repaired iteration procedure to remove the divergence in guess of fan beta as described in section **3.6.2**. The following sections describe further changes that were needed to ensure that all of the engine models with the different fan models were functioning.

4.7.3.1 DirectMap convergence findings

When DirectMap was first tested, it was found to have divergent iteration to infinity for the guess of fan beta and the check of HPC inlet flow function compared to fan core exit flow function. The iteration scheme is shown in **Appendix 5** (updated version). **Table 17** shows the list of guesses and checks for the performance simulation along with the tolerances set for the checks as used in the performance code with the conventional fan characteristic and 2D-fan codes (including WholeMap and ZonalMap fan models).

An analysis was made of the computations by the Newton-Raphson solver (subroutine ITER) leading up to the divergence. **Table 17** shows the normal original 2D fan

performance program simulation convergence tolerances. This shall henceforth be termed "DatumTol". **Table 18** shows the simulation attempt at a TET of 1299K, using on the check of HPC inlet flow function (check DQ30, defined in **Table 17**). The initial and final iterations are shown. The solver operates as intended, and gradually converges to higher decimal places of FanBta. The fan inlet flow function is interpolated from FanBta, and the mass flow then obtained using the averaged inlet total pressure profile and total temperature. This mass flow is input into the SLC to compute the fan exit profiles and fan performance. It can be seen that the SLC output in the final two completed iterations; no. 32 and 33 give the same fan performance (e.g. Q29H) and therefore the same check value (DQ30), although the input mass flow is different. This leads the next guess of FanBta diverging to infinity.

A detailed investigation of the SLC code was necessary. It was known that the program had been written in single precision Fortran 77 code, probably due to the limited computational resources at the time. Generally, single precision preserves about 7 decimal places whereas double precision preserves about 14 decimal places.

However, the SLC code was also written to be an engineering student teaching tool and it stores intermediate data to enable restart capability. This may also be due to a lack of available RAM at the time as the program transfers data between subroutines at various stages of the SLC iteration by these data files. Unfortunately, very few decimal places were kept of all parameters in these data files, usually only 4. It was apparent that the SLC code in its present form was unable to output a change in computed fan performance beyond 6 decimal places of mass flow (kg/s) at a rotational speed as apparent from **Table 18**.

To enable convergence of the guess of FanBta and check of DQ30, it was necessary to relax the tolerance on the check from $DQ30<10^{-7}$ to $DQ30<50x10^{-5}$. This enables convergence at the 6^{th} decimal place of the fan mass flow.

From **Appendix 5** and **Table 17**, it can be seen that the guess no.1 of RPMFAN occurs before the guess no.2 of FanBta and is checked by the power balance on the LP shaft in the form of DWKLP. The value of RPMFAN accepted by the SLC program is also limited to single precision. It was found that the tolerance on DWKLP was also required to be relaxed in order to achieve convergence in this check. This guess and check is shown in **Table 19** for the calculation with handle TET=1299K and using a tolerance of 10^{-8} on DWKLP. It can be seen that the minimum value of DWKLP in this case is about $5x10^{-7}$ and in fact, is unable to fall below 10^{-7}.

Table 17 Tolerances on checks for serial iteration scheme of separate-exhaust 2-shaft turbofan simulation.

Guess No.	Guess	Check	Checked parameter	Normal check tolerance - DatumTol (WholeMap, ZonalMap)	Adjusted check tolerance - DMTol (for DirectMap)
1	RPMFAN	FANPOWER= LPTPOWER	**DWKLP** = (LPTPOWER - FANPOWER)/ (LPTPOWER + FANPOWER)	$<10^{-8}$	$<50x10^{-5}$
2	BETAFAN	Q29H=Q30HPC	**DQ30** = (Q29H - Q30HPC)/ (Q29H + Q30HPC)	$<10^{-7}$	$<50x10^{-5}$
3	BPR	Q29F=QCNZ	**DQ90** = (Q29F – Q90CNZ)/ (Q29F + Q90CNZ)	$<10^{-7}$	unchanged
4	RPMHPC	HPCPOWER= HPTPOWER	**DWKHP** = (HPCPOWER - HPTPOWER)/ (HPCPOWER + HPTPOWER)	$<10^{-8}$	unchanged
5	BETAHPC	Q50CC=Q50HPT	**DQ50** = (Q50CC - Q50HPT)/ (Q50CC + Q50HPT)	$<10^{-4}$	unchanged
6	DH/T(HPT)	Q60HPT=Q60LPT	**DQ60** = (Q60HPT - Q60LPT)/ (Q60HPT + Q60LPT)	$<10^{-5}$	unchanged
7	DH/T(LPT)	Q70LPT=Q70HNZ	**DQ70** = (Q70LPT - Q70HNZ)/ (Q70LPT + Q70HNZ)	$<10^{-5}$	unchanged

Itera -tion no.	FanBta	Fan inlet flow function	Fan mass flow	Q29H	Q30HPC	Q29H-Q30HPC	DQ30	New guess FanBta
1	0.280315082	0.0027432988606	16.37496663	3.5957127E-04	3.5854610E-04	0.0000010252	0.00142758	0.283118232
2	0.283118232	0.0027429693010	16.37299946	3.5932448E-04	3.5855431E-04	0.0000007702	0.00107283	0.291595470
3	0.291595470	0.0027419726528	16.36705039	3.5749131E-04	3.5844024E-04	-0.0000009489	-0.00132545	0.286910389
4	0.286910389	0.0027425234664	16.37033824	3.5857822E-04	3.5850931E-04	0.0000000689	0.00009609	0.287227091
↓	↓	↓	↓	↓	↓	↓	↓	↓
↓	↓	↓	↓	↓	↓	↓	↓	↓
29	0.287021791	0.0027425103691	16.37026006	3.5830299E-04	3.5848678E-04	-0.000000184	-0.00025640	0.287163717
30	0.287163717	0.0027424936832	16.37016046	3.5851029E-04	3.5850601E-04	0.000000004	0.00000597	0.287160489
31	0.287160489	0.0027424940627	16.37016273	3.5834856E-04	3.5849598E-04	-0.000000147	-0.00020565	0.287163626
32	0.287163626	0.0027424936939	16.37016052	3.5851029E-04	3.5850601E-04	0.000000004	0.00000597	0.287163537
33	0.287163537	0.0027424937043	16.37016059	3.5851029E-04	3.5850601E-04	0.000000004	0.00000597	NaN
34	NaN	NaN	NaN					

Table 18 DirectMap calculation of Engine1 TET=1299K, failure after 33 iterations of FanBta: Newton-Raphson solver fan beta guess and check parameters for check on HPC inlet flow function (DQ30 tolerance $<10^{-7}$)

I11CHEC	RPMFAN	DWKLP	DWKLPO	WKFAN	WKLPT	(WKLPT-WKFAN)	RPMFAN New guess
1	21892.0000	-4.9592269153E-04	-4.9592269153E-04	2907163.01488380	2904280.98793226	-2882.026952	
2	21673.0800	8.9338432805E-03	8.9338432805E-03	2810717.75871753	2861391.49384971	50673.735132	21880.4867
3	21880.4867	8.8222855322E-05	8.8222855322E-05	2902481.54602937	2902993.72163399	512.175605	21882.5553
4	21882.5553	-2.5335261250E-05	-2.5335261250E-05	2903251.36287633	2903104.25733978	-147.105537	21882.0938
5	21882.0938	-2.4166887970E-04	-2.4166887970E-04	2903063.19681144	2901660.37576870	-1402.821043	21882.6094
6	21882.6094	-5.0263613451E-05	-5.0263613451E-05	2903137.67387877	2902845.84416751	-291.829711	21882.7448
7	21882.7448	2.8828066901E-05	2.8828066901E-05	2904164.85288747	2904332.30063201	167.447745	21882.6954
8	21882.6954	1.7760326442E-05	1.7760326442E-05	2903371.78151843	2903474.91301133	103.131493	21882.6162
9	21882.6162	-2.6443824126E-05	-2.6443824126E-05	2903200.32301186	2903046.78363454	-153.539377	21882.6636
49	21881.7211	-6.0318973329E-06	-6.0318973329E-06	2903358.85489243	2903323.82957863	-35.025314	21881.7251
50	21881.7251	2.6898137000E-05	2.6898137000E-05	2903265.41082922	2903421.59989195	156.189063	21881.7219
51	21881.7219	-1.2086968462E-04	-1.2086968462E-04	2903314.69666304	2902612.93602114	-701.760642	21881.7245
52	21881.7245	2.8954154450E-06	2.8954154450E-06	2902502.02692226	2902518.83486932	16.807947	21881.7245
53	21881.7245	2.8944233962E-06	2.8944233962E-06	2902502.02692226	2902518.82911044	16.802188	21881.5434
54	21881.5434	-4.9122115232E-07	-4.9122115232E-07	2902608.51121389	2902605.65956989	-2.851644	21881.5697
55	21881.5697	-3.9076303484E-06	-3.9076303484E-06	2903618.95243395	2903596.25998355	-22.692450	21881.5396
56	21881.5396	-3.8605700013E-05	-3.8605700013E-05	2902720.99875934	2902496.88425924	-224.114500	21881.5731
57	21881.5731	-4.8016069113E-05	-4.8016069113E-05	2902417.02204682	2902138.31011682	-278.711930	21881.4025
58	21881.4025	7.1931402754E-05	7.1931402754E-05	2903085.53131829	2903503.20739148	417.676073	21881.5048
59	21881.5048	-1.8177879723E-05	-1.8177879723E-05	2902571.46053898	2902465.93726738	-105.523272	21881.4841
60	21881.4841	-4.6751269382E-05	-4.6751269382E-05	2902399.90394234	2902128.53486966	-271.369073	21881.5179
61	21881.5179	4.2116911057E-06	4.2116911057E-06	2902805.93493592	2902830.38648278	24.451547	21881.5151
62	21881.5151	-5.7646819916E-05	-5.7646819916E-05	2902213.12318597	2901878.53575933	-334.587427	21881.5177
63	21881.5177	-1.1333362402E-04	-1.1333362402E-04	2902280.47754035	2901622.70015975	-657.777381	21881.5124
64	21881.5124	-7.5967035391E-05	-7.5967035391E-05	2902755.29519199	2902314.30126450	-440.993927	21881.5017
65	21881.5017	2.2308548572E-05	2.2308548572E-05	2902648.643431490	2902778.15407718	129.510646	21881.5041

Table 19 DirectMap calculation of Engine1 TET=1299K, unable to converge: Newton-Raphson solver RPMFAN guess and check parameters for check on LP power balance (DWKLP tolerance $<10^{-8}$).

The iteration repeatedly attempts to achieve the set tolerance and eventually the program fails, usually in the form of the guess and check (relaxed to 50 $x10^{-5}$) for FanBta diverging to infinity.

A series of runs of DirectMap were then performed to find the tolerance that could achieve program convergence, with the tolerance on DQ30 set at $50x10^{-5}$ and that for DWKLP being varied, starting from $5x10^{-7}$ and incrementally increased. Despite being able to achieve $\approx 5x10^{-7}$ tolerance on DWLKLP, the value had to be increased to $50x10^{-5}$ before a converged overall engine performance point was achieved. Although the LP power convergence could be achieved with $\approx 5x10^{-7}$, the guess of RPMFAN is too restrictive due to the inability of the fan to resolve in enough detail to match to the core engine flow. The final simulation convergence tolerances to enable DirectMap to work are shown in **Table 17** with the two changes for the fan, henceforth to be termed "DatumTol".

4.7.3.2 Assessment of effect of relaxed convergence tolerances

Having relaxed the constraints on the checks for the guesses of FanBta and RPMFAN, it was then required to check how much difference they made to converged performance points. This is explained for example for the iteration guess of fan beta and check of HPC inlet flow function in **Fig. 4.51**. At point E, the guess of fan beta gives exactly equal fan core exit and HPC inlet flow functions. This is in computing terms the difference between two numbers to the smallest decimal place possible with double precision programming and is not desirable as a fast convergence time is the objective. At the DatumTol (section **4.7.3.1**) convergence tolerance of 10^{-7}, the performance calculation should give an answer such that the convergence falls on point A or point B, depending on which direction the guess of FanBta is moving, directed by the Newton-Raphson solver. Whether the convergence is on A or B, both of which meet the convergence criterion, converged performance calculation parameters such as thrust, pressure ratio are accurate to an acceptable number of decimal places. Points C and D represent relaxed the convergence tolerance points running DMTol. A similar diagram can be drawn for the guess of RPMFAN and check of LP shaft work. This investigation checks to what extent the differences of relaxed convergence on the guesses for FanBta and RPMFAN have on the performance.

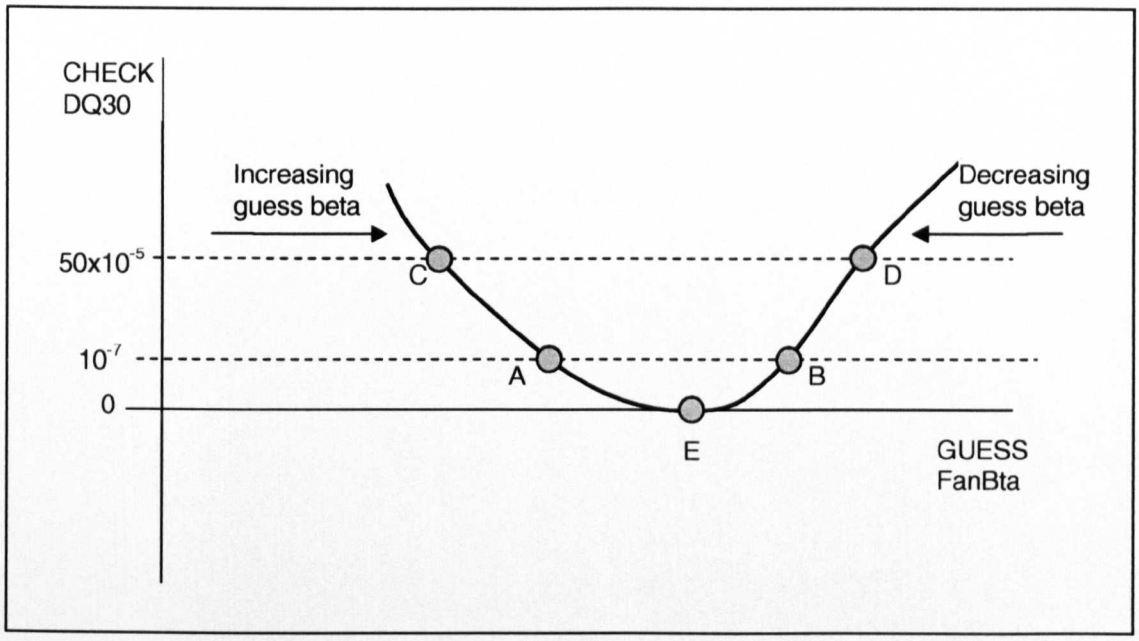

Fig. 4.51 Relaxation of constraints on guess of FanBta, check DQ30.

As DirectMap is unable to converge at the smallest tolerances, the only way to check the effect of different tolerances is with the fan models that use conventional fan characteristic interpolation where the double precision variables could be used throughout the simulation. Therefore, both WholeMap and ZonalMap were used to investigate the differences. A strategy was devised to compute some points in sequence (decreasing TET) and then to compute the same TET points in the opposite increasing direction. The same geometry engine was used for all runs (DM scaling factors, **Table 7**). The following are the findings:

- WholeMap DatumTol tolerance checks. **Fig. 4.52** shows a performance plot and **Fig. 4.54** to **Fig. 4.57** are compressor working line graphs representing a sequence of performance points of decrease from 1300 to 1250K and then increase of TET from 1250 to 1300K in one run using (DatumTol). As expected, the converged points are the same regardless of differences in the starting guesses to achieve convergence caused by the calculation sequence. The only point showing differences is for TET = 1290K, (21719.48 rpm, 16.179 kg/s). As this is the only point not matching, it is possible that there is a sudden change in the 2D fan characteristic data at this point (not apparent from the 1D maps). These graphs confirm that the DatumTol set of tolerances is correctly giving converged performance points. This is backed up by a comparison of selected points in **Table 20**, showing negligible difference between the parameters displayed.

- WholeMap DMTol tolerance checks. **Fig. 4.53** shows thrust vs. TET. **Fig. 4.58** to **Fig. 4.61** are compressor working line graphs. These graphs are the equivalent of the graphs described above, but for the DMTol case. Clearly, the relaxed tolerance causes a mismatch for each handle of TET when different starting guesses are used to compute the points. This is especially noticeable for example from **Fig. 4.59**, pressure ratio vs. rotational speed, in the region 21650 – 21850 rpm (≈99.9% design speed). The equivalent comparison of DatumTol is also tabulated for DMTol in **Table 20**. The differences in converged points are up to 0.4% for thrust, 0.2% for speed, 0.3% for pressure ratio, 0.1% for efficiency and .0.25% for mass flow. This is for the more extremely mismatched points.
- Concluding that DatumTol is sufficiently stringent for reproducible results, the two different tolerances are now compared to see how far away DMTol is from the datum. Only the runs with descending TET are considered here. **Fig. 4.62** is Thrust vs. TET, the differences are very small. **Fig. 4.63** to **Fig. 4.66** are the working line comparisons. It can be seen that although there are differences, all points fall on the same working line. Selected points are tabulated in **Table 21**. Generally, the differences are 0.2% for thrust, 0.1% for speed, 0.15% for pressure ratio, 0.05% for efficiency and 0.1% for mass flow. It is concluded that while not accurate enough for a normal simulation program, any converged points run with DMTol convergence tolerances still give a reasonable indication close to the real answer. Therefore, the calculations with DMTol using DirectMap will give valid comparisons of the engine performance keeping in mind the likely deviations from the answer that would have been obtained with more stringent tolerances. Therefore, it is recommended that all results from DirectMap calculations be compared to the equivalent WholeMap model calculation with DatumTol.

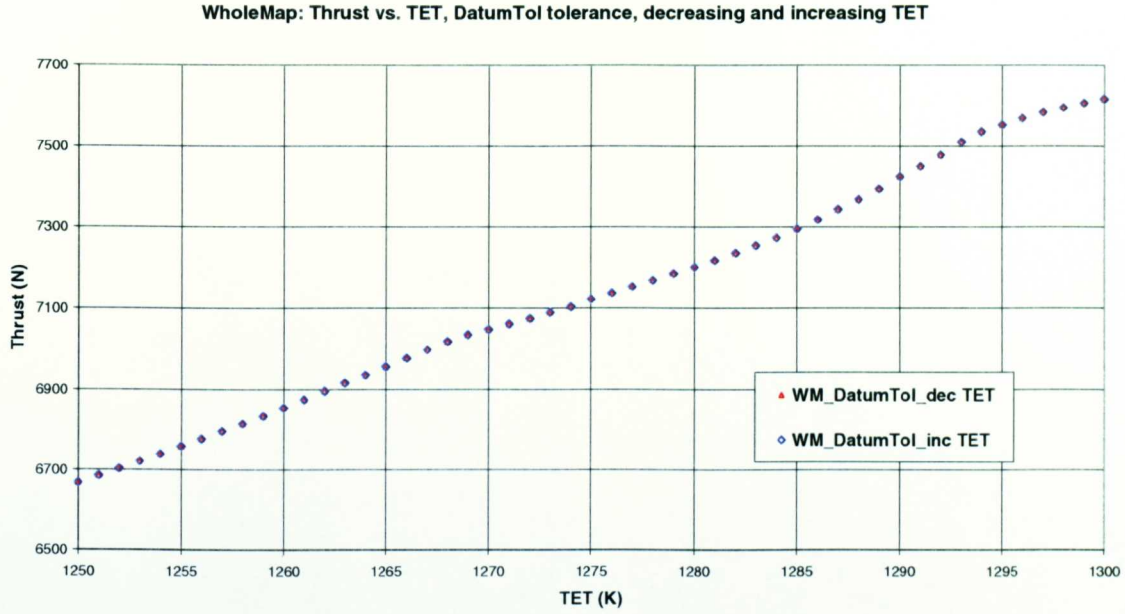

Fig. 4.52 Engine1 thrust vs. TET calculated using WholeMap fan model with undistorted inlet flow at DatumTol tolerance level, run with decreasing and increasing TET.

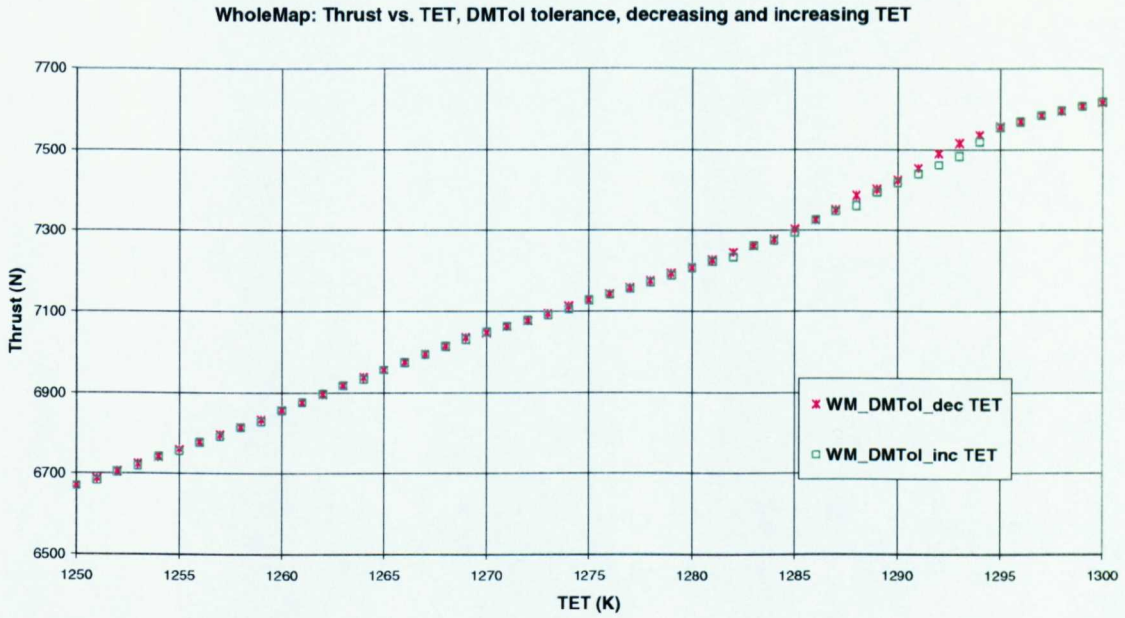

Fig. 4.53 Engine1 thrust vs. TET calculated using WholeMap fan model with undistorted inlet flow at DMTol tolerance level, run with decreasing and increasing TET

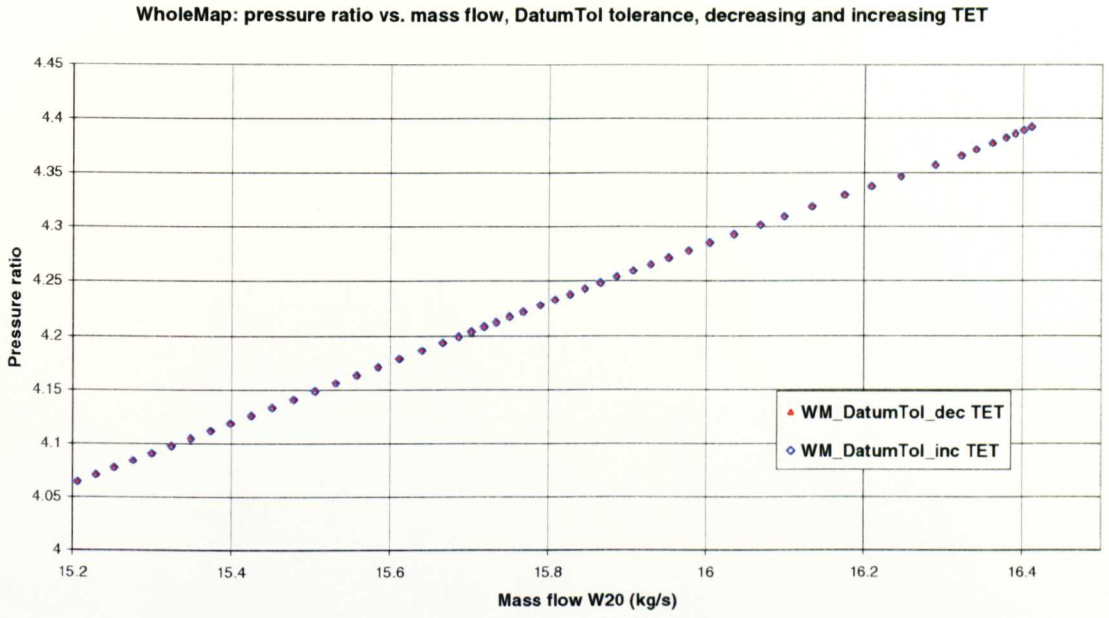

Fig. 4.54 Engine1 working line, pressure ratio vs. mass flow, calculated using WholeMap fan model with undistorted inlet flow at DatumTol tolerance level, run with decreasing and increasing TET.

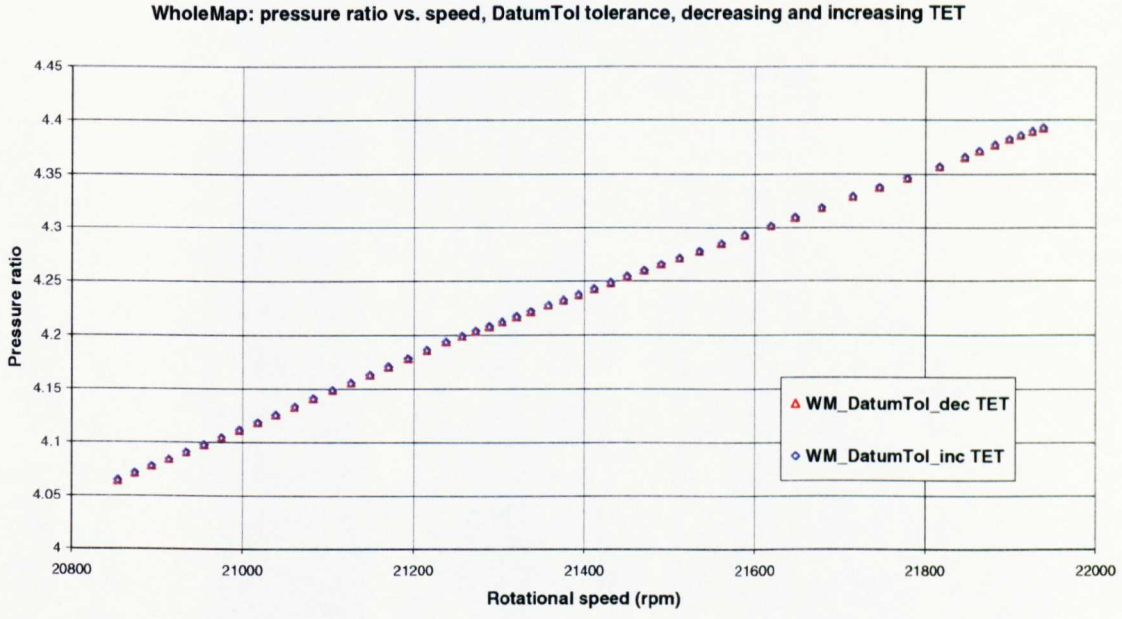

Fig. 4.55 Engine1 working line, pressure ratio vs. speed, calculated using WholeMap fan model with undistorted inlet flow at DatumTol tolerance level, run with decreasing and increasing TET.

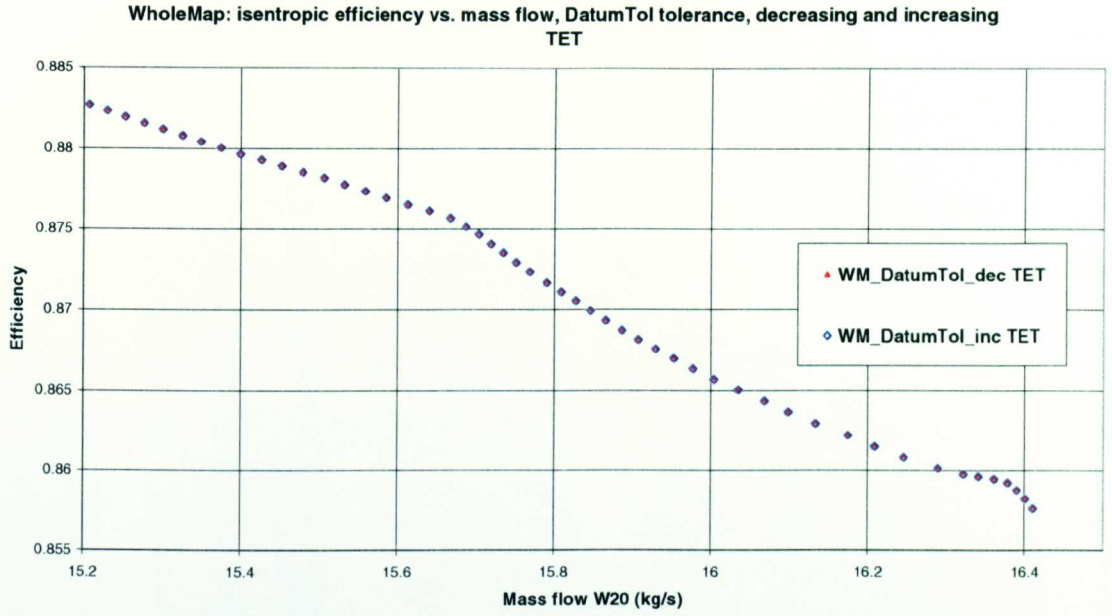

Fig. 4.56 Engine1 working line, isentropic efficiency vs. mass flow, calculated using WholeMap fan model with undistorted inlet flow at DatumTol tolerance level, run with decreasing and increasing TET.

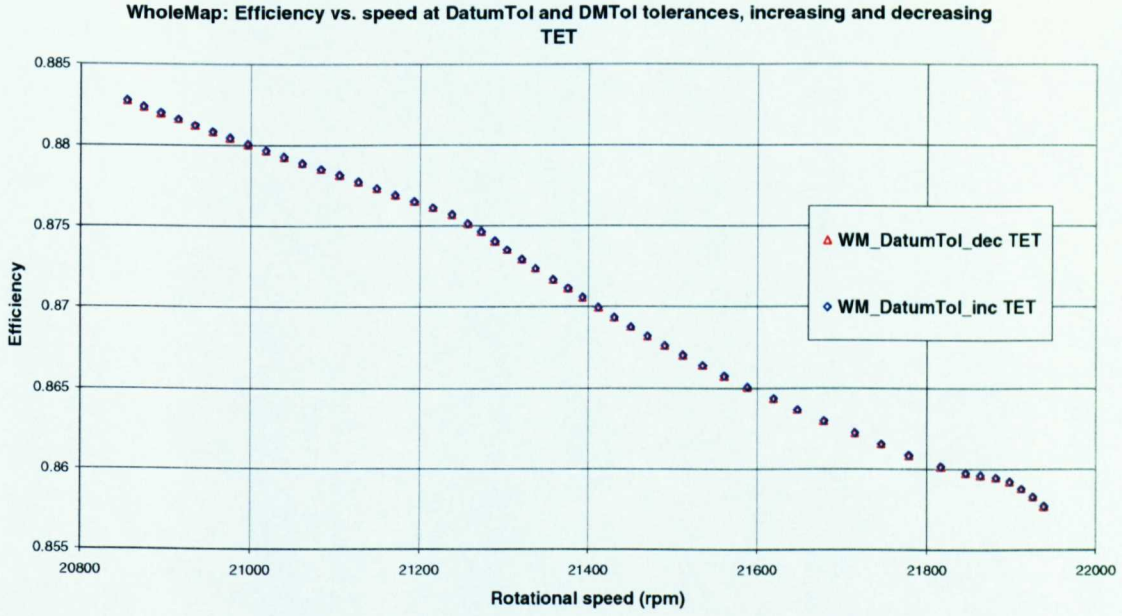

Fig. 4.57 Engine1 working line, isentropic efficiency vs. speed, calculated using WholeMap fan model with undistorted inlet flow at DatumTol tolerance level, run with decreasing and increasing TET.

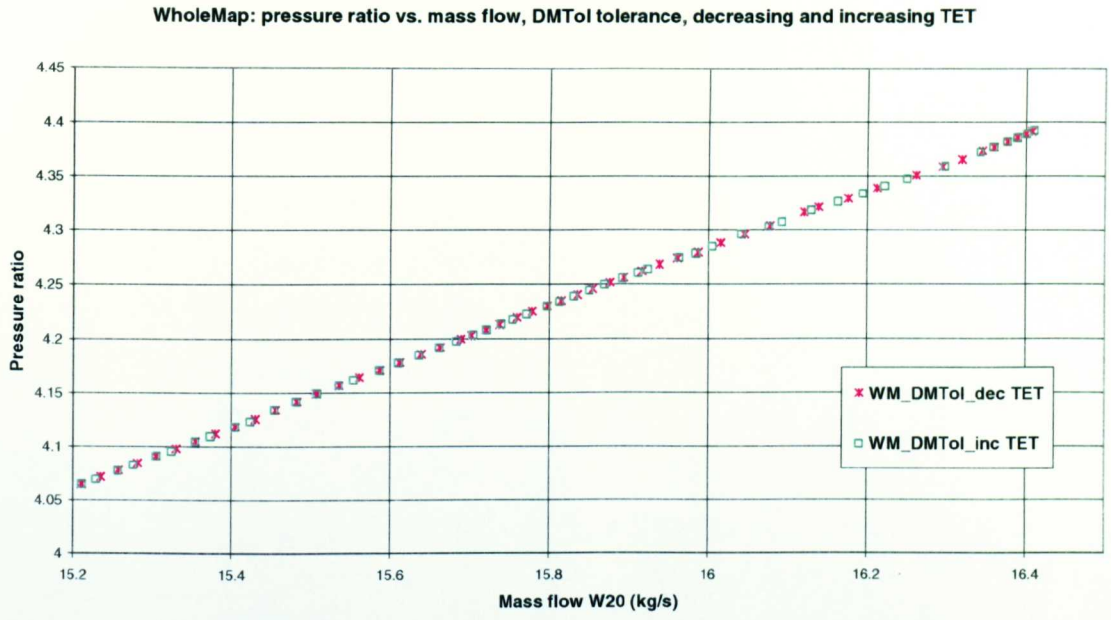

Fig. 4.58 Engine1 working line, pressure ratio vs. mass flow, calculated using WholeMap fan model with undistorted inlet flow at DMTol tolerance level, run with decreasing and increasing TET.

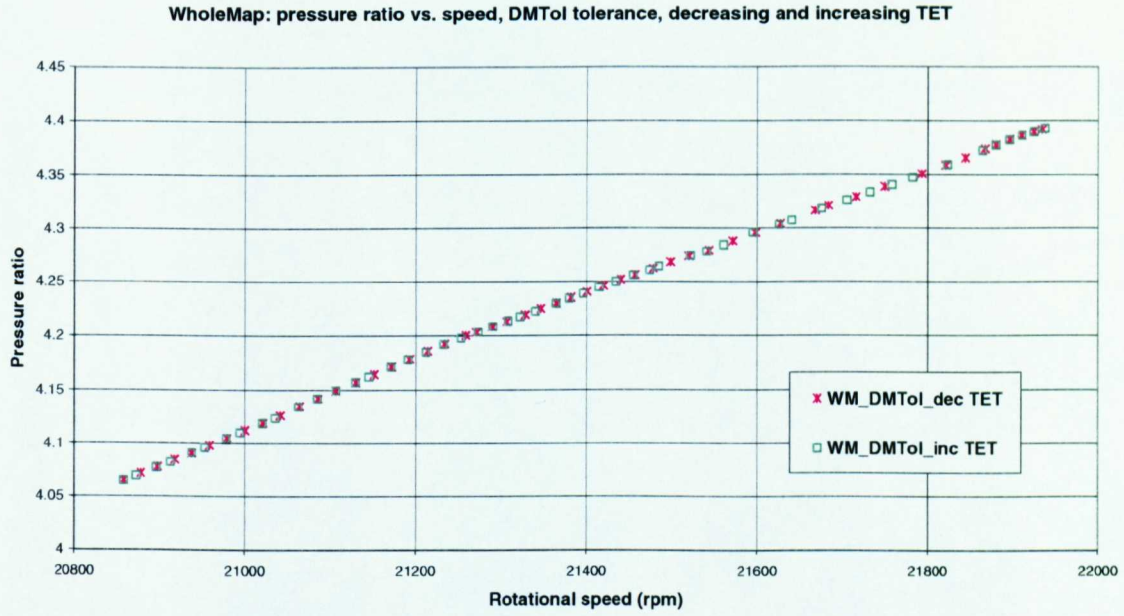

Fig. 4.59 Engine1 working line, pressure ratio vs. speed, calculated using WholeMap fan model with undistorted inlet flow at DMTol tolerance level, run with decreasing and increasing TET.

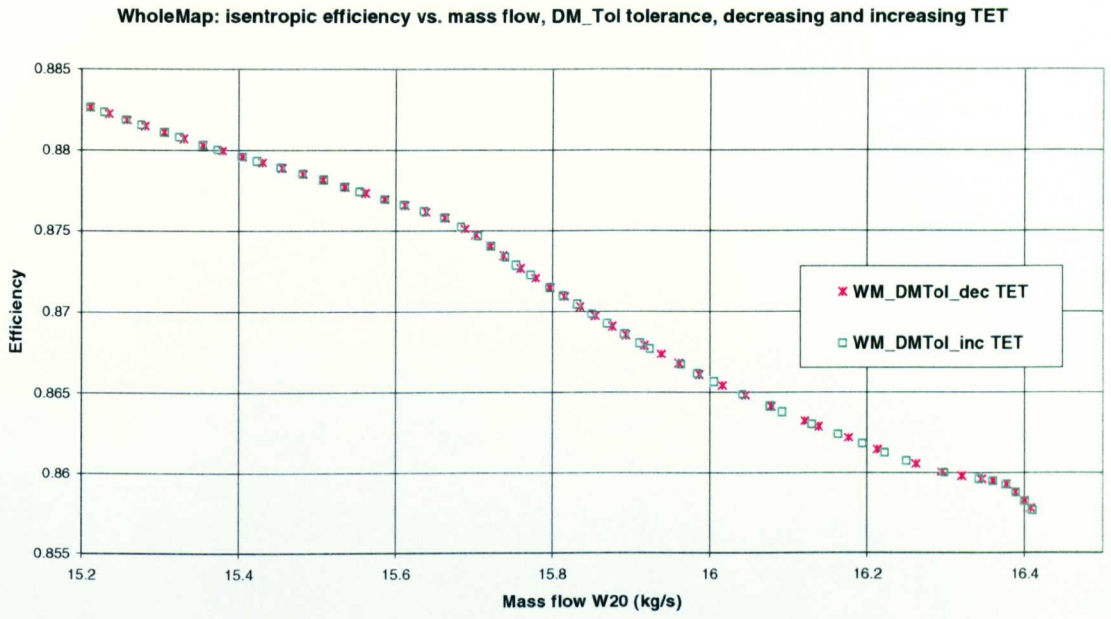

Fig. 4.60 Engine1 working line, isentropic efficiency vs. mass flow, calculated using WholeMap fan model with undistorted inlet flow at DMTol tolerance level, run with decreasing and increasing TET.

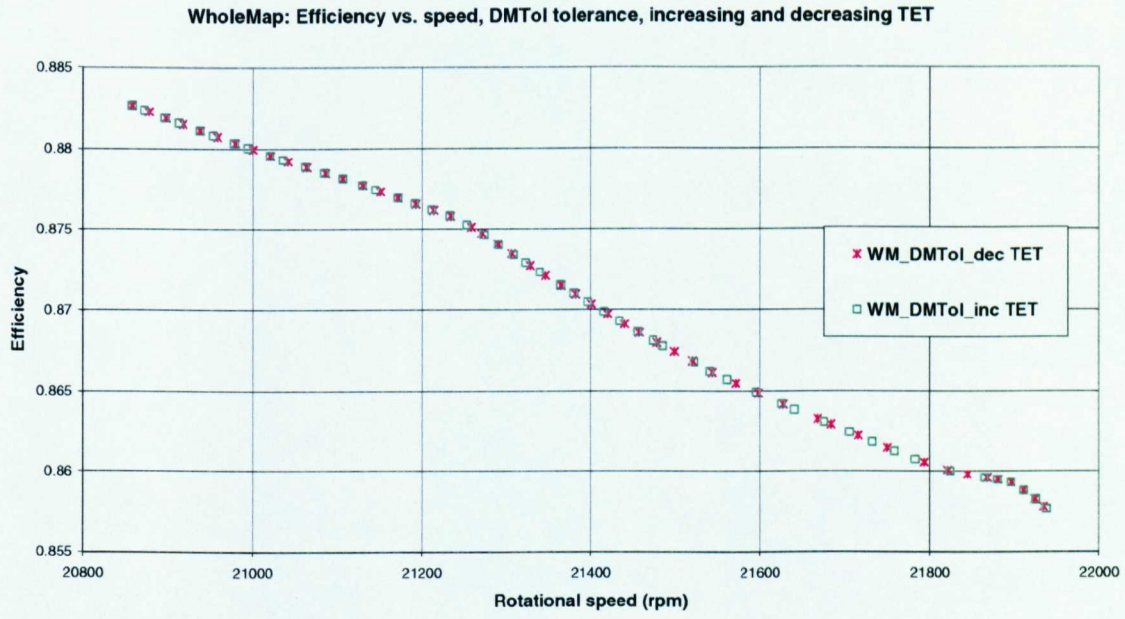

Fig. 4.61 Engine1 working line, isentropic efficiency vs. speed, calculated using WholeMap fan model with undistorted inlet flow at DMTol tolerance level, run with decreasing and increasing TET.

Selected point		WM_DatumTol decreasing. TET	WM_DatumTol increasing TET		WM_DMTol decreasing. TET	WM_DMTol increasing TET
TET	(K)	1292	1292		1292	1292
Thrust	Abs (N)	7478.893474	7478.843949		7489.996653	7462.348064
	Diff (%)		-0.001%			-0.369%
RPMFAN	Abs (rpm)	21779.0225	21778.88918		21793.40044	21758.02773
	Diff (%)		-0.001%			-0.162%
RFAN	Abs	4.34656789	4.346535885		4.350640416	4.340694488
	Diff (%)		-0.001%			-0.297%
ETAFan	Abs	0.86083921	0.860842073		0.860561401	0.861274774
	Diff (%)		0.000%			0.083%
WFAN	Abs (kg/s)	16.24528727	16.24513147		16.26172704	16.22166101
	Diff (%)		-0.001%			-0.246%
TET	(K)	1275	1275		1275	1275
Thrust	Abs (N)	7122.333342	7122.322958		7127.885345	7127.496657
	Diff (%)		0.000%			-0.005%
RPMFAN	Abs (rpm)	21358.23709	21358.27176		21364.96261	21364.4324
	Diff (%)		0.000%			-0.002%
RFAN	Abs	4.227666738	4.227677079		4.22998125	4.229820613
	Diff (%)		0.000%			-0.005%
ETAFan	Abs	0.871664482	0.871663363		0.871460063	0.871476923
	Diff (%)		0.000%			0.002%
WFAN	Abs (kg/s)	15.790108	15.79014416		15.79684216	15.79628856
	Diff (%)		0.000%			-0.004%
TET		1257	1257		1257	1257
Thrust	Abs (N)	6796.598779	6796.598676		6796.962952	6792.133741
	Diff (%)		0.000%			-0.071%
RPMFAN	Abs (rpm)	20996.24229	20996.23118		21000.10746	20994.25954
	Diff (%)		0.000%			-0.028%
RFAN	Abs	4.111910245	4.111905148		4.112139882	4.109937398
	Diff (%)		0.000%			-0.071%
ETAFan	Abs	0.880055169	0.88005532		0.879945433	0.880042499
	Diff (%)		0.000%			0.011%
WFAN	Abs (kg/s)	15.37359788	15.37358603		15.37937196	1537.263%
	Diff (%)		0.000%			-0.044%

Table 20 Turbofan engine performance with undistorted inlet WholeMap fan model: comparison of selected points with different starting guesses using DatumTol and DMTol convergence tolerances.

Selected point		WM_DatumTol decreasing. TET	WM_DMTol decreasing TET
TET	(K)	1292	1292
Thrust	Abs (N)	7478.893474	7489.996653
	Diff (%)		0.148%
RPMFAN	Abs (rpm)	21779.0225	21793.40044
	Diff (%)		0.066%
RFAN	Abs	4.34656789	4.350640416
	Diff (%)		0.122%
ETAFan	Abs	0.86083921	0.860561401
	Diff (%)		-0.032%
WFAN	Abs (kg/s)	16.24528727	16.26172704
	Diff (%)		0.101%
TET	(K)	1275	1275
Thrust	Abs (N)	7122.333342	7127.885345
	Diff (%)		0.078%
RPMFAN	Abs (rpm)	21358.23709	21364.96261
	Diff (%)		0.031%
RFAN	Abs	4.227666738	4.22998125
	Diff (%)		0.072%
ETAFan	Abs	0.871664482	0.871460063
	Diff (%)		-0.023%
WFAN	Abs (kg/s)	15.790108	15.79684216
	Diff (%)		0.043%
TET		1257	1257
Thrust	Abs (N)	6796.598779	6796.962952
	Diff (%)		0.005%
RPMFAN	Abs (rpm)	20996.24229	21000.10746
	Diff (%)		0.018%
RFAN	Abs	4.111910245	4.112139882
	Diff (%)		0.007%
ETAFan	Abs	0.880055169	0.879945433
	Diff (%)		-0.012%
WFAN	Abs (kg/s)	15.37359788	15.37937196
	Diff (%)		0.038%

Table 21 Turbofan engine performance with undistorted inlet WholeMap fan model: comparison of selected points using DatumTol and DMTol convergence tolerances.

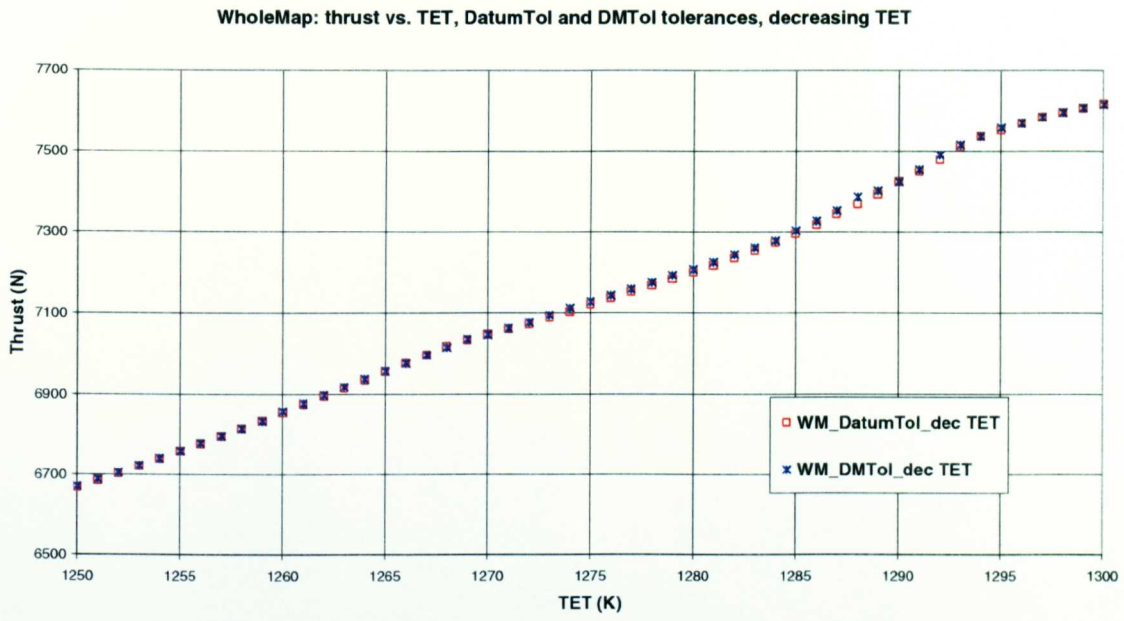

Fig. 4.62 Engine1 thrust vs. TET calculated using WholeMap fan model with undistorted inlet flow at DatumTol and DMTol tolerance levels, run with decreasing TET.

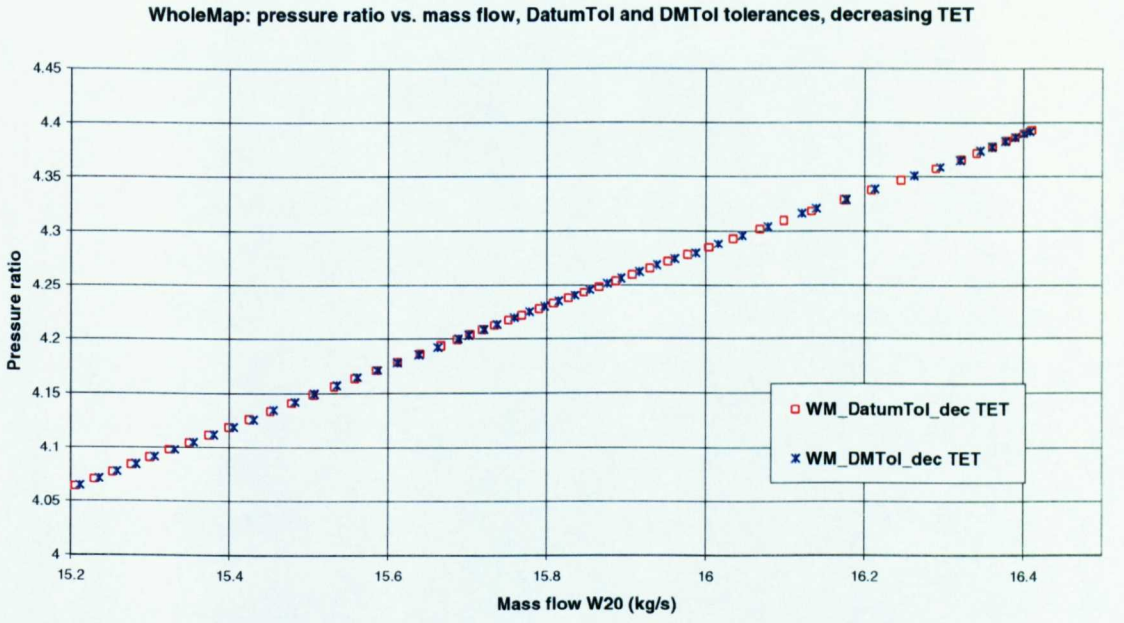

Fig. 4.63 Engine1 working line, pressure ratio vs. mass flow, calculated using WholeMap fan model with undistorted inlet flow at DatumTol and DMTol tolerance levels, run with decreasing TET.

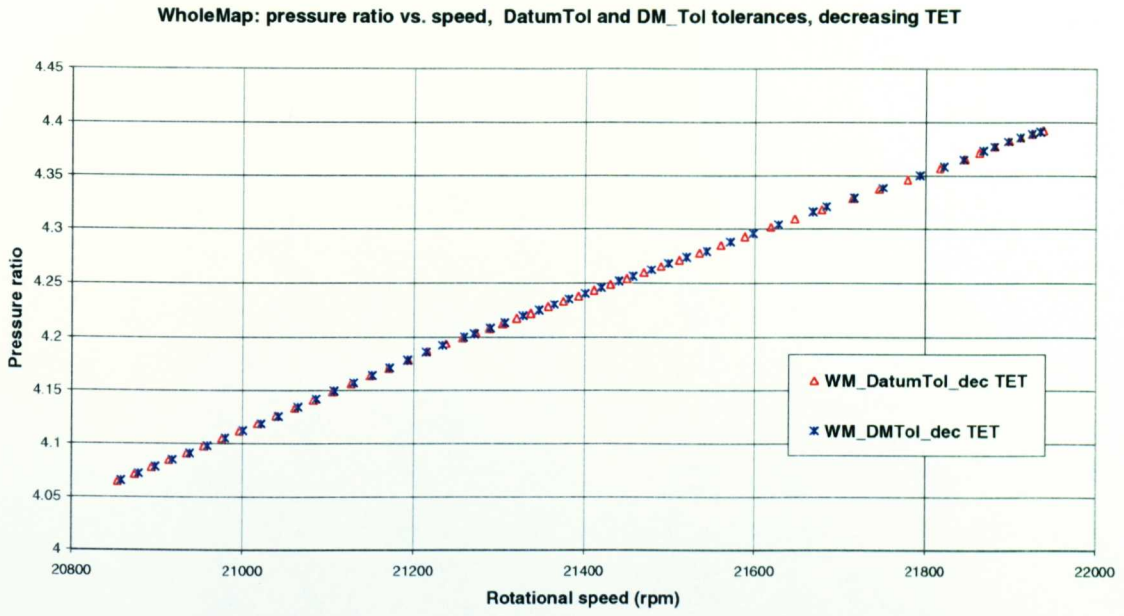

Fig. 4.64 Engine1 working line, pressure ratio vs. speed, calculated using WholeMap fan model with undistorted inlet flow at DatumTol and DMTol tolerance levels, run with decreasing TET.

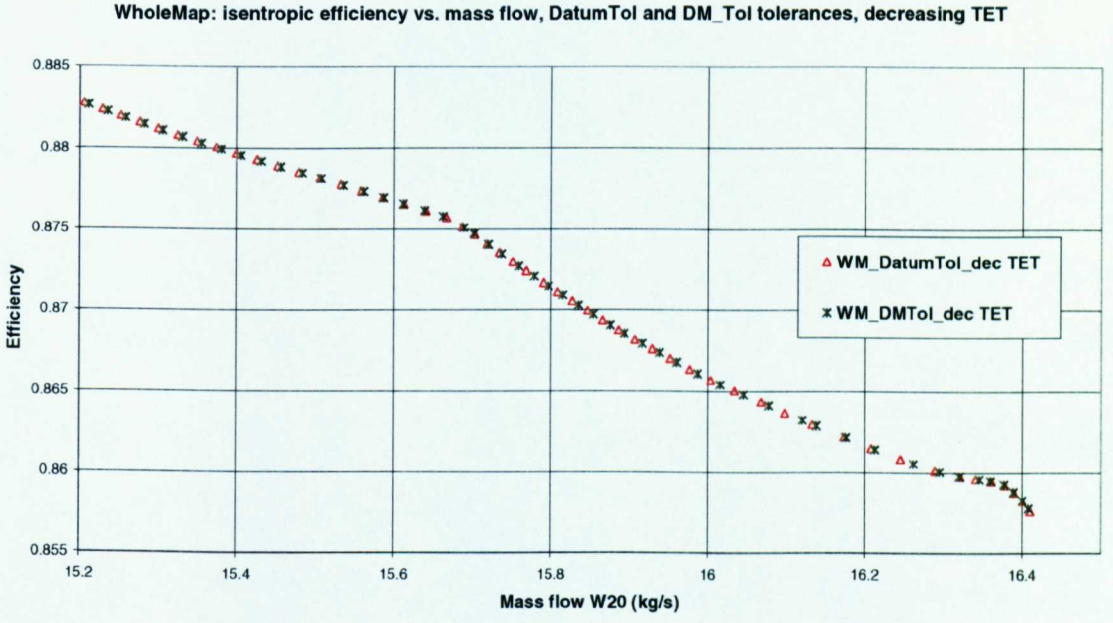

Fig. 4.65 Engine1 working line, isentropic efficiency vs. mass flow, calculated using WholeMap fan model with undistorted inlet flow at DatumTol and DMTol tolerance levels, run with decreasing TET.

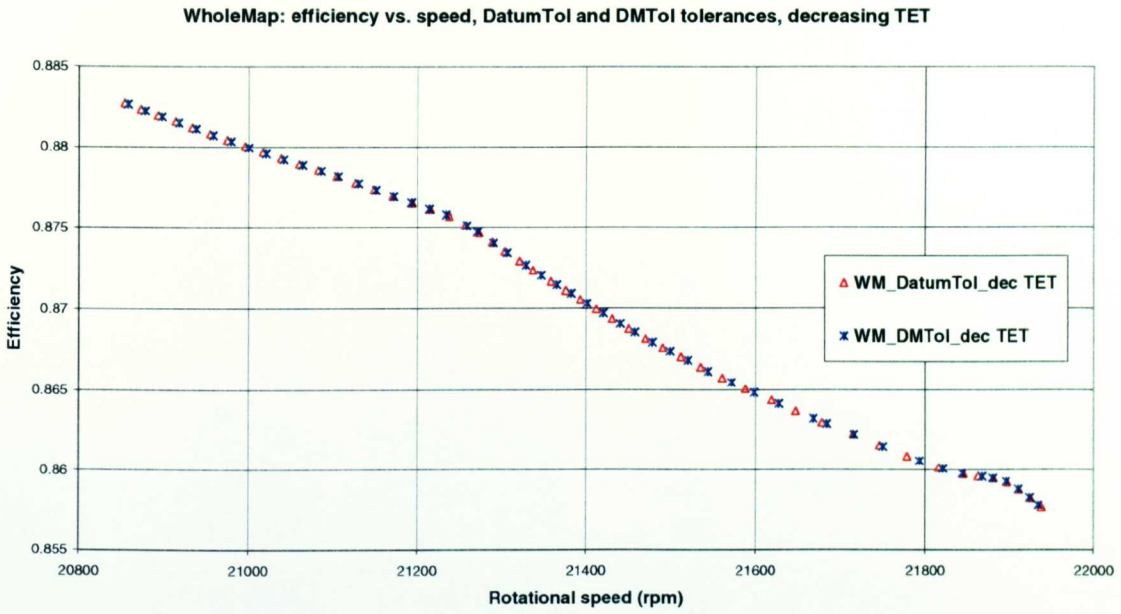

Fig. 4.66 Engine1 working line, isentropic efficiency vs. speed, calculated using WholeMap fan model with undistorted inlet flow at DatumTol and DMTol tolerance levels, run with decreasing TET.

- ZonalMap comparisons. With ZonalMap, there is the added complication of shifts in operating points due to interpolation from zones of different speed lines, as shown in section **4.7.1.3**. What this means is that the calculation of one operating point for example as a single point or as one of a sequence of points will differ in a small way depending on the starting guesses for each. These will influence what speed lines go into forming the 2-speed line zone for the converged fan guess and check. This effect is not apparent in WholeMap as the speed lines are fixed, so that any point on the map is always linearly interpolated from the two fixed nearest speed lines.

- Different zone comparisons in section **4.7.1.3** recommended having very close speed lines to the guessed speed. However, runs of ZonalMap1 (with ±0.5% speed lines), and up to ZonalMap6 (with ±1.0% speed lines) found that it could occasionally fail with the check of DQ30 for FanBta going to infinity and took several magnitudes of time longer than with WholeMap to converge. The problem was identified as follows. When using a very narrow zone, the guess of speed regularly falls outside the zone and a new one is then created. However, FanBta carried over from the previous zone will not be related to the FanBta in the new zone as each new pair of speed line zones is freshly reapplied with beta lines. The Newton-Raphson solver will adjust the next guess on account of the differences

in DQ30 from the previous check (from a different map) and so occasionally, when there are several rapid zone changes in succession, if the change is not smooth, the next guesses could go to infinity. A fix could be devised for this by breaking the check link from the previous one during a zone change. However, it was found that the problem did not occur with larger zones, e.g. ZM10 with ±1.5% speed lines, where it is concluded that the zone is large enough to contain the variation in speed guesses each time a zone is changed.

- The effect of the moving zones means that is exacerbated by this version of the program that truncates the speed lines to avoid stall and choke regions as described in section **4.7.1.3**. Different length speed lines in the zone will distort the flow profiles at the interpolated operating point. **Fig. 4.67** shows the thrust vs. TET plot for Engine1 with ZonalMap10 (ZM10) fan model using DatumTol tolerance, and **Fig. 4.69** to **Fig. 4.72** are the fan working line graphs. From **Table 22**, the variation is 0.03% for thrust, 0.03% for speed, 0.03% for pressure ratio, 0.02% for efficiency and 0.025% for flow. These are still well within the variation found for the relaxation of the constraints. For completeness, the DMTol runs with ZM10 are shown, thrust in **Fig. 4.68** and the working line graphs in **Fig. 4.73** to **Fig. 4.76**. The variations are in **Table 22**, up to 1.3% for thrust, 0.5% for speed, 0.9% for pressure ratio, 0.4% for efficiency units and 0.12% for mass flow. These are as expected higher than the variations with DMTol using WholeMap model, the effect being the combined effect of the relaxed tolerance and of the use of varying speed lines plus the truncation of speed lines.

- ZonalMap vs. WholeMap. The final check is then to compare the ZonalMap results with the WholeMap results for the best tolerance case (DatumTol). Thrust is shown in **Fig. 4.77**, and working line graphs are shown in **Fig. 4.78** to **Fig. 4.81**. Variations are shown in **Table 23**, up to 0.8% for thrust, 0.25% for speed, 0.7% for pressure ratio, 0.07% for efficiency and 0.5% for mass flow. The clearest mismatch is for the efficiency working lines, **Fig. 4.80** and **Fig. 4.81**. As the variations for DatumTol calculations with ZonalMap are much smaller, these mismatches can be put down to the effect of more resolution between speed lines compared to WholeMap and also due to use of truncated speed lines in this ZonalMap implementation compared to WholeMap.

- The conclusion of the ZonalMap analysis is that the method should give similar precision results (with stringent convergence tolerance) to the conventional WholeMap method since both methods are dependent on interpolation between speed lines. However, the nature of the ZonalMap method means that it is expected for small differences to occur when arriving at the converged point from different starting guesses as different map zones may be used for the final converged iteration. This does not occur in the fixed speed line WholeMap methods (which would actually be less accurate if there are fewer speed lines and a wider gap between speed lines to interpolate in between). In order to get ZonalMap to behave in the same way, yet still derive the benefits of quicker convergence time for the distorted inlet cases, a method could be devised that ZonalMap only be allow to produce speed lines at pre-selected fixed speeds at the best allowable increment between speeds. There may however be problems at the interface between speed lines with the change in beta as zones are changed. A fix here could be to maintain the beta on the common speed line when switching zones, so that there is no discontinuity of beta between zones. There could be convergence problems with this if the beta lines do not vary smoothly as a result. An advantage of this is that speed lines could be saved as the program progresses, but this is only practical in this current implementation of the inlet distortion program, where the inlet distortion is imposed as an intake model is not considered. A full implementation would need to regularly change the overall fan characteristic with the intake involved in the overall iteration scheme producing different profiles depending on the compressor operating condition and the flight velocity of the engine.

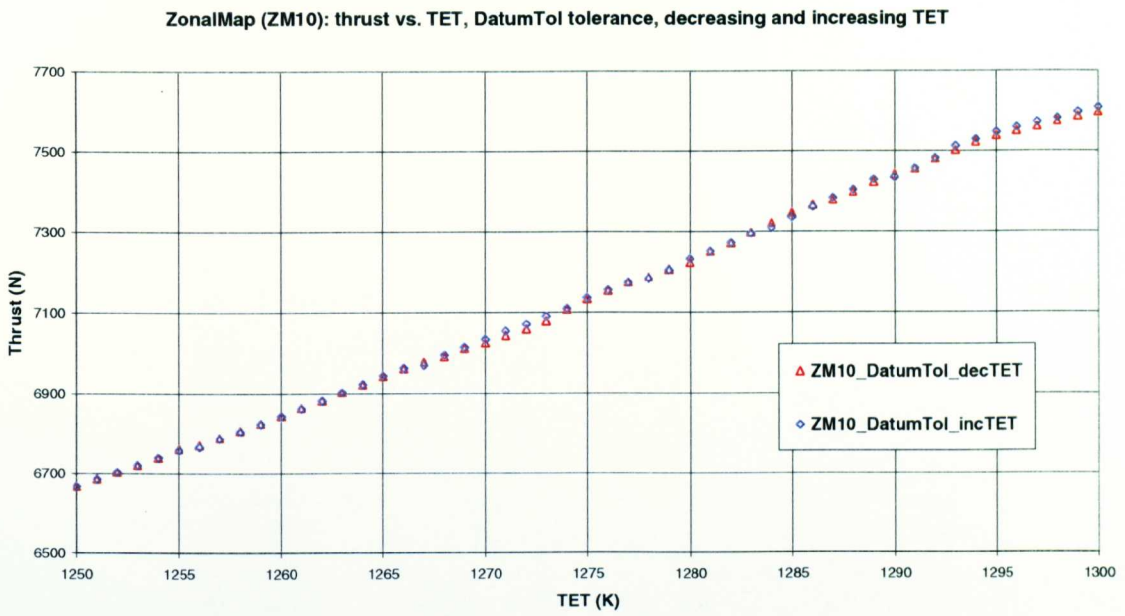

Fig. 4.67 Engine1 thrust vs. TET calculated using ZonalMap10 fan model with undistorted inlet flow at DatumTol tolerance level, run with decreasing and increasing TET.

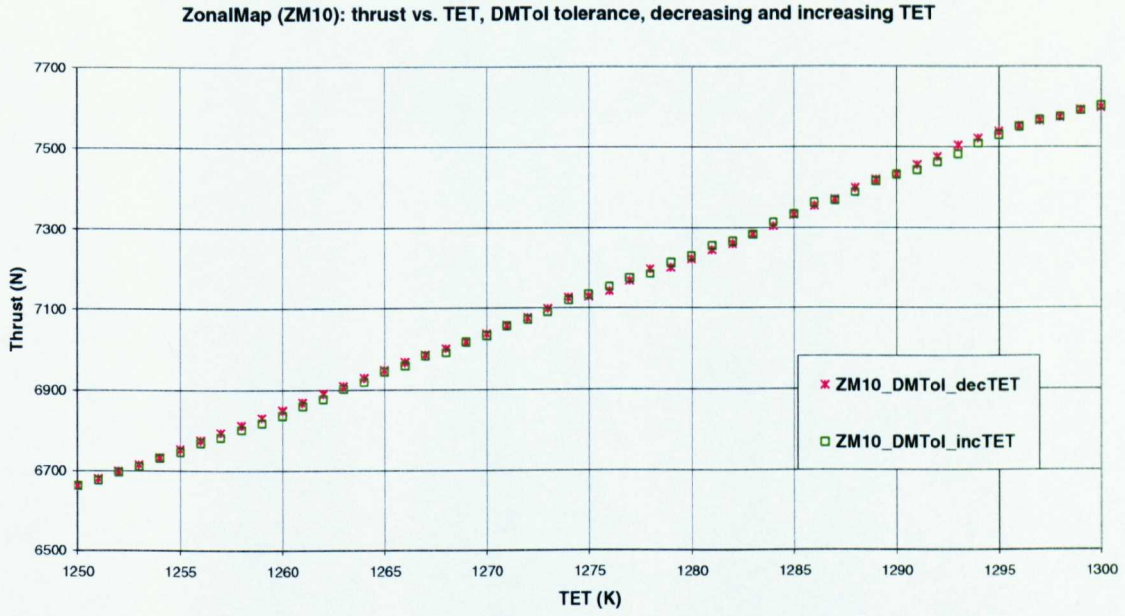

Fig. 4.68 Engine1 thrust vs. TET calculated using ZonalMap10 fan model with undistorted inlet flow at DMTol tolerance level, run with decreasing and increasing TET.

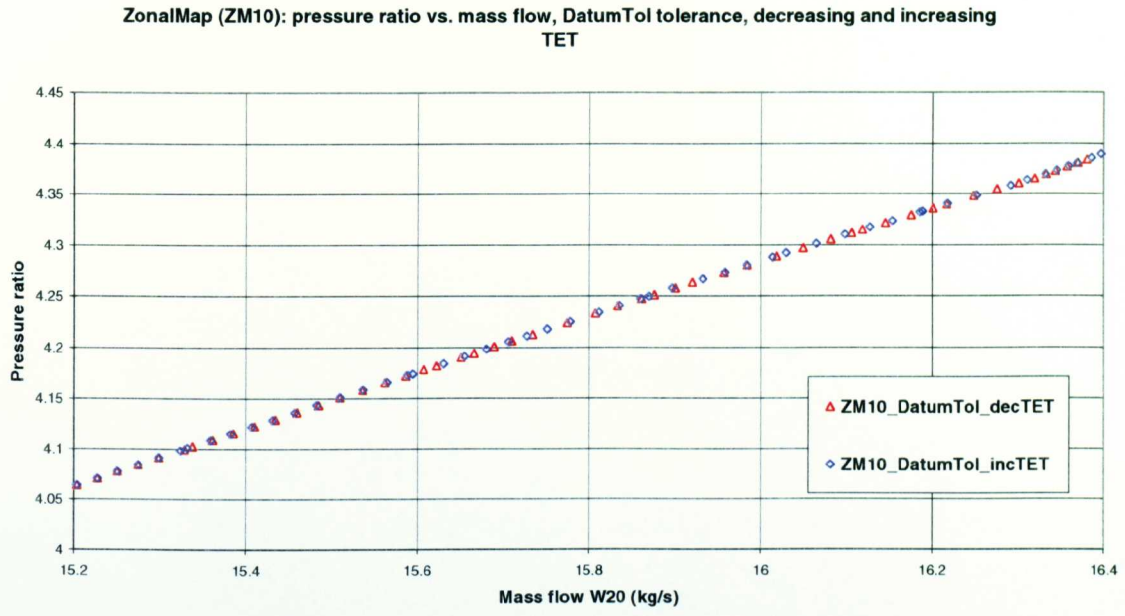

Fig. 4.69 Engine1 working line, pressure ratio vs. mass flow, calculated using ZonalMap10 fan model with undistorted inlet flow at DatumTol tolerance level, run with decreasing and increasing TET.

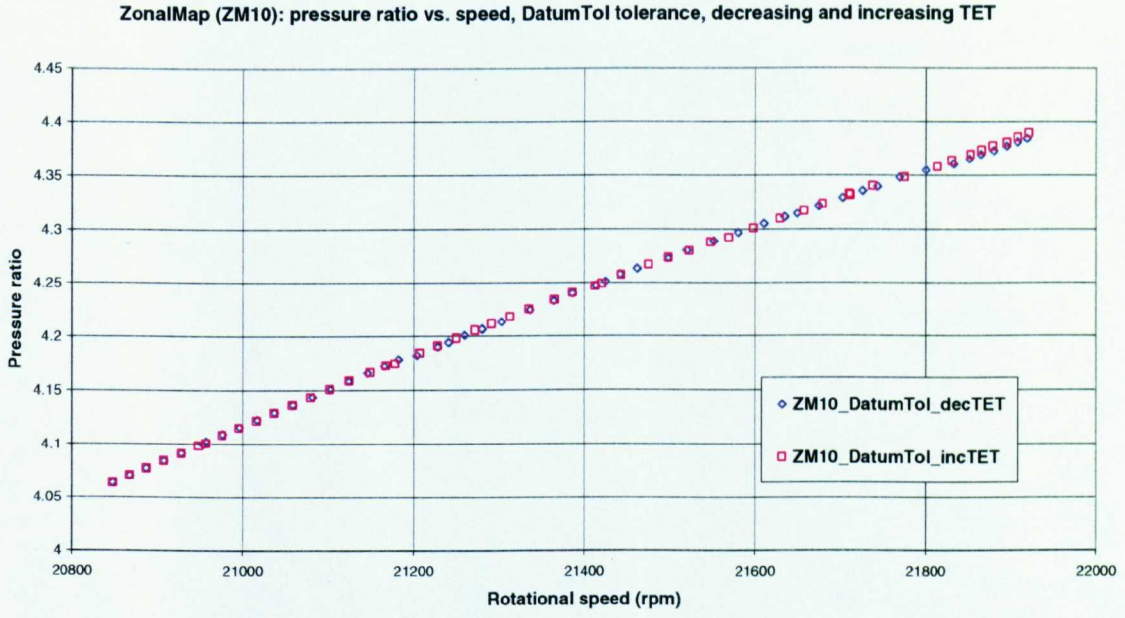

Fig. 4.70 Engine1 working line, pressure ratio vs. rotational speed, calculated using ZonalMap10 fan model with undistorted inlet flow at DatumTol tolerance level, run with decreasing and increasing TET.

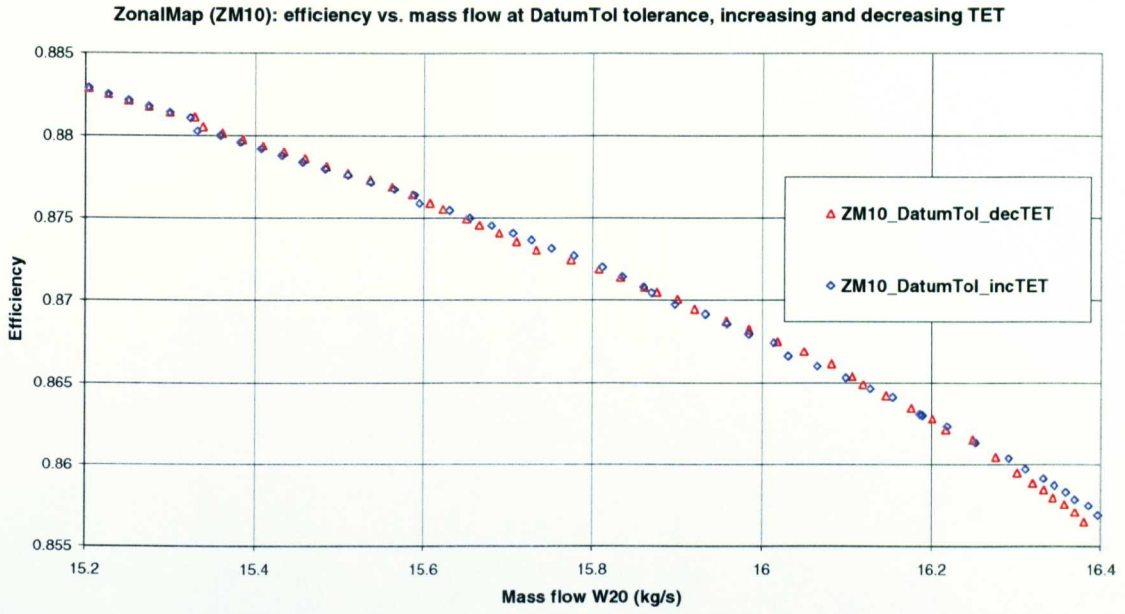

Fig. 4.71 Engine1 working line, isentropic efficiency vs. mass flow, calculated using ZonalMap10 fan model with undistorted inlet flow at DatumTol tolerance level, run with decreasing and increasing TET.

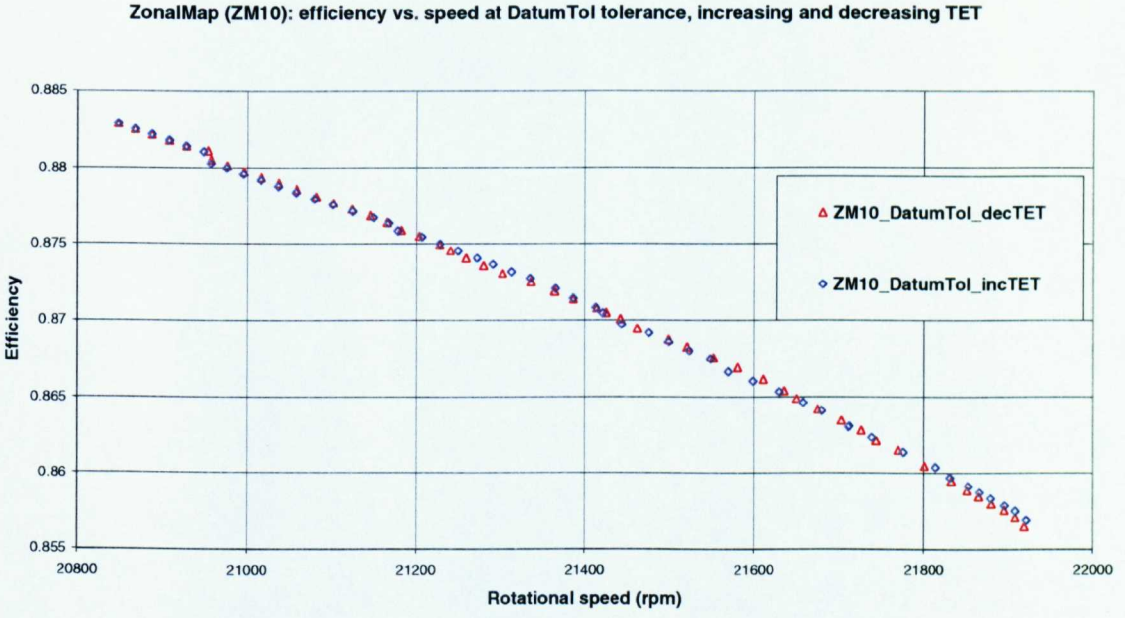

Fig. 4.72 Engine1 working line, efficiency vs. mass flow, calculated using ZonalMap10 fan model with undistorted inlet flow at DatumTol tolerance level, run with decreasing and increasing TET.

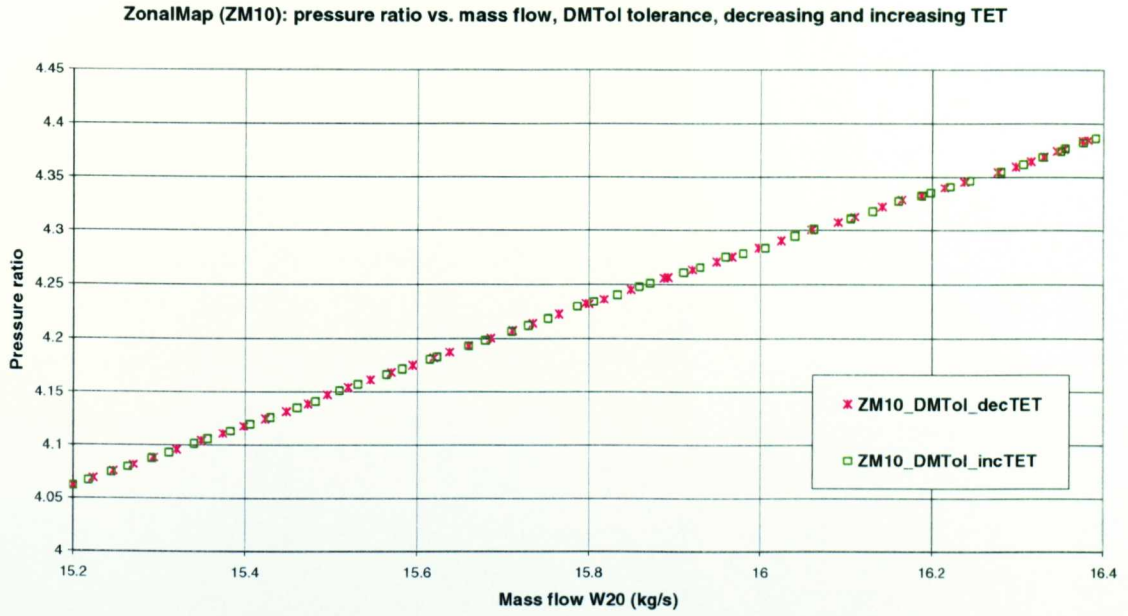

Fig. 4.73 Engine1 working line, pressure ratio vs. mass flow, calculated using ZonalMap10 fan model with undistorted inlet flow at DMTol tolerance level, run with decreasing and increasing TET.

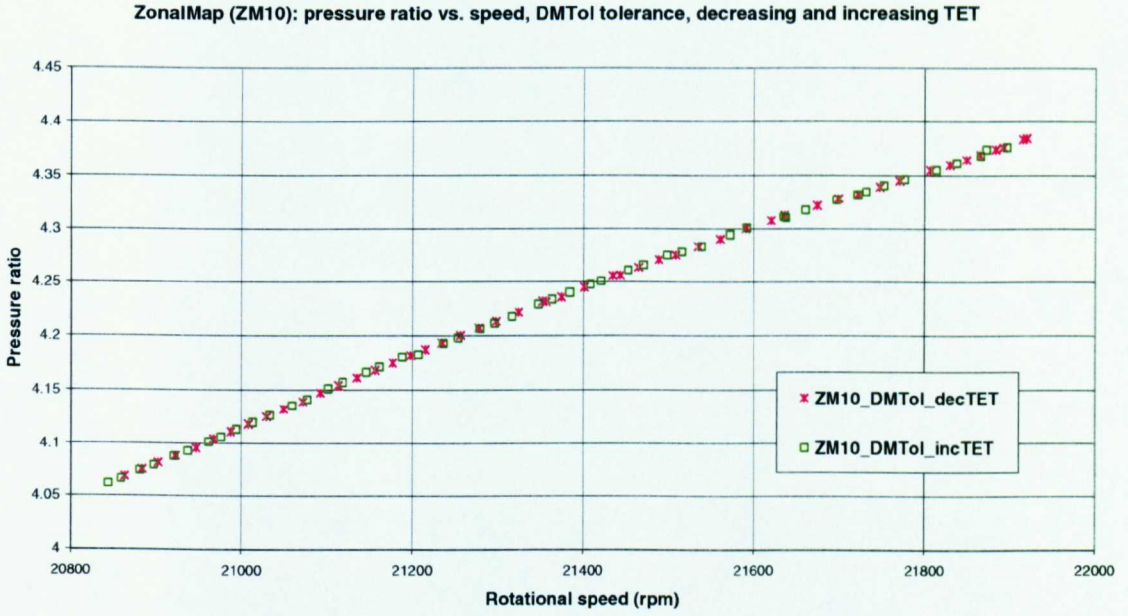

Fig. 4.74 Engine1 working line, pressure ratio vs. speed, calculated using ZonalMap10 fan model with undistorted inlet flow at DMTol tolerance level, run with decreasing and increasing TET.

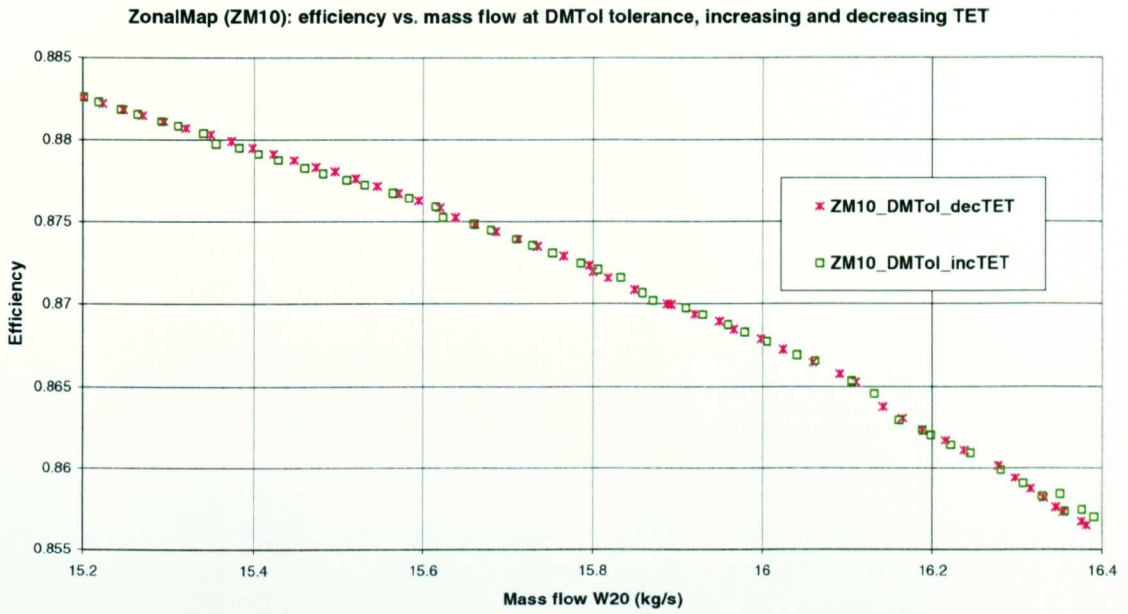

Fig. 4.75 Engine1 working line, isentropic efficiency vs. mass flow, calculated using ZonalMap10 fan model with undistorted inlet flow at DMTol tolerance level, run with decreasing and increasing TET.

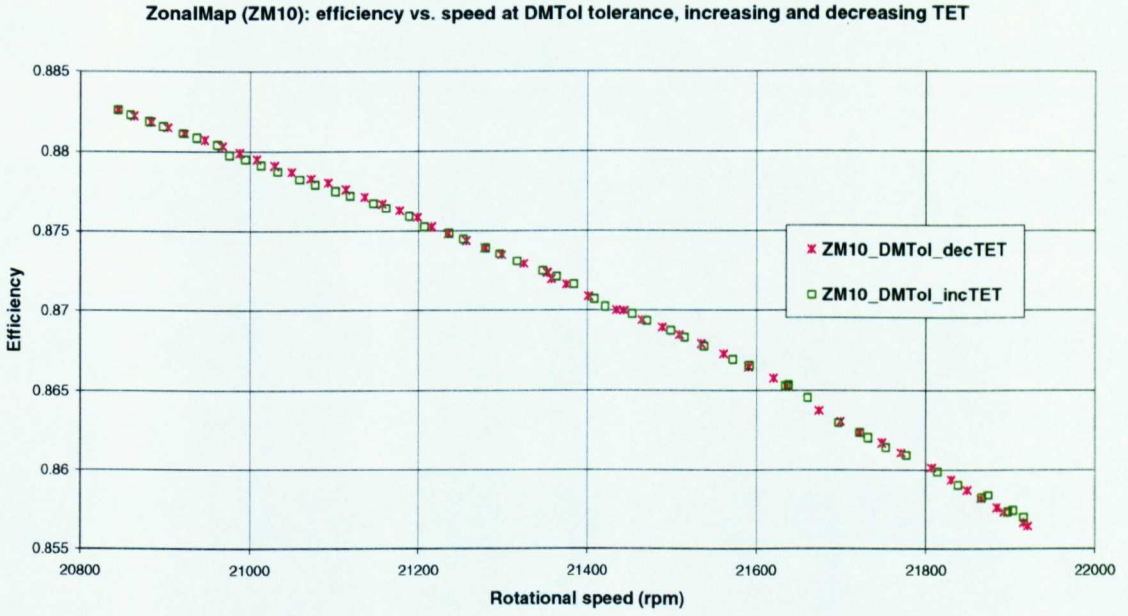

Fig. 4.76 Engine1 working line, isentropic efficiency vs. speed, calculated using ZonalMap10 fan model with undistorted inlet flow at DMTol tolerance level, run with decreasing and increasing TET.

Selected point		ZM10_DatumTol decreasing. TET	ZM10_DatumTol increasing TET	ZM10_DMTol decreasing. TET	ZM10_DMTol increasing TET
TET	(K)	1292	1292	1292	1297
Thrust	Abs (N)	7480.971857	7483.019102	7474.081109	7565.99063
	Diff (%)		0.027%		1.230%
RPMFAN	Abs (rpm)	21769.991	21775.82899	21771.02908	21873.05415
	Diff (%)		0.027%		0.469%
RFAN	Abs	4.348127264	4.348521891	4.344953642	4.37407653
	Diff (%)		0.012%		0.871%
ETAFan	Abs	0.861508932	0.861356048	0.861078121	0.858382438
	Diff (%)		-0.018%		-0.313%
WFAN	Abs (kg/s)	16.24910183	16.25206076	16.23782988	1622.096%
	Diff (%)		0.018%		-0.104%
TET	(K)	1275	1275	1275	1275
Thrust	Abs (N)	7133.614673	7135.752067	7129.214039	7134.40698
	Diff (%)		0.030%		0.073%
RPMFAN	Abs (rpm)	21364.5236	21365.35502	21357.73465	21363.71752
	Diff (%)		0.004%		0.028%
RFAN	Abs	4.233036419	4.233956664	4.231313137	4.233782944
	Diff (%)		0.028%		0.076%
ETAFan	Abs	0.871849661	0.87200649	0.871944347	0.872089795
	Diff (%)		0.018%		0.017%
WFAN	Abs (kg/s)	15.80772594	15.81144045	15.80078298	1580.613%
	Diff (%)		0.023%		0.034%
TET		1257	1257	1257	1257
Thrust	Abs (N)	6789.175347	6787.563365	6793.108638	6781.21633
	Diff (%)		-0.024%		-0.175%
RPMFAN	Abs (rpm)	20976.65533	20976.04163	20987.64002	20975.80587
	Diff (%)		-0.003%		-0.056%
RFAN	Abs	4.108801215	4.108344183	4.110753366	4.105787784
	Diff (%)		-0.015%		-0.160%
ETAFan	Abs	0.880138746	0.879978841	0.879898018	0.879750483
	Diff (%)		-0.018%		-0.017%
WFAN	Abs (kg/s)	15.36202173	15.35959926	15.37393572	1535.626%
	Diff (%)		-0.016%		-0.115%

Table 22 Turbofan engine performance with undistorted inlet ZonalMap10 fan model: comparison of selected points with different starting guesses using DatumTol and DMTol convergence tolerances.

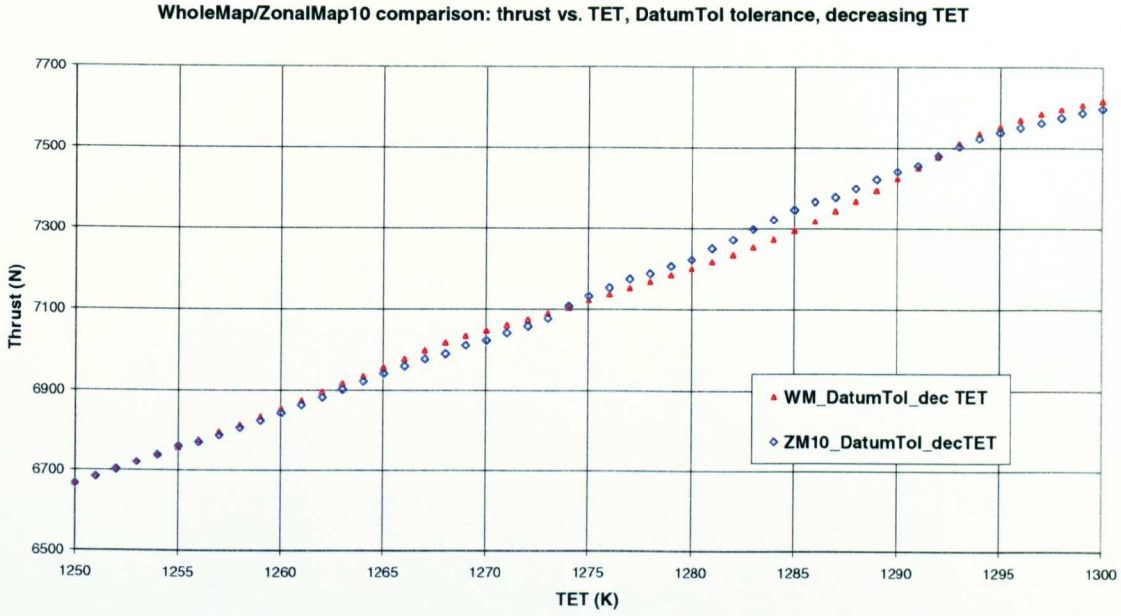

Fig. 4.77 Engine1 thrust vs. TET calculated using WholeMap and ZonalMap10 fan models with undistorted inlet flow at DatumTol tolerance level, run with decreasing TET.

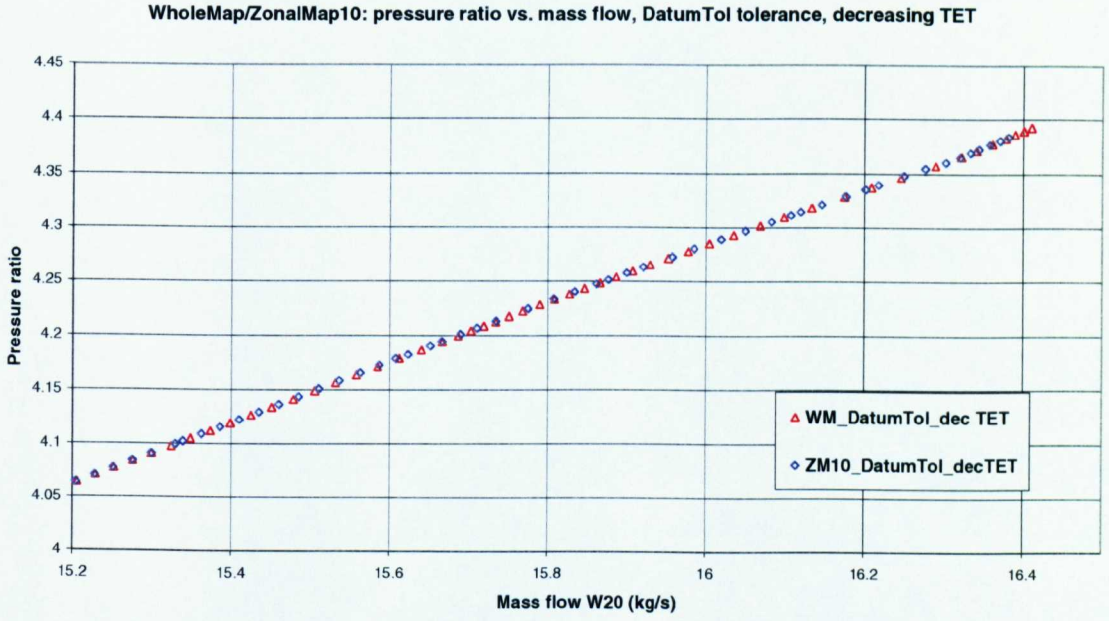

Fig. 4.78 Engine1 working line, pressure ratio vs. mass flow, calculated using WholeMap and ZonalMap10 fan models with undistorted inlet flow at DatumTol tolerance level, run with decreasing TET.

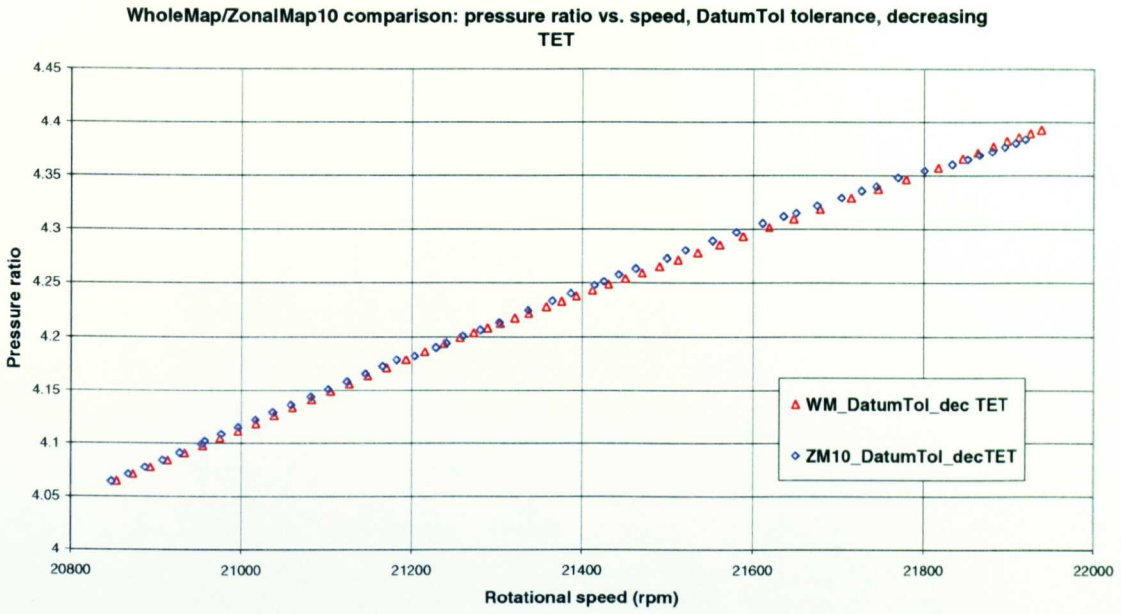

Fig. 4.79 Engine1 working line, pressure ratio vs. rotational speed, calculated using WholeMap and ZonalMap10 fan models with undistorted inlet flow at DatumTol tolerance level, run with decreasing TET.

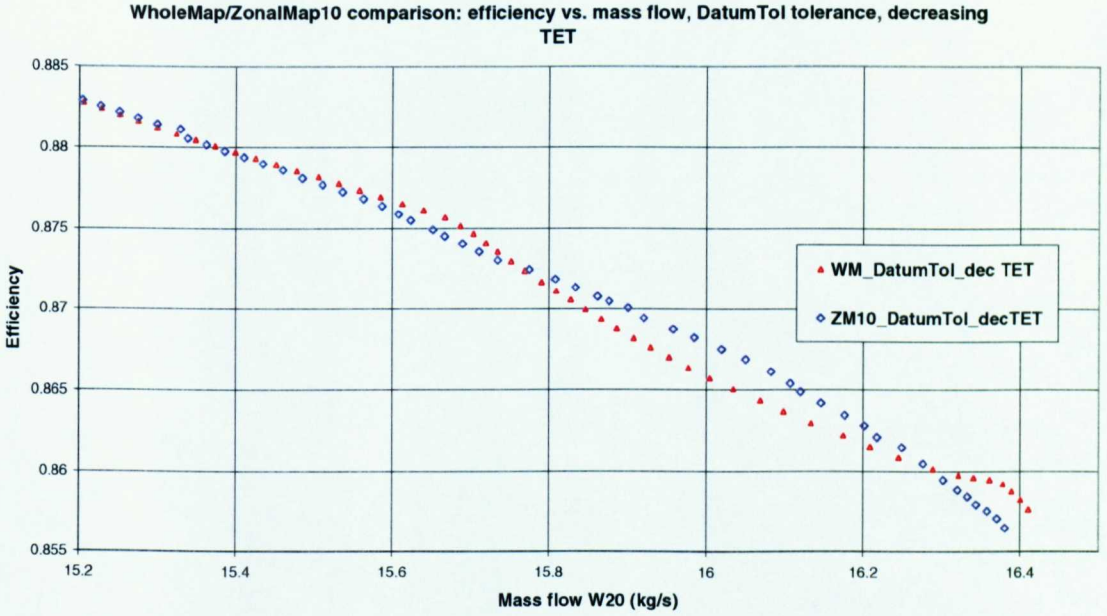

Fig. 4.80 Engine1 working line, isentropic efficency vs. mass flow, calculated using WholeMap and ZonalMap10 fan models with undistorted inlet flow at DatumTol tolerance level, run with decreasing TET.

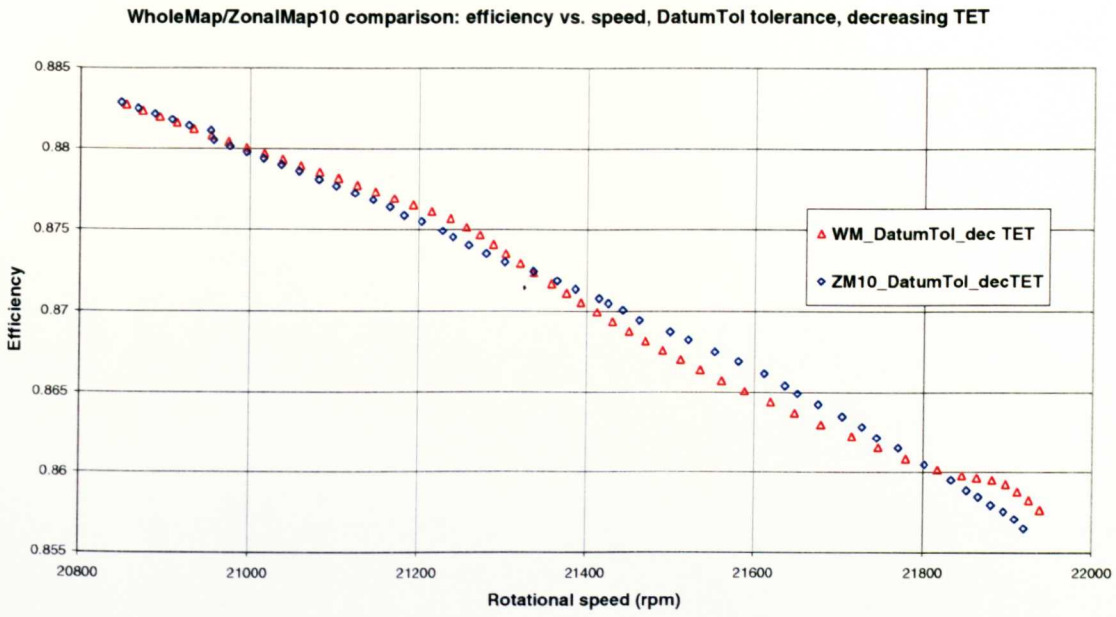

Fig. 4.81 Engine1 working line, isentropic efficency vs. rotational speed, calculated using WholeMap and ZonalMap10 fan models with undistorted inlet flow at DatumTol tolerance level, run with decreasing TET.

Selected point		WM_DatumTol decreasing. TET	ZM10_DatumTol decreasing TET		WM_DatumTol decreasing. TET	ZM10_DatumTol decreasing TET
TET	(K)	1292	1292		1285	1285
Thrust	Abs (N)	7478.893474	7480.971857		7295.229339	7346.570906
	Diff (%)		0.028%			0.704%
RPMFAN	Abs (rpm)	21779.0225	21769.991		21560.53619	21610.70488
	Diff (%)		-0.041%			0.233%
RFAN	Abs	4.34656789	4.348127264		4.285115803	4.305441422
	Diff (%)		0.047%			0.619%
ETAFan	Abs	0.86083921	0.861508932		0.86571496	0.866138758
	Diff (%)		0.078%			0.049%
WFAN	Abs (kg/s)	16.24528727	16.24910183		16.0039291	16.08220449
	Diff (%)		0.023%			0.489%
TET	(K)	1275	1275			
Thrust	Abs (N)	7122.333342	7133.614673			
	Diff (%)		0.158%			
RPMFAN	Abs (rpm)	21358.23709	21364.5236			
	Diff (%)		0.029%			
RFAN	Abs	4.227666738	4.233036419			
	Diff (%)		0.166%			
ETAFan	Abs	0.871664482	0.871849661			
	Diff (%)		0.021%			
WFAN	Abs (kg/s)	15.790108	15.80772594			
	Diff (%)		0.112%			
TET		1257	1257			
Thrust	Abs (N)	6796.598779	6796.598676			
	Diff (%)		0.000%			
RPMFAN	Abs (rpm)	20996.24229	20976.65533			
	Diff (%)		-0.093%			
RFAN	Abs	4.111910245	4.108801215			
	Diff (%)		-0.100%			
ETAFan	Abs	0.880055169	0.880138746			
	Diff (%)		0.009%			
WFAN	Abs (kg/s)	15.37359788	1536.202%			
	Diff (%)		-0.075%			

Table 23 Turbofan engine performance with undistorted inlet ZonalMap10 fan model: comparison of selected points using DatumTol and DMTol convergence tolerances.

4.7.4 Conclusions from program convergence studies with different fan models.

- Running the DirectMap program with normal simulation program tolerances resulted in non-convergence due to the inability of this version of the SLC program to resolve fan mass flow and rotational speed inputs into sufficient number of significant figures. A more relaxed set of tolerances for the FanBta and RPMFAN guesses resulted in convergence.
- The relaxed tolerances could be tested on the WholeMap and ZonalMap models to gain an idea of the effect on engine and fan performance parameters.
- Overall, the results with DMTol indicate that the relaxed tolerances cause variations from the results with the default normal DatumTol tolerance but that the results do not show extreme outliers in the graphs and that the correct trends in performance prediction can be captured and analysed, although the inaccuracies should be noted from the above study. The analysis has also picked up differences in the ZonalMap from the conventional WholeMap method, which should be addressed in future implementations (section **5.3**).

4.8 UNIFORM INLET FLOW CASE STUDIES

The results of the simulation of Engine1 with the 3 radial inlet pressure distortion models are now compared.

4.8.1 Fan working lines for engine with three fan models.

Engine1 was tested with WholeMap, ZonalMap, and DirectMap fan models using DM scaling factor set for all, DMTol convergence tolerance for DirectMap, and DatumTol for the other 2 models. The engine handle is TET. **Fig. 4.83** shows the working lines for all three models plotted on the undistorted WholeMap pressure ratio characteristic. The use of the same scaling factors so that the bypass nozzle area, core nozzle areas are the same and turbine characteristics are the same give the same fan working line, indicating that the compressor characteristic for each fan model is effectively the same. The convergence tolerance differences are sufficiently small not to show up as working line changes.

The engine routine was run to ±5K increments of TET from 1300K. The differences between the models are within the limits as described in Section **4.7.3.2**. In **Fig. 4.83** the WholeMap working line continues until running up to the beta=1 limit (**Fig. 4.20**), at 80.2%

speed at 1090K TET. The ZonalMap10 line reaches only 84.2% speed at 1120K TET and similarly, DirectMap reaches 85.0% speed at 1120K TET.

The speed lines involved with the latter two fan models are limited in this version of the program by the truncated speed line calculation of the SLC program. This lowers the beta=1 line in each of these models; at a particular iteration, the guess of beta may go beyond 1 and stop the program if operating near this beta line (**Fig. 4.83**). At the high power end, in the 103% speed line region, the speed lines produced by the SLC become shorter in the choke region relative to lower speeds, and the beta=0 line then limits the working line.

The efficiency fan working line in Fig. 4.85 shows a deviation in the WholeMap model; a decrease in the regions around 16kg/s and 13kg/s mass flow. This leads to similar deviations in the SFC plot (**Fig. 4.87**). Examination of sample efficiency profiles in the TET 1150K region (**Fig. 4.95**; 12.87 kg/s mass flow) show that the deviations occur in the upper radial range compared to the closer efficiency profiles of **Fig. 4.93**, which correspond to where the three fan models match more closely.

As the rotational speed falls (running the simulation to decreasing TET), the core pressure falls and less flow passes through the core relative to the bypass duct with the bypass ratio increasing (**Fig. 4.88**). **Fig. 4.89** shows the inner and outer fan pressure ratios. The outer fan has generally approx 2.3% lower pressure ratio than the inner fan except towards the higher speed range where the difference is approximately 0.8%. **Fig. 4.90** shows the fan exit total pressure profiles for the three models at 1300K (≈21900rpm) and 1180K (≈19520rpm). It can be seen that going from the higher to lower speed, the fan exit total pressure falls in the outer fan region relative to the average. This is more clearly indicated in **Fig. 4.91** in the profiles of total pressure normalised to the radial average for each case. The fan bypass split flow is indicated in this figure, and the range of split radius between the 2 speeds is only approximately from 47 to 45% radius ratio. This is calculated from the cumulative radial mass flow profile (**Fig. 4.94**). The change in split radius increases the fan outer average total pressure slightly but the overall effect in this fan is the higher fan inner pressure ratio. For any particular fan, the change in fan inner relative to the outer will depend on the particular total pressure profiles (i.e. designed radial work input and loss profiles) and the mass flow profiles of each case, the latter being usually uniform.

Radial station	1	2	3	4	5	6	7	8	9	10	11
Radius (m)	0.005	0.030	0.055	0.080	0.104	0.129	0.154	0.179	0.204	0.229	0.254
Undistorted	101325.00	101325.00	101325.00	101325.00	101325.00	101325.00	101325.00	101325.00	101325.00	101325.00	101325.00
TipDist1	101325.00	101325.00	101325.00	101325.00	101325.00	101325.00	101044.97	100907.66	100772.18	100501.26	98679.42
HubDist	98662.45	100462.23	100751.84	100897.32	101041.50	101325.00	101325.00	101325.00	101325.00	101325.00	101325.00
TipHubDist	98662.45	100462.23	100751.84	100897.32	101041.50	101325.00	101044.97	100907.66	100772.18	100501.26	98679.42
TipDist2	101325.00	101181.21	101038.42	100754.76	100474.50	100197.84	99924.85	99655.62	99251.93	98936.15	98733.97

Table 24 Table of undistorted inlet total pressure input with respect to inlet radius, with cases of inlet distortion total pressure profiles.

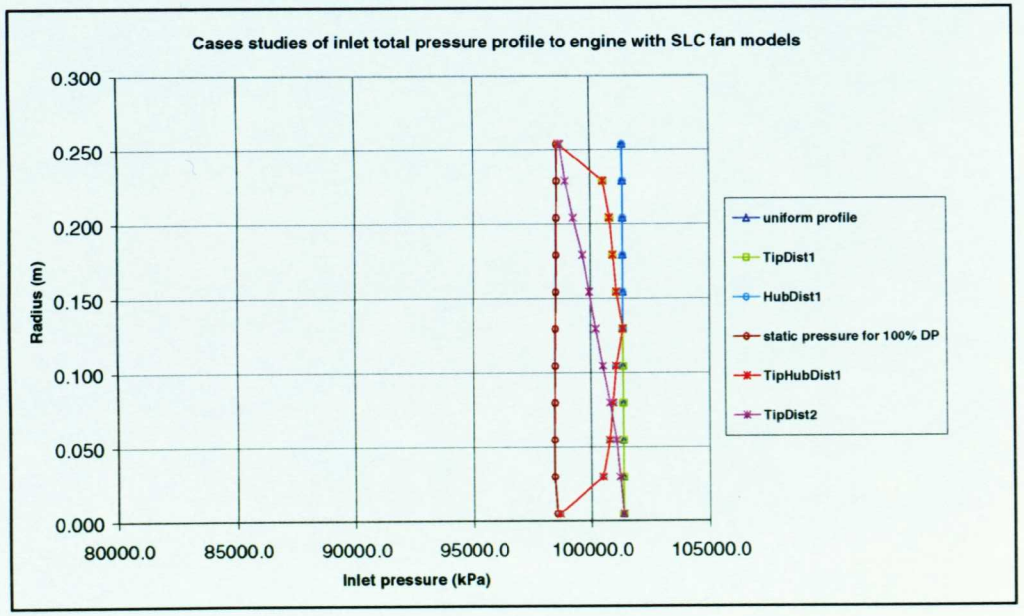

Fig. 4.82 Cases of inlet total pressure profile applied to engine model with SLC-derived fan models.

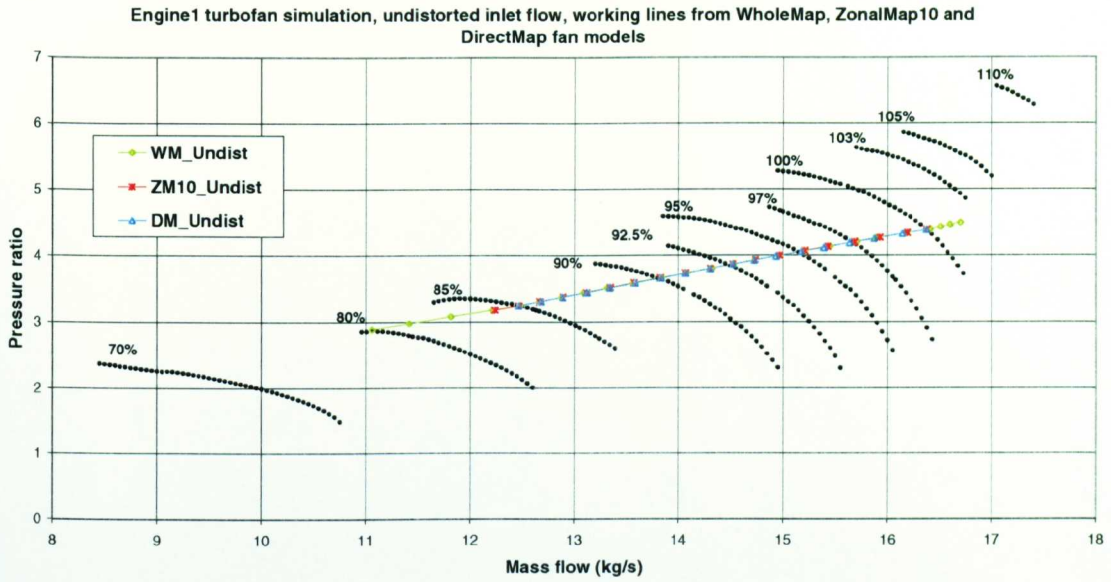

Fig. 4.83 Engine1 fan characteristic, undistorted inlet flow, working lines from WholeMap, ZonalMap10 and DirectMap models plotted on WholeMap fan characteristic map.

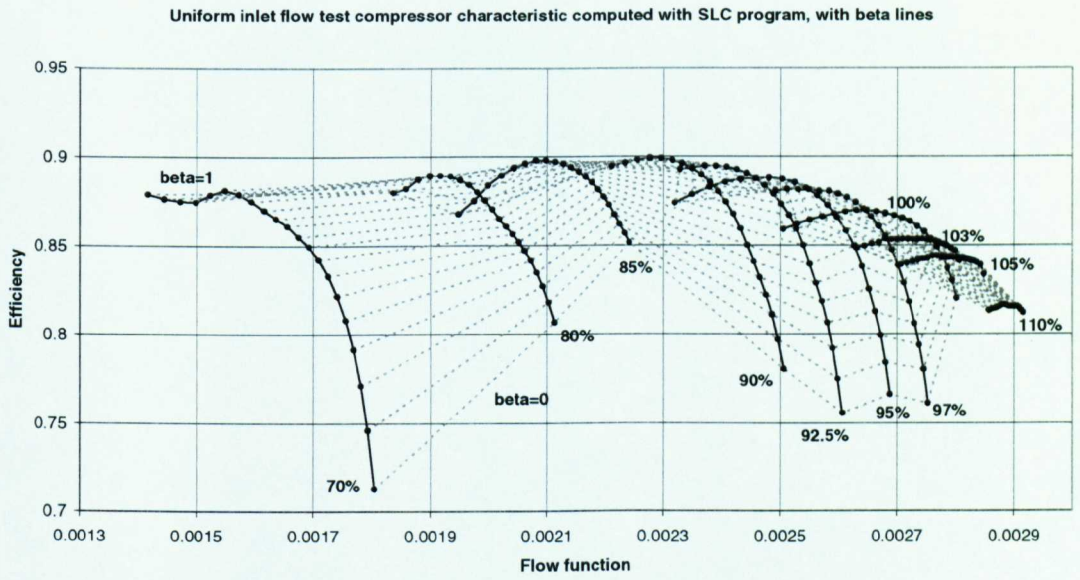

Fig. 4.84 Engine1 fan isentropic efficiency characteristic, undistorted inlet flow.

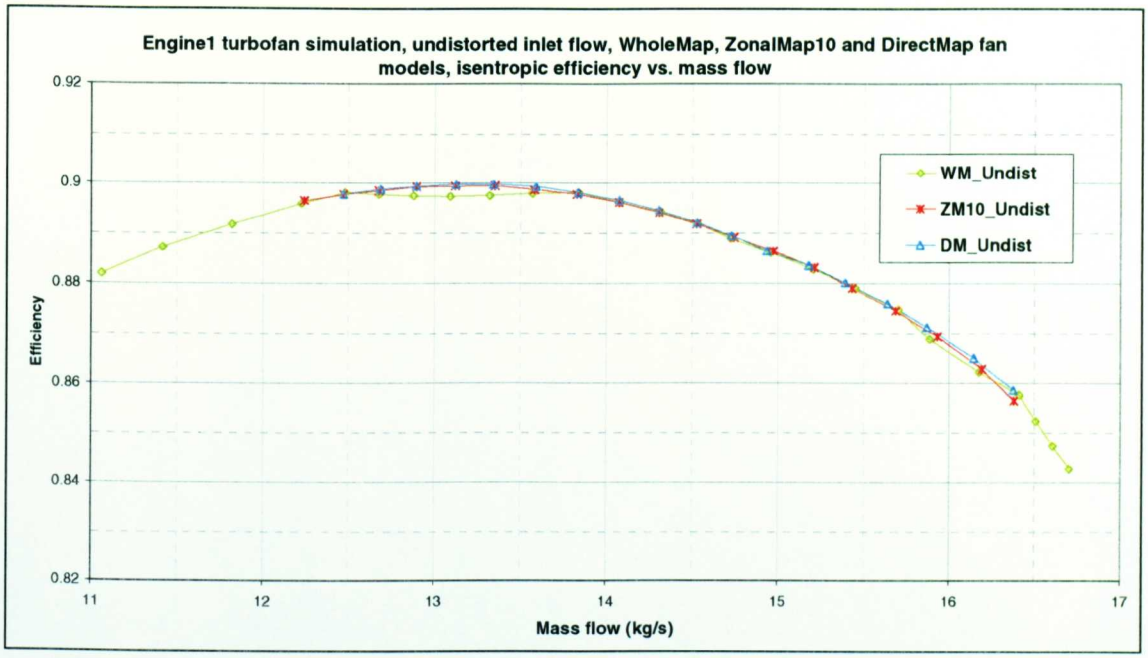

Fig. 4.85 Engine1 fan working line: isentropic efficiency vs. mass flow for 3 fan models with undistorted fan inlet flow.

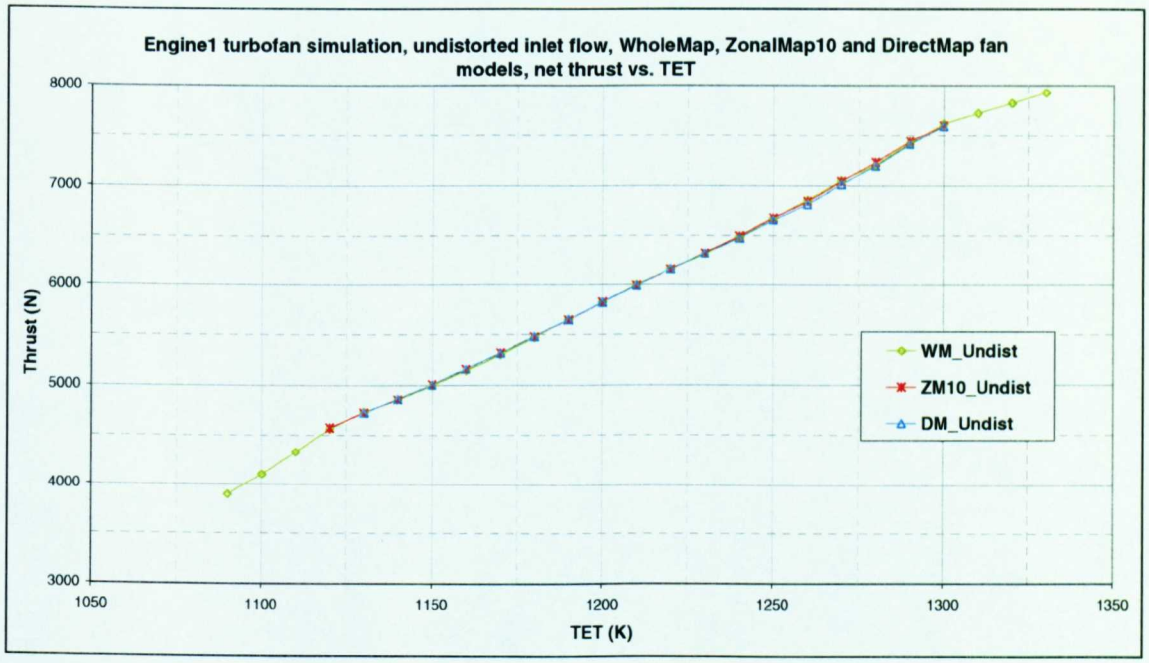

Fig. 4.86 Engine1 performance simulation: thrust vs. TET flow for 3 fan models with undistorted fan inlet flow.

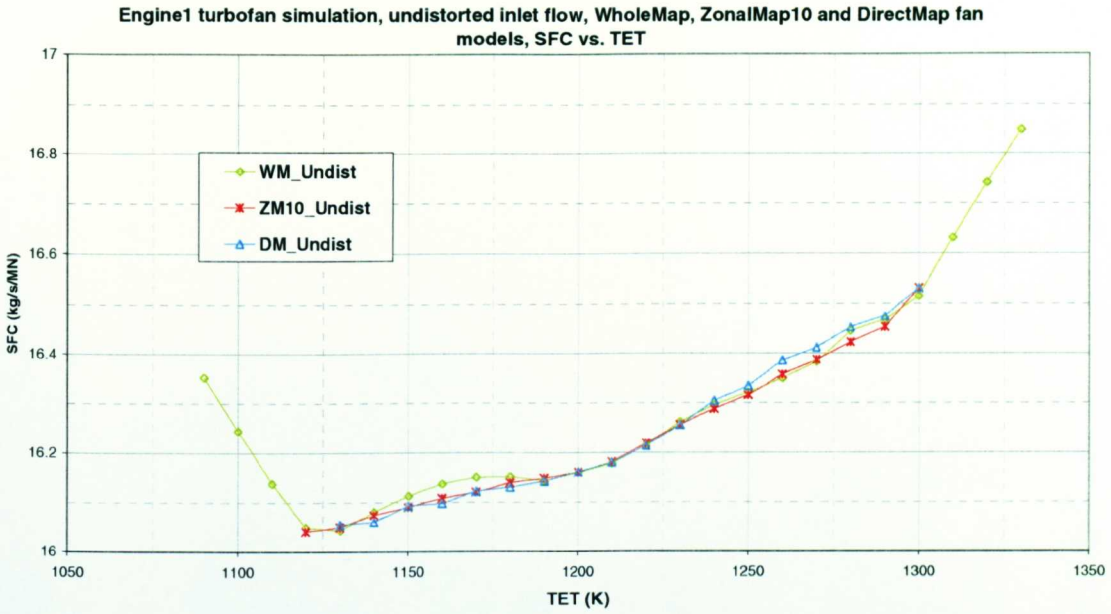

Fig. 4.87 Engine1 performance simulation: SFC vs. TET flow for 3 fan models with undistorted fan inlet flow.

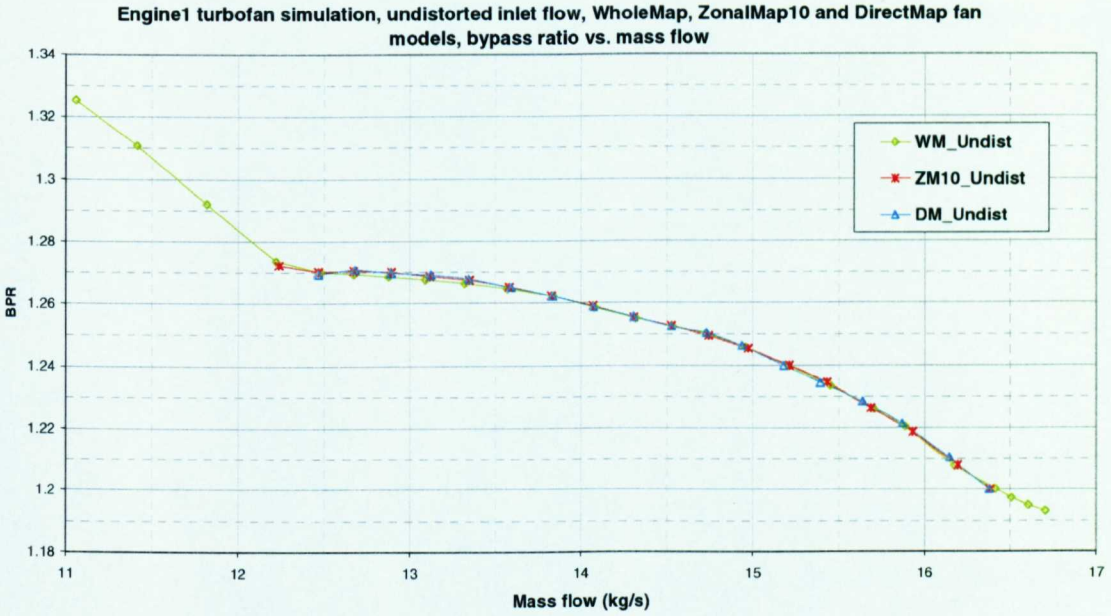

Fig. 4.88 Engine1 performance simulation: Bypass ratio vs. mass flow for 3 fan models with undistorted fan inlet flow.

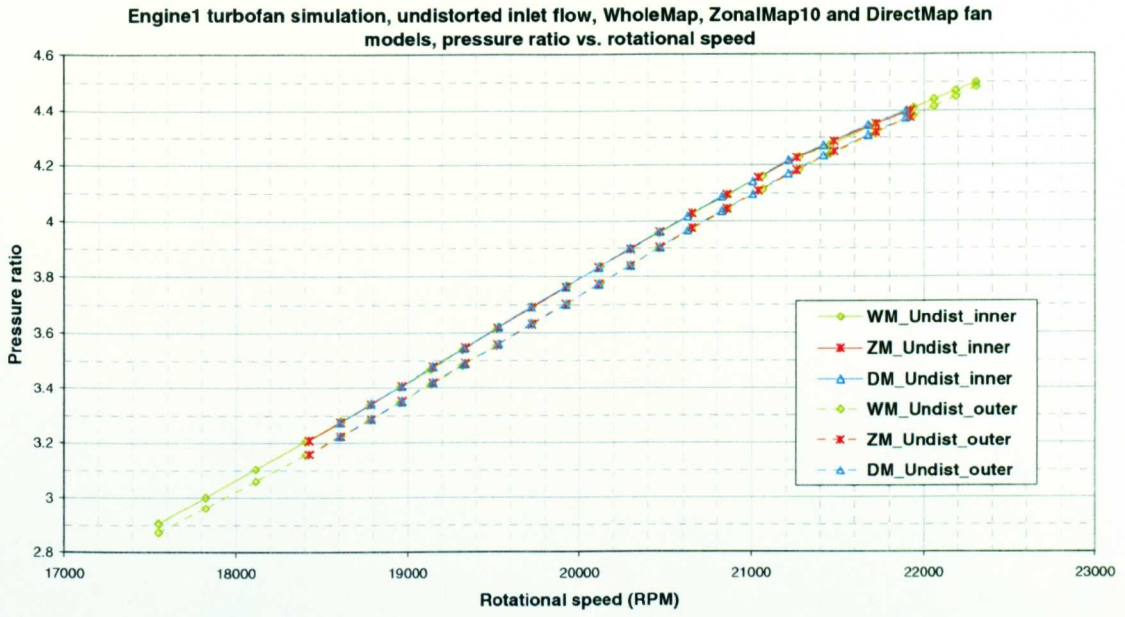

Fig. 4.89 Engine1 performance simulation: Pressure ratio vs. rotational speed for core (inner) and bypass (outer) fan of 3 fan models with undistorted fan inlet flow.

The fan exit total temperature profiles (**Fig. 4.92**) show higher temperature regions in the hub and tip regions relative to the average, as would be expected from increased turning of lower axial velocity flow in the hub, increased work due to higher blade speed in the tip regions and also due to increased losses in both these regions, as shown by the efficiency profiles (**Fig. 4.93**). The overall fan efficiency rises with reducing speed in this engine as shown by the efficiency working line (Fig. 4.85) which peaks at approximately 13 kg/s mass flow (≈19200rpm). This is probably due to reduced shock losses.

4.8.2 WholeMap undistorted inlet flow

As described in section **4.8.1**, the WholeMap simulation suffers from a discrepancy in the region around 12.7 to 13.5 kg/s mass flow shown for example by differences in the isentropic efficiency profile calculation compared to WholeMap and DirectMap. This is caused by the interpolation between the shorter 85% speed line and the much longer neighbouring 90% speed line in the fan characteristic (**Fig. 4.83**). It would have helped to have put in more speed lines between these two speeds although it is normal to have a limited number of speed lines in current methods because of the cost of testing. Had time permitted, a study could be carried out to trim the higher mass flow end of the 90% speed line and then check the effect on the profiles.

The WholeMap model gives by far the most rapid calculations once the map has been computed. Full implementation of the model will require iteration of the inlet profile and therefore, computation of the full map is not likely to be done or a strategy devised to interpolate between pre-calculated maps with fixed inlet profiles.

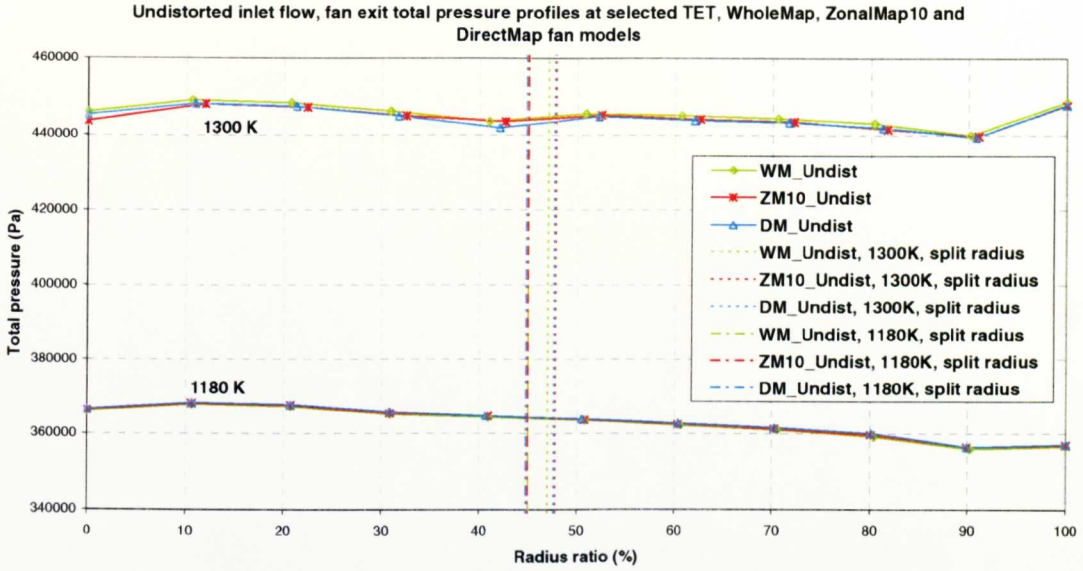

Fig. 4.90 Undistorted inlet flow, engine simulation fan exit total pressure profiles at 1300K, 1180K TET for WholeMap, ZonalMap10 and DirectMap fan models with indicated radial split position for bypass flow.

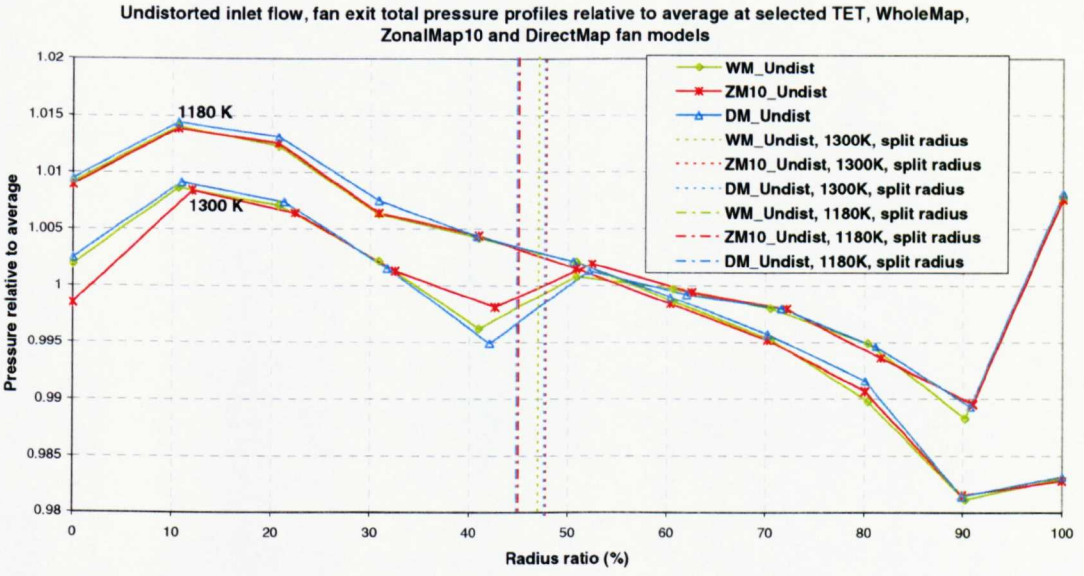

Fig. 4.91 Undistorted inlet flow, engine simulation fan exit total pressure profiles normalised to radial average at 1300K, 1180K TET for WholeMap, ZonalMap10 and DirectMap fan models with indicated radial split position for bypass flow.

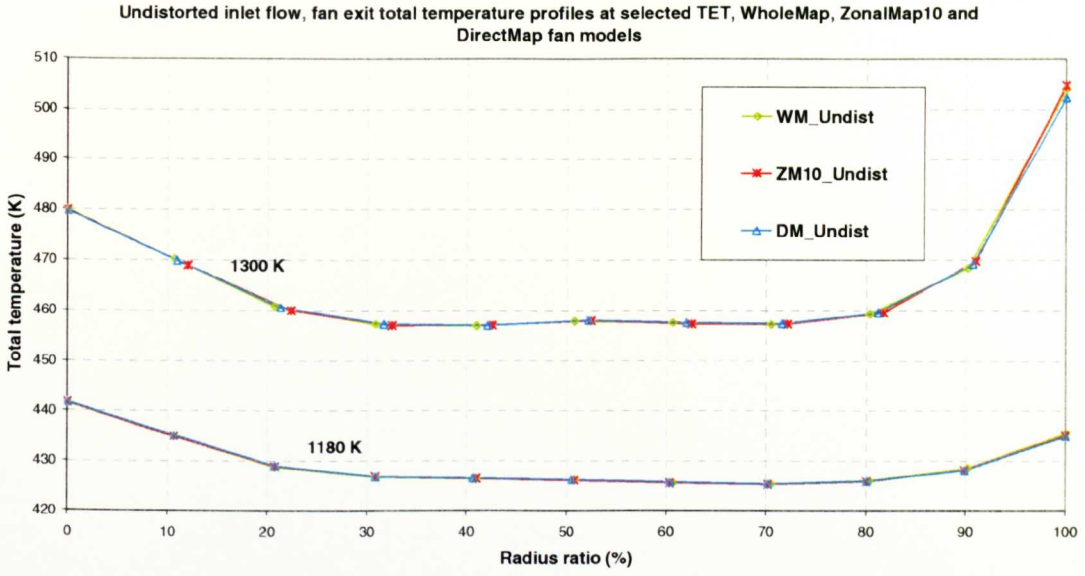

Fig. 4.92 Undistorted inlet flow, engine simulation fan exit total temperature profiles at 1300K, 1180K TET for WholeMap, ZonalMap10 and DirectMap fan models.

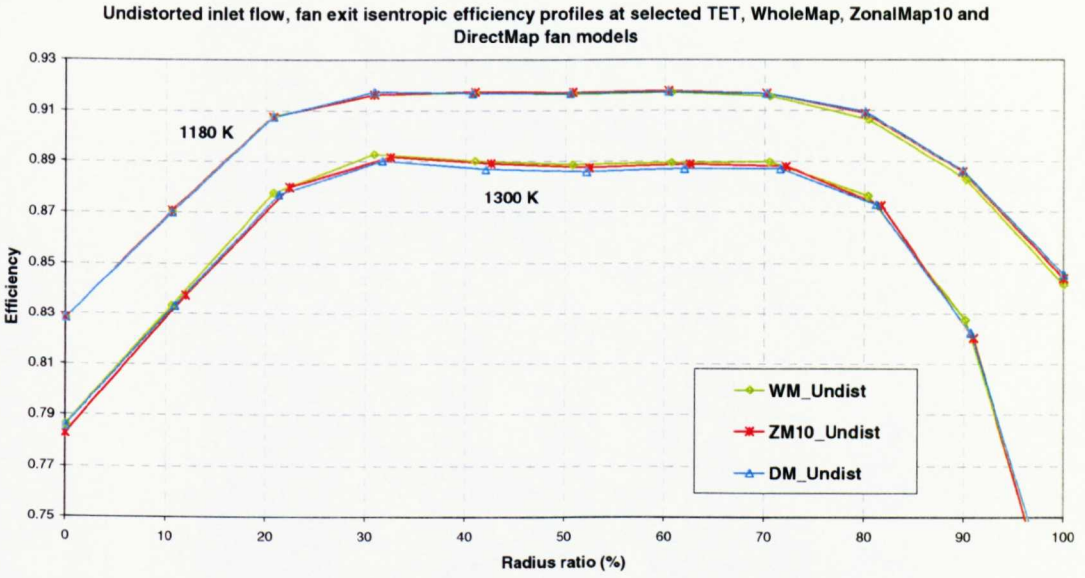

Fig. 4.93 Undistorted inlet flow, engine simulation fan isentropic efficiency profiles at 1300K, 1180K TET for WholeMap, ZonalMap10 and DirectMap fan models.

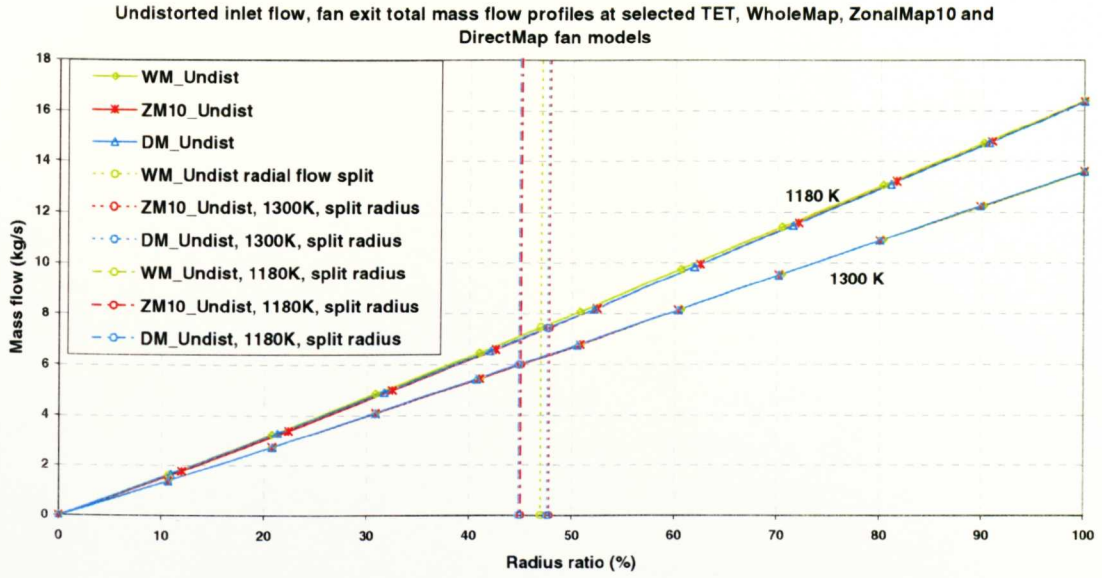

Fig. 4.94 Undistorted inlet flow, engine simulation fan exit total mass flow profiles at 1300K, 1180K TET for WholeMap, ZonalMap10 and DirectMap fan models with indicated radial split position for bypass flow.

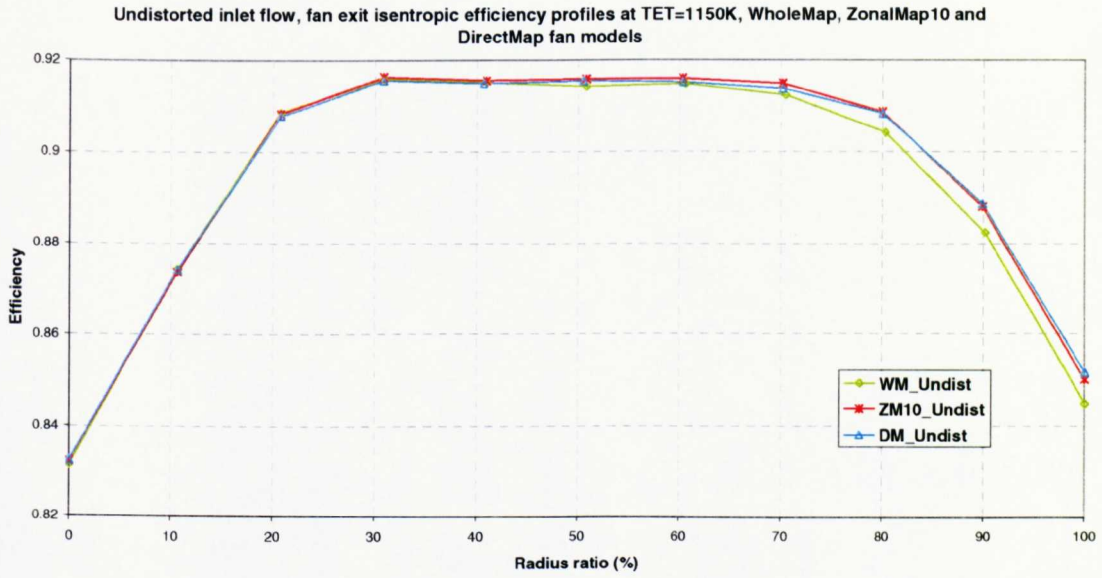

Fig. 4.95 Undistorted inlet flow, engine simulation fan isentropic efficiency profiles at 1150K TET for WholeMap, ZonalMap10 and DirectMap fan models.

4.8.3 ZonalMap

ZonalMap results are generally the same as the WholeMap conventional 2D-fan method in terms of the working line results and the 2D-profiles. The results do not show the profile distortions shown by WholeMap in the regions described in section **4.8.2**. Therefore,

although it has differences depending on which two speed lines are used in the zone, these are smaller than the differences caused by using different length speed lines that result in WholeMap from the SLC program.

4.8.4 DirectMap

DirectMap calculations give generally the same results as WholeMap and ZonalMap within the accuracy loss caused by the relaxed convergence limits. There is confidence in the future fully implemented method having the best accuracy of the three methods. It is felt that the artificial stall checker that has not been tested yet would have extended the working line calculation by allowing use of the full speed lines, also true of ZonalMap.

4.9 DISTORTED INLET CASE STUDIES

4.9.1 Cases of inlet distortions

The cases of tested distortions in **Fig. 4.82** were designed as follows.

(i) The streamline curvature code was run for the nominally selected design point and speed with undistorted uniform inlet flow and the static pressure profile obtained at the inlet. The choice of inlet profile was purely arbitrary, and a loss of total pressure at any point along the inlet radius can be regarded simply as a loss of dynamic pressure (total – static pressure) with respect to the undistorted inlet flow. Loss of the undistorted inlet dynamic pressure profile therefore sets a realistic limit for distortion.

(ii) The inlet static pressure profile from the converged undistorted SLC result will refer to different radii (where the converged streamtubes have equal mass flow) compared to the input inlet total pressure profile input into the SLC code (which is set at 10% increments of radius ratio from blade hub to tip). The loss of the undistorted design point dynamic pressure is purely used only to design aribitrary inlet total pressure profiles.

(iii) Percentage loss of the undistorted inlet dynamic pressure (**Table 25)** was arbitrarily adjusted to obtain the different cases of inlet distortion as shown in **Table 24** and **Fig. 4.82.**

(iv) A limitation is that the inlet distortion is applied at the first dummy blade row and not at IGV face. Although there is no work is applied in the dummy rows, the profile is not the same shape in the two locations as the area is very different, (**Fig. 4.4**).

Radial station	1	2	3	4	5	6	7	8	9	10	11
Radius (m)	0.005	0.030	0.055	0.080	0.104	0.129	0.154	0.179	0.204	0.229	0.254
TipDist1	0	0	0	0	0	0	10	15	20	30	97
HubDist1	97	30	20	15	10	0	0	0	0	0	0
TipHubDist1	97	30	20	15	10	0	10	15	20	30	97
TipDist2	0	5	10	20	30	40	50	60	75	87	95

Table 25 Arbitrary percentage loss of fan inlet dynamic pressure of undistorted design point case to create inlet distortion cases.

4.9.2 Comparison of 3 fan models

Fig. 4.96 compares the converged fan exit total pressure profiles for all 3 fan models with undistorted inlet flow and TipDist1 case of inlet distortion run at 1300K and 1220K TETs. The 3 fan models give the same shape profile, and this is also true of other parameters such as total temperature and efficiency. The result is repeated for the other distortion cases tested.

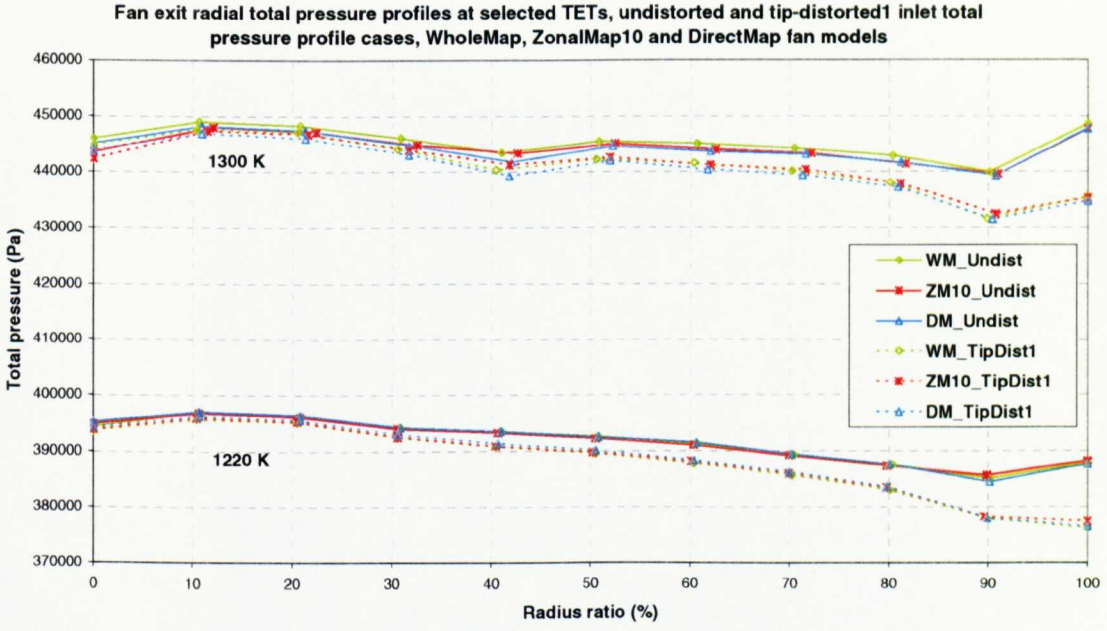

Fig. 4.96 Fan exit radial total pressure profiles: comparison of TipDist1 inlet distortion with undistorted inlet flow for 3 fan models.

The variability between the 3 fan models is greater at higher power settings, for example, in **Fig. 4.96**, for TET=1300K the maximum spread in fan exit total pressure at a radius is 0.2% of the average value, compared to only 0.1% at 1220K despite the lower level of pressure.

The 3 fan models all give the same pattern when run with a particular inlet distortion case. The fan exit total pressure profile for TipDist1 for ZonalMap in **Fig. 4.97** is replicated by the other 2 fan models. For simplicity, the presentation of results will therefore not show all 3 models each time. As the engine thrust is decreased, the increase in bypass ratio is reflected by a change in the fan exit flow split radius, from approximately 47.8% radius ratio to 45.4% for the undistorted case (the mass flow at these thrusts are different). The flow split radii for the distorted flow cases do not vary much from the undistorted case when the engine is run to a TET; within a 0.5 to 1% radius ratio spread (higher for higher power setting), although the trends are fairly repeatable.

4.9.3 Tip-distorted case 1 (TipDist1)

This inlet distortion averages to a 0.6% loss of total pressure compared to the undistorted case. **Fig. 4.97** shows the fan exit total pressure profiles for the 4 inlet distorted cases compared to the undistorted case at 1300K and 1220K (approximately 100% and 89% fan speed respectively).

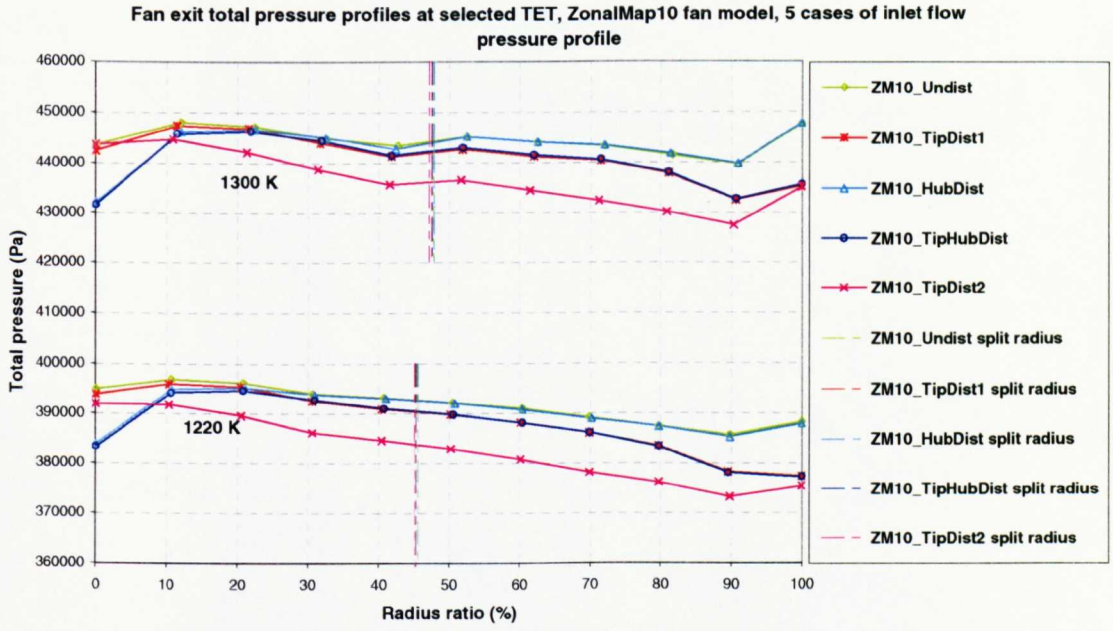

Fig. 4.97 Fan exit radial total pressure for engine1 at 1300K and 1220K TET, for 5 cases of inlet total pressure profiles, ZonalMap10 fan model.

The inlet tip distortion is fairly unattenuated passing through the 3 fan stages. The radial pressure ratio profile of this fan is fairly flat as indicated by the undistorted fan exit profile. A

fan with a higher tip pressure ratio would attenuate a tip distorted profile, (e.g. Tamaki and Nagano, 1979, see section **2.4.2**).

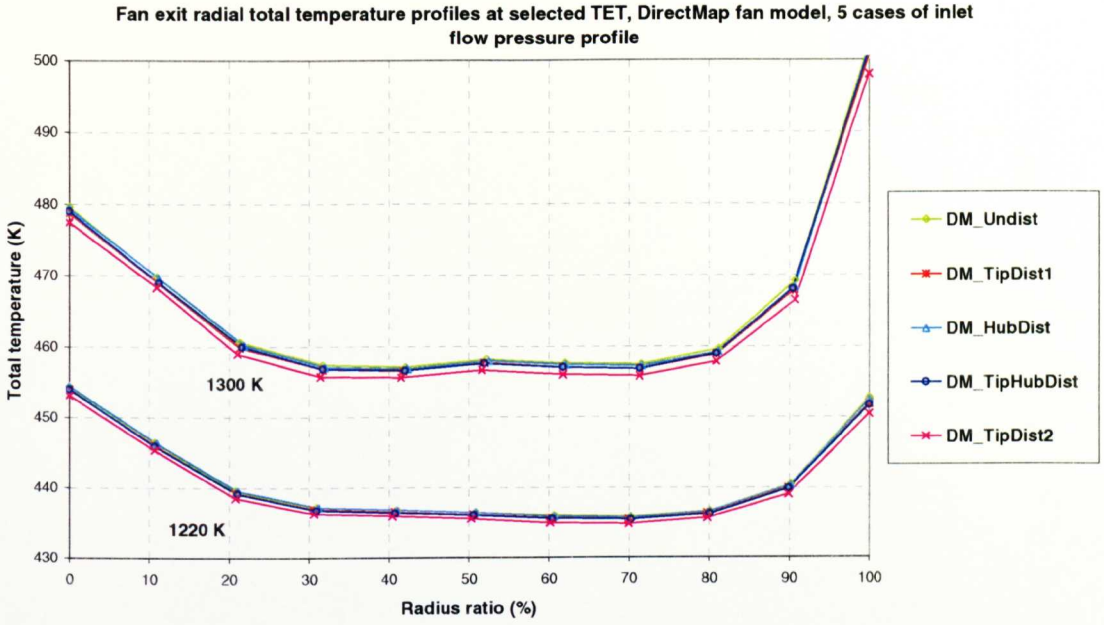

Fig. 4.98 Fan exit radial total temperature for engine1 at 1300K and 1220K TET, for 5 cases of inlet total pressure profiles, DirectMap fan model.

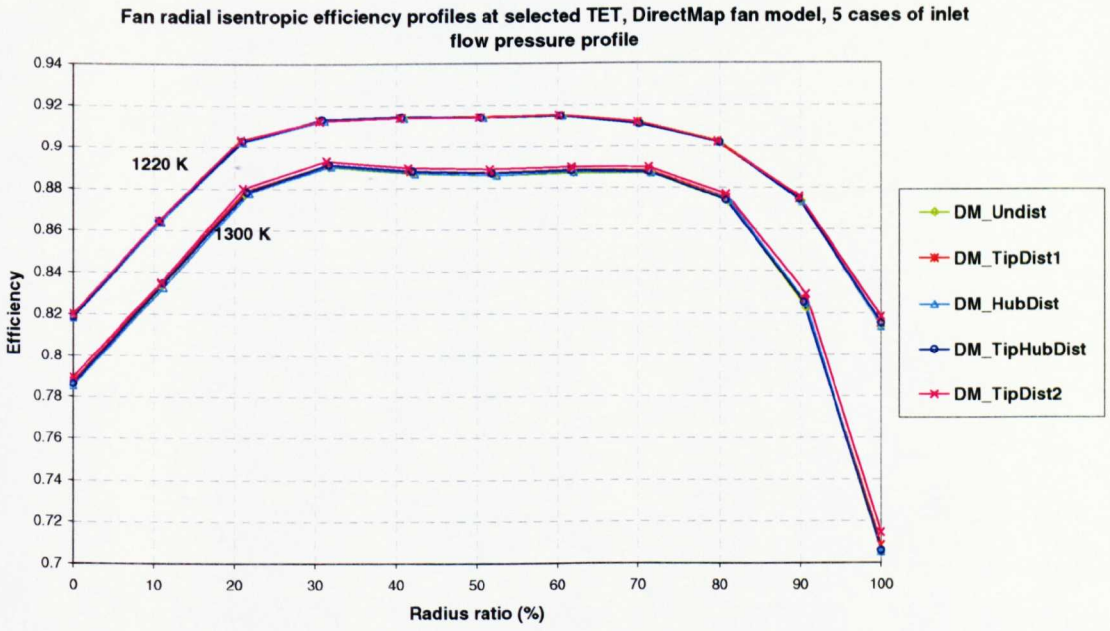

Fig. 4.99 Fan radial isentropic efficiency profiles for engine1 at 1300K and 1220K TET, for 5 cases of inlet total pressure profiles, DirectMap fan model.

	Fan model	ZM10 Undist	ZM10 TipDist1	ZM10 TipDist2	ZM10 HubDist	ZM10 TipHubDist
TET		**1300K**	**1300K**	**1300K**	**1300K**	**1300K**
P20	Abs (Pa)	101325	100754.2	99703.9	101213.7	100642.9
	Diff (%)		-0.56%	-1.60%	-0.11%	-0.67%
Thrust	Abs (N)	7597.0	7524.6	7402.9	7586.9	7518.6
	Diff (%)		-0.953%	-2.555%	-0.133%	-1.033%
RPMFAN	Abs (rpm)	21919.3	21900.7	21884.1	21920.3	21904.6
	Diff (%)		-0.085%	-0.160%	0.005%	-0.067%
RFAN	Abs	4.384	4.378	4.373	4.384	4.381
	Diff (%)		-0.174%	-0.311%	0.011%	-0.103%
ETAFan	Abs	0.8565	0.8568	0.8577	0.8568	0.8572
	Diff (%)		0.033%	0.146%	0.042%	0.082%
W20	Abs (kg/s)	16.3805	16.2721	16.0877	16.3653	16.2627
	Diff (%)		-0.662%	-1.788%	-0.093%	-0.719%
BPR	Abs	1.20015	1.2002	1.1996	1.2003	1.1999
	Diff (%)		0.004%	-0.047%	0.015%	-0.018%
Wcore	Abs (kg/s)	7.4452	7.3958	7.3140	7.4377	7.3924
	Diff (%)		-0.664%	-1.763%	-0.101%	-0.709%
Wbypass	Abs (kg/s)	8.9353	8.8764	8.7738	8.9276	8.8704
	Diff (%)		-0.660%	-1.808%	-0.086%	-0.727%
R_core	Abs	4.3976	4.3911	4.3892	4.3974	4.3942
	Diff (%)		-0.191%	-0.248%	-0.007%	-0.101%
R_bypass	Abs	4.3727	4.3673	4.3604	4.3736	4.3692
	Diff (%)		-0.160%	-0.365%	0.025%	-0.105%
R_core/bypass	Diff (%)	-0.73%	-0.70%	-0.85%	-0.70%	-0.74%
P_core	Abs (Pa)	445585.7	442421.6	437617.5	445072.3	442240.1
	Diff (%)		-0.710%	-1.788%	-0.115%	-0.751%
P_bypass	Abs (Pa)	443066.7	440028.7	434750.5	442666.5	439727.7
	Diff (%)		-0.686%	-1.877%	-0.090%	-0.754%
Fuel	Abs (kg/s)	0.1256	0.1248	0.1235	0.1255	0.1247
	Diff (%)		-0.620%	-1.648%	-0.086%	-0.663%
SFC	Abs (kg/s/MN)	16.529	16.584	16.683	16.536	16.590
	Diff (%)		0.336%	0.931%	0.047%	0.373%

Table 26 Comparison of engine parameters for simulation of Engine1 at 1300K TET with undistorted and 4 inlet distortion pressure profiles, ZonalMap10 fan model.

The fan exit total temperature profiles for all the distortion cases are shown in **Fig. 4.98**. The profile for TipDist1 is almost the same as the undistorted profile, within 0.5K at each radius. The efficiency profile is similarly nearly identical as shown in **Fig. 4.99**. These findings are checked using the standalone SLC code, inputting the converged values of rotational speed and mass flow and the radial inlet conditions for each distortion. The results confirmed the true simulation of the SLC code within each fan model in the simulation code.

	Fan model	ZM10 Undist	ZM10 TipDist1	ZM10 TipDist2	ZM10 HubDist	ZM10 TipHubDist
TET		**1220K**	**1220K**	**1220K**	**1220K**	**1220K**
P20	Abs (Pa)	101325	100754.2	99703.9	101213.7	100642.9
	Diff (%)		-0.56%	-1.60%	-0.11%	-0.67%
Thrust	Abs (N)	6155.2	6085.6	5960.8	6141.2	6075.3
	Diff (%)		-1.131%	-3.158%	-0.227%	-1.298%
RPM	Abs (rpm)	20296.9	20267.7	20219.9	20288.5	20267.2
	Diff (%)		-0.144%	-0.379%	-0.041%	-0.146%
RFAN	Abs	3.865	3.855	3.837	3.863	3.855
	Diff (%)		-0.260%	-0.717%	-0.056%	-0.265%
ETAFan	Abs	0.8918	0.8918	0.8921	0.8918	0.8921
	Diff (%)		0.007%	0.037%	0.004%	0.035%
W20	Abs (kg/s)	14.5260	14.4135	14.2068	14.5035	14.3971
	Diff (%)		-0.774%	-2.197%	-0.155%	-0.887%
BPR	Abs	1.252626	1.2521	1.2531	1.2526	1.2520
	Diff (%)		-0.042%	0.039%	-0.001%	-0.049%
Wcore	Abs (kg/s)	6.4485	6.4000	6.3054	6.4385	6.3930
	Diff (%)		-0.751%	-2.218%	-0.154%	-0.861%
Wbypass	Abs (kg/s)	8.0775	8.0135	7.9014	8.0650	8.0041
	Diff (%)		-0.793%	-2.180%	-0.155%	-0.909%
R_core	Abs	3.8976	3.8882	3.8695	3.8954	3.8884
	Diff (%)		-0.327%	-0.972%	-0.077%	-0.319%
R_bypass	Abs	3.8390	3.8285	3.8116	3.8368	3.8279
	Diff (%)		-0.369%	-0.963%	-0.076%	-0.390%
R_core/bypass	Diff (%)	-2.02%	-2.07%	-2.02%	-2.02%	-2.09%
P_core	Abs (Pa)	394929.4	391749.1	385802.7	394270.9	391340.1
	Diff (%)		-0.805%	-2.311%	-0.167%	-0.909%
P_bypass	Abs (Pa)	388984.3	385736.7	380034.6	388339.1	385251.6
	Diff (%)		-0.835%	-2.301%	-0.166%	-0.960%
Fuel	Abs (kg/s)	0.0998	0.0991	0.0978	0.0997	0.0990
	Diff (%)		-0.682%	-1.982%	-0.141%	-0.786%
SFC	Abs (kg/s/MN)	16.218	16.292	16.415	16.232	16.302
	Diff (%)		0.453%	1.214%	0.086%	0.519%

Table 27 Comparison of engine parameters for simulation of Engine1 at 1220K TET with undistorted and 4 inlet distortion pressure profiles, ZonalMap10 fan model.

The following simplified analysis is made with reference to **Table 26** and **Table 27**. With the HPT nozzle guide vanes choked, the flow function $(W\sqrt{T}/P)_4$ there is effectively constant. The handle being TET fixes T, the W and P at combustor exit must change to satisfy the choking flow function. With the HPT temperature ratio and pressure ratio effectively constant because of operating between choked nozzles, and efficiency not varying much with small speed changes, the HPC non-dimensional operating condition will change only a small amount. Therefore, the fan determines the W and P arising at the HPT inlet.

The fan must rematch at a speed that gives the required lower W and P to maintain choking at HPT inlet. This occurs at a lower rotational speed and the fan efficiency only slightly higher. Both inner and outer fan pressure ratios fall because of the lower speed. Fan outer exit pressures fall because of both the lower speed and the unattenuated tip distortion. Both the lower pressure levels and the lower mass flow lead to a decrease in thrust. Fuel flow decreases because of the decrease in mass flow, but the thrust falls faster and leads to an increase in SFC.

The fan efficiency characteristic for distorted flow can be seen in part for 95% and 100% design speeds in **Fig. 4.100**. The corresponding pressure ratio characteristic is shown in **Fig. 4.101**. Efficiency falls at a fixed mass flow in the right hand region of the speed line with the TipDist1 distortion applied to the inlet. For a fixed efficiency and speed, the fan passes about 3% less flow. The fan is operating near the optimum efficiency region of the efficiency lines where the change at a mass flow is smallest (merged efficiency lines), as shown by the working lines. As speed falls along the working line in the 90-100% region of the characteristic (also see **Fig. 4.84**), the efficiency rises, but the effect of the TipDist1 distortion effectively negates this in the region of the working line. This explains the small changes in the converged fan efficiency profiles with the distortion.

The pressure ratio characteristic does change in the working line region with pressure ratio falling approximately 4% at a fixed mass flow and speed, and mass flow drops about 0.6% at a fixed pressure ratio and speed.

4.9.4 Tip-distorted case 2 (TipDist2)

This is a much larger inlet distortion (**Fig. 4.82**) averaging to 1.6% decrease in total pressure compared to the undistorted case. Referring to **Fig. 4.101** and **Fig. 4.100**, the effect on the characteristic is larger at a fixed speed and mass flow. As for TipDist1, the inlet total pressure profile distortion carries through to the fan exit (**Fig. 4.97**). This observation is different from observations from circumferential distortion (Mazzawy, 1977), where low pressure inlet sectors operate in the lower flow region of the undistorted compressor map at higher pressure ratio. With circumferential distortion, the blades act to separate the low pressure sector from the higher pressure sector (in the 2 compressors in parallel model). The axial gaps between blade rows are too small to allow redistribution of flow (Mazzawy, 1977). With radial distortion, there is no structure to prevent radial redistribution of the flow.

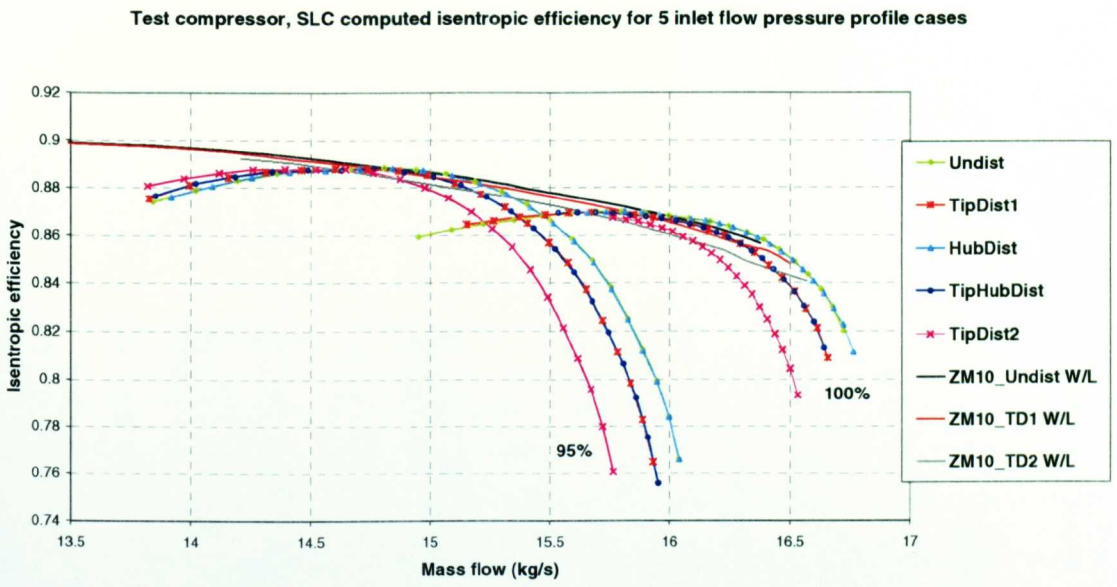

Fig. 4.100 Efficiency characteristics for Engine1 fan with 5 inlet flow profile cases computed by SLC program, working lines from 3 distortion cases.

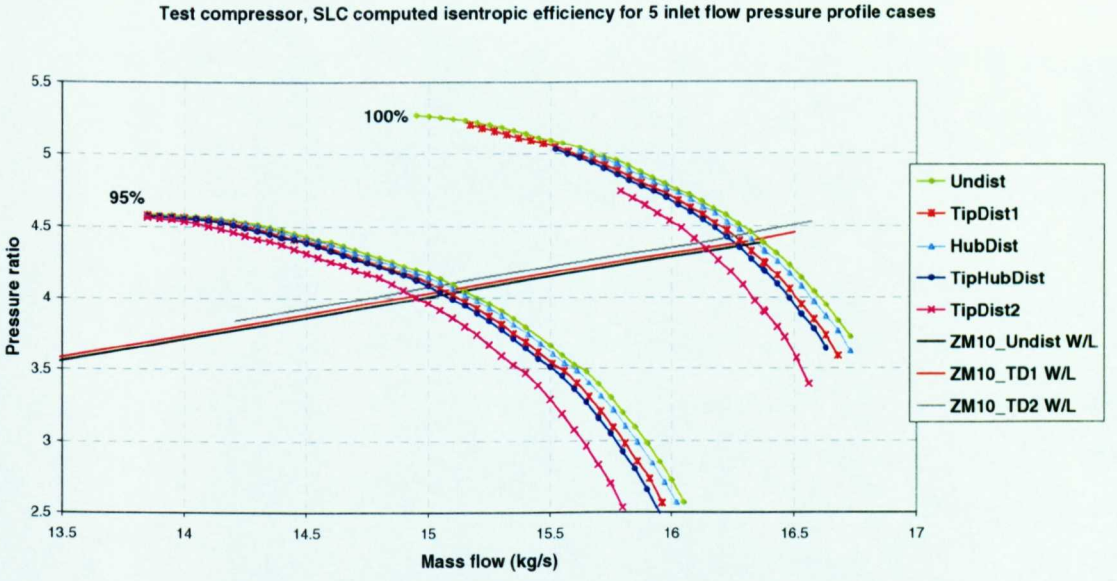

Fig. 4.101 Pressure ratio characteristics for Engine1 fan with 5 inlet flow profile cases computed by SLC program, working lines from 3 distortion cases.

The fan rematches at a lower rotational speed and at a lower mass flow in order to achieve the overall conditions for the choking HPT nozzles at the TET setting. Again, the lower efficiency at a flow due to distortion offsets the increased efficiency at the lower speed and the working line region is in the region of the efficiency line at which all the distorted lines merge (**Fig. 4.101**). The net effect is only a small increase in efficiency from the undistorted

flow (**Fig. 4.99**). At the higher distortion levels, the SLC program becomes more unstable at the stall region of the speed lines, as shown by stopping of calculation of low mass flows of the 100% speed line. This is unpredictable as closely adjacent speeds may not experience this computational instability. Percentage performance changes from undistorted flow are larger at the lower TET setting.

4.9.5 Hub-distorted case (HubDist)

The hub distortion is very small, representing only an averaged 0.1% decrease of averaged inlet total pressure. It was devised to investigate the effect of a similar distortion to TipDist1 in radial length magnitude at the hub (using a simplistic assumption of distortions having same thicknesses at the walls). The depressed pressure region acts over a smaller area at the hub than TipDist1 given the same radial length.

The resulting converged outlet pressure profile (**Fig. 4.97**) matches the undistorted flow profile except at the hub-distorted region. The outlet total temperature and isentropic efficiency profiles (**Fig. 4.98** and **Fig. 4.99** respectively) show rematching of the fan to produce almost no change in profiles. The HubDist efficiency characteristic is the same as the undistorted efficiency characteristic (**Fig. 4.100**) and the pressure ratio characteristic shows only a small change (**Fig. 4.101**).

4.9.6 Tip and hub-distorted case (TipHubDist)

The overall inlet pressure decrease is approximately 0.7%. The profile was designed to match HubDist inlet profile over the hub and TipDist1 towards the casing. The outlet total pressure profile (**Fig. 4.97**) shows the same hub profile as HubDist and the same profile over the remainder of the span as (TipDist1). The TipHubDist efficiency characteristic is the same as the TipDist1 characteristic (**Fig. 4.100**). The hub distortion applied has no effect on efficiency and a small effect on pressure ratio (**Fig. 4.101**). Consequently, the performance changes of the engine run to a TET gives virtually the same performance change from undistorted as the TipDist1 distortion.

4.9.7 Fan rotational speed as engine handle

With the conversion of the engine simulation program to use a Newton-Raphson solver for shaft power balance, the ability of the current code to use fan speed as the handle is still

to be re-implemented (section **3.6.1**). To see the effect of constant fan speed the distorted cases were run at different TET until the undistorted case fan speed was achieved.

From **Fig. 4.101**, the effect of distortion on the fan characteristic performance when running the engine at a fixed fan rotational speed is decreased mass flow and pressure ratio. However, particularly for the larger TipDist2 distortion, the working line is also raised and the net effect is to run at nearly the same pressure ratio as the undistorted case.

	Fan model	ZM10 Undist	ZM10 TipDist1	ZM10 TipDist1	ZM10 TipDist2	ZM10 TipDist2
TET		**1300**	**1300**	**1301.3**	**1300**	**1302.6**
P20	Abs (Pa)	101325	100754.2	100754.2	99703.9	99703.9
	Diff (%)		-0.56%	-0.56%	-1.60%	-1.60%
Thrust	Abs (N)	7597.0	7524.6	7539.8	7402.9	7433.7
	Diff (%)		-0.953%	-0.753%	-2.555%	-2.150%
RPM	Abs (rpm)	21919.3	21900.7	21919.2	21884.1	21919.4
	Diff (%)		-0.085%	0.000%	-0.160%	0.001%
RFAN	Abs	4.384	4.378	4.383	4.373	4.384
	Diff (%)		-0.174%	-0.028%	-0.311%	-0.012%
ETAFan	Abs	0.8565	0.8568	0.8564	0.8577	0.8567
	Diff (%)		0.033%	-0.010%	0.146%	0.023%
W20	Abs (kg/s)	16.3805	16.2721	16.2883	16.0877	16.1226
	Diff (%)		-0.662%	-0.563%	-1.788%	-1.575%
BPR	Abs	1.2002	1.2002	1.2002	1.1996	1.1986
	Diff (%)		0.004%	0.008%	-0.047%	-0.130%
Wcore	Abs (kg/s)	7.4452	7.3958	7.4030	7.3140	7.3331
	Diff (%)		-0.664%	-0.567%	-1.763%	-1.505%
Wbypass	Abs (kg/s)	8.9353	8.8764	8.8854	8.7738	8.7894
	Diff (%)		-0.660%	-0.559%	-1.808%	-1.633%
R_core	Abs	4.3976	4.3911	4.3951	4.3892	4.3988
	Diff (%)		-0.191%	-0.075%	-0.248%	0.035%
R_bypass	Abs	4.3727	4.3673	4.3731	4.3604	4.3710
	Diff (%)		-0.160%	0.011%	-0.365%	-0.051%
R_core/bypass	Diff (%)	-0.73%	-0.70%	-0.65%	-0.85%	-0.82%
P_core	Abs (Pa)	445585.7	442421.6	442820.2	437617.5	438576.7
	Diff (%)		-0.710%	-0.621%	-1.788%	-1.573%
P_bypass	Abs (Pa)	443066.7	440028.7	440609.4	434750.5	435804.8
	Diff (%)		-0.686%	-0.555%	-1.877%	-1.639%
Fuel	Abs (kg/s)	0.1256	0.1248	0.1251	0.1235	0.1242
	Diff (%)		-0.620%	-0.351%	-1.648%	-1.093%
SFC	Abs (kg/s/MN)	16.529	16.584	16.596	16.683	16.707
	Diff (%)		0.336%	0.405%	0.931%	1.080%

Table 28 Comparison of performance with undistorted inlet flow (TET 1300K) for 2 tip distorted inlet flows with engine run at constant TET and at then at constant fan rotational speed.

	Fan model	ZM10 Undist	ZM10 TipDist1	ZM10 TipDist1	ZM10 TipDist2	ZM10 TipDist2
TET		**1220**	**1220**	**1221.92**	**1220**	**1224.3**
P20	Abs (Pa)	101325	100754.2	100754.2	99703.9	99703.9
	Diff (%)		-0.56%	-0.56%	-1.60%	-1.60%
Thrust	Abs (N)	6155.2	6085.6	6112.2	5960.8	6025.0
	Diff (%)		-1.131%	-0.698%	-3.158%	-2.114%
RPM	Abs (rpm)	20296.9	20267.7	20297.0	20219.9	20296.0
	Diff (%)		-0.144%	0.000%	-0.379%	-0.004%
RFAN	Abs	3.865	3.855	3.865	3.837	3.864
	Diff (%)		-0.260%	0.006%	-0.717%	-0.031%
ETAFan	Abs	0.8918	0.8918	0.8914	0.8921	0.8913
	Diff (%)		0.007%	-0.041%	0.037%	-0.055%
W20	Abs (kg/s)	14.5260	14.4135	14.4485	14.2068	14.2976
	Diff (%)		-0.774%	-0.533%	-2.197%	-1.572%
BPR	Abs	1.2526	1.2521	1.2522	1.2531	1.2508
	Diff (%)		-0.042%	-0.037%	0.039%	-0.149%
Wcore	Abs (kg/s)	6.4485	6.4000	6.4118	6.3054	6.3524
	Diff (%)		-0.751%	-0.569%	-2.218%	-1.490%
Wbypass	Abs (kg/s)	8.0775	8.0135	8.0293	7.9014	7.9452
	Diff (%)		-0.793%	-0.597%	-2.180%	-1.637%
R_core	Abs	3.8976	3.8882	3.8971	3.8695	3.8967
	Diff (%)		-0.327%	-0.019%	-0.972%	-0.031%
R_bypass	Abs	3.8390	3.8285	3.8398	3.8116	3.8375
	Diff (%)		-0.369%	0.029%	-0.963%	-0.051%
R_core/bypass	Diff (%)	-2.02%	-2.07%	-1.98%	-2.02%	-2.04%
P_core	Abs (Pa)	394929.4	391749.1	392430.9	385802.7	388519.9
	Diff (%)		-0.805%	-0.633%	-2.311%	-1.623%
P_bypass	Abs (Pa)	388984.3	385736.7	386650.6	380034.6	382615.7
	Diff (%)		-0.835%	-0.600%	-2.301%	-1.637%
Fuel	Abs (kg/s)	0.0998	0.0991	0.0996	0.0978	0.0991
	Diff (%)		-0.682%	-0.199%	-1.982%	-0.772%
SFC	Abs (kg/s/MN)	16.218	16.292	16.299	16.415	16.440
	Diff (%)		0.453%	0.502%	1.214%	1.371%

Table 29 Comparison of performance with undistorted inlet flow (TET 1220K) for 2 tip distorted inlet flows with engine run at constant TET and then at constant fan rotational speed.

Only the tip distortions have been investigated as the hub distortions analysed in sections **4.9.5** and **4.9.6** show very little effect. Overall, at constant fan speed, the distortions result in running at a higher TET, the difference being higher at lower power settings (**Table 28**, **Table 29**). The effect on performance at a fixed speed is slightly less than for a fixed TET setting. When controlling to a fan speed, the increase in TET needs to be known in the design phase when setting the surge margin due to the higher working line and the uncertainty of the effect of distortion on lowering the surge line. Also, better knowledge will

help in setting the TET limit margins for blade life, as the effect has to be added to other effects such as ageing and control tolerances.

4.9.8 Comparison with uniform inlet

The inlet distortion cases tested previously have also been compared to the engine running with uniform inlet total pressures equivalent to the area averaged total pressures of the distortion cases. The results are tabulated in **Table 30** and **Table 31** for 1300K and 1220K TET respectively. The difference in engine performance between the averaged inlet and the distorted inlet is quite small, though larger for the TipDist2 case.

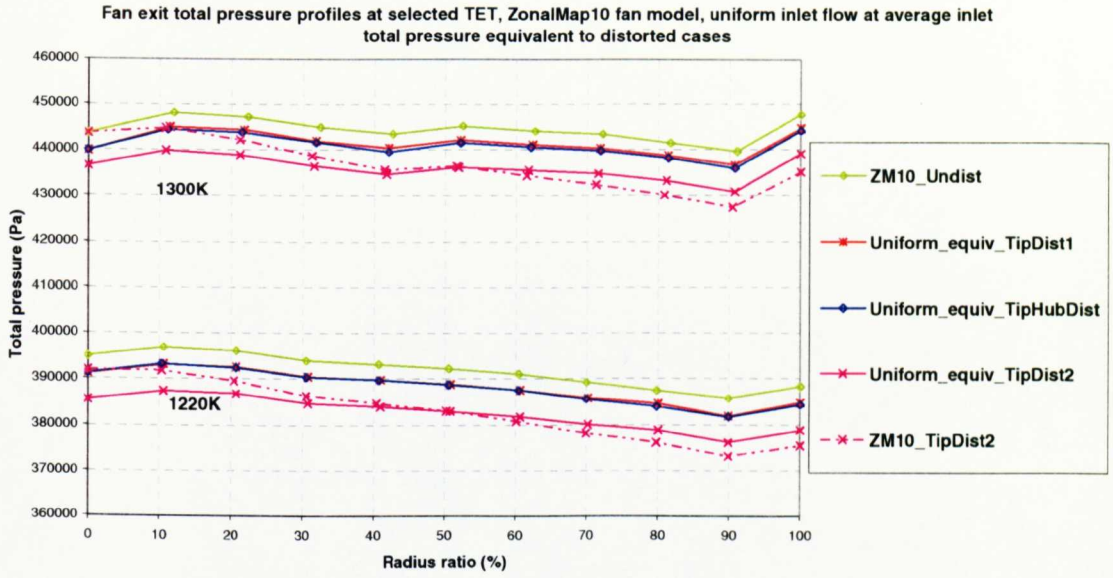

Fig. 4.102 Fan exit total pressure profiles for uniform flow at inlet total pressure equivalent to area averaged distorted inlet cases.

The fan exit profiles for the tested cases are shown in **Fig. 4.102** with the distorted TipDist2 profile for comparison. The change in profile for TipDist2 for example from its undistorted equivalent is appreciable, but makes a fairly small difference on the engine performance. It is concluded that the major determinant on fan performance in this case is the underlying fan exit total pressure level. A combination of the underlying pressure ratio profile (i.e. radial work distribution) and the high pressure ratios of multistage low bypass fans determine the pressure profile at fan exit. With a low bypass fan, the pressure ratio profile is likely to be fairly flat such that changes due to inlet distortion become a small

proportion of the exit total pressure. This also means that bypass ratio changes are fairly small as distortions have a fairly small effect on core and bypass entry total pressures.

	Fan model	ZM10 Undist	ZM10 TipDist1	ZM10 Undist equiv.	ZM10 TipDist2	ZM10 Undist equiv.	ZM10 TipHubDist	ZM10 Undist equiv.
TET		**1300**	**1300**	**1300**	**1300**	**1300**	**1300**	**1300**
P20	Abs (Pa)	101325	100754.2	100754.2	99703.9	99703.9	100642.9	100642.9
	Diff (%)		-0.56%	-0.56%	-1.60%	-1.60%	-0.67%	-0.67%
Thrust	Abs (N)	7597.0	7524.6	7526.1	7402.9	7394.1	7518.6	7513.1
	Diff (%)		-0.953%	-0.934%	-2.555%	-2.671%	-1.033%	-1.105%
RPM	Abs (rpm)	21919.3	21900.7	21901.8	21884.1	21867.3	21904.6	21901.4
	Diff (%)		-0.085%	-0.080%	-0.160%	-0.237%	-0.067%	-0.082%
RFAN	Abs	4.384	4.378	4.379	4.373	4.371	4.381	4.378
	Diff (%)		-0.174%	-0.154%	-0.311%	-0.395%	-0.103%	-0.169%
ETAFan	Abs	0.8565	0.8568	0.8569	0.8577	0.8583	0.8572	0.8569
	Diff (%)		0.033%	0.046%	0.146%	0.209%	0.082%	0.049%
W20	Abs (kg/s)	16.3805	16.2721	16.2744	16.0877	16.0757	16.2627	16.2548
	Diff (%)		-0.662%	-0.648%	-1.788%	-1.861%	-0.719%	-0.767%
BPR	Abs	1.2002	1.2002	1.2002	1.1996	1.2005	1.1999	1.2000
	Diff (%)		0.004%	0.007%	-0.047%	0.033%	-0.018%	-0.016%
Wcore	Abs (kg/s)	7.4452	7.3958	7.3966	7.3140	7.3053	7.3924	7.3887
	Diff (%)		-0.664%	-0.652%	-1.763%	-1.878%	-0.709%	-0.759%
Wbypass	Abs (kg/s)	8.9353	8.8764	8.8777	8.7738	8.7704	8.8704	8.8661
	Diff (%)		-0.660%	-0.645%	-1.808%	-1.846%	-0.727%	-0.774%
R_core	Abs	4.3976	4.3911	4.3919	4.3892	4.3862	4.3942	4.3919
	Diff (%)		-0.191%	-0.167%	-0.248%	-0.334%	-0.101%	-0.168%
R_bypass	Abs	4.3727	4.3673	4.3679	4.3604	4.3577	4.3692	4.3670
	Diff (%)		-0.160%	-0.142%	-0.365%	-0.446%	-0.105%	-0.171%
R_core/ bypass	Diff (%)	-0.73%	-0.70%	-0.71%	-0.85%	-0.84%	-0.74%	-0.74%
P_core	Abs (Pa)	445585.7	442421.6	442504.9	437617.5	437325.3	442240.1	442013.2
	Diff (%)		-0.710%	-0.691%	-1.788%	-1.854%	-0.751%	-0.802%
P_bypass	Abs (Pa)	443066.7	440028.7	440086.8	434750.5	434477.8	439727.7	439502.7
	Diff (%)		-0.686%	-0.673%	-1.877%	-1.939%	-0.754%	-0.804%
Fuel	Abs (kg/s)	0.1256	0.1248	0.1248	0.1235	0.1234	0.1247	0.1247
	Diff (%)		-0.620%	-0.612%	-1.648%	-1.719%	-0.663%	-0.713%
SFC	Abs (kg/s/MN)	16.529	16.584	16.582	16.683	16.690	16.590	16.594
	Diff (%)		0.336%	0.325%	0.931%	0.978%	0.373%	0.396%

Table 30 Distorted inlet flow cases and their respective undistorted inlet flow case at equivalent inlet averaged total pressure, all compared to undistorted flow at ISASLS, TET 1300K.

	Fan model	ZM10 Undist	ZM10 TipDist1	ZM10 Undist equiv.	ZM10 TipDist2	ZM10 Undist equiv.	ZM10 TipHubDist	ZM10 Undist equiv.
TET		**1220**	**1220**	**1220**	**1220**	**1220**	**1220**	**1220**
P20	Abs (Pa)	101325	100754.2	100754.2	99703.9	99703.9	100642.9	100642.9
	Diff (%)		-0.56%	-0.56%	-1.60%	-1.60%	-0.67%	-0.67%
Thrust	Abs (N)	6155.2	6085.6	6081.6	5960.8	5956.1	6075.3	6076.0
	Diff (%)		-1.131%	-1.195%	-3.158%	-3.234%	-1.298%	-1.286%
RPM	Abs (rpm)	20296.9	20267.7	20264.0	20219.9	20215.7	20267.2	20269.8
	Diff (%)		-0.144%	-0.162%	-0.379%	-0.400%	-0.146%	-0.133%
RFAN	Abs	3.865	3.855	3.853	3.837	3.835	3.855	3.855
	Diff (%)		-0.260%	-0.315%	-0.717%	-0.778%	-0.265%	-0.254%
ETAFan	Abs	0.8918	0.8918	0.8919	0.8921	0.8923	0.8921	0.8924
	Diff (%)		0.007%	0.008%	0.037%	0.056%	0.035%	0.069%
W20	Abs (kg/s)	14.5260	14.4135	14.4073	14.2068	14.2043	14.3971	14.3988
	Diff (%)		-0.774%	-0.817%	-2.197%	-2.214%	-0.887%	-0.875%
BPR	Abs	1.2526	1.2521	1.2527	1.2531	1.2521	1.2520	1.2526
	Diff (%)		-0.042%	0.002%	0.039%	-0.041%	-0.049%	-0.006%
Wcore	Abs (kg/s)	6.4485	6.4000	6.3957	6.3054	6.3071	6.3930	6.3922
	Diff (%)		-0.751%	-0.818%	-2.218%	-2.192%	-0.861%	-0.872%
Wbypass	Abs (kg/s)	8.0775	8.0135	8.0116	7.9014	7.8972	8.0041	8.0066
	Diff (%)		-0.793%	-0.816%	-2.180%	-2.232%	-0.909%	-0.878%
R_core	Abs	3.8976	3.8882	3.8849	3.8695	3.8673	3.8884	3.8884
	Diff (%)		-0.327%	-0.440%	-0.972%	-1.047%	-0.319%	-0.318%
R_bypass	Abs	3.8390	3.8285	3.8273	3.8116	3.8091	3.8279	3.8287
	Diff (%)		-0.369%	-0.413%	-0.963%	-1.053%	-0.390%	-0.361%
R_core/ bypass	Diff (%)	-2.02%	-2.07%	-2.00%	-2.02%	-2.03%	-2.09%	-2.07%
P_core	Abs (Pa)	394929.4	391749.1	391420.4	385802.7	385586.8	391340.1	391342.1
	Diff (%)		-0.805%	-0.889%	-2.311%	-2.366%	-0.909%	-0.908%
P_bypass	Abs (Pa)	388984.3	385736.7	385611.6	380034.6	379780.1	385251.6	385333.4
	Diff (%)		-0.835%	-0.867%	-2.301%	-2.366%	-0.960%	-0.939%
Fuel	Abs (kg/s)	0.0998	0.0991	0.0991	0.0978	0.0978	0.0990	0.0990
	Diff (%)		-0.682%	-0.738%	-1.982%	-1.989%	-0.786%	-0.800%
SFC	Abs (kg/s/MN)	16.218	16.292	16.293	16.415	16.427	16.302	16.298
	Diff (%)		0.453%	0.463%	1.214%	1.286%	0.519%	0.492%

Table 31 Distorted inlet flow cases and their respective undistorted inlet flow case at equivalent inlet averaged total pressure, all compared to undistorted flow at ISASLS, TET 1220K.

These results explain how the non-dimensional characteristics of the inlet distortions show very little changes (**Fig. 4.103**). This diagram shows how all of the distorted speed lines remain with the undistorted flow. The TipDist2 shows the largest change. This confirms the finding that the performance of the fan is equivalent to that with the average total pressure.

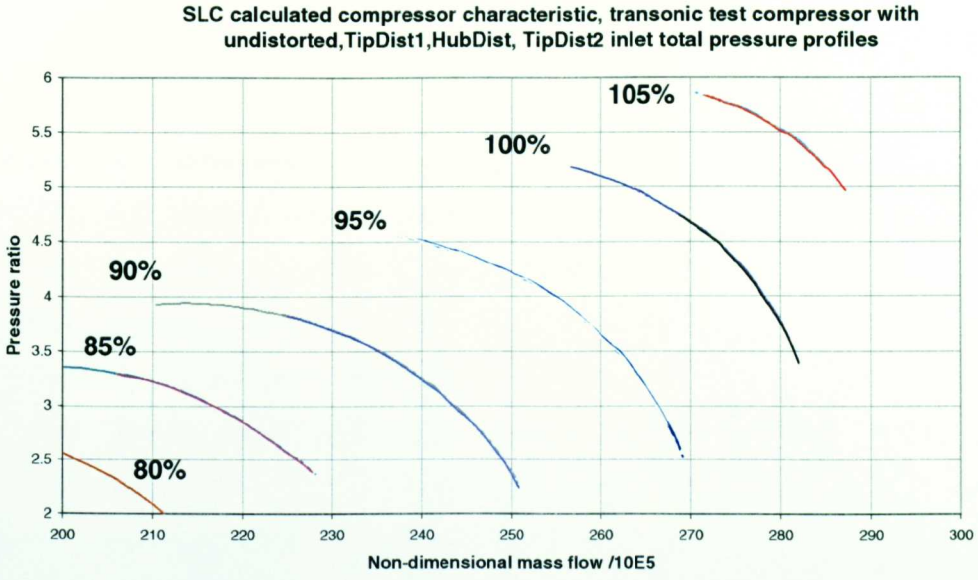

Fig. 4.103 Non-dimensional pressure ratio characteristic measured by SLC

4.10 CONCLUSIONS

The following conclusions are made

- The contribution to knowledge of this work is in detailed modelling of the fan component of a turbofan engine in an engine performance simulation. The work done has applied a known method of calculating compressor 2D performance (SLC) and merge it with a turbofan engine simulation and with a 2D fan model that uses the engine BPR to split and average fan exit profiles so that the performance change of a LBPR turbofan engine can be calculated due to a radial inlet distortion of total pressure. Although streamline curvature is often used for compressor performance prediction, this is the first known usage of it with a turbofan engine simulation.
- Interpolation within the fan characteristic of the map interpolation methods (WholeMap, ZonalMap). In 1D method fan characteristics, the beta lines are arbitrary mapping parameters to obtain operating points between speed lines. It has always been necessary to ensure that the output of rig tests gives consistent speed lines, so for example, any lack of data that results in one shortened speed line does not distort the interpolation of a point at any guess of speed. This has sometimes required manual extrapolation of speed lines, smoothing of speed lines and manual plotting of beta lines. However, because the map is 1D, the only interpolated value that is converged upon is the one that satisfies the required checks in the iteration scheme. With 2D methods, the added complication is that

each "beta" point or speed line intersection with beta now also contains the profiles that will average to the 1D value, but these profiles are split into two for the bypass and core ducts in the matching scheme. Effectively, what is being asked is that the interpolation between 2 speeds and 2 betas (in the 2D-HBPR model), and also between 2 BPRs in the 2D-LBPR model of Chapter 3 will match the profiles that would exist at that point if it could be tested. In the limit, 2 speed lines and 2 beta lines infinitely close to each other should reproduce this, but at the expense of a method that would be impractical. It has been demonstrated that interpolation between 2 speed lines of different "length" at more than 1.5% of design speed apart can give distorted profiles and affect the converged performance.

- Non-dimensionals vs. dimensionals. The success of the 1D fan characteristic has been the assumption of non-dimensional performance of the fan except at low Reynolds numbers conditions (where viscous flows become more important) and due to P1, T1 effects. These have been normally accounted for by corrections to the 1D characteristics. The prediction of performance due to inlet total pressure distortions has necessitated having a fan prediction method. It has been possible with this to perform fan calculations with dimensional parameters, directly inputting the inlet temperature, pressure, speed and mass flow. There is potential then for directly computing those effects due to viscous real flow as described depending on the effectiveness of the loss models in the streamline curvature model. The SLC fan model can also be adapted to model varying angle of VGVs with the scheduling of the angles dependent on $N/\sqrt{T}$.
- Several cases of inlet distortions have been tested which are realistic in terms of the loss of dynamic pressure of the undistorted inlet flow case. The overall conclusion with this fan is that the inlet profile continues through the 3 stage fan without attenuation to give a fan exit profile. Results have been presented for performance changes from undistorted flow at a fixed TET and fixed rotational speed. The changes are approximately equivalent to that of the undistorted inlet flow at the average of the distorted, probably due to high pressure ratio of this fan.
- The overriding conclusion from the simulation program runs in Chapter **4** is that for multistage high hub-to-casing ratio fans, there are two main drivers for radial inlet distortion effects on performance. The first is the relatively high fan pressure ratios to give the optimum cycle in LBPR fans mean that any changes in the inlet radial pressure profiles have a smaller effect on the fan exit profiles as variations in fan exit profiles

become a small percentage of the overall pressure. This is also due to the freedom of the airflow to rematch radially in the fan in contrast to circumferential distortions. For this fan, the approximation of the effect of a radial distortion is that it is equivalent to the effect of a uniform profile at the area-averaged inlet total pressure of the distortion. The second is the shape of the fan exit pressure profile, dependent on the radial input of work and the radial isentropic efficiency. A flat profile, as with the fan examined in this thesis, will have less effect on the difference in bypass duct and HPC core entry pressures with inlet distortion changes. BPR changes with inlet distortion were found to be extremely small for the test fan. A steeper profile may show greater changes in downstream pressures given an inlet distortion and therefore greater performance changes.

- The recommendations as a result of the testing of the 3 fan models. All 3 models give the same result within the limits of the accuracies that have been determined due to interpolation and due to the reduced convergence limits in DirectMap. The WholeMap model was implemented as a research exercise only. The inlet distortion model is designed to compute the performance as a result of any arbitrary inlet radial profile. The final desired implementation would include a varying inlet profile from an intake model. Therefore, the WholeMap model would be impractical as there is no need to compute the whole characteristic when only part of the fan map is required at any time, and no point in storing characteristics for a fixed distortion for interpolation when constantly varying distortions would be output by the intake model during the calculation of one operating point. The preferred method is the DirectMap model. The advantage is to avoid any of the inaccuracies due to interpolation between speed lines and beta lines. The disadvantage is when time is a constraint as every guess of speed and beta will access the SLC code. The compromise would then be to use the ZonalMap model with the recommended speed line zone of ±1.5 % design speed for the first guess. Where ZonalMap is used, the recommendation is to restrict the speed line computations to predetermined speed values to ensure repeatability of results since use of different pairs of speed lines to compute the same operating point may give a slightly different answer. A future improvement may be to restrict the calculation of the speed line lengths in the zone to save more computation, but there should be caution not to distort the interpolated profile with different length speed lines.
- Distortion descriptors. Radial distortion descriptors, e.g. K_D (ARP1420, 1978) are used by aeroengine companies to set tolerance acceptability levels for an engine. These cannot be

used as iteration guess variables in any scheme involving the intake since the descriptor refers to the worst radial difference from the radial average and so can have a random profile. The K_D can be calculated and set as a program output.

4.11 FURTHER WORK

The following points of further work have been identified:

4.11.1.1 Current modelling

- The current turbofan engine model can be amended to allow the effect of distortions to be ascertained properly at a fixed rotational speed. The mixed exhaust turbofan can also be implemented.
- The SLC code provides a wide range of data which has been captured but not made use of. For example, the meridional plot of the streamlines can be made for each converged result. This will then give an idea of streamline variations when comparing the same fan mass flow (the converged result divides the streamtubes into equivalent mass flows).
- The overall code should be simplified to enable the inputs to be applied in one file rather than several at present (due to integration of several different programs).

4.11.1.2 Future modelling

- Modelling a range of different fans. As identified above, the effect of radial distortions may have a larger effect on fans with lower FPR and with fewer stages. Also of interest would be lower hub-to-tip ratio fans as the current LBPR fan displays little variation of BPR with distortion. Fans with a more variability in exit total pressure profile should also be investigated. Time can be invested to determine how to model different fans with the current SLC code by changes to the geometry inputs. Either new geometry from a known fan can be input, or a design can be made to generate a desired radial profile of work (the original SLC code (Barbosa, 1987) also had a design mode). The user will also need to invest time to learn how to make the necessary adjustments to a range of input parameters to achieve convergence, e.g. relaxation factors in the iterative loops.
- SLC program improvements - theory. The main improvement in capability would be to update the loss, deviation and blockage models. In the opinion of Denton and Dawes (1999), the accuracy of SLC methods is dependent on the empiricism of these models. In particular, the models of Gallimore and Cumpsty (1986), Adkins and Smith (1982) should be considered. These models distribute the prediction of loss from a multistage SLC fan

model at the hub and casing to better simulate actual findings of the radial temperature profile across the span. Without it, the loss at the mid-span tends to be under-predicted, and the loss at the walls over-predicted. Further improvements include adding the capability of modelling prescribed vane shapes compared to fixed blade profile types.

- SLC program improvements – theory. The difference in averaging for calculation of 1D efficiency in the SLC code and the performance code needs investigating. The 1D-averaged values differed by 2% throughout the characteristic map although no difference was detected in the averaging for pressure ratio. This did not affect the findings of this work as only the same calculation procedure for efficiency was used at all times.
- SLC program improvements – theory. Further improvements can be made to the setting of stall and choke in the SLC code. The current detection of stall is when a local (i.e. a streamtube) diffusion factor is exceeded after program convergence. The diffusion factor is based on Lieblein (Barbosa, 1987). This appears not to work in the version of the program used. Detection of choke in the SLC procedure is when an increase in the guess of the mid-span meridional velocity gives rise to a decrease in mass flow when the radial velocity distribution is integrated. This may also not be working correctly in the current code given the length of some speed lines compared to others.
- SLC program development: The SLC code should be modified to apply the inlet distortion to the IGV inlet face instead of the first "dummy" blade row.
- SLC program improvements – practicality: As identified, all inputs and outputs to the code should be made double precision to provide sufficient precision for the checking procedure in the engine performance code. A thorough understanding of the internal convergence procedures within the SLC code needs to be understood to carry this out as a initial trial that was carried out had failed. The use of text files for communication between the engine code and the SLC code needs to be removed. This would improve drastically the performance convergence times, currently at approximately 25mins on a 2GHz Athlon 2400 with 512MB ram. The SLC convergence is approximately 1 second. It is recommended therefore to integrate the SLC program with the performance program. The subroutines can be kept separate but a thorough review would be required to ensure parameter names are not repeated within the 2 codes.
- SLC program development: Although this has less relevance to fans, there is potential to investigate the steady-state effect of bleeds and heat soakage in a compressor. A bleed could be modelled as a step change in mass flow across part of the radius of a blade row.

Heat transfer effects to the air could be modelled as changes in ΔH. An investigation could also be made to see if a change of stator vane angle with change in $N/\sqrt{T}$ is practical. This would be a study of whether the code would converge without user intervention in terms of the convergence parameters.

- SLC program development: BPR investigations. To investigate the effect of the bypass splitter and to potentially provide data for the 2D-LBPR fan model in Chapter 3, a study should be made to see how this feature can be modelled within the existing SLC program. It has already been intimated that a SLC code can be adapted to model the bypass flow (Novak, 1967).
- Intake model scheme. A steady-state 2D-intake model needs to be added to completely compute 2D inlet distortion of an aeroengine. The current model applies an inlet distortion to the fan inlet face (or strictly speaking in this SLC model, at the dummy blade row upstream of the fan face). The converged output of the SLC includes the static pressure profile at this station. The flow through the intake will be a function of the suction from the fan (which depends on the fan operating point) and the forward flight speed. For the intake, the inlet total pressure, the total pressure loss and static pressure at exit could determine the mass flow. A possible scheme could be to have a range of CFD computed intake maps at different ambient and flight conditions using an intake exit static pressure. An experiment could be conducted to match the static pressure between the intake and the fan.

Chapter 5

CONCLUSIONS AND FURTHER WORK

5 CONCLUSIONS AND FURTHER WORK

The conclusions and further work at the end of Chapters 3 and 4 are reiterated here.

5.1 FAN EXIT PROFILE AND BYPASS RATIO EFFECTS

The contribution to knowledge of the fan exit profile research is to understand an existing scenario of LBPR fan performance from literature review evidence and examination of fan test data to provide a fan model within an engine simulation model that can model the scenario in a higher detail than presently possible, and also to provide a more versatile fan model that is able to automatically adjust to the effect of changes in other components' performances for example. The following are the key points.

- HBPR fans show constant fan performance at fixed non-dimensional speed and flow function when the bypass ratio is varied. They have small fan pressure ratios and large hub-to-casing ratios. The design bypass ratio is very high to maximise propulsive efficiency of the engine. Bypass ratio changes in the normal operating region of the fan are higher than for LBPR fans, which have smaller BPR and higher fan pressure ratios. Fan exit profile changes in HBPR fans should have a proportionally larger effect than on LBPR fans.
- The data available to study LBPR fans was inconclusive as to whether fan performance is independent of bypass ratio at fixed non-dimensional speed and flow function for 2 reasons. One was the situation of the measurement probes for these rig tests were not exactly at the fan exit station before the bypass splitter. Secondly, LBPR data that was examined showed the presence of fan exit circumferential total pressure and total temperature profiles, possibly an effect of the presence of stators and other struts in the flow field on fan work input. Information has been obtained in the literature review to conclude that cases of LBPR turbofans occur where the bypass ratio affects the fan performance at fixed speed and flow function with the effects being a significant change in the fan characteristic compared to an unaffected case. The expense of testing has meant that these cases may occur but are not normally tested for.
- The fan exit circumferential profiles were arithmetically averaged to give axisymmetric radial profiles for modelling. These profiles have not greatly affected the use of the resulting fan characteristic in performance simulation possibly because the profiles are a small proportion of the absolute average thermodynamic parameters at the fan exit due to relatively high fan pressure ratios.

- The conventional industry method is the inner and outer fan model. This is restricted to the BPR vs. $N/\sqrt{T}$ schedule used to obtain the inner and outer fan data. Deviation from the schedule can occur for example with component efficiency changes, bleeds, transients and nozzle area changes. Factors and deltas will need to be applied to the inner and outer fan to model these changes.
- The 2D-HBPR method is able to accept variable BPR vs. $N/\sqrt{T}$ schedules as it changes the split fan exit streamline position with BPR changes to effectively obtain different inner and outer fan maps. This depends on performance being independent of BPR at a speed and flow function.
- The 2D-LBPR has the same capability as the 2D-HBPR method but in addition, can use the extra fan data if available for when the fan performance is dependent on BPR at a speed and flow function.
- The method will produce savings of time for studies using scaled fans from past engines for example when designing a new engine. The BPR vs. $N/\sqrt{T}$ schedules are automatically computed.
- The method of averaging exit radial profiles divided by the split flow streamline dependent on BPR has been used in this work for radial inlet distortion modelling, where the working line and BPR vs. $N/\sqrt{T}$ will also be altered.
- Rig to engine effects may in part be accounted for when more of the engine can be modelled in 2D detail. The 2D profiles can then be transmitted from one component to the next with subtle changes in component performance. It is likely that the components least affected are where deviations from the average of the radial profile are a small proportion of the average. This is seen in higher pressure ratio LBPR fans compared to lower pressure ration large civil fans.

5.2 RADIAL INLET DISTORTION EFFECTS

The contribution to knowledge of this work is in detailed modelling of the fan component of a turbofan engine in an engine performance simulation. The work done has applied a known method of calculating compressor 2D performance (SLC) and merge it with a turbofan engine simulation and with a 2D fan model that uses the engine BPR to split and average fan exit profiles so that the performance change of a LBPR turbofan engine can be calculated due to a radial inlet distortion of total pressure. Although streamline curvature is

often used for compressor performance prediction, this is the first known usage of it with a turbofan engine simulation. This is a start in understanding a common scenario of LBPR fan performance in greater detail.

- 3 fan methods have been implemented and analysed; WholeMap, ZonalMap and DirectMap, the first 2 are SLC computed compressor maps as interpolative methods, the latter is a direct use of SLC in the performance simulation iteration.
- Interpolation within the fan characteristic of the map interpolation methods (WholeMap, ZonalMap). In 1D method fan characteristics, the beta lines are arbitrary mapping parameters to obtain operating points between speed lines. It has always been necessary to ensure that the output of rig tests gives consistent speed lines, so for example, any lack of data that results in one shortened speed line does not distort the interpolation of a point at any guess of speed. This has sometimes required manual extrapolation of speed lines, smoothing of speed lines and manual plotting of beta lines. However, because the map is 1D, the only interpolated value that is converged upon is the one that satisfies the required checks in the iteration scheme. With 2D methods, the added complication is that each "beta" point or speed line intersection with beta now also contains the profiles that will average to the 1D value, but these profiles are split into two for the bypass and core ducts in the matching scheme. Effectively, what is being asked is that the interpolation between 2 speeds and 2 betas (in the 2D-HBPR model), and also between 2 BPRs in the 2D-LBPR model of Chapter 3 will match the profiles that would exist at that point if it could be tested. In the limit, 2 speed lines and 2 beta lines infinitely close to each other should reproduce this, but at the expense of a method that would be impractical. It has been demonstrated that interpolation between 2 speed lines of different "length" at more than 1.5% of design speed apart can give distorted profiles and affect the converged performance.
- Non-dimensionals vs. dimensionals. The success of the 1D fan characteristic has been the assumption of non-dimensional performance of the fan except at low Reynolds numbers conditions (where viscous flows become more important) and due to P1, T1 effects. These have been normally accounted for by corrections to the 1D characteristics. The prediction of performance due to inlet total pressure distortions has necessitated having a fan prediction method. It has been possible with this to perform fan calculations with dimensional parameters, directly inputting the inlet temperature, pressure, speed and mass flow. There is potential then for directly computing those effects due to viscous real flow

as described depending on the effectiveness of the loss models in the streamline curvature model. The SLC fan model can also be adapted to model varying angle of VGVs with the scheduling of the angles dependent on $N/\sqrt{T}$.

- Several cases of inlet distortions have been tested which are realistic in terms of the loss of dynamic pressure of the undistorted inlet flow case. The overall conclusion with this fan is that the inlet profile continues through the 3 stage fan without attenuation to give a fan exit profile. Results have been presented for performance changes from undistorted flow at a fixed TET and fixed rotational speed. The changes are approximately equivalent to that of the undistorted inlet flow at the average of the distorted, probably due to high pressure ratio of this fan.
- The overriding conclusion from the simulation program runs in Chapter **4** is that for multistage high hub-to-casing ratio fans, there are two main drivers for radial inlet distortion effects on performance. The first is the relatively high fan pressure ratios to give the optimum cycle in LBPR fans mean that any changes in the inlet radial pressure profiles have a smaller effect on the fan exit profiles as variations in fan exit profiles become a small percentage of the overall pressure. This is also due to the freedom of the airflow to rematch radially in the fan in contrast to circumferential distortions. For this fan, the approximation of the effect of a radial distortion is that it is equivalent to the effect of a uniform profile at the area-averaged inlet total pressure of the distortion. The second is the shape of the fan exit pressure profile, dependent on the radial input of work and the radial isentropic efficiency. A flat profile, as with the fan examined in this thesis, will have less effect on the difference in bypass duct and HPC core entry pressures with inlet distortion changes. BPR changes with inlet distortion were found to be extremely small for the test fan. A steeper profile may show greater changes in downstream pressures given an inlet distortion and therefore greater performance changes.
- The figures obtained are only applicable to this fan and engine combination, for example, for the worst distortion case (tip distorted case 2), 1.6% decrease in total pressure from undistorted ISASLS: at a fixed TET=1220K, Δthrust=-3.2%, Δsfc=+1.2%. At a fixed fan rotational speed of 20296 rpm, ΔTET=4.3K, Δthrust=-2.1%, Δsfc=+1.4%.
- The recommendations as a result of the testing of the 3 fan models. All 3 models give the same result within the limits of the accuracies that have been determined due to interpolation and due to the reduced convergence limits in DirectMap. The WholeMap

model was implemented as a research exercise only. The inlet distortion model is designed to compute the performance as a result of any arbitrary inlet radial profile. The final desired implementation would include a varying inlet profile from an intake model. Therefore, the WholeMap model would be impractical as there is no need to compute the whole characteristic when only part of the fan map is required at any time, and no point in storing characteristics for a fixed distortion for interpolation when constantly varying distortions would be output by the intake model during the calculation of one operating point. The preferred method is the DirectMap model. The advantage is to avoid any of the inaccuracies due to interpolation between speed lines and beta lines. The disadvantage is when time is a constraint as every guess of speed and beta will access the SLC code. The compromise would then be to use the ZonalMap model with the recommended speed line zone of ±1.5 % design speed for the first guess. Where ZonalMap is used, the recommendation is to restrict the speed line computations to predetermined speed values to ensure repeatability of results since use of different pairs of speed lines to compute the same operating point may give a slightly different answer. A future improvement may be to restrict the calculation of the speed line lengths in the zone to save more computation, but there should be caution not to distort the interpolated profile with different length speed lines.

- Distortion descriptors. Radial distortion descriptors, e.g. K_D (ARP1420, 1978) are used by aeroengine companies to set tolerance acceptability levels for an engine. These cannot be used as iteration guess variables in any scheme involving the intake since the descriptor refers to the worst radial difference from the radial average and so can have a random profile. The K_D can be calculated and set as a program output.

5.3 FURTHER WORK

Further work for the main Chapters 3 and 4 are also reiterated here. More details are available in sections **3.13** and **4.11**.

5.3.1 Radial profile and bypass modelling

5.3.1.1 General

- A wider range of low-bypass ratio fan data should be examined, in particular, a range of multistage fans with hub-to-casing ratios from military (higher) decreasing down to the large civil fans. This includes some of the older LBPR civil fans, e.g. Spey class.

- Similar modelling work to Chapter **3** can be done to model a turbofan engine with smaller fan pressure ratios and lower hub-to-casing ratios. The work in Chapter **4** has shown that bypass ratio changes over the higher power region of the engine are very small in a higher pressure ratio fan. Bypass ratio changes may be greater in turbofans with lower hub-to-casing ratios (larger pressure ratio differences between hub and casing) and in fans with lower fan pressure ratios (fan exit profile changes are larger proportionally to the absolute exit profiles).

5.3.1.2 Current modelling

- The user can arbitrarily alter the profiles for varying BPR to achieve the 1D map requirement. For example, the map in **Fig. 3.11** can be reproduced in 1D terms at least to give an idea of the degree of performance changes due to working line excursions in BPR affected fans. The present work has not yet considered a flow function change or efficiency change for the new BPR values.
- More cases of engine BPR vs. $N.\sqrt{T}$ changes may be investigated. This includes the effect of bleeds and transient performance calculations where the working line excursions are very significant.
- The engine simulation would be enhanced with 2 additions. One is the mixed exhaust turbofan, which already exists in the Cranfield School of Engineering (Yin, 1999), and the other is to implement the matrix method of iteration with Newton-Raphson solver. A range of solver strategies could be investigated as the current 2D-LBPR fan takes longer to converge than the 2D-LBPR and inner and outer fan models.

5.3.1.3 Future modelling

- The profiles created for varying bypass ratio are purely hypothetical. The fan flow field model used in Chapter **4** may be developed to investigate the effect of the bypass splitter proximity to the fan turbomachinery in order to compute profile changes that have a better physical basis. The use of a physical model will be a great advantage and will relieve the need to obtain test data for this research that is usually hard to obtain. It will allow the user to vary all of the important contributing fan parameters to carry out a systematic study to understand when profiles are BPR affected and when the effect on fan performance becomes significant.
- The model computes axisymmetric radial fan exit profiles. These are averaged for the entry conditions to the next components downstream. This work can be viewed as one

part of a move to greater detail performance modelling. Eventually, all components may be examined in 2D (radial) and also circumferential. This fan model may also be experimented as part of a circumferential parallel compressor model (section **4.11**), as part of a scheme to model inlet distortions as discrete radial and circumferential parts.

5.3.2 Fan radial inlet distortion performance modelling

5.3.2.1 Current modelling

- The current turbofan engine model can be amended to allow the effect of distortions to be ascertained properly at a fixed rotational speed. The mixed exhaust turbofan can also be implemented.
- The SLC code provides a wide range of data which has been captured but not made use of. For example, the meridional plot of the streamlines can be made for each converged result. This will then give an idea of streamline variations when comparing the same fan mass flow (the converged result divides the streamtubes into equivalent mass flows).
- The overall code should be simplified to enable the inputs to be applied in one file rather than several at present (due to integration of several different programs).

5.3.2.2 Future modelling

- Modelling a range of different fans. As identified above, the effect of radial distortions may have a larger effect on fans with lower FPR and with fewer stages. Also of interest would be lower hub-to-tip ratio fans as the current LBPR fan displays little variation of BPR with distortion. Fans with a more variability in exit total pressure profile should also be investigated. Time can be invested to determine how to model different fans with the current SLC code by changes to the geometry inputs. Either new geometry from a known fan can be input, or a design can be made to generate a desired radial profile of work (the original SLC code (Barbosa, 1987) also had a design mode). The user will also need to invest time to learn how to make the necessary adjustments to a range of input parameters to achieve convergence, e.g. relaxation factors in the iterative loops.
- SLC program improvements - theory. The main improvement in capability would be to update the loss, deviation and blockage models. In the opinion of Denton and Dawes (1999), the accuracy of SLC methods is dependent on the empiricism of these models. In particular, the models of Gallimore and Cumpsty (1986), Adkins and Smith (1982) should be considered. These models distribute the prediction of loss from a multistage SLC fan

model at the hub and casing to better simulate actual findings of the radial temperature profile across the span. Without it, the loss at the mid-span tends to be under-predicted, and the loss at the walls over-predicted. Further improvements include adding the capability of modelling prescribed vane shapes compared to fixed blade profile types.

- SLC program improvements – theory. The difference in averaging for calculation of 1D efficiency in the SLC code and the performance code needs investigating. The 1D-averaged values differed by 2% throughout the characteristic map although no difference was detected in the averaging for pressure ratio. This did not affect the findings of this work as only the same calculation procedure for efficiency was used at all times.
- SLC program improvements – theory. Further improvements can be made to the setting of stall and choke in the SLC code. The current detection of stall is when a local (i.e. a streamtube) diffusion factor is exceeded after program convergence. The diffusion factor is based on Lieblein (Barbosa, 1987). This appears not to work in the version of the program used. Detection of choke in the SLC procedure is when an increase in the guess of the mid-span meridional velocity gives rise to a decrease in mass flow when the radial velocity distribution is integrated. This may also not be working correctly in the current code given the length of some speed lines compared to others.
- SLC program development: The SLC code should be modified to apply the inlet distortion to the IGV inlet face instead of the first "dummy" blade row.
- SLC program improvements – practicality: As identified, all inputs and outputs to the code should be made double precision to provide sufficient precision for the checking procedure in the engine performance code. A thorough understanding of the internal convergence procedures within the SLC code needs to be understood to carry this out as a initial trial that was carried out had failed. The use of text files for communication between the engine code and the SLC code needs to be removed. This would improve drastically the performance convergence times, currently at approximately 25mins on a 2GHz Athlon 2400 with 512MB ram. The SLC convergence is approximately 1 second. It is recommended therefore to integrate the SLC program with the performance program. The subroutines can be kept separate but a thorough review would be required to ensure parameter names are not repeated within the 2 codes.
- SLC program development: Although this has less relevance to fans, there is potential to investigate the steady-state effect of bleeds and heat soakage in a compressor. A bleed could be modelled as a step change in mass flow across part of the radius of a blade row.

Heat transfer effects to the air could be modelled as changes in ΔH. An investigation could also be made to see if a change of stator vane angle with change in $N/\sqrt{T}$ is practical. This would be a study of whether the code would converge without user intervention in terms of the convergence parameters.

- SLC program development: BPR investigations. To investigate the effect of the bypass splitter and to potentially provide data for the 2D-LBPR fan model in Chapter 3, a study should be made to see how this feature can be modelled within the existing SLC program. It has already been intimated that a SLC code can be adapted to model the bypass flow (Novak, 1967).
- Intake model scheme. A steady-state 2D-intake model needs to be added to completely compute 2D inlet distortion of an aeroengine. The current model applies an inlet distortion to the fan inlet face (or strictly speaking in this SLC model, at the dummy blade row upstream of the fan face). The converged output of the SLC includes the static pressure profile at this station. The flow through the intake will be a function of the suction from the fan (which depends on the fan operating point) and the forward flight speed. For the intake, the inlet total pressure, the total pressure loss and static pressure at exit could determine the mass flow. A possible scheme could be to have a range of CFD computed intake maps at different ambient and flight conditions using an intake exit static pressure. An experiment could be conducted to match the static pressure between the intake and the fan.

5.3.3 Circumferential flow distortion

- **Two compressors in parallel compressor**

A 2-compressors-in-parallel code has been started to analyse the circumferential problem. This includes the radial fan exit profiles in each compressor using the 2D-HBPR fan code. Further work could attempt to couple the radial inlet distortion code to this parallel compressor.

- **Multiple compressors in parallel**

This could be done in the manner of Mazzawy (1977) but with the SLC code. There can be radial distortion in each sector, but with separated parallel compressors. The difficulty would be how to reconcile different radial inlet and exit sectors into an overall smooth continuously varying inlet face contour.

5.3.4 Scaling of SLC output

Some thought should be given to how the SLC program can be scaled as this frequently occurs in compressor projects, to predict performance of a new compressor from previous knowledge. In particular, the blockage models should be looked at as it reflects the boundary layer growth at the walls and has the greatest effect on the profile predictions.

5.3.5 Modelling of rig to engine effects

Apart from the effect of iteration throughout the performance code with 2D profiles, which should account for some of the differences between rig and engine measured performance, in modelling, there can also be effects such as back pressure effects, e.g. clocking of stators and OGVs. These have been modelled by actuator disk models. Some thought should be given as to whether these may be considered for 2nd order effects. Other differences include component coupling e.g. Williams, 1976. For example, for a single stage fan, the HPC has a greater influence on its performance than on a multistage fan.

REFERENCES

Adkins, G. G., Jr., Smith, L. H., Jr. (1982). Spanwise mixing in axial flow turbomachines. *ASME Journal of engineering for power*, vol. 104, no. 1, 97-110.

AIR 1419. (1999). Society of Automotive Engineers. Aerospace information report, AIR 1419, Revision A. *Inlet total-pressure-distortion considerations for gas-turbine engines.*

ARP 1420. (1978). Society of Automotive Engineers. Aerospace recommended practice, ARP 1420. *Gas turbine engine inlet flow distortion guidelines.*

Biraud, B. Despierre, A., Gayraud, S. (2001). Simulation of the WR-21 advanced cycle engine. *International Gas Turbine and Aeroengine Congress & Exhibition*, Paper 2001-GT-020, New Orleans, US, June 4-7, 2001.

Barbosa, J. R. (1987). *A streamline curvature computational programme for axial compressor performance prediction.* PhD thesis, Cranfield University, School of Mechanical Engineering, September 1987.

Biesiadny, T. J., Braithwaite, W. M., Soeder, R. H., Abdelwahab, M. (1987). Summary of investigations of engine response to distorted inlet conditions. In: *Engine response to distorted inflow conditions, AGARD conference proceedings No. 400 (AGARD-CP-400), the propulsion and energetics 68th (A) specialists' meeting,* Munich, Germany, September 8-9 1986, part 15.

Calogeras, J. E., Mehalic, C. M., Burstadt, P. L., (1971). *Experimental Investigation of the Effect of Screen-Induced Total Pressure Distortion on Turbojet Stall Margin.* NASA TM X-2239. Lewis Research Center, Cleveland, Ohio, USA.

Daneshyar, H., Shaalan, M. R. A., (1972). *The Off-Design Analysis of Flow in Axial Compressors.* Aeronautical Research Council Current Papers, C.P. No. 1234.

Day, I. J., Freeman, C. (1994). The unstable behavior of low and high-speed compressors. *Transactions of the ASME, Journal of turbomachinery*, vol. 116, April, 194-201.

Davis, W. R., Millar, D. A. J. (1976). Through-flow calculations based on matrix inversion: loss prediction. In: *Through-flow calculations in axial turbomachinery. In: AGARD conference proceedings No. 195 (AGARD-CP-195), the propulsion and energetics 47th specialists' meeting,* Cologne, Germany, May 20-21 1976.

Denton, J. D. (1993). Loss mechanisms in turbomachines. *Transactions of the ASME, Journal of turbomachinery*, vol. 115, October, 621-656.

Denton, J. D., Dawes, W. N. (1999). Computational fluid dynamics for turbomachinery design. *Proceedings of the Institution of Mechanical Engineers,* vol. 213 part C, 107-124.

Drummond, C., Follen, G., Cannon, M. (1994). Object-oriented technology for compressor simulation. In: 30th AIAA/SAE/ASME/ASEE Joint Propulsion Conference, Indianapolis, IN, USA, June 27-29 1994, AIAA 94-3095.

Dunham, J. (1982). The averaging of traverse results. *National gas turbine establishment memorandum 82033*, (NGTE M82033).

Dunham, J. (1986). The role of flow field computation in improving turbomachinery. In: *ICAS, congress, 15th*, September 7-12 1986, London, England, vol. 2, 967-980.

Escuret, J. F., Nicoud, F., Veysseyre, Ph., (1998). Recent Advances in Compressor Aerodynamic Design and Analysis. In: *Integrated Multidisciplinary Design of High Pressure Multistage Compressor Systems*, RTO Lecture Series, RTO-EN-1, 14-15 September 1998, Lyon, France, and 22-23 September 1998, Cleveland, USA.

ESDU 95011, (1995). One-dimensional representation of steady, spatially non-unform flow. An equivalent mean-value set for compressible flow. Part 1. Implementation for an ideal, calorically-perfect gas. *ESDU Item no. 95011*, ESDU International, London.

ESDU 97029, (1998). One-dimensional representation of steady, spatially non-unform flow. An equivalent mean-value set for compressible flow. Part 2. Implementation for an ideal, thermally-perfect gas. *ESDU Item no. 97029*, ESDU International, London.

Evans, A., Follen, G., Naiman, C., Lopez, I. (1998). Numerical propulsion system simulation's national cycle program. In: 34th AIAA/SAE/ASME/ASEE Joint Propulsion Conference, Cleveland, Ohio, USA, July 13-15 1998, AIAA 98-3113.

Flack, R. D. (1990). Analysis and matching of gas turbine components. *International journal of turbo and jet engines*, vol. 7, 217-226.

Flitcroft, J. E., Dunham, J., Abbott, W. A. (1987). Transmission of inlet distortion through a fan. In: *Engine response to distorted inflow conditions, AGARD conference proceedings No. 400 (AGARD-CP-400), the propulsion and energetics 68th (A) specialists' meeting*, Munich, Germany, September 8-9 1986, part 13.

Follen, G., Naiman, C., Evans, A. (1998). National cycle program (NCP) common analysis tool for aeropropulsion. *In: HPCCP/CAS workshop proceedings 1998, NASA No. 19990019865*, 177-181

Follen, G., auBuchon, M. (1999). Numerical zooming between the NPSS version 1 and a 1-D meanline design analysis code. *ISABE 99-7196.*

Gallimore, S. J., Cumpsty, N. A. (1986). Spanwise mixing in multistage axial flow compressors: Part 1 – Experimental investigation. *Transactions of the ASME Journal of Turbomachinery*, vol. 108, July, 2-16.

Gallimore, S. J. (1999). Axial flow compressor design. *Proceedings of the Institution of Mechanical Engineers*, vol. 213 part C, 437-449.

Glenny, D. E. (1974). An application of streamline curvature methods to the calculation of flow in a multistage axial compressor. *Mechanical engineering note 346 (ARL/M.E. 346)*, Australian defence scientific service aeronautical research laboratories.

Goyal, R. K. (1993). A comparison of the measured and predicted flow field in a modern fan-bypass configuration. *Transactions of the ASME Journal of Turbomachinery*, vol. 115, April, 273-282.

Greitzer, Edward, M., (1979). Inlet Distortion Effects in Axial Compressors. In: *Unsteady Flow in Turbomachines.* Von Karman Lecture Series 1979-3, January 29 - February 2, 1979.

Grienpentrog, H. R. – Secondary flow losses in axial compressors. AGARD LS-39.

Hale, A., O'Brien, W. A Three-Dimensional Turbine Engine Analysis Compressor Code (TEACC) for Steady-State Inlet Distortion. *Transactions of the ASME, Journal of Turbomachinery*, Vol.120, July 1998, 422-430.

Höss, B., Leinhos, D., Fottner, L. (2000). Stall inception in the compressor system of a turbofan engine. *Transactions of the ASME, Journal of turbomachinery*, vol. 122, January, 32-44.

Hu, Jun. (2000). Calculation of off-design performance of multistage compressors with uniform and radial distorted inlet flow. *Journal of aerospace power*, vol. 15, no. 3, 225-228

Ismail, I. H., Bhinder, F. S. (1991). Simulation of aircraft gas turbine engines. *Transactions of the ASME, Journal of engineering* for gas turbines and power, vol. 113, 95-99.

Jansen, W., Moffatt, W. C. (1967). The off-design analysis of axial flow compressors. *Transactions of the ASME, Journal of engineering for power*, October, 453-462.

Kerrebrock, J. L., Mikolajczak, A. A. (1970). Intra-stator transport of rotor wakes and its effect on compressor performance. *ASME Journal of engineering for power*, vol. 92, no. 4, 359-368.

Klepper, J. (1998). *Technique to predict stage-by-stage, pre-stall compressor performance characteristics using a streamline curvature code with loss and deviation correlations.* MSc thesis, University of Tennessee, Knoxville, USA, August 1998.

Kurzke, J. (1995). Advanced user-friendly gas turbine performance calculations on a personal computer. *International Gas Turbine and Aeroengine Congress & Exhibition*, Paper 95-GT-147, Houston, USA, June 5-8, 1995.

Kurzke, J. (1996). How to get component maps for aircraft gas turbine performance calculations. *International Gas Turbine and Aeroengine Congress & Exhibition*, Paper 96-GT-164, Birmingham, UK, June 10-13, 1996.

Lewis, R. I. (1996). *Turbomachinery performance analysis,* 1st ed. John Wiley & Sons Inc., New York, USA.

[1]Li, M. S. (2001). RR UTC WP2 Low bypass ratio turbofan modelling. Data analysis report. Report for Cranfield UTC, School of Engineering.

[2]Li, M. S. (2001). *Low bypass ratio turbofan modelling,* 1st year PhD review report, Cranfield University, School of Engineering, September 2001.

Liu Yan, (1992). A digital simulation and its experimental investigation for the response of gas-turbine engines to intake flow distortion. *ICAS, Congress, 18th, Proceedings vol 2, September 20-25th, 1723-1727.*

Longley, J. P., Greitzer, E. M. (1992). Inlet distortion effects in aircraft propulsion system integration. In: *Steady and transient performance prediction of gas turbine engines, AGARD lecture series No. 183 (AGARD-LS-183),* Cambridge, MA, USA, May 27-28 1992, Neubiberg, Germany, June 9-10 1992, Châtillon/Bagneux, France, June 11-12, part 6.

Lytle, J. K. (1997). The numerical propulsion system simulation: concept to product. *ISABE 97-7107.* 748-757.

Marshall, C. D. (1998). *The modelling of high bypass ratio turbofans.* MSc thesis, Cranfield University, School of Mechanical Engineering, September 1998.

Macchio, E., (1985). The Use of Radial Equilibrium and Streamline Curvature Methods for Turbomachinery Design and Prediction. In: Ucer, A. S., Stow, P., Hirsch, Ch. *Thermodynamics and Fluid Mechanics of Turbomachinery, Volume 1.* Proceedings of the NATO Advanced Study Institute on Thermodynamics and Fluid Mechanics of Turbomachinery, Izmir, Turkey, September 17-28, 1984. Dordrecht, The Netherlands: Martinus Nijhoff Publishers.

Mazzawy, R. S. (1976). Multiple segment parallel compressor model for circumferential flow distortion. In: *Unsteady phenomena in turbomachinery, AGARD conference proceedings No. 177 (AGARD-CP-177), the 46th meeting of the AGARD propulsion and energetics panel,* Monterey, California, USA, September 22-26 1975, part 21.

Mazzawy, R. S., Banks, G. A. (1977) Circumferential distortion modelling of the TF30-P-3 compression system. NASA CR-135124, 1977.

Mazzawy, R. S. (1977). Multiple segment parallel compressor model for circumferential flow distortion. *Transactions of the ASME, Journal of engineering for power,* April 1977, 288-297.

Monsarrat, N. T., Keenan, M. J., Tramm, P. C. (1969). Design report – single stage evaluation of highly loaded high Mach number compressor stages. NASA CR-72562.

NASA SP-36 (1965). Aerodynamic design of axial-flow compressors. NASA Scientific and Technical Information Division, Washington DC, USA.

NATO RTO-TR-044, (2002). Performance prediction and simulation of gas turbine engine operation. RTO Technical Report 44.

Novak, R. A. (1967). Streamline curvature computing procedures for fluid-flow problems. *Transactions of the ASME, Journal of Engineering for Power,* October 1967, 478-490.

Novak, R. A. (1976). Flow field and performance map computation for axial-flow compressors and turbines. In: *Modern prediction methods for turbomachine performance, AGARD lecture series No. 83 (AGARD-LS-83),* Munich, Germany, June 14-15 1976, London, England, June 17-18 1976, part 5.

Pianko, M., Wazelt, F. (1983). Propulsion and energetics panel working group 14 on suitable averaging techniques in non-uniform internal flows. *AGARD advisory report No. 182 (AGARD-AR-182).*

Plourde, G. A., Stenning, A. H. (1967). The attenuation of circumferential inlet distortion in multi-stage axial compressors. *AIAA 3rd Propulsion Joint Specialist Conference*, Washington DC, USA, July 17-21, 1967.

Reed, J. A., Afjeh, A. A. (1996). An intelligent visualization and monitoring system for multidisciplinary numerical propulsion system simulation. *AIAA-96-4034-CP.* 482-492.

Reid, C. (1969). The response of axial flow compressors to intake flow distortion. ASME paper 69-GT-29.

Riegler, C., Bauer, M. Kurzke, J. (2001). Some aspects of modelling compressor behavior in gas turbine performance calculations. *Transactions of the ASME, Journal of engineering* for gas turbines and power, vol. 123, 372-378.

Sanghi, V., Lakshmanan, B. K., Sundararajan, V. (1998). Digital simulator for steady-state performance of military turbofan engine. *Journal of propulsion and power*, vol. 14, no. 1, 74-81.

[1]Saravanamuttoo, H. I. H. (1992). Component performance requirements. In: *Steady and transient performance prediction of gas turbine engines, AGARD lecture series No. 183 (AGARD-LS-183),* Cambridge, MA, USA, May 27-28 1992, Neubiberg, Germany, June 9-10 1992, Châtillon/Bagneux, France, June 11-12, part 4.

[2]Saravanamuttoo, H. I. H. (1992). Overview on basis and use of performance prediction methods. In: *Steady and transient performance prediction of gas turbine engines, AGARD lecture series No. 183 (AGARD-LS-183),* Cambridge, MA, USA, May 27-28 1992, Neubiberg, Germany, June 9-10 1992, Châtillon/Bagneux, France, June 11-12, part 1.

Schwenk, F. C., Hartmann, M. J. (1957). A preliminary analysis of the magnitude of shock losses in transonic compressors. NACA RM E57A30.

Serovy, G. K. (1976). Compressor and turbine performance prediction system development – lessons from thirty years of history. In: *Modern prediction methods for turbomachine performance, AGARD lecture series No. 83 (AGARD-LS-83),* Munich, Germany, June 14-15 1976, London, England, June 17-18 1976, part 3.

Shaw, M., Murdoch, R.W. Computer modelling of fan-exit-splitter spacing effects on F100 response to distortion, NASA CR-167879, March 1982.

Smith, Jr., L. H. (1966). The radial-equilibrium equation of turbomachinery. *Transactions of the ASME, Journal of Engineering for Power.* Series A, vol. 88, 1966, 1-12.

Smith, Jr., L. H. (1974). Some aerodynamic design considerations for high bypass ratio fans. In: 2nd International Symposium on Air Breathing Engines, 1974, Sheffield, UK.

Song, W., Ming., Fan, F. (1997). Multiple-sector parallel compressor model for flow field calculation under distortion. *Journal of aerospace power*, vol. 12, no. 2 April 155-158.

Spurr, A. (1982). A prediction of 3D transonic flow in turbomachinery using a combined throughflow and blade-to-blade time marching method. *International journal of heat and fluid flow*, vol. 2, no. 4 189-199.

Stenning, A.H. (1980). Inlet distortion effects in axial compressors. *Transactions of the ASME, Journal of Fluids Engineering*, Vol. 102, 7-13.

Swan, W. C. (1961). A practical method of predicting transonic compressor performance. *Journal of Engineering Power*, July, 1961.

Tamaki, T., Nagano, S. (1979). Effects of Inlet Distortions on a Multi-Stage Compressor. In: *Fourth International Symposium on Air Breathing Engines*, Orlando, Florida, USA, April 1-6, 1979, Paper 79-7003, pp17 – 24.

Visser, W. P. J., Broomhead, M. J. (2000). GSP A generic object-oriented gas turbine simulation environment. *NLR-TP-2000-267*. National Aerospace Laboratory NLR.

Wall, R. A. (1976). Axial flow compressor performance prediction. In: *Modern prediction methods for turbomachine performance, AGARD lecture series No. 83 (AGARD-LS-83)*, Munich, Germany, June 14-15 1976, London, England, June 17-18 1976, part 4.

Wennerstrom, A. J. (1999). A review of predictive efforts for transport phenomena in axial flow compressors. *Transactions of the ASME, Journal of turbomachinery*, vol. 113, April, 175-179.

Williams, D. D. and Yost, J. O., (1973). Some Aspects of Inlet/Engine Flow Compatibility. *The Aeronautical Journal*, Supplementary Paper, September 1973.

Williams, D. D. (1987). Review of current knowledge on engine response to distorted inflow conditions. In: *Engine response to distorted inflow conditions, AGARD conference proceedings. No. 400 (AGARD-CP-400), the propulsion and energetics 68th (A) specialists' meeting*, Munich, Germany, September 8-9 1986, part 1.

Williams, D. D. (2002). Private communication, Cranfield University.

Wilson, A. G. (1990). The averaging of aerodynamic data. Rolls-Royce plc internal report RCR 86065.

Wu, C. H. (1952). A general theory of three-dimensional flow in subsonic and supersonic turbomachines of axial-, radial-, and mixed-flow types. *National advisory committee for aeronautics. Technical note 2604 (NACA TN 2604).*

Yan, L., FuQun, C. (1992). A digital simulation and its experimental investigation for the response of gas-turbine engines to intake flow distortion. In: *ICAS, congress, 18th*, September 20-25 1992, Beijing, China, vol. 2, 1723-1727.

Yin, J. (1999). *Proposed calculation procedures for the generation and application of 2-D fan characteristics.* Report PE005. Cranfield University/Rolls-Royce University Technology Centre.

Yin, J-F., Hales, R., Pilidis, P., Curnock, B. (2001). 2-shaft high bypass ratio turbofan performance calculations using a new 2-D fan model. In: 37th AIAA/SAE/ASME/ASEE Joint Propulsion Conference, Salt Lake City, Utah, USA, July 8-11 2001, AIAA 2001-3302.

BIBLIOGRAPHY

Anderson, J. D., Jr. (1995). *Computational fluid dynamics. The basics with applications.* 1st international ed. McGraw-Hill Inc., Singapore.

Cohen, H., Rogers, G.F.C., Saravanamuttoo, H. (1996). *Gas turbine theory.* 4th edition . Longman, UK.

Cumpsty, N. A. (1989). *Compressor aerodynamics,* 1st ed. Addison Wesley Longman Limited, Harlow, England.

Cumpsty, N. A. (1997). *Jet propulsion,* 1st ed. Cambridge Engine Technology Series, Cambridge University Press, Cambridge, England.

Dixon, S. L., (1998). *Fluid Mechanics and Thermodynamics of Turbomachinery.* 4th edition, Boston, USA: Butterworth-Heinemann.

Hooker, S. (1990). *Not much of an engineer,* 1st ed. Airlife Publishing Ltd., England.

Lakshminarayana, B. (1996). *Fluid dynamics and heat transfer of turbomachinery,* 1st ed. John Wiley & Sons Inc., New York, USA.

Mattingly, J. D., Heiser, W.H., Daley, D.H. (1987). *Aircraft engine design,* AIAA Education Series, American Institute of Aeronautics and Astronautics, New York, USA.

Pao, R. H. F. (1967). *Fluid dynamics,* 1st ed. Charles E. Merrill Books, Inc., Columbus, Ohio.

Pilidis, P. *Gas turbine theory and performance.* MSc lecture notes. Cranfield University School of Mechanical Engineering.

Seddon, J., Goldsmith, E. L. (1999). *Intake aerodynamics,* 2nd ed. Blackwell Science Ltd., London, England.

Walsh, P. P. *Gas turbine performance.* Blackwell Science, Oxford, England. 1998.

Wilson, David Gordon and Korakianitis, Theodosios., (1998). *The Design of High-Efficiency Turbomachinery and Gas Turbines,* 2nd ed. Prentice-Hall, Inc., NJ, USA.

Yahya, S. M. *Fundamentals of compressible flow with aircraft and rocket propulsion,* 2nd ed. New Age International (P) Limited, New Delhi, India.

APPENDIX 1. CYLINDRICAL COORDINATE SYSTEM

Transformation between Cartesian and cylindrical coordinate system:

Cylindrical

$$r = \sqrt{x^2 + y^2}$$

$$\theta = \tan^{-1}\left(\frac{y}{x}\right) \qquad \text{(A1.1)}$$

$$z = z$$

Cartesian

$$x = \rho \cos\theta$$

$$y = \rho \sin\theta \qquad \text{(A1.2)}$$

$$z = z$$

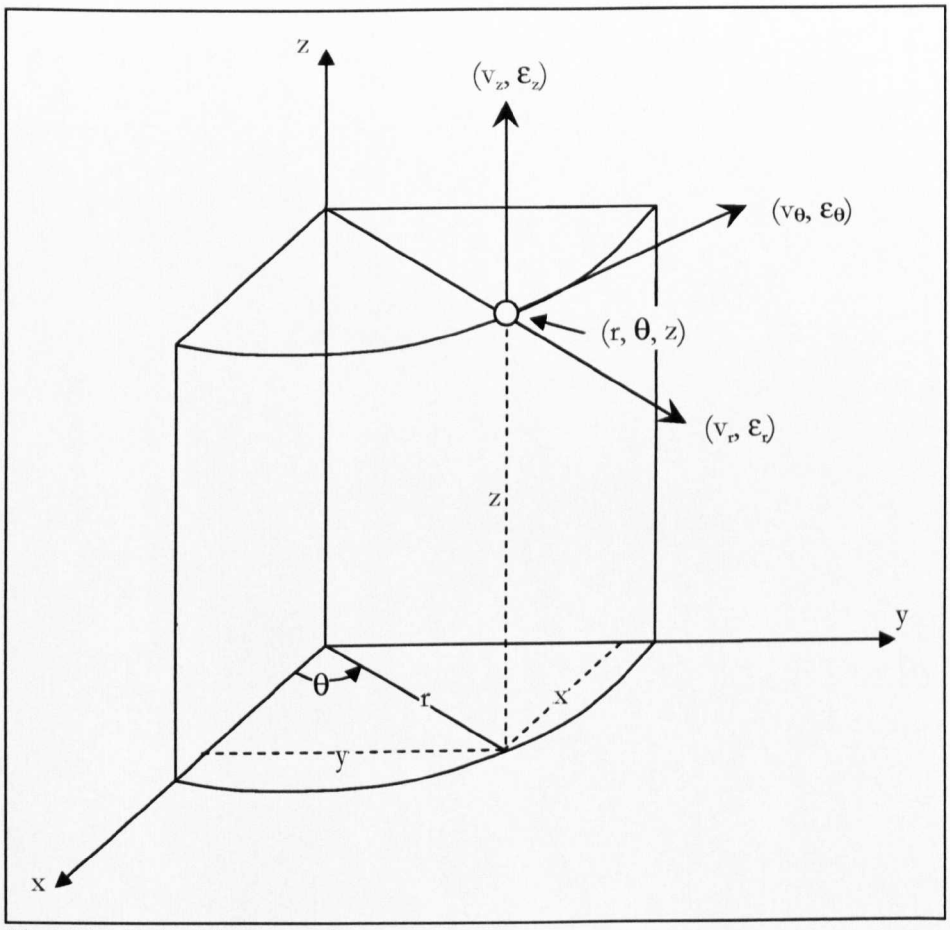

Fig. A1.1 Cylindrical coordinate system

Unit vectors:

Cartesian positional unit vectors:

$$\vec{R} = x\vec{i} + y\vec{j} + z\vec{k} \qquad \text{(A1.3)}$$

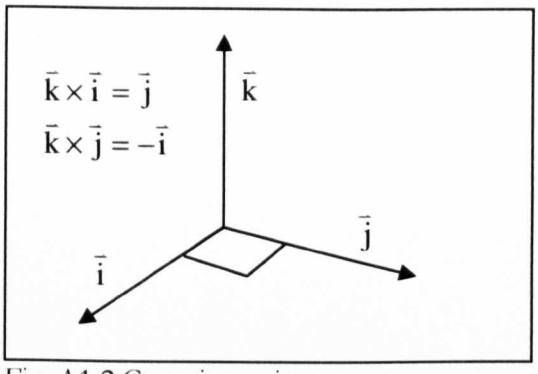

Fig. A1.2 Cartesian unit vectors.

Cylindrical positional unit vectors:

$$\vec{R} = r\vec{\varepsilon}_r + z\vec{\varepsilon}_z \qquad \text{(A1.4)}$$

$$\vec{\varepsilon}_r = \frac{\vec{r}}{r} = \frac{x\vec{i}+y\vec{j}}{r} = \frac{r\cos\theta\vec{i}+r\sin\theta\vec{j}}{r} = \cos\theta\vec{i}+\sin\theta\vec{j} \qquad \text{(A1.5)}$$

$$\vec{\varepsilon}_\theta = \vec{\varepsilon}_z\times\vec{\varepsilon}_r = \vec{k}\times\left(\cos\theta\vec{i}+\sin\theta\vec{j}\right) = \left(\vec{k}\times\cos\theta\vec{i}\right)+\left(\vec{k}\times\sin\theta\vec{j}\right) = (1\times\cos\theta)\vec{j}-(1\times\sin\theta)\vec{i}$$
$$= -\sin\theta\vec{i}+\cos\theta\vec{j} \qquad \text{(A1.6)}$$

$$\vec{\varepsilon}_z = \vec{k} \qquad \text{(A1.7)}$$

Variation of unit vectors

Some unit vectors change direction with θ.

$$\frac{\partial\vec{\varepsilon}_r}{\partial r}=0 \qquad \frac{\partial\vec{\varepsilon}_\theta}{\partial r}=0 \qquad \frac{\partial\vec{\varepsilon}_z}{\partial r}=0 \qquad \text{(A1.8)}$$

$$\frac{\partial\vec{\varepsilon}_r}{\partial\theta}=-\sin\theta\vec{i}+\cos\theta\vec{j}=\vec{\varepsilon}_\theta \qquad \frac{\partial\vec{\varepsilon}_\theta}{\partial\theta}=-\cos\theta\vec{i}-\sin\theta\vec{j}=-\vec{\varepsilon}_r \qquad \frac{\partial\vec{\varepsilon}_z}{\partial\theta}=0 \qquad \text{(A1.9)}$$

$$\frac{\partial\vec{\varepsilon}_r}{\partial z}=0 \qquad \frac{\partial\vec{\varepsilon}_\theta}{\partial z}=0 \qquad \frac{\partial\vec{\varepsilon}_z}{\partial z}=0 \qquad \text{(A1.10)}$$

Time derivatives of unit vectors

$$\frac{d\vec{\varepsilon}_r}{dt}=\frac{\partial\vec{\varepsilon}_r}{\partial r}\frac{dr}{dt}+\frac{\partial\vec{\varepsilon}_r}{\partial\theta}\frac{d\theta}{dt}+\frac{\partial\vec{\varepsilon}_r}{\partial z}\frac{dz}{dt}=0+\vec{\varepsilon}_\theta\frac{d\theta}{dt}+0=\vec{\varepsilon}_\theta\frac{d\theta}{dt} \qquad \text{(A1.11)}$$

$$\frac{d\vec{\varepsilon}_\theta}{dt}=\frac{\partial\vec{\varepsilon}_\theta}{\partial r}\frac{dr}{dt}+\frac{\partial\vec{\varepsilon}_\theta}{\partial\theta}\frac{d\theta}{dt}+\frac{\partial\vec{\varepsilon}_\theta}{\partial z}\frac{dz}{dt}=0-\vec{\varepsilon}_r\frac{d\theta}{dt}+0=-\vec{\varepsilon}_r\frac{d\theta}{dt} \qquad \text{(A1.12)}$$

$$\frac{d\vec{\varepsilon}_z}{dt}=\frac{\partial\vec{\varepsilon}_z}{\partial r}\frac{dr}{dt}+\frac{\partial\vec{\varepsilon}_z}{\partial\theta}\frac{d\theta}{dt}+\frac{\partial\vec{\varepsilon}_z}{\partial z}\frac{dz}{dt}=0+0+0=0 \qquad \text{(A1.13)}$$

Increment of path

$$d\vec{R} = d(r\vec{\varepsilon}_r + z\vec{\varepsilon}_z) = \vec{\varepsilon}_r dr + r d\vec{\varepsilon}_r + \vec{\varepsilon}_z dz + z d\vec{\varepsilon}_z$$

$$= \vec{\varepsilon}_r dr + r\left(\frac{\partial \vec{\varepsilon}_r}{\partial r}dr + \frac{\partial \vec{\varepsilon}_r}{\partial \theta}d\theta + \frac{\partial \vec{\varepsilon}_r}{\partial z}dz\right) + \vec{\varepsilon}_z dz + z\left(\frac{\partial \vec{\varepsilon}_z}{\partial r}dr + \frac{\partial \vec{\varepsilon}_z}{\partial \theta}d\theta + \frac{\partial \vec{\varepsilon}_z}{\partial z}dz\right)$$

$$= \vec{\varepsilon}_r dr + r(0 + \vec{\varepsilon}_\theta d\theta + 0) + \vec{\varepsilon}_z dz + z(0 + 0 + 0)$$

$$= \vec{\varepsilon}_r dr + \vec{\varepsilon}_\theta r d\theta + \vec{\varepsilon}_z dz \qquad \text{(A1.14)}$$

Del operator

A static scalar field e.g. p, is a function of r, θ and z. p changes by an infinitesimal amount dp when path is changed by $d\vec{R}$.

$$dp = \frac{\partial p}{\partial r}dr + \frac{\partial p}{\partial \theta}d\theta + \frac{\partial p}{\partial z}dz \qquad \text{(A1.15)}$$

Define the gradient to obtain:

$$dp = \vec{\nabla} p \cdot d\vec{R} \qquad \text{(A1.16)}$$

Then,

$$\frac{\partial p}{\partial r}dr + \frac{\partial p}{\partial \theta}d\theta + \frac{\partial p}{\partial z}dz = \vec{\nabla} p \cdot d\vec{R} \qquad \text{(A1.17)}$$

In cylindrical coordinates:

$$\frac{\partial p}{\partial r}dr + \frac{\partial p}{\partial \theta}d\theta + \frac{\partial p}{\partial z}dz = (\vec{\nabla} p)_r dr + (\vec{\nabla} p)_\theta r d\theta + (\vec{\nabla} p)_z dz \qquad \text{(A1.17)}$$

Therefore:

$$(\vec{\nabla} p)_r = \frac{\partial p}{\partial r},\ (\vec{\nabla} p)_\theta = \frac{1}{r}\frac{\partial p}{\partial \theta},\ \text{and}\ (\vec{\nabla} p)_z = \frac{\partial p}{\partial z} \qquad \text{(A1.18)}$$

So del is:

$$\vec{\nabla} = \frac{\partial}{\partial r}\vec{\varepsilon}_r + \frac{1}{r}\frac{\partial}{\partial \theta}\vec{\varepsilon}_\theta + \frac{\partial}{\partial z}\vec{\varepsilon}_z \qquad \text{(A1.19)}$$

APPENDIX 2. DERIVATION OF EQUATION OF CONTINUITY IN CYLINDRICAL COORDINATES

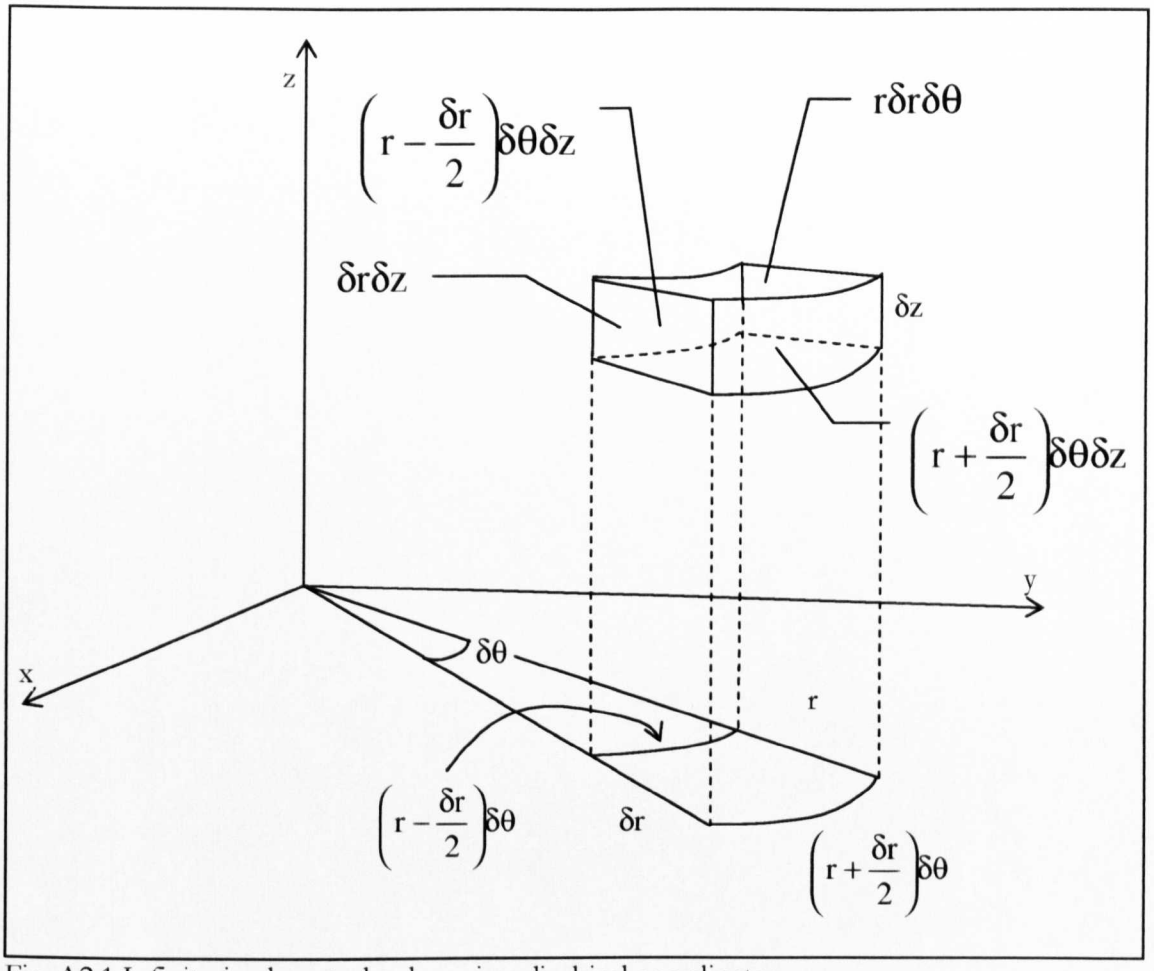

Fig. A2.1 Infinitesimal control volume in cylindrical coordinates.

Differential form of the continuity equation:

The mass of the control system remains constant as the system moves through the flow field. The control volume is a small fluid element with density ρ at the centre of the element and the velocity components are V_r, V_θ and V_z.
The control volume representation of the conservation of mass is:

$$\frac{\partial}{\partial t}\int_{cv}\rho dV + \int_{cs}\rho \mathbf{V}\cdot\hat{\mathbf{n}}dA = 0 \qquad \text{(A2.1)}$$

with the control volume bounded by a control surface.

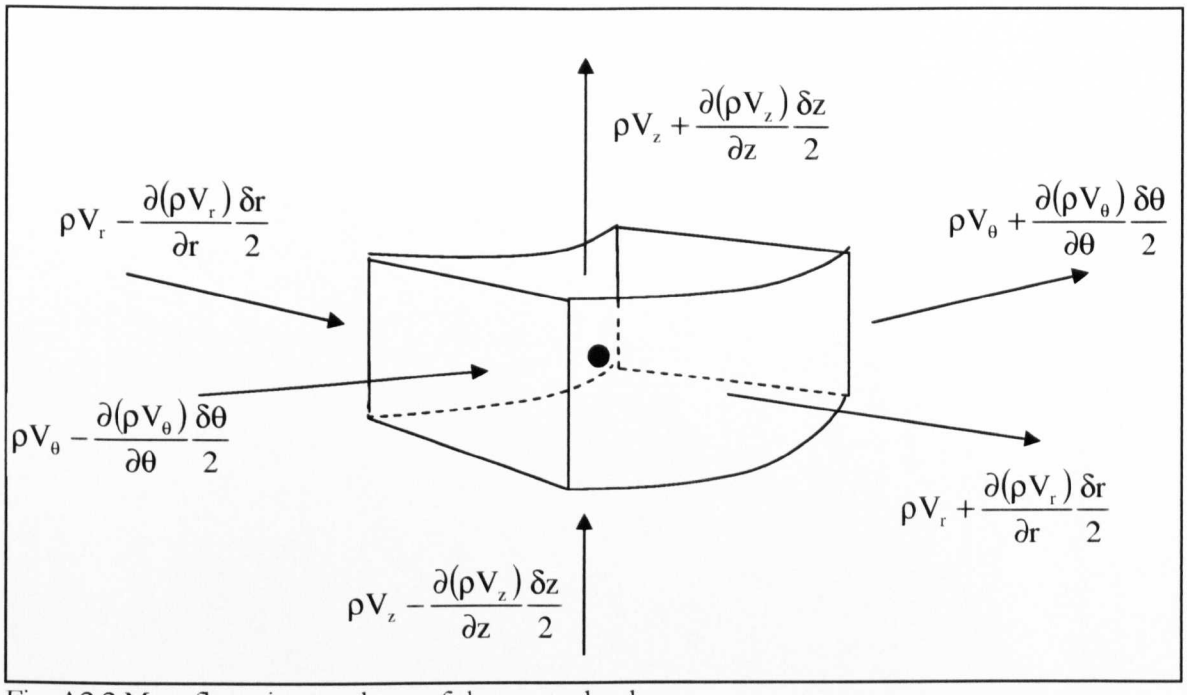

Fig. A2.2 Mass flows into and out of the control volume.

The first term on the LHS is the rate of increase of mass within the control volume. The second integral is the net rate of mass flow through the control surface. For the differential form of the continuity equation, Equation (A2.1) is applied to an infinitesimal control volume as shown in **Fig. A2.2**. Since the element is small, the volume integral is:

$$\frac{\partial}{\partial t}\int_{cv}\rho dV \approx \frac{\partial \rho}{\partial t} r\delta r\delta\theta\delta z \qquad \text{(A2.2)}$$

In r direction:

Net outflow in r direction:

$$\left[\rho V_r + \frac{\partial(\rho V_r)}{\partial r}\frac{\delta r}{2}\right]\left(r + \frac{\delta r}{2}\right)\delta\theta\delta z - \left[\rho V_r - \frac{\partial(\rho V_r)}{\partial r}\frac{\delta r}{2}\right]\left(r - \frac{\delta r}{2}\right)\delta\theta\delta z$$

$$= \left[\rho V_r + \frac{\partial(\rho V_r)}{\partial r}\frac{\delta r}{2}\right]\left(r\delta\theta\delta z + \frac{\delta r}{2}\delta\theta\delta z\right) - \left[\rho V_r - \frac{\partial(\rho V_r)}{\partial r}\frac{\delta r}{2}\right]\left(r\delta\theta\delta z - \frac{\delta r}{2}\delta\theta\delta z\right)$$

$$= \cancel{\rho V_r r\delta\theta\delta z} + \rho V_r\frac{\delta r}{2}\delta\theta\delta z + \frac{\partial(\rho V_r)}{\partial r}\frac{\delta r}{2}r\delta\theta\delta z + \cancel{\frac{\partial(\rho V_r)}{\partial r}\frac{\delta r}{2}\frac{\delta r}{2}\delta\theta\delta z}$$
$$\cancel{-\rho V_r r\delta\theta\delta z} + \rho V_r\frac{\delta r}{2}\delta\theta\delta z + \frac{\partial(\rho V_r)}{\partial r}\frac{\delta r}{2}r\delta\theta\delta z - \cancel{\frac{\partial(\rho V_r)}{\partial r}\frac{\delta r}{2}\frac{\delta r}{2}\delta\theta\delta z}$$

$$= \rho V_r\delta r\delta\theta\delta z + \frac{\partial(\rho V_r)}{\partial r}r\delta r\delta\theta\delta z \qquad \text{(A2.3)}$$

In θ direction:

Net outflow in θ direction:

$$\left[\rho V_\theta + \frac{\partial(\rho V_\theta)}{\partial\theta}\frac{\delta\theta}{2}\right]\delta r\delta z - \left[\rho V_\theta - \frac{\partial(\rho V_\theta)}{\partial\theta}\frac{\delta\theta}{2}\right]\delta r\delta z$$

$$= \frac{\partial(\rho V_\theta)}{\partial\theta}\delta r\delta\theta\delta z \qquad \text{(A2.4)}$$

In z direction:

Net outflow in z direction:

$$\left[\rho V_z + \frac{\partial(\rho V_z)}{\partial z}\frac{\delta z}{2}\right]\delta r r\delta\theta - \left[\rho V_z - \frac{\partial(\rho V_z)}{\partial z}\frac{\delta z}{2}\right]\delta r r\delta\theta$$

$$= \frac{\partial(\rho V_z)}{\partial z} r\delta r\delta\theta\delta z \qquad \text{(A2.5)}$$

Therefore, the net mass flow out of the control surface is:

$$\rho V_r \delta r\delta\theta\delta z + \frac{\partial(\rho V_r)}{\partial r} r\delta r\delta\theta\delta z + \frac{\partial(\rho V_\theta)}{\partial\theta}\delta r\delta\theta\delta z + \frac{\partial(\rho V_z)}{\partial z} r\delta r\delta\theta\delta z \qquad \text{(A2.6)}$$

The rate of increase of mass within the control volume is:

$$\frac{\partial\rho}{\partial t} r\delta r\delta\theta\delta z \qquad \text{(A2.7)}$$

The sum of these two equations equal zero in steady flow, from equations (A2.1) and (A2.2).

$$\frac{\partial\rho}{\partial t} r\delta r\delta\theta\delta z + \rho V_r \delta r\delta\theta\delta z + \frac{\partial(\rho V_r)}{\partial r} r\delta r\delta\theta\delta z + \frac{\partial(\rho V_\theta)}{\partial\theta}\delta r\delta\theta\delta z + \frac{\partial(\rho V_z)}{\partial z} r\delta r\delta\theta\delta z = 0$$

Giving the differential equation for conservation of mass in cylindrical coordinates:

$$\frac{\partial\rho}{\partial t} + \frac{\rho V_r}{r} + \frac{\partial(\rho V_r)}{\partial r} + \frac{1}{r}\frac{\partial(\rho V_\theta)}{\partial\theta} + \frac{\partial(\rho V_z)}{\partial z} = 0 \qquad \text{(A2.8)}$$

Since:

$$\frac{1}{r}\frac{\partial(r\rho V_r)}{\partial r} = \frac{1}{r}\left(\rho V_r + r\frac{\partial(\rho V_r)}{\partial r}\right) = \frac{\rho V_r}{r} + \frac{\partial(\rho V_r)}{\partial r} \qquad \text{(A2.9)}$$

The final equation is:

$$\frac{\partial\rho}{\partial t} + \frac{1}{r}\frac{\partial(r\rho V_r)}{\partial r} + \frac{1}{r}\frac{\partial(\rho V_\theta)}{\partial\theta} + \frac{\partial(\rho V_z)}{\partial z} = 0 \qquad \text{(A2.10)}$$

APPENDIX 3. STREAMLINE CURVATURE PROGRAM COMPRESSOR PERFORMANCE CALCULATION

(Refs. Novak (1967), Jansen and Moffatt (1967)

These authors have provided an explanation of the method which give a good understanding of the use of the SLC equations. The method in the program used in this work (Barbosa, 1987) has subtle differences but fundamentally is the same as the process described here. The meridional velocity equation is derived in **Appendix 4**. Refer to **Fig. A4.1** and **Fig. A4.2** for the parameters and angles.

The approximate analysis is to consider the flow separately on two sets of intersecting streamsurfaces of revolution (Cumpsty, 1989), as described earlier, namely the blade-to-blade (S1) and the hub-to-casing (S2) surfaces. In the meridional throughflow streamline curvature method, the S1 flow is related to two-dimensional compressor cascade flow. The S2 flow (the throughflow), is also approximated as a single axisymmetric streamsurface within the blades. Outside the blades, the actual near loss-free flow would rapidly return to axisymmetry so the approximation there is better. The S2 flow is projected onto the meridional plane for calculations.

One of the more frequently quoted papers in the earlier era of SLC methods contains the necessary features of a typical calculation procedure (Jansen and Moffatt, 1967). It uses the SLC method to estimate the flow at radial stations between the blade rows. Streamsurfaces between blade rows are assumed to be concentric cylinders since there is no blade work to cause Coriolis accelerations.

Through the rotors, flow deflection leads to total pressure and total temperature increase of the flow, and through stators, the flow deflects with total pressure drops. In the calculation procedure, there will be step changes in total temperature and total pressures from one station to the next.

(1). An equation is obtained for the meridional velocity variation from the radial equilibrium condition from the equation of motion:

$$\frac{\partial V_m^2}{\partial r} + E(r)V_m^2 = G(r) \qquad \text{(A3.1)}$$

The objective is to guess by iteration a set of streamlines that satisfy this and the equation of continuity:

$$w = \int_{r_{hub}}^{r_{casing}} \rho V_m 2\pi r \cos\phi dr \qquad \text{(A3.2)}$$

These equations cannot be solved explicitly; a finite-difference method is used for solution.

(2). The annulus is first subdivided into a finite number of streamtubes by assuming a constant axial velocity along the radius. For the remainder of the procedure, the flow through these streamtubes remains constant. The streamlines only change position when a better estimation of meridional velocity is obtained. Note that in Barbosa's (1987) method, the mass flow in each streamline can be varied at the beginning of the calculation in order to concentrate streamlines at a desired position.

(3). Required terms such as for radii of curvature are obtained. Streamline properties are obtained by fitting a least-squares or spline curve through the points defining each streamtube.

(4). The equation of motion is integrated so the calculation proceeds along streamlines from hub to casing, in finite steps of size Δr_j.

$$(V_m)_{j+1} = \left[V_{mj}^2 e^{G\Delta r_j} - \frac{G}{E}\left(1 - e^{G\Delta r_j}\right) \right]^{\frac{1}{2}} \qquad \text{(A3.3)}$$

E and G are evaluated for the streamtube midway between the jth and (j+1)th streamline and are assumed constant for the streamtube. Equation (A3.3) relates the meridional velocity of each streamline along a radial line. It can be expressed in terms of the hub meridional velocity V_{mhub}. The value of V_{mhub} is found from the continuity equation applied at the particular station. It is essentially a constant of integration. Note that in Barbosa's (1987) method, V_{mhub} is a starting guess at blade inlet and V_{mhub} or V_{mmid} is a choice of start guess at blade exit as rapid loss near the walls affect the stability of the iteration.

A guess is made of V_{mhub} and the values for V_{mj} from Equation (A3.3) are put into the continuity equation (A3.2). The mass flow through each streamtube has been set constant

and equal as input from station to station, so the streamtube width Δr_j can be found from the continuity equation. The sum of the streamtube widths should equal the annulus width at the particular station. Generally, an annulus that is too large or too small is calculated when all of the Δr_j values are summed. A new value of V_{mhub} based on the difference between the estimated and known annulus is made and this iteration is continued until the continuity equation is satisfied when the summed Δr_j values equals the annulus width. New streamline positions are stored to replace those set in (1).

(4). The above iterations are carried out at each axial station to obtain streamline coordinates for the whole compressor.

This description uses the radial direction for the meridional velocity equation. Barbosa (1987) uses the tangent to the blade edge direction. Katsanis (1964) used the velocity gradient equation along an arbitrary quasi-orthogonal rather than the normal to the streamline used in previous methods. The normal to the streamline can change considerably in length and direction during calculations. The quasi-orthogonals are fixed at each calculating station and remain fixed while the streamline guesses change.

Daneshyar and Shaalan (1972) have discussed the operation of the streamline curvature method in the regions of stall and choke. Choking and negative velocities (flow reversals) may occur in the process of the calculation. When these occur in an intermediate streamline pattern and are not present in the final solution, the basic techniques have to be modified to deal with the situation. The method does not allow for the case where choked or reversed flows (generally surge region) occur in the final solution without substantial modifications. The only way to satisfy the system of equation is then to allow for negative meridional velocities to occur. Mathematically, when choking or zero meridional velocities occur, the conditions for the existence and uniqueness of the solution of the governing differential-integral equations are violated. In the computer program, the finite difference equations replace these original equations, and the behaviour of these is of interest. The authors also noted that when losses are involved in the computation, a dissipative body force should be included in the momentum equation. This can usually be neglected for small losses. For the

particular axial compressor they analysed, it was found that this correction term was negligible even for large losses.

Glenny (1974) sumamrises the overall basis of a streamline curvature model. First, a streamline distribution in the meridional plane is estimated with an initially assumed mass flow distribution. The axisymmetric radial equation of motion is solved at grid points situated between blade rows in combination with the energy equation (in terms of the relative enthalpy along a streamline), the equation of state, approximations of the slope and curvature of the streamline. An iterative solution gives the radial distribution of the meridional velocity. The turning imparted by each blade row is calculated using empirical correlations for blade deviations to obtain flow angles at exit of the blade row. Now the radial flow parameters can be checked in another iterative process to satisfy the integral continuity equation.

The whole procedure is repeated at each axial station to give a new mass flow distribution through the compressor, with new values for the curvatures and slopes of streamlines.

The whole cycle is repeated until there is no change in the mass flow distributions within a certain tolerance.

Assumptions of a streamline curvature method:

(1). Flow is steady and adiabatic.

(2). Constant relative total enthalpy along a streamline.

(3). Working fluid is perfect gas.

(4). Frictionless flow at stations where radial equation of motion is solved.

(5). Entropy rises allowed between calculating stations along a streamline, to account for blade profile losses, annulus losses and secondary flow losses.

(6). Blade deflections and losses are calculated from 2-D cascade data.

(7). Annulus and secondary losses are determined from empirical relations.

(8). Area variations from the development of the annulus boundary layer are accounted for by use of a blockage factor at each calculating plane through the compressor.

The method of Glenny (1974) had included the effect of secondary flow on the turning of the main flow and on the turning of the flow in the vicinity of the annulus walls in the blockage factor distribution.

APPENDIX 4. TYPICAL DERIVATION OF STREAMLINE CURVATURE EQUATIONS

This section will calculate the meridional velocity variation with full radial equilibrium as derived by Novak (1967) and will include the full steps of the derivation.

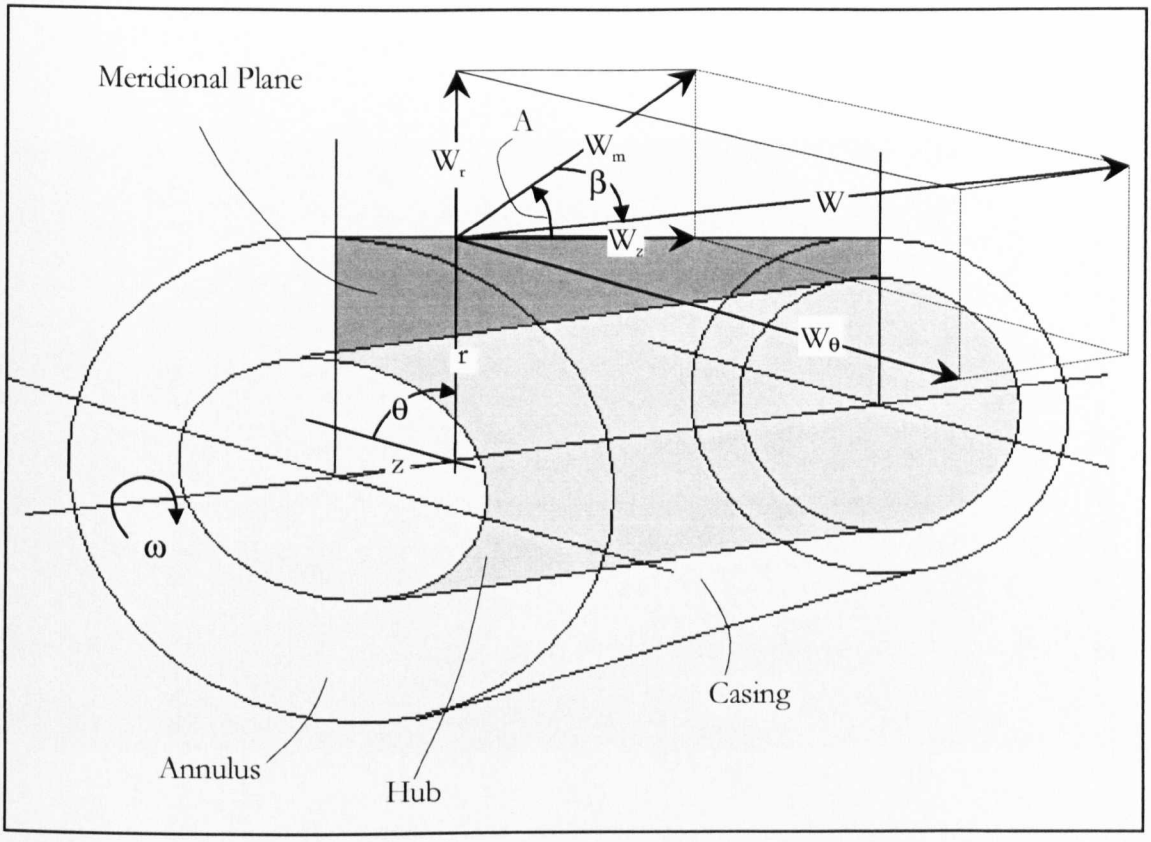

Fig A4.1 Compressor annulus and meridional plane with relative velocities.

A cylindrical coordinate system is used, (Fig. A1.1). The meridional plane is the r-z plane, (Fig. A4.1, Fig. A4.2), and the annulus geometry is defined in this plane. The cylindrical streamsurfaces pass through the meridional plane, such that in the meridional plane, streamlines are defined by the fitting of a curve through the points at axial calculating stations for each streamsurface. The streamlines are generally inclined at an angle A with the z-axis. The meridional flow velocity follows the streamline and has magnitude $W_m = \sqrt{(W_r^2 + W_z^2)}$.

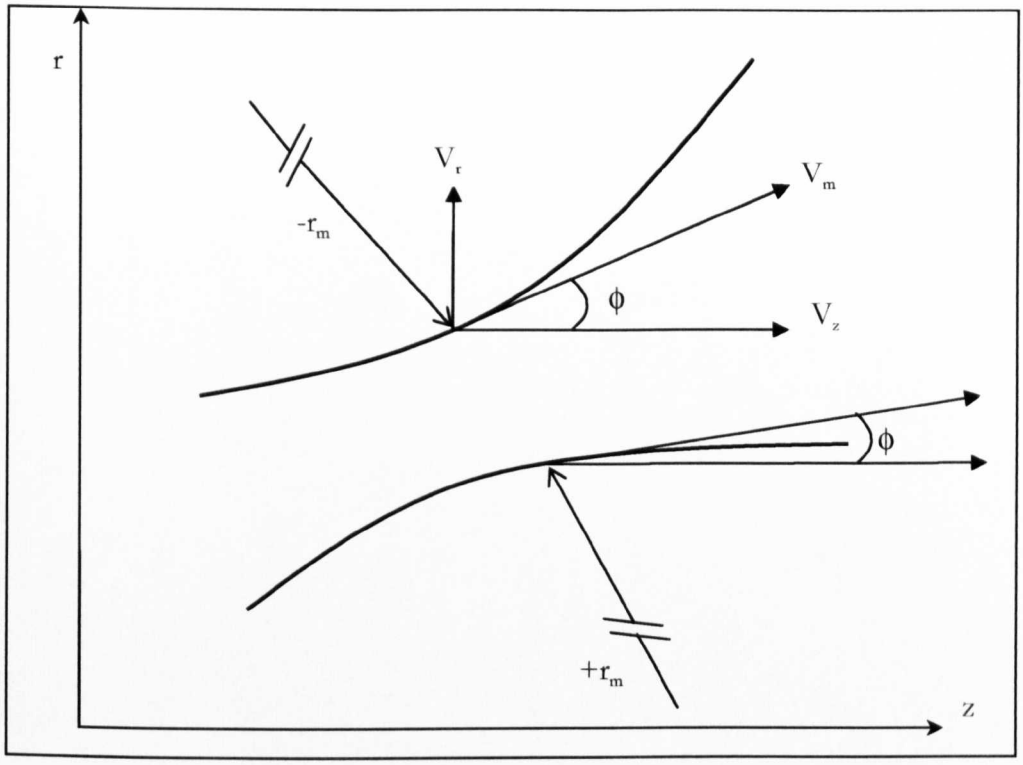

Fig A4.2 Meridional plane.

Streamline curvature methods solve for the radial component of the momentum equation, the equation of continuity, and the energy equation.

The cylindrical coordinate system in Fig. A4.1: del is,

$$\bar{\nabla} = \bar{\varepsilon}_r \frac{\partial}{\partial r} + \bar{\varepsilon}_\theta \frac{1}{r}\frac{\partial}{\partial \theta} + \bar{\varepsilon}_z \frac{\partial}{\partial z} \qquad \text{(A4.1)}$$

with $\bar{\varepsilon}_r, \bar{\varepsilon}_\theta, \bar{\varepsilon}_z$ being the unit vectors in the r, θ and z directions respectively.

The acceleration of a fluid particle is the time rate of change of the velocity vector along the path of the particle in the velocity field:

$$\frac{d\bar{V}}{dt} = \frac{\partial \bar{V}}{\partial t} + (\bar{V} \cdot \bar{\nabla})\bar{V} \qquad \text{(A4.2)}$$

with V (V_r, V_θ, V_z) in the cylindrical coordinate system.

The net force on a fluid particle also gives the acceleration, ignoring the gravitational force term and for inviscid flow, ignoring the frictional force exerted on the particle.

$$\frac{d\vec{V}}{dt} = -\frac{1}{\rho}\vec{\nabla}p \tag{A4.3}$$

$$\frac{\partial\vec{V}}{\partial t} + \vec{V}\cdot\nabla\vec{V} = -\frac{1}{\rho}\vec{\nabla}p \tag{A4.4}$$

In the cylindrical coordinate system:

$$\vec{R} = r\vec{\varepsilon}_r + z\vec{\varepsilon}_z \tag{A4.5}$$

Define velocity:

$$\vec{V} = V_r\vec{\varepsilon}_r + V_\theta\vec{\varepsilon}_\theta + V_z\vec{\varepsilon}_z \tag{A4.6}$$

$$\vec{V} = \frac{d\vec{R}}{dt} = \frac{d(r\vec{\varepsilon}_r)}{dt} + \frac{d(z\vec{\varepsilon}_z)}{dt} \tag{A4.7}$$

$$\vec{V} = \frac{dr}{dt}\vec{\varepsilon}_r + r\frac{d\vec{\varepsilon}_r}{dt} + \frac{dz}{dt}\vec{\varepsilon}_z + z\frac{d\vec{\varepsilon}_z}{dt} \tag{A4.8}$$

$$\vec{V} = \frac{dr}{dt}\vec{\varepsilon}_r + r\vec{\varepsilon}_\theta\frac{d\theta}{dt} + \frac{dz}{dt}\vec{\varepsilon}_z \tag{A4.9}$$

Now acceleration:

$$\begin{aligned}
a = \frac{\partial\vec{V}}{\partial t} &= \left(\frac{\partial V}{\partial t}\right)_r\vec{\varepsilon}_r + \left(\frac{\partial V}{\partial t}\right)_\theta\vec{\varepsilon}_\theta + \left(\frac{\partial V}{\partial t}\right)_z\vec{\varepsilon}_z \\
&= \frac{dr}{dt}\frac{d\vec{\varepsilon}_r}{dt} + \vec{\varepsilon}_r\frac{d^2r}{dt^2} + r\frac{d\theta}{dt}\frac{d\vec{\varepsilon}_\theta}{dt} + \vec{\varepsilon}_\theta\left(r\frac{d^2\theta}{dt^2} + \frac{d\theta}{dt}\frac{dr}{dt}\right) + \frac{dz}{dt}\frac{d\vec{\varepsilon}_z}{dt} + \vec{\varepsilon}_z\frac{d^2z}{dt^2} \\
&= \vec{\varepsilon}_\theta\frac{dr}{dt}\frac{d\theta}{dt} + \vec{\varepsilon}_r\frac{d^2r}{dt^2} - r\vec{\varepsilon}_r\left(\frac{d\theta}{dt}\right)^2 + r\vec{\varepsilon}_\theta\frac{d^2\theta}{dt^2} + \vec{\varepsilon}_\theta\frac{dr}{dt}\frac{d\theta}{dt} + 0 + \vec{\varepsilon}_z\frac{d^2z}{dt^2} \\
&= \left(\frac{d^2r}{dt^2} - r\left(\frac{d\theta}{dt}\right)^2\right)\vec{\varepsilon}_r + \left(r\frac{d^2\theta}{dt^2} + 2\frac{dr}{dt}\frac{d\theta}{dt}\right)\vec{\varepsilon}_\theta + \left(\frac{d^2z}{dt^2}\right)\vec{\varepsilon}_z \\
&= \left(\frac{dV_r}{dt} - \frac{1}{r}(r\omega)^2\right)\vec{\varepsilon}_r + \left(\left(r\frac{d\omega}{dt} + \omega\frac{dr}{dt}\right) + \frac{1}{r}r\omega\frac{dr}{dt}\right)\vec{\varepsilon}_\theta + \left(\frac{dV_z}{dt}\right)\vec{\varepsilon}_z \\
&= \left(\frac{dV_r}{dt} - \frac{1}{r}V_\theta^2\right)_r\vec{\varepsilon}_r + \left(\frac{dV_\theta}{dt} + \frac{1}{r}V_\theta V_r\right)\vec{\varepsilon}_\theta + \left(\frac{dV_z}{dt}\right)\vec{\varepsilon}_z
\end{aligned} \tag{A4.10}$$

Separating the components of acceleration in the cylindrical coordinate system:

$$\left(\frac{dV}{dt}\right)_r = \frac{dV_r}{dt} - \frac{V_\theta^2}{r}$$
$$\left(\frac{dV}{dt}\right)_\theta = \frac{dV_\theta}{dt} + \frac{V_\theta V_r}{r} \qquad \text{(A4.11)}$$
$$\left(\frac{dV}{dt}\right)_z = \frac{dV_z}{dt}$$

Considering equations (4) and (11):

$$\frac{\partial \bar{V}}{\partial t} = \frac{\partial V_r}{\partial t}\bar{\varepsilon}_r + \frac{\partial V_\theta}{\partial t}\bar{\varepsilon}_\theta + \frac{\partial V_z}{\partial t}\bar{\varepsilon}_z \qquad \text{(A4.12)}$$

Using Equation (A4.6):

$$\vec{\nabla}\cdot\vec{\nabla} = \vec{\nabla}\cdot\left(\frac{\partial}{\partial r}\vec{\varepsilon}_r + \frac{1}{r}\frac{\partial}{\partial\theta}\vec{\varepsilon}_\theta + \frac{\partial}{\partial z}\vec{\varepsilon}_z\right)$$

$$= \frac{\partial\vec{\nabla}}{\partial r}\cdot\vec{\varepsilon}_r + \frac{1}{r}\frac{\partial\vec{\nabla}}{\partial\theta}\cdot\vec{\varepsilon}_\theta + \frac{\partial\vec{\nabla}}{\partial z}\cdot\vec{\varepsilon}_z$$

$$= \left[\vec{\varepsilon}_r\cdot\left(\frac{\partial\left(V_r\vec{\varepsilon}_r + V_\theta\vec{\varepsilon}_\theta + V_z\vec{\varepsilon}_z\right)}{\partial r}\right)\right] + \left[\frac{\vec{\varepsilon}_\theta}{r}\cdot\left(\frac{\partial\left(V_r\vec{\varepsilon}_r + V_\theta\vec{\varepsilon}_\theta + V_z\vec{\varepsilon}_z\right)}{\partial\theta}\right)\right]$$

$$+ \left[\vec{\varepsilon}_z\cdot\left(\frac{\partial\left(V_r\vec{\varepsilon}_r + V_\theta\vec{\varepsilon}_\theta + V_z\vec{\varepsilon}_z\right)}{\partial z}\right)\right]$$

$$= \left[\vec{\varepsilon}_r\cdot\left(V_r\frac{\partial\vec{\varepsilon}_r}{\partial r} + \vec{\varepsilon}_r\frac{\partial V_r}{\partial r} + V_\theta\frac{\partial\vec{\varepsilon}_\theta}{\partial r} + \vec{\varepsilon}_\theta\frac{\partial V_\theta}{\partial r} + V_z\frac{\partial\vec{\varepsilon}_z}{\partial r} + \vec{\varepsilon}_z\frac{\partial V_z}{\partial r}\right)\right]$$

$$+ \left[\frac{\vec{\varepsilon}_\theta}{r}\cdot\left(V_r\frac{\partial\vec{\varepsilon}_r}{\partial\theta} + \vec{\varepsilon}_r\frac{\partial V_r}{\partial\theta} + V_\theta\frac{\partial\vec{\varepsilon}_\theta}{\partial\theta} + \vec{\varepsilon}_\theta\frac{\partial V_\theta}{\partial\theta} + V_z\frac{\partial\vec{\varepsilon}_z}{\partial\theta} + \vec{\varepsilon}_z\frac{\partial V_z}{\partial\theta}\right)\right]$$

$$+ \left[\vec{\varepsilon}_z\cdot\left(V_r\frac{\partial\vec{\varepsilon}_r}{\partial z} + \vec{\varepsilon}_r\frac{\partial V_r}{\partial z} + V_\theta\frac{\partial\vec{\varepsilon}_\theta}{\partial z} + \vec{\varepsilon}_\theta\frac{\partial V_\theta}{\partial z} + V_z\frac{\partial\vec{\varepsilon}_z}{\partial z} + \vec{\varepsilon}_z\frac{\partial V_z}{\partial z}\right)\right]$$

$$= \left[\vec{\varepsilon}_r\cdot\left(0 + \vec{\varepsilon}_r\frac{\partial V_r}{\partial r} + 0 + \vec{\varepsilon}_\theta\frac{\partial V_\theta}{\partial r} + 0 + \vec{\varepsilon}_z\frac{\partial V_z}{\partial r}\right)\right]$$

$$+ \left[\frac{\vec{\varepsilon}_\theta}{r}\cdot\left(V_r\vec{\varepsilon}_\theta + \vec{\varepsilon}_r\frac{\partial V_r}{\partial\theta} + V_\theta\left(-\vec{\varepsilon}_r\right) + \vec{\varepsilon}_\theta\frac{\partial V_\theta}{\partial\theta} + 0 + \vec{\varepsilon}_z\frac{\partial V_z}{\partial\theta}\right)\right]$$

$$+ \left[\vec{\varepsilon}_z\cdot\left(0 + \vec{\varepsilon}_r\frac{\partial V_r}{\partial z} + 0 + \vec{\varepsilon}_\theta\frac{\partial V_\theta}{\partial z} + 0 + \vec{\varepsilon}_z\frac{\partial V_z}{\partial z}\right)\right] \qquad \text{(A4.13)}$$

$$= \left(\frac{\partial V_r}{\partial r} + 0 + 0\right) + \left(\frac{V_r}{r} + 0 + 0 + \frac{1}{r}\frac{\partial V_\theta}{\partial\theta} + 0\right) + \left(0 + 0 + \frac{\partial V_z}{\partial z}\right)$$

$$= \left(\frac{\partial V_r}{\partial r} + \frac{V_r}{r}\right) + \left(\frac{1}{r}\frac{\partial V_\theta}{\partial\theta}\right) + \left(\frac{\partial V_z}{\partial z}\right)$$

$$= \frac{1}{r}\frac{\partial(rV_r)}{\partial r} + \frac{1}{r}\frac{\partial V_\theta}{\partial\theta} + \frac{\partial V_z}{\partial z}$$

$$\vec{V} = V_r\vec{\varepsilon}_r + V_\theta\vec{\varepsilon}_\theta + V_z\vec{\varepsilon}_z \qquad \text{(A4.6)}$$

The velocity vectors $\vec{V}_r, \vec{V}_\theta, \vec{V}_z$ are functions of r, θ and z and t in the Eulerian method to describe fluid motion, i.e., observing particles passing by in the acceleration field from a fixed position in space.

$$\bar{V}_r = f(r,\theta,z,t)$$

$$\bar{V}_\theta = f(r,\theta,z,t) \qquad \text{(A4.14)}$$

$$\bar{V}_z = f(r,\theta,z,t)$$

Acceleration is the time rate of change of the velocity of the fluid. The velocity is a function of both position and time. Use the chain rule of differentiation to obtain the acceleration.

$$\frac{d\bar{V}}{dt} = \frac{\partial \bar{V}}{\partial t} + \left(\frac{\partial \bar{V}}{\partial r}\frac{dr}{dt}\right) + \left(\frac{\partial \bar{V}}{\partial \theta}\frac{d\theta}{dt}\right) + \left(\frac{\partial \bar{V}}{\partial z}\frac{dz}{dt}\right) \qquad \text{(A4.15)}$$

$$V_r = \frac{dr}{dt}$$

$$V_\theta = r\frac{d\theta}{dt} \qquad \text{(A4.16)}$$

$$V_z = \frac{dz}{dt}$$

This obtains the acceleration field from the velocity field.

$$\frac{d\bar{V}}{dt} = \frac{\partial \bar{V}}{\partial t} + \frac{\partial \bar{V}}{\partial r}V_r + \frac{\partial \bar{V}}{\partial \theta}\frac{V_\theta}{r} + \frac{\partial \bar{V}}{\partial z}V_z \qquad \text{(A4.17)}$$

The scalar components of this are:

$$\frac{dV_r}{dt} = \frac{\partial V_r}{\partial t} + \frac{\partial V_r}{\partial r}V_r + \frac{\partial V_r}{\partial \theta}\frac{V_\theta}{r} + \frac{\partial V_r}{\partial z}V_z$$

$$\frac{dV_\theta}{dt} = \frac{\partial V_\theta}{\partial t} + \frac{\partial V_\theta}{\partial r}V_r + \frac{\partial V_\theta}{\partial \theta}\frac{V_\theta}{r} + \frac{\partial V_\theta}{\partial z}V_z \qquad \text{(A4.18)}$$

$$\frac{dV_z}{dt} = \frac{\partial V_z}{\partial t} + \frac{\partial V_z}{\partial r} V_r + \frac{\partial V_z}{\partial \theta} \frac{V_\theta}{r} + \frac{\partial V_z}{\partial z} V_z$$

This is the substantial derivative, which in shorthand form is:

$$\frac{D\vec{V}}{Dt} = \frac{\partial \vec{V}}{\partial t} + (\vec{V} \cdot \vec{\nabla})\vec{V}$$

$(\vec{V} \cdot \vec{\nabla})(\ )$ represents the operator:

$$(\vec{V} \cdot \vec{\nabla})(\ ) = V_r \frac{\partial(\ )}{\partial r} + \frac{V_\theta}{r} \frac{\partial(\ )}{\partial \theta} + V_z \frac{\partial(\ )}{\partial z} \qquad \text{(A4.19)}$$

In conjunction with equations( ), then

$$a_r = \left(\frac{dV}{dt}\right)_r = \frac{\partial V_r}{\partial t} + \frac{\partial V_r}{\partial r} V_r + \frac{\partial V_r}{\partial \theta} \frac{V_\theta}{r} + \frac{\partial V_r}{\partial z} V_z - \frac{V_\theta^2}{r} \qquad \text{(A4.20)}$$

$$a_\theta = \left(\frac{dV}{dt}\right)_\theta = \frac{\partial V_\theta}{\partial t} + \frac{\partial V_\theta}{\partial r} V_r + \frac{\partial V_\theta}{\partial \theta} \frac{V_\theta}{r} + \frac{\partial V_\theta}{\partial z} V_z + \frac{V_r V_\theta}{r} \qquad \text{(A4.21)}$$

$$a_z = \left(\frac{dV}{dt}\right)_z = \frac{\partial V_z}{\partial t} + \frac{\partial V_z}{\partial r} V_r + \frac{\partial V_z}{\partial \theta} \frac{V_\theta}{r} + \frac{\partial V_z}{\partial z} V_z \qquad \text{(A4.22)}$$

Finally, combining this with Equation (A4.3) gives the three components of the equation of motion for inviscid, compressible fluids.

$$\frac{\partial V_r}{\partial t} + \frac{\partial V_r}{\partial r} V_r + \frac{\partial V_r}{\partial \theta} \frac{V_\theta}{r} + \frac{\partial V_r}{\partial z} V_z - \frac{V_\theta^2}{r} = -\frac{1}{\rho} \frac{\partial p}{\partial r} \qquad \text{(A4.23)}$$

$$\frac{\partial V_\theta}{\partial t} + \frac{\partial V_\theta}{\partial r} V_r + \frac{\partial V_\theta}{\partial \theta} \frac{V_\theta}{r} + \frac{\partial V_\theta}{\partial z} V_z + \frac{V_r V_\theta}{r} = -\frac{1}{r}\left(\frac{1}{\rho} \frac{\partial p}{\partial \theta}\right) \qquad \text{(A4.24)}$$

$$\frac{\partial V_z}{\partial t}+\frac{\partial V_z}{\partial r}V_r+\frac{\partial V_z}{\partial \theta}\frac{V_\theta}{r}+\frac{\partial V_z}{\partial z}V_z=-\frac{1}{\rho}\frac{\partial p}{\partial z} \qquad \text{(A4.25)}$$

These equations can be arranged to show the components of vorticity by adding and subtracting:

$$V_\theta\frac{\partial V_\theta}{\partial r}+V_z\frac{\partial V_z}{\partial r} \text{ to Equation (A4.23)} \qquad \text{(A4.26)}$$

$$\frac{1}{r}\left(V_r\frac{\partial V_r}{\partial \theta}+V_z\frac{\partial V_z}{\partial \theta}\right) \text{ to Equation (A4.24)} \qquad \text{(A4.27)}$$

$$V_r\frac{\partial V_r}{\partial z}+V_\theta\frac{\partial V_\theta}{\partial z} \text{ to Equation (A4.25)} \qquad \text{(A4.28)}$$

e.g. for r-component of momentum equation:

$$\frac{\partial V_r}{\partial t}+\frac{\partial V_r}{\partial r}V_r+\frac{\partial V_r}{\partial \theta}\frac{V_\theta}{r}+\frac{\partial V_r}{\partial z}V_z-\frac{V_\theta^2}{r}$$
$$+\left(V_\theta\frac{\partial V_\theta}{\partial r}+V_z\frac{\partial V_z}{\partial r}\right)-\left(V_\theta\frac{\partial V_\theta}{\partial r}+V_z\frac{\partial V_z}{\partial r}\right)=-\frac{1}{\rho}\frac{\partial p}{\partial r}$$

$$\frac{\partial V_r}{\partial t}+\left(V_r\frac{\partial V_r}{\partial r}+V_\theta\frac{\partial V_\theta}{\partial r}+V_z\frac{\partial V_z}{\partial r}\right)$$
$$+\left(\frac{\partial V_r}{\partial \theta}\frac{V_\theta}{r}-\frac{V_\theta^2}{r}-V_\theta\frac{\partial V_\theta}{\partial r}\right)+\left(\frac{\partial V_r}{\partial z}V_z-V_z\frac{\partial V_z}{\partial r}\right)=-\frac{1}{\rho}\frac{\partial p}{\partial r}$$

Since

$$\left(\frac{\partial V_r}{\partial r}V_r+V_\theta\frac{\partial V_\theta}{\partial r}+V_z\frac{\partial V_z}{\partial r}\right)=\frac{1}{2}\left(2V_r\frac{\partial V_r}{\partial r}+2V_\theta\frac{\partial V_\theta}{\partial r}+2V_z\frac{\partial V_z}{\partial r}\right)$$
$$=\frac{\partial\frac{1}{2}\left(V_r^2+V_\theta^2+V_z^2\right)}{\partial r}=\frac{\partial\frac{1}{2}\left(\sqrt{V_r^2+V_\theta^2+V_z^2}\right)^2}{\partial r}=\frac{\partial\left(\frac{1}{2}V^2\right)}{\partial r}$$

therefore,

$$\frac{\partial V_r}{\partial t}+\frac{\partial\left(\frac{1}{2}V^2\right)}{\partial r}-\frac{V_\theta}{r}\left(+\frac{r\partial V_\theta}{\partial r}+V_\theta-\frac{\partial V_r}{\partial \theta}\right)+V_z\left(\frac{\partial V_r}{\partial z}-\frac{\partial V_z}{\partial r}\right)=-\frac{1}{\rho}\frac{\partial p}{\partial r}$$

$$\frac{\partial V_r}{\partial t}+\frac{\partial\left(\frac{1}{2}V^2\right)}{\partial r}-\frac{V_\theta}{r}\left(\frac{\partial(rV_\theta)}{\partial r}-\frac{\partial V_r}{\partial \theta}\right)+V_z\left(\frac{\partial V_r}{\partial z}-\frac{\partial V_z}{\partial r}\right)=-\frac{1}{\rho}\frac{\partial p}{\partial r} \qquad \text{(A4.29)}$$

The last two bracketed terms are the components of vorticity.

For the θ-component:

$$\frac{\partial V_\theta}{\partial t}+\frac{\partial V_\theta}{\partial r}V_r+\frac{\partial V_\theta}{\partial \theta}\frac{V_\theta}{r}+\frac{\partial V_\theta}{\partial z}V_z+\frac{V_r V_\theta}{r}$$
$$+\frac{1}{r}\left(V_r\frac{\partial V_r}{\partial \theta}+V_z\frac{\partial V_z}{\partial \theta}\right)-\frac{1}{r}\left(V_r\frac{\partial V_r}{\partial \theta}+V_z\frac{\partial V_z}{\partial \theta}\right)=-\frac{1}{r}\left(\frac{1}{\rho}\frac{\partial p}{\partial \theta}\right)$$

$$\frac{\partial V_\theta}{\partial t}+\frac{1}{r}\left(V_r\frac{\partial V_r}{\partial \theta}+V_\theta\frac{\partial V_\theta}{\partial \theta}+V_z\frac{\partial V_z}{\partial \theta}\right)$$
$$+\frac{V_z}{r}\left(\frac{r\partial V_\theta}{\partial z}-\frac{\partial V_z}{\partial \theta}\right)+\frac{V_r}{r}\left(\frac{r\partial V_\theta}{\partial r}+V_\theta-\frac{\partial V_r}{\partial \theta}\right)=-\frac{1}{r}\left(\frac{1}{\rho}\frac{\partial p}{\partial \theta}\right)$$

$$\frac{\partial V_\theta}{\partial t}+\frac{1}{r}\frac{\partial\left(\frac{1}{2}V^2\right)}{\partial \theta}-\frac{V_z}{r}\left(\frac{\partial V_z}{\partial \theta}-\frac{\partial(rV_\theta)}{\partial z}\right)+\frac{V_r}{r}\left(\frac{\partial(rV_\theta)}{\partial r}-\frac{\partial V_r}{\partial \theta}\right)=-\frac{1}{r}\left(\frac{1}{\rho}\frac{\partial p}{\partial \theta}\right) \qquad \text{(A4.30)}$$

since $\frac{\partial r}{\partial z}=0$

For the z-component:

$$\frac{\partial V_z}{\partial t}+\frac{\partial V_z}{\partial r}V_r+\frac{\partial V_z}{\partial \theta}\frac{V_\theta}{r}+\frac{\partial V_z}{\partial z}V_z$$
$$+\left(V_r\frac{\partial V_r}{\partial z}+V_\theta\frac{\partial V_\theta}{\partial z}\right)-\left(V_r\frac{\partial V_r}{\partial z}+V_\theta\frac{\partial V_\theta}{\partial z}\right)=-\frac{1}{\rho}\frac{\partial p}{\partial z}$$

$$\frac{\partial V_z}{\partial t}+\left(\frac{\partial V_r}{\partial z}V_r+\frac{\partial V_\theta}{\partial z}V_\theta+\frac{\partial V_z}{\partial z}V_z\right)$$
$$+V_r\left(\frac{\partial V_z}{\partial r}-\frac{\partial V_r}{\partial z}\right)+\frac{V_\theta}{r}\left(\frac{\partial V_z}{\partial \theta}-\frac{r\partial V_\theta}{\partial z}\right)=-\frac{1}{\rho}\frac{\partial p}{\partial z}$$

$$\frac{\partial V_z}{\partial t}+\frac{\partial\left(\frac{1}{2}V^2\right)}{\partial z}-V_r\left(\frac{\partial V_r}{\partial z}-\frac{\partial V_z}{\partial r}\right)+\frac{V_\theta}{r}\left(\frac{\partial V_z}{\partial \theta}-\frac{\partial(rV_\theta)}{\partial z}\right)=-\frac{1}{\rho}\frac{\partial p}{\partial z} \qquad \text{(A4.31)}$$

The components of vorticity are:

$$\left(\bar{\nabla}\times\bar{V}\right)_r=\frac{1}{r}\left(\frac{\partial V_z}{\partial \theta}-\frac{\partial(rV_\theta)}{\partial z}\right) \qquad \text{(A4.32)}$$

$$\left(\bar{\nabla}\times\bar{V}\right)_\theta=\left(\frac{\partial V_r}{\partial z}-\frac{\partial V_z}{\partial r}\right) \qquad \text{(A4.33)}$$

$$\left(\bar{\nabla}\times\bar{V}\right)_z=\frac{1}{r}\left(\frac{\partial(rV_\theta)}{\partial r}-\frac{\partial V_r}{\partial \theta}\right) \qquad \text{(A4.34)}$$

Therefore, the above 3 terms in Equations (A4.29-A4.31) represent the components of the cross product of the velocity and the vorticity:

$$\bar{V}\times\left(\bar{\nabla}\times\bar{V}\right)$$

Equations (A4.29-A4.31) in vector form are therefore:

$$\frac{\partial\bar{V}}{\partial t}-\bar{V}\times\left(\bar{\nabla}\times\bar{V}\right)+\nabla\left(\frac{\bar{V}^2}{2}\right)=-\frac{1}{\rho}\bar{\nabla}p \qquad \text{(A4.35)}$$

The following well-known equation relates pressure and density to the stagnation enthalpy, static temperature and entropy:

$$\frac{1}{\rho}\bar{\nabla}p=\bar{\nabla}H-t\bar{\nabla}S-\nabla\left(\frac{\bar{V}^2}{2}\right) \qquad \text{(A4.36)}$$

Combining with Equation (A4.35) leads to the form of the equation of motion known as the Crocco equation:

$$\frac{\partial \bar{V}}{\partial t} - \bar{V} \times (\bar{\nabla} \times \bar{V}) = -\bar{\nabla} H + t\bar{\nabla} S \qquad \text{(A4.37)}$$

This inviscid equation of motion can also be written in a rotating coordinate system:

$$\frac{\partial \bar{W}}{\partial t} - \bar{W} \times (\bar{\nabla} \times \bar{W}) = -\bar{\nabla} I + t\bar{\nabla} S \qquad \text{(A4.38)}$$

where

$$\bar{W} = \bar{V} - \bar{U} = \bar{V} - \omega r \bar{\varepsilon}_\theta \qquad \text{(A4.39)}$$

and

$$I = H - UV_\theta = H - \omega r V_\theta \qquad \text{(A4.40)}$$

I is the stagnation enthalpy relative to the rotating system, or the rothalpy.

Now some assumptions will simplify the equation.

(1). Steady-state conditions mean all terms with local time derivatives $\frac{\partial}{\partial t}$ are omitted.

(2). Given steady-state conditions, a streamline can be defined with equation:

$$d\bar{R} \times \bar{V} = 0. \qquad \text{(A4.41)}$$

This says that the path $d\bar{r}$ is parallel to V at each point in the field. The three-component equations then require:

$$dr : rd\theta : dz : ds = V_r : V_\theta : V_z : V \qquad \text{(A4.42)}$$

s is the streamline direction.

(3). Define the meridional direction so that:

$$dm : dr : dz = V_m : V_r : V_z$$

$$V_m^2 = V_r^2 + V_z^2$$

$$\phi = \tan^{-1}\left(\frac{V_r}{V_z}\right) \qquad \text{(A4.43)}$$

$$V_r = V_m \sin\phi \qquad \sin\phi = \frac{V_r}{V_m} = \frac{\partial r}{\partial m}$$

$$V_z = V_m \cos\phi \qquad \cos\phi = \frac{V_z}{V_m} = \frac{\partial z}{\partial m}$$

$$\tan\phi = \frac{V_r}{V_z} = \frac{\partial r}{\partial z}$$

The m-direction is defined by the projection of any streamline in the meridional r-z plane. When the flow field is axisymmetric, the m-direction is usually referred to as the meridional direction.

If u is any direction, the directional derivative in cylindrical coordinates is:

$$\frac{\partial}{\partial u} = \frac{\partial}{\partial r}\frac{dr}{du} + \frac{1}{r}\frac{\partial}{\partial \theta}\frac{d\theta}{du} + \frac{\partial}{\partial z}\frac{dz}{du}$$

Therefore, taking the direction derivative in the meridional m-direction:

$$\frac{\partial}{\partial m} = \frac{\partial}{\partial r}\frac{dr}{dm} + \frac{\partial}{\partial z}\frac{dz}{dm}$$

since m is perpendicular to the θ-direction and for axisymmetric flow, $\frac{\partial}{\partial \theta} = 0$.

If the streamline is written in terms of r and m, (m=m(r,z))

$$\frac{\partial}{\partial m} = \frac{\partial}{\partial r}\frac{dr}{dm} + \frac{\partial}{\partial z}\frac{dz}{dm}$$

Therefore,

$$V_m \frac{\partial}{\partial m} = V_r \frac{\partial}{\partial r} + V_z \frac{\partial}{\partial z} \qquad \text{(A4.44)}$$

and

$$\frac{\partial}{\partial m} = \sin\phi\frac{\partial}{\partial r} + \cos\phi\frac{\partial}{\partial z} \qquad \text{(A4.45)}$$

Now derivatives in the z-direction are replaced by derivatives in the m and r-directions. From Equation (A4.45),

$$\frac{\partial}{\partial z} = \frac{1}{\cos\phi}\left(\frac{\partial}{\partial m} - \sin\phi\frac{\partial}{\partial r}\right) \qquad \text{(A4.46)}$$

Note this is not a coordinate transformation. When applied to the momentum equations (A4.29-A4.31), the results remain the r, θ and z components.

(4). The fluid is adiabatic and inviscid along any streamtube. One of the three components of the momentum equation is redundant: only the r and θ- components are used. The entropy and enthalpy does not need to be everywhere constant as it does not violate the Euler equation to specify differing values of entropy and enthalpy at each point through the field. It would mean the fluid is inviscid and adiabatic in that no mechanism internal to it can change the entropy or enthalpy, but an "outside" means of doing this is permissible. Only the acceleration terms involving the enthalpy and entropy changes in the streamline direction need to be zero.

(5). For the stagnation enthalpy:

$$\bar{V}\cdot\bar{\nabla}H = 0 = V_r\frac{\partial H}{\partial r} + \frac{V_\theta}{r}\frac{\partial H}{\partial \theta} + V_z\frac{\partial H}{\partial z} \qquad \text{(A4.47)}$$

From Equation (A4.45), since:

$$V_m\frac{\partial H}{\partial m} = V_r\frac{\partial H}{\partial r} + V_z\frac{\partial H}{\partial z}$$

$$\bar{V}\cdot\bar{\nabla}H = 0 = V_m\frac{\partial H}{\partial m} + \frac{V_\theta}{r}\frac{\partial H}{\partial \theta} \qquad \text{(A4.48)}$$

For axisymmetric flow, $\frac{\partial H}{\partial \theta} = 0$

Therefore,

$$\frac{\partial H}{\partial m} = 0 \qquad \text{(A4.49)}$$

The same argument applies to S and I, so that:

$$\frac{\partial S}{\partial m} = \frac{\partial I}{\partial m} = 0 \qquad \text{(A4.50)}$$

The r and θ- components of the Crocco equation of motion can now be considered with the above assumptions (Equations A4.29, A4.30). These expressed with Equation (A4.37) become:

The r-component:

$$\frac{V_\theta}{r}\left(\frac{\partial(rV_\theta)}{\partial r} - \frac{\partial V_r}{\partial \theta}\right) - V_z\left(\frac{\partial V_r}{\partial z} - \frac{\partial V_z}{\partial r}\right) = \frac{\partial H}{\partial r} - t\frac{\partial S}{\partial r} \qquad \text{(A4.51)}$$

The θ-component:

$$-\frac{V_r}{r}\left(\frac{\partial(rV_\theta)}{\partial r} - \frac{\partial V_r}{\partial \theta}\right) + \frac{V_z}{r}\left(\frac{\partial V_z}{\partial \theta} - \frac{\partial(rV_\theta)}{\partial z}\right) = \frac{1}{r}\left(\frac{\partial H}{\partial \theta} - t\frac{\partial S}{\partial \theta}\right) \qquad \text{(A4.52)}$$

Assuming that H and S have no θ-derivatives, which generally cannot be done, but can be temporarily assumed to be so, then arranging the circumferential component Equation (A4.52) gives:

$$V_z\left(\frac{\partial V_z}{\partial \theta} - \frac{\partial(rV_\theta)}{\partial z}\right) - V_r\left(\frac{\partial(rV_\theta)}{\partial r} - \frac{\partial V_r}{\partial \theta}\right) = 0$$

$$V_r\frac{\partial V_r}{\partial \theta} + V_z\frac{\partial V_z}{\partial \theta} = V_r\frac{\partial(rV_\theta)}{\partial r} + V_z\frac{\partial(rV_\theta)}{\partial z} \qquad \text{(A4.53)}$$

$$\frac{1}{2}\left(\frac{\partial V_r^2}{\partial \theta} + \frac{\partial V_z^2}{\partial \theta}\right) = V_m\frac{\partial(rV_\theta)}{\partial m}$$

$$\frac{1}{2}\left(\frac{\partial V_m^2}{\partial \theta}\right) = V_m \frac{\partial (rV_\theta)}{\partial m}$$
$$V_m \frac{\partial V_m}{\partial \theta} = V_m \frac{\partial (rV_\theta)}{\partial m} \qquad \text{(A4.54)}$$
$$\frac{\partial V_m}{\partial \theta} = \frac{\partial (rV_\theta)}{\partial m}$$

For a truly axisymmetric flow, then $\frac{\partial V_m}{\partial \theta} = 0$, so the equation above then states that the momentum along the meridional projection of a streamline in the absence of circumferential velocity or pressure gradient needs to be constant. Within a blade row, this equation can be used to calculate the blade surface pressure distribution as a function of the meridional rate of change or rV_θ.

For the radial component of the equation of motion, the components of vorticity are usefully first rearranged by first, replacing all V_r terms by $V_m \sin\phi$, and all $V_m \cos\phi$. All z-derivatives are replaced by m and r-derivatives. $\frac{\partial V_m}{\partial \theta}$ term is replaced by Equation (A4.54).

Radial component of the equation of motion:

$$\frac{V_\theta}{r}\left(\frac{\partial (rV_\theta)}{\partial r} - \frac{\partial V_r}{\partial \theta}\right) + V_z\left(\frac{\partial V_r}{\partial z} - \frac{\partial V_z}{\partial r}\right) = \frac{\partial H}{\partial r} - t\frac{\partial S}{\partial r} \qquad \text{(A4.51)}$$

Vorticity components:

Radial vorticity component rearrangement:

$$\left(\bar{\nabla}\times\bar{V}\right)_r = \frac{1}{r}\left(\frac{\partial V_z}{\partial\theta} - \frac{\partial(rV_\theta)}{\partial z}\right)$$

$$= \frac{1}{r}\left[\frac{\partial(V_m\cos\phi)}{\partial\theta} - \frac{1}{\cos\phi}\left(\frac{\partial(rV_\theta)}{\partial m} - \sin\phi\frac{\partial(rV_\theta)}{\partial r}\right)\right]$$

$$= \frac{1}{r}\left[V_m\frac{\partial(\cos\phi)}{\partial\theta} + \cos\phi\frac{\partial V_m}{\partial\theta} - \frac{1}{\cos\phi}\frac{\partial(rV_\theta)}{\partial m} + \tan\phi\frac{\partial(rV_\theta)}{\partial r}\right]$$

$$= \frac{1}{r}\left[V_m\left(\frac{\partial(\cos\phi)}{\partial\phi}\frac{\partial\phi}{\partial\theta}\right) + \cos\phi\frac{\partial(rV_\theta)}{\partial m} - \frac{1}{\cos\phi}\frac{\partial(rV_\theta)}{\partial m} + \tan\phi\frac{\partial(rV_\theta)}{\partial r}\right]$$

$$= \frac{1}{r}\left[-V_m\left(\sin\phi\frac{\partial\phi}{\partial\theta}\right) + \cos\phi\frac{\partial(rV_\theta)}{\partial m} - \frac{1}{\cos\phi}\frac{\partial(rV_\theta)}{\partial m} + \tan\phi\frac{\partial(rV_\theta)}{\partial r}\right]$$

$$= \frac{1}{r}\left[-V_m\left(\frac{\cos\phi}{\cos\phi}\sin\phi\frac{\partial\phi}{\partial\theta}\right) + \frac{\partial(rV_\theta)}{\partial m}\left(\cos\phi - \frac{1}{\cos\phi}\right) + \tan\phi\frac{\partial(rV_\theta)}{\partial r}\right]$$

$$= \frac{1}{r}\left[-\frac{V_m^2}{V_m}\left(\cos\phi\tan\phi\frac{\partial\phi}{\partial\theta}\right) + \frac{\partial(rV_\theta)}{\partial m}\left(\frac{\cos^2\phi - 1}{\cos\phi}\right) + \tan\phi\frac{\partial(rV_\theta)}{\partial r}\right]$$

$$= \frac{1}{r}\left[-\tan\phi V_m^2\left(\frac{\cos\phi}{V_m}\right)\frac{\partial\phi}{\partial\theta} + \frac{\partial(rV_\theta)}{\partial m}\left(\frac{\sin^2\phi}{\cos\phi}\right) + \tan\phi\frac{\partial(rV_\theta)}{\partial r}\right]$$

$$= \frac{\tan\phi}{r}\left[-V_m^2\left(\frac{\cos\phi}{V_m}\right)\frac{\partial\phi}{\partial\theta} + \frac{\partial(rV_\theta)}{\partial m}\sin\phi + \frac{\partial(rV_\theta)}{\partial r}\right] \qquad \text{(A4.55)}$$

$$\therefore \left(\bar{\nabla}\times\bar{V}\right)_r = \frac{\tan\phi}{r}\left[\frac{\partial(rV_\theta)}{\partial r} + \sin\phi\frac{\partial(rV_\theta)}{\partial m} - V_m^2\left(\frac{\cos\phi}{V_m}\right)\frac{\partial\phi}{\partial\theta}\right]$$

Circumferential vorticity component rearrangement:

$$\left(\bar{\nabla}\times\bar{V}\right)_\theta = \left(\frac{\partial V_r}{\partial z} - \frac{\partial V_z}{\partial r}\right)$$

$$= \left[\frac{1}{\cos\phi}\left(\frac{\partial(V_r)}{\partial m} - \sin\phi\frac{\partial(V_r)}{\partial r}\right) - \frac{\partial V_z}{\partial r}\right]$$

$$= \left[\frac{1}{\cos\phi}\left(\frac{\partial(V_m\sin\phi)}{\partial m} - \sin\phi\frac{\partial(V_m\sin\phi)}{\partial r}\right) - \frac{\partial(V_m\cos\phi)}{\partial r}\right]$$

$$= \left[\frac{1}{\cos\phi}\left(V_m\frac{\partial(\sin\phi)}{\partial m} + \sin\phi\frac{\partial V_m}{\partial m} - \sin\phi V_m\frac{\partial(\sin\phi)}{\partial r} - \sin^2\phi\frac{\partial V_m}{\partial r}\right) - V_m\frac{\partial(\cos\phi)}{\partial r} - \cos\phi\frac{\partial V_m}{\partial r}\right]$$

$$= \left[\frac{1}{\cos\phi}\left(V_m\cos\phi\frac{\partial\phi}{\partial m} + \sin\phi\frac{\partial V_m}{\partial m} - \sin\phi V_m\cos\phi\frac{\partial\phi}{\partial r} - \sin^2\phi\frac{\partial V_m}{\partial r}\right) + V_m\sin\phi\frac{\partial\phi}{\partial r} - \cos\phi\frac{\partial V_m}{\partial r}\right]$$

$$= \left[\frac{1}{\cos\phi}\left(V_m\cos\phi\frac{\partial\phi}{\partial m} + \sin\phi\frac{\partial V_m}{\partial m} - \sin^2\phi\frac{\partial V_m}{\partial r}\right) - \cos\phi\frac{\partial V_m}{\partial r}\right]$$

$$= \left[\frac{1}{\cos\phi}\left(V_m\cos\phi\frac{\partial\phi}{\partial m} + \sin\phi\frac{\partial V_m}{\partial m} - \sin^2\phi\frac{\partial V_m}{\partial r} - \cos^2\phi\frac{\partial V_m}{\partial r}\right)\right]$$

$$= \left[\frac{1}{V_m\cos\phi}\left(V_m^2\cos\phi\frac{\partial\phi}{\partial m} + V_m\sin\phi\frac{\partial V_m}{\partial m} - V_m\frac{\partial V_m}{\partial r}\right)\right]$$

$$= \left[\frac{1}{V_m\cos\phi}\left(V_m^2\left(\cos\phi\frac{\partial\phi}{\partial m} + \frac{\sin\phi}{V_m}\frac{\partial V_m}{\partial m}\right) - \frac{1}{2}\frac{\partial V_m^2}{\partial r}\right)\right]$$

since $\dfrac{\partial\phi}{\partial m} = -\dfrac{1}{r_m}$

$$\therefore \left(\bar{\nabla}\times\bar{V}\right)_\theta = \left[\frac{1}{V_m\cos\phi}\left(V_m^2\left(\frac{\sin\phi}{V_m}\frac{\partial V_m}{\partial m} - \frac{\cos\phi}{r_m}\right) - \frac{1}{2}\frac{\partial V_m^2}{\partial r}\right)\right]$$

(A4.56)

Axial vorticity component rearrangement:

$$
\begin{aligned}
\left(\bar{\nabla}\times\bar{V}\right)_z &= \frac{1}{r}\left(\frac{\partial(rV_\theta)}{\partial r}-\frac{\partial V_r}{\partial\theta}\right)\\
&= \frac{1}{r}\left[\frac{\partial(rV_\theta)}{\partial r}-\frac{\partial(V_m\sin\phi)}{\partial\theta}\right]\\
&= \frac{1}{r}\left[\frac{\partial(rV_\theta)}{\partial r}-V_m\frac{\partial(\sin\phi)}{\partial\theta}-\sin\phi\frac{\partial V_m}{\partial\theta}\right]\\
&= \frac{1}{r}\left[\frac{\partial(rV_\theta)}{\partial r}-V_m\cos\phi\frac{\partial\phi}{\partial\theta}-\sin\phi\frac{\partial(rV_\theta)}{\partial m}\right]\\
&= \frac{1}{r}\left[\frac{\partial(rV_\theta)}{\partial r}-V_m^2\left(\frac{\cos\phi}{V_m}\right)\frac{\partial\phi}{\partial\theta}-\sin\phi\frac{\partial(rV_\theta)}{\partial m}\right]\\
\therefore\left(\bar{\nabla}\times\bar{V}\right)_z &= \frac{1}{r}\left[\frac{\partial(rV_\theta)}{\partial r}-\sin\phi\frac{\partial(rV_\theta)}{\partial m}-V_m^2\left(\frac{\cos\phi}{V_m}\right)\frac{\partial\phi}{\partial\theta}\right]
\end{aligned}
\qquad \text{(A4.57)}
$$

The sign convention for radius of curvature of the meridional projection of the streamline is arbitrarily set as negative for a concave upwards streamline, and positive for a concave down streamline as shown in Fig. 4.2.

$$\frac{1}{r_m}=-\frac{\partial\phi}{\partial m} \qquad \text{(A4.58)}$$

The term containing $\frac{\partial V_m}{\partial m}$ is the acceleration component as a result of rate of change of meridional velocity in the meridional direction. Evaluation of this using the differential form of the continuity equation results in the following result for the axisymmetric case:

$$\frac{\sin\phi}{V_m}\frac{\partial V_m}{\partial m}=-\frac{\left(1+M_\theta^2+\frac{r}{r_m\cos\phi}\right)\frac{\sin^2\phi}{r}+\tan\phi\frac{\partial\varphi}{\partial r}}{1-M_m^2} \qquad \text{(A4.59)}$$

Here, $M_\theta=\frac{V_\theta}{a}$ and $M_m=\frac{V_m}{a}$

The r-component of the equation of motion can be solved explicitly for V_m if $\frac{\sin\phi}{V_m}\frac{\partial V_m}{\partial m}$ is known. However, M_m and the sonic velocity a require a prior knowledge of V_m. An iterative solution is required for the solution. In this form of the streamline curvature method, the

denominator of Equation (A4.59) contains a $\left(1-M_m^2\right)$ term so that a singularity occurs when $M_m = 1.0$.

$\frac{\partial\phi}{\partial\theta}$ is zero for the axisymmetric case. This refers to a mean streamsurface around the annulus. In the actual flow, any streamsurface passing through a blade row will warp and twist, so that $\frac{\partial\phi}{\partial\theta}$ is not zero. The streamsurface twist contributes an acceleration term to the equation of motion. The twisting of the streamsurface is due to secondary flow. $\frac{\partial\phi}{\partial\theta}$ can be explicitly found by secondary flow problem mathematical techniques. It is non-zero whenever there is a streamwise component of vorticity.

The components of vorticity for axisymmetric flows are therefore:

$$\left(\bar{\nabla}\times\bar{V}\right)_r = \frac{\tan\phi}{r}\left[\frac{\partial(rV_\theta)}{\partial r}\right] \tag{A4.60}$$

$$\left(\bar{\nabla}\times\bar{V}\right)_\theta = \left[\frac{1}{V_m\cos\phi}\left(V_m^2\left(\frac{\sin\phi}{V_m}\frac{\partial V_m}{\partial m}-\frac{\cos\phi}{r_m}\right)-\frac{1}{2}\frac{\partial V_m^2}{\partial r}\right)\right] \tag{A4.61}$$

$$\left(\bar{\nabla}\times\bar{V}\right)_z = \frac{1}{r}\left[\frac{\partial(rV_\theta)}{\partial r}\right] \tag{A4.62}$$

The aim is to obtain the r-component of the equation of motion. First, Q is defined:

$$Q = e^{-\frac{S}{C_p}} = \frac{\left(\frac{P_{in}}{p}\right)^{\frac{\gamma-1}{\gamma}}}{\frac{T_{in}}{t}} \tag{A4.63}$$

or

$$S = -C_p \ln Q \tag{A4.64}$$

Given that

$$C_p t = H - \frac{V^2}{2}$$
$$= H - \frac{\left(V_r^2 + V_\theta^2 + V_z^2\right)}{2} \qquad \text{(A4.65)}$$
$$= H - \frac{\left(V_m^2 + V_\theta^2\right)}{2}$$

The RHS of the r-component of the Crocco equation Equation (A4.51):

$$\left(\bar{\nabla}H - t\bar{\nabla}S\right)_r = \frac{\partial H}{\partial r} - t\frac{\partial S}{\partial r}$$
$$= \frac{\partial H}{\partial r} - t\left(-C_p \frac{1}{Q}\frac{\partial Q}{\partial r}\right)$$
$$= \frac{\partial H}{\partial r} + \left(H - \frac{V_m^2}{2} - \frac{V_\theta^2}{2}\right)\frac{1}{Q}\frac{\partial Q}{\partial r} \qquad \text{(A4.66)}$$
$$= \frac{\partial H}{\partial r} + \frac{H}{Q}\frac{\partial Q}{\partial r} - \frac{V_\theta^2}{2}\left(\frac{1}{Q}\frac{\partial Q}{\partial r}\right) - \frac{V_m^2}{2}\left(\frac{1}{Q}\frac{\partial Q}{\partial r}\right)$$
$$= \frac{1}{Q}\frac{\partial HQ}{\partial r} - \frac{V_\theta^2}{2}\left(\frac{1}{Q}\frac{\partial Q}{\partial r}\right) - \frac{V_m^2}{2}\left(\frac{1}{Q}\frac{\partial Q}{\partial r}\right)$$

This is used with the LHS of the radial component of the equation of motion Equation (A4.51) and with the vorticity equations:

$$\frac{V_\theta}{r}\left(\frac{\partial(rV_\theta)}{\partial r} - \frac{\partial V_r}{\partial \theta}\right) - V_z\left(\frac{\partial V_r}{\partial z} - \frac{\partial V_z}{\partial r}\right) = \frac{\partial H}{\partial r} - t\frac{\partial S}{\partial r}$$

$$V_\theta\left(\bar{\nabla}\times\bar{V}\right)_z - V_z\left(\bar{\nabla}\times\bar{V}\right)_\theta = \frac{1}{Q}\frac{\partial HQ}{\partial r} - \frac{V_\theta^2}{2}\left(\frac{1}{Q}\frac{\partial Q}{\partial r}\right) - \frac{V_m^2}{2}\left(\frac{1}{Q}\frac{\partial Q}{\partial r}\right)$$

$$\frac{V_\theta}{r}\left[\frac{\partial(rV_\theta)}{\partial r}\right] - \left[\frac{V_z}{V_m\cos\phi}\left(V_m^2\left(\frac{\sin\phi}{V_m}\frac{\partial V_m}{\partial m} - \frac{\cos\phi}{r_m}\right) - \frac{1}{2}\frac{\partial V_m^2}{\partial r}\right)\right] = \qquad \text{(A4.67)}$$
$$\frac{1}{Q}\frac{\partial HQ}{\partial r} - \frac{V_\theta^2}{2}\left(\frac{1}{Q}\frac{\partial Q}{\partial r}\right) - \frac{V_m^2}{2}\left(\frac{1}{Q}\frac{\partial Q}{\partial r}\right)$$

Since $V_z = V_m\cos\phi$, rearranging this equation into a differential equation for V_m leads to:

$$\frac{1}{2}\frac{\partial V_m^2}{\partial r}-\left[V_m^2\left(\frac{\sin\phi}{V_m}\frac{\partial V_m}{\partial m}-\frac{\cos\phi}{r_m}\right)\right]+\frac{V_m^2}{2}\left(\frac{1}{Q}\frac{\partial Q}{\partial r}\right)=$$
$$\frac{1}{Q}\frac{\partial HQ}{\partial r}-\frac{V_\theta^2}{2}\left(\frac{1}{Q}\frac{\partial Q}{\partial r}\right)-\frac{V_\theta}{r}\left[\frac{\partial(rV_\theta)}{\partial r}\right]$$

$$\frac{\partial V_m^2}{\partial r}-2\left(\frac{\sin\phi}{V_m}\frac{\partial V_m}{\partial m}-\frac{\cos\phi}{r_m}\right)V_m^2+2\left(\frac{1}{2}\left(\frac{1}{Q}\frac{\partial Q}{\partial r}\right)\right)V_m^2=$$
$$2\frac{1}{Q}\frac{\partial HQ}{\partial r}-2\frac{V_\theta^2}{2}\left(\frac{1}{Q}\frac{\partial Q}{\partial r}\right)-2\frac{V_\theta}{r}\left[\frac{\partial(rV_\theta)}{\partial r}\right]$$

$$\frac{\partial V_m^2}{\partial r}+2\left[-\frac{\sin\phi}{V_m}\frac{\partial V_m}{\partial m}+\frac{\cos\phi}{r_m}+\frac{1}{2}\left(\frac{1}{Q}\frac{\partial Q}{\partial r}\right)\right]V_m^2=$$
$$2\left[\frac{1}{Q}\frac{\partial HQ}{\partial r}-\frac{V_\theta}{r}\frac{\partial(rV_\theta)}{\partial r}-\frac{V_\theta^2}{2}\left(\frac{1}{Q}\frac{\partial Q}{\partial r}\right)\right] \qquad (A4.68)$$

This can be simplified in the form of:

$$\frac{\partial V_m^2}{\partial r}+C(r)V_m^2=D(r) \qquad (A4.69)$$

$$C(r)=2\left[-\frac{\sin\phi}{V_m}\frac{\partial V_m}{\partial m}+\frac{\cos\phi}{r_m}+\frac{1}{2}\left(\frac{1}{Q}\frac{\partial Q}{\partial r}\right)\right] \qquad (A4.70)$$

$$D(r)=2\left[\frac{1}{Q}\frac{\partial HQ}{\partial r}-\frac{V_\theta}{r}\frac{\partial(rV_\theta)}{\partial r}-\frac{V_\theta^2}{2}\left(\frac{1}{Q}\frac{\partial Q}{\partial r}\right)\right] \qquad (A4.71)$$

If C(r) and D(r) are known functions of r, Equation (A4.69) can be treated as a linear differential equation with constant coefficients in one independent variable r. The solution is then:

$$V_m^2=Ke^{-\int C(r)dr}+e^{-\int C(r)dr}\int e^{-\int C(r)dr}D(r)dr \qquad (A4.72)$$

K is a constant of integration which must satisfy the continuity condition.

From Equation (A4.69):

$$2V_m \frac{\partial V_m}{\partial r} = D(r) - C(r)V_m^2$$

$$\frac{\partial V_m}{\partial r} = \left(\frac{1}{2}D(r)\right)\frac{1}{V_m} - \left(\frac{1}{2}C(r)\right)V_m \qquad \text{(A4.73)}$$

which is a better form than Equation (A4.72) for computer calculations.

So far, the static pressure gradient has been replaced by the equivalent in terms of stagnation enthalpy and entropy gradients.

The radial component of the equation of motion equivalent to Equation (A4.68) is derived from Equation (A4.29) with the appropriate assumptions:

$$\frac{\partial\left(\frac{1}{2}V^2\right)}{\partial r} - \frac{V_\theta}{r}\left(\frac{\partial(rV_\theta)}{\partial r} - \frac{\partial V_r}{\partial \theta}\right) + V_z\left(\frac{\partial V_r}{\partial z} - \frac{\partial V_z}{\partial r}\right) = -\frac{1}{\rho}\frac{\partial p}{\partial r} \qquad \text{(A4.74)}$$

$$\frac{1}{\rho}\frac{\partial p}{\partial r} = -\frac{\partial\left(\frac{1}{2}V^2\right)}{\partial r} + \frac{V_\theta}{r}\left(\frac{\partial(rV_\theta)}{\partial r} - \frac{\partial V_r}{\partial \theta}\right) - V_z\left(\frac{\partial V_r}{\partial z} - \frac{\partial V_z}{\partial r}\right)$$

$$= -\frac{\partial\left(\frac{1}{2}V^2\right)}{\partial r} + V_\theta\left(\vec{\nabla}\times\vec{V}\right)_z - V_z\left(\vec{\nabla}\times\vec{V}\right)_\theta$$

$$= -\frac{\partial\left(\frac{1}{2}V^2\right)}{\partial r} + \frac{V_\theta}{r}\left[\frac{\partial(rV_\theta)}{\partial r}\right] - \left[\frac{V_z}{V_m\cos\phi}\left(V_m^2\left(\frac{\sin\phi}{V_m}\frac{\partial V_m}{\partial m} - \frac{\cos\phi}{r_m}\right) - \frac{1}{2}\frac{\partial V_m^2}{\partial r}\right)\right]$$

$$= -\frac{\partial\frac{1}{2}\left[V_r^2 + V_\theta^2 + V_z^2\right]}{\partial r} + \frac{V_\theta}{r}\left[r\frac{\partial V_\theta}{\partial r} + V_\theta\frac{\partial r}{\partial r}\right] - \left[\frac{V_z}{V_z}\left(V_m^2\left(\frac{\sin\phi}{V_m}\frac{\partial V_m}{\partial m} - \frac{\cos\phi}{r_m}\right) - \frac{1}{2}\frac{\partial V_m^2}{\partial r}\right)\right]$$

$$= -\frac{\partial\frac{1}{2}\left[V_m^2 + V_\theta^2\right]}{\partial r} + \frac{V_\theta}{r}\left[r\frac{\partial V_\theta}{\partial r} + V_\theta\right] - \left[V_m^2\left(\frac{\sin\phi}{V_m}\frac{\partial V_m}{\partial m} - \frac{\cos\phi}{r_m}\right)\right] + \frac{1}{2}\frac{\partial V_m^2}{\partial r}$$

$$= -\frac{\partial\frac{1}{2}\left[V_m^2 + V_\theta^2\right]}{\partial r} + \frac{V_\theta}{r}\left[r\frac{\partial V_\theta}{\partial r} + V_\theta\right] - \left[V_m^2\left(\frac{\sin\phi}{V_m}\frac{\partial V_m}{\partial m} - \frac{\cos\phi}{r_m}\right)\right] + \frac{1}{2}\frac{\partial V_m^2}{\partial r}$$

$$= -V_m\frac{\partial V_m}{\partial V_r} - V_\theta\frac{\partial V_\theta}{\partial V_r} + V_\theta\frac{\partial V_\theta}{\partial V_r} + \frac{V_\theta^2}{r} + V_m^2\left(\frac{\cos\phi}{r_m} - \frac{\sin\phi}{V_m}\frac{\partial V_m}{\partial m}\right) + V_m\frac{\partial V_m}{\partial r}$$

$$\therefore \frac{1}{\rho}\frac{\partial p}{\partial r} = \frac{V_\theta^2}{r} + V_m^2\left(\frac{\cos\phi}{r_m} - \frac{\sin\phi}{V_m}\frac{\partial V_m}{\partial m}\right) \qquad \text{(A4.75)}$$

Now there are three basic forms of the equation of motion, Equations (A4.72), (A4.73), and (A4.75). How are these suited to the indirect, axisymmetric turbomachine problem. The integrated form, Equation (A4.72) is most suited to a hand calculation. The meridional velocity gradient form, Equation (A4.73) is most useful for computer calculations. Equation (A4.75), the static pressure gradient version is as good as (A4.73) for the design case, but not for off-design computations, or to the case where measured test data is input.

APPENDIX 5. SEPARATE EXHAUST TURBOFAN ENGINE SIMULATION

The following flowchart shows the original scheme for the separate exhaust turbofan on the left (as used in **Chapter 3**) and the amended scheme as described in section **4.4.1** and carried out in section **4.7.3**. Note that the fan calculations in these schemes are replaced by the 2D-HBPR, inner and outer and 2D-LBPR fan models for the work done in **Chapter 4**, and by WholeMap, ZonalMap or DirectMap fan models in Chapter **4**.

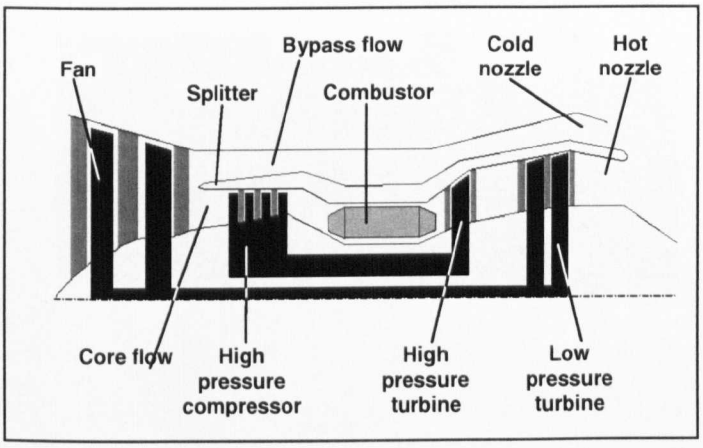

Fig. A5.1 2-shaft separated nozzle turbofan schematic.

Original turbofan iteration scheme (Chapter 3)

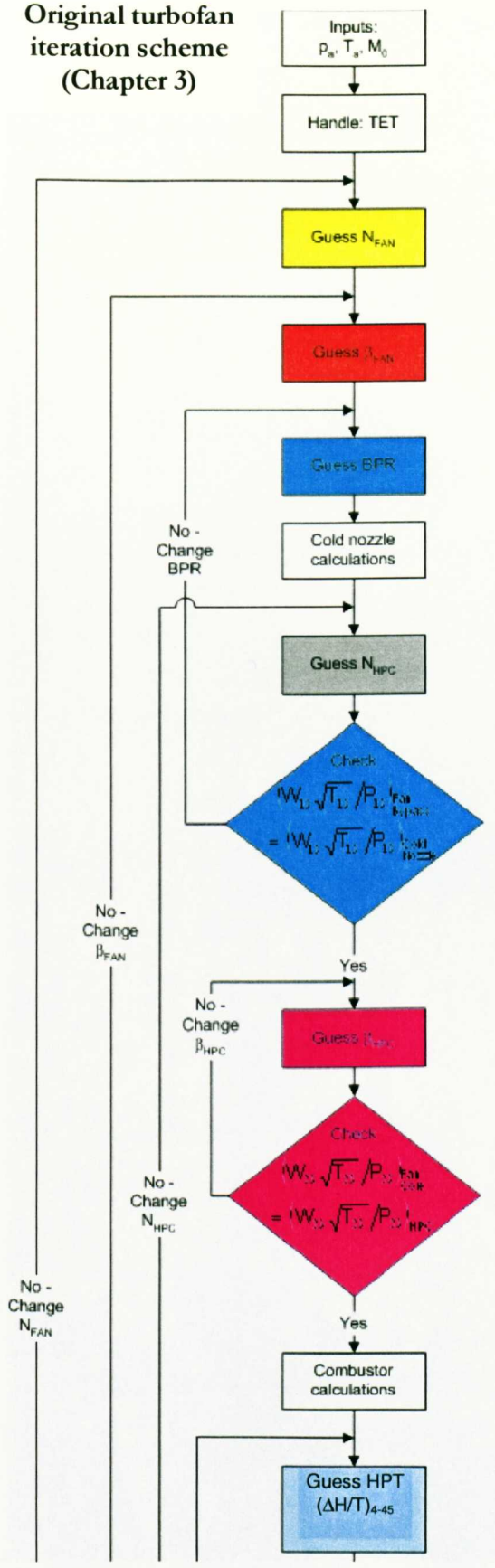

Amended turbofan iteration scheme (Chapter 4)

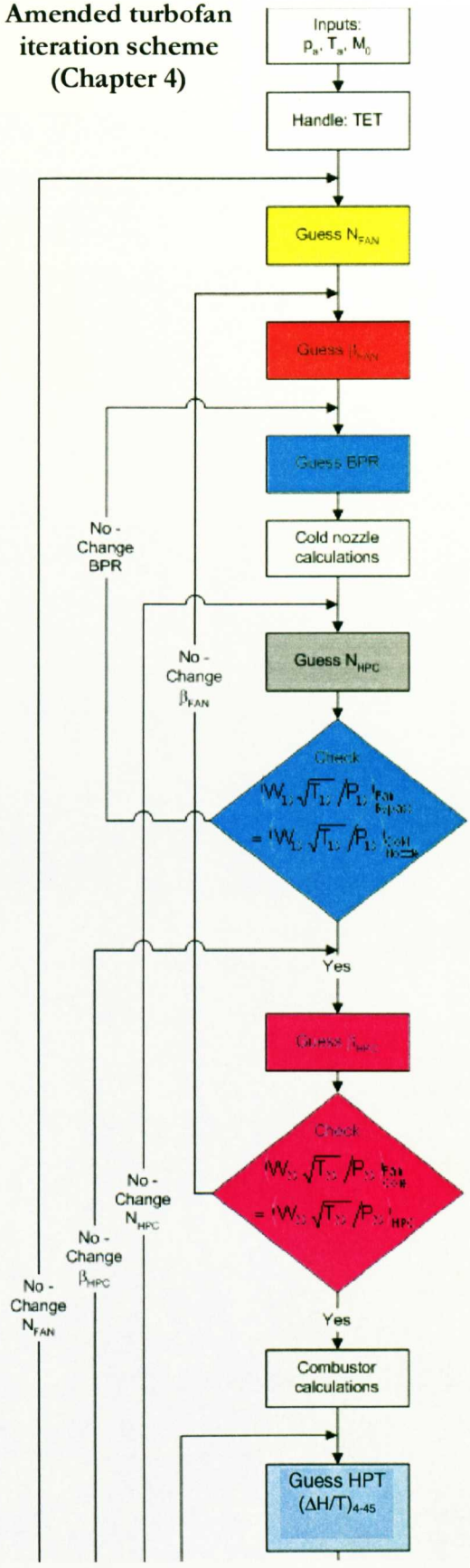

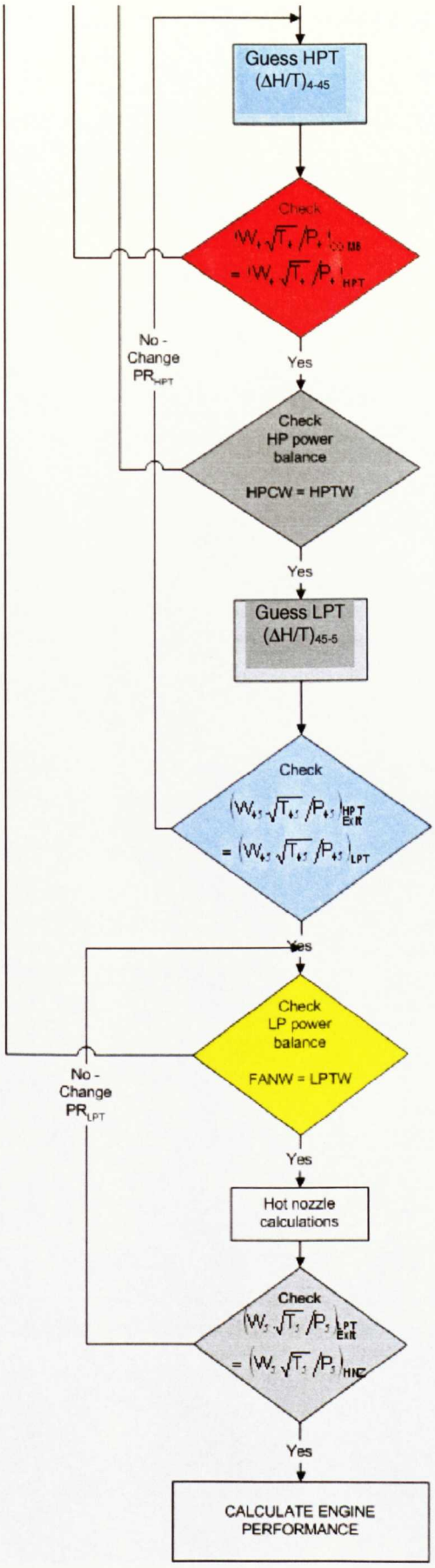
Guess HPT
(ΔH/T)4-45
Check
$W_4\sqrt{T_4}/P_4$ CD Exit = $W_4\sqrt{T_4}/P_4$ HPT
No - Change PR_{HPT}
Yes
Check HP power balance
HPCW = HPTW
Yes
Guess LPT
(ΔH/T)45-5
Check
$(W_5\sqrt{T_5}/P_5)_{HPT\ Exit}$ = $(W_5\sqrt{T_5}/P_5)_{LPT}$
Yes
Check LP power balance
FANW = LPTW
No - Change PR_{LPT}
Yes
Hot nozzle calculations
Check
$(W_5\sqrt{T_5}/P_5)_{LPT\ Exit}$ = $(W_5\sqrt{T_5}/P_5)_{HNC}$
Yes
CALCULATE ENGINE PERFORMANCE

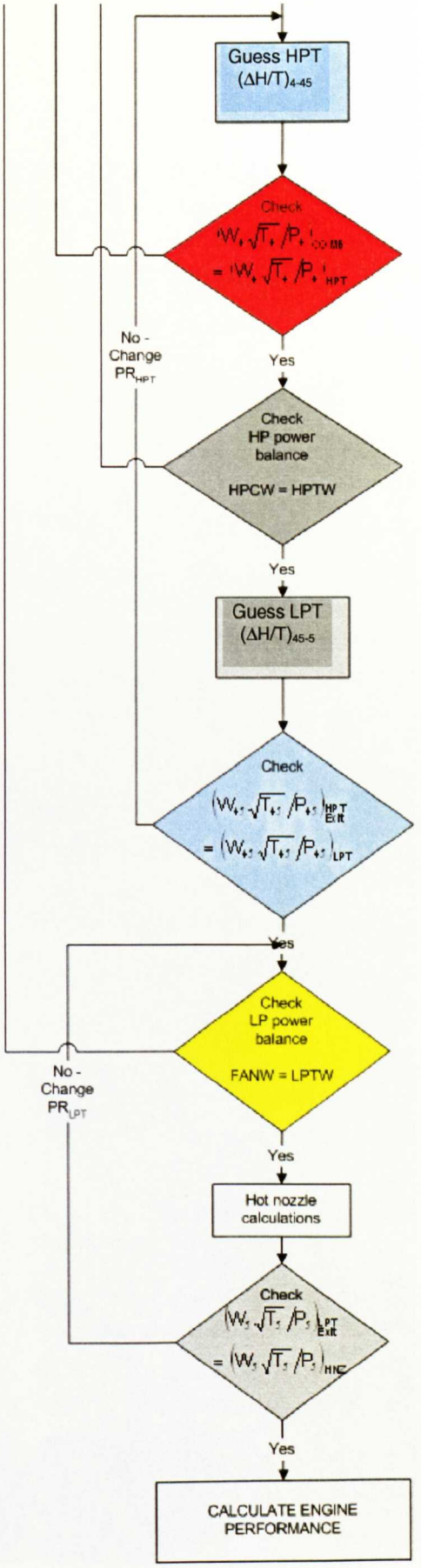
Guess HPT
(ΔH/T)4-45
Check
$W_4\sqrt{T_4}/P_4$ CD Exit = $W_4\sqrt{T_4}/P_4$ HPT
No - Change PR_{HPT}
Yes
Check HP power balance
HPCW = HPTW
Yes
Guess LPT
(ΔH/T)45-5
Check
$(W_5\sqrt{T_5}/P_5)_{HPT\ Exit}$ = $(W_5\sqrt{T_5}/P_5)_{LPT}$
Yes
Check LP power balance
FANW = LPTW
No - Change PR_{LPT}
Yes
Hot nozzle calculations
Check
$(W_5\sqrt{T_5}/P_5)_{LPT\ Exit}$ = $(W_5\sqrt{T_5}/P_5)_{HNC}$
Yes
CALCULATE ENGINE PERFORMANCE

APPENDIX 6. 2D-HBPR FAN MODEL

The following flowchart shows the general calculation procedure for 2D-HBPR fan.

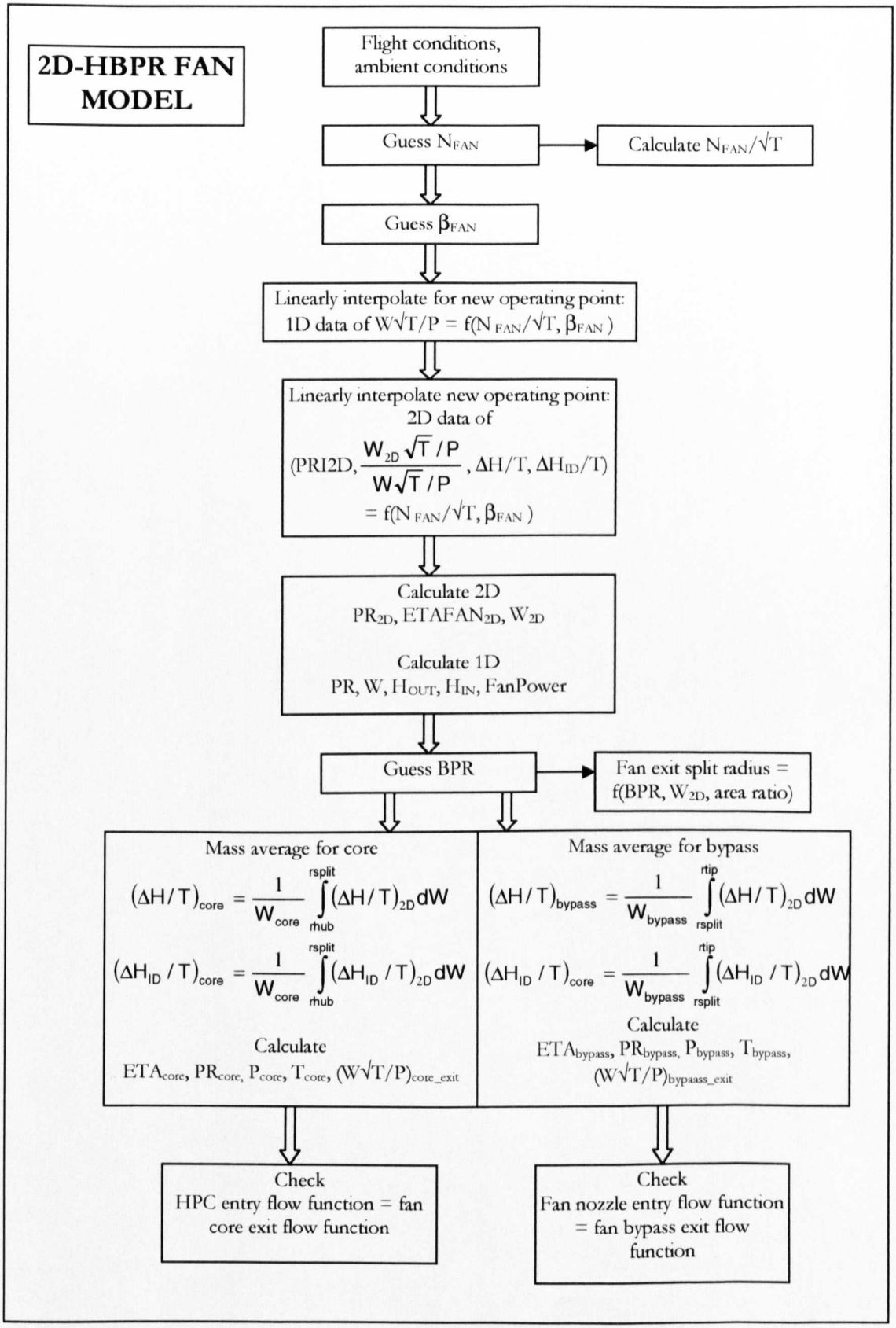

APPENDIX 7. 2D-LBPR FAN MODEL

The following flowchart shows the general calculation procedure for 2D-HBPR fan.

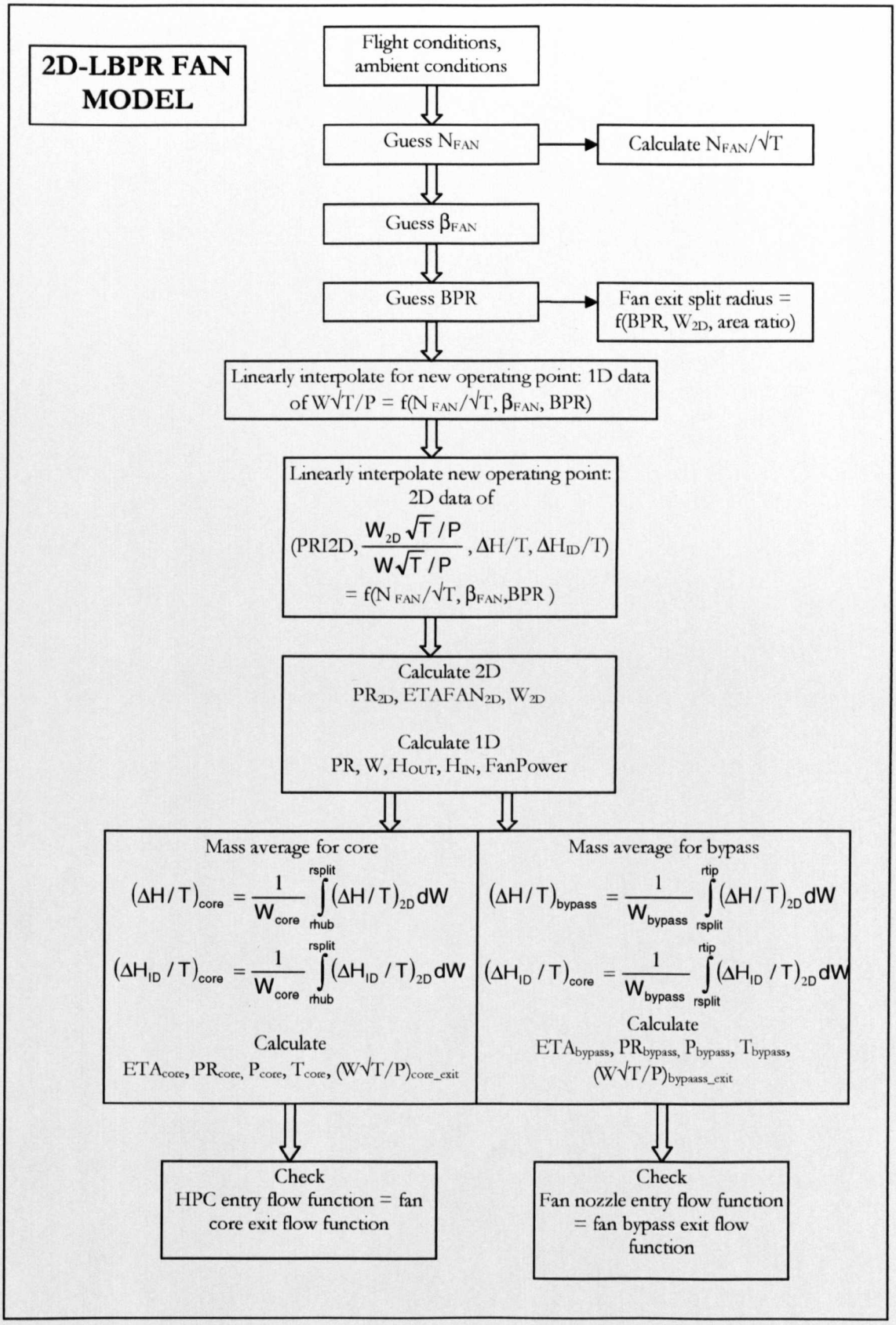

APPENDIX 8. INNER AND OUTER FAN MAP MODEL

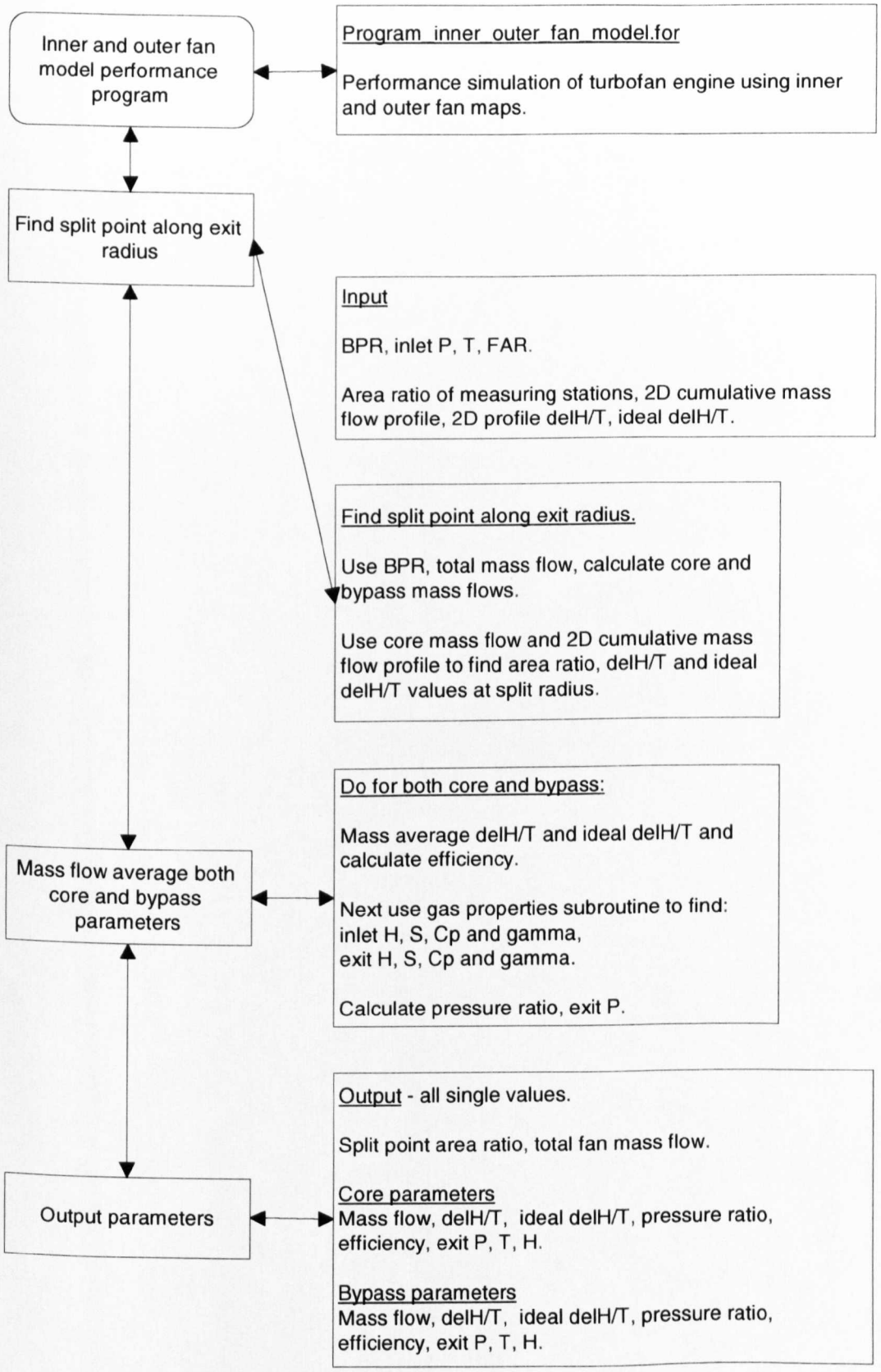

APPENDIX 9. INNER AND OUTER FAN MAP GENERATOR